FINAL REPORT

FHWA/IN/JTRP-2001/20

Study of the Performance of Acoustic Barriers for Indiana Toll Roads

By

Sam Sanghoon Suh
Research Assistant

Luc Mongeau
Professor

J. Stuart Bolton
Professor

School of Mechanical Engineering
Purdue University

Joint Highway Research Program
Project No. C-36-67EEE
File No. 9-10-56
SPR-2418

Prepared in Cooperation with the
Indiana Department of Transportation
and the
U.S. Department of Transportation
Federal Highway Administration

Purdue University
West Lafayette, IN 47907
December 2001

TECHNICAL REPORT STANDARD TITLE PAGE

1. Report No.	2. Government Accession No.	3. Recipient's Catalog No.
FHWA/IN/JTRP-2001/20		

4. Title and Subtitle	5. Report Date
Study of the Performance of Acoustic Barriers for Indiana Toll Roads	December 2001
	6. Performing Organization Code

7. Author(s)	8. Performing Organization Report No.
Sam Sanghoon Suh, Luc Mongeau, and J. Stuart Bolton	FHWA/IN/JTRP-2001/20

9. Performing Organization Name and Address	10. Work Unit No.
Joint Transportation Research Program 1284 Civil Engineering Building Purdue University West Lafayette, IN 47907-1284	
	11. Contract or Grant No. SPR-2418

12. Sponsoring Agency Name and Address	13. Type of Report and Period Covered
Indiana Department of Transportation State Office Building 100 North Senate Avenue Indianapolis, IN 46204	Final Report
	14. Sponsoring Agency Code

15. Supplementary Notes

Prepared in cooperation with the Indiana Department of Transportation and Federal Highway Administration.

16. Abstract

The purpose of this study was to optimize the geometry and the acoustic properties of sound barriers for traffic noise applications. The approach consisted of developing and validating boundary element predictive models, which were subsequently exercised in order to refine the barrier characteristic and determine optimized configurations.

The simple geometry of a circular disk was chosen to validate the boundary element model in the first part of this work. Experiments were performed in an anechoic chamber to validate the numerical model. Complex barrier geometries were then investigated to study the effects of geometry on sound barrier performance. Boundary element models were used to quantify the accuracy of existing, approximate diffraction-based models. Diffraction-based models have been widely applied in noise control engineering applications owing to their relative ease of use. Recent research suggests that multi-path diffraction components should be summed on a phase-coherent basis instead of on an energy basis. The accuracy of a phase-coherent diffraction model has been verified against the boundary element solution and the limitations of the diffraction model are discussed for both the case of infinite length barriers and barriers of finite length. A new barrier performance metric, based on the sound power propagating within the shadow zone was also investigated. It was found that variation of barrier geometry while maintaining the surface area constant did not yield any meaningful difference in the sound power propagating within the shadow zone.

The performance of straight-edge barriers with various top geometries and sound absorptive treatments was then investigated. Experiments were performed using a finite size barrier in an anechoic chamber to verify the boundary element model. Good agreement was obtained between the results from the numerical model and the experimental data. The most important finding was that absorptive treatment applied to the top of a barrier was more effective at reducing sound levels in the shadow zone than a simple increase of barrier height. The use of the boundary element method to calculate the new barrier sound power performance metric is also discussed in connection with the complex geometry. It is shown that the propagating sound power calculated on a recovery plane in the barrier shadow zone provides a more effective performance measure than insertion loss when comparing the performance of different barrier designs.

17. Key Words	18. Distribution Statement
sound barriers, traffic noise, sound propagation, toll roads	No restrictions. This document is available to the public through the National Technical Information Service, Springfield, VA 22161

19. Security Classif. (of this report)	20. Security Classif. (of this page)	21. No. of Pages	22. Price
Unclassified	Unclassified	153	

Form DOT F 1700.7 (8-69)

TABLE OF CONTENTS

LIST OF FIGURES

1. IMPLEMENTATION REPORT

Boundary element models were developed first for the simple geometry of a circular disk to solve the diffraction problem that is the key to highway noise barrier analysis. Experiments in an anechoic chamber were used to verify the results from the numerical models. After this verification, boundary element models were employed to predict the performance of various disks with complicated edge geometries to study the effect of an obstacle's shape on barrier performance. It was found that complex-shaped barriers do not necessarily offer any net performance benefit when compared with an equivalent uniform barrier. However, it would be worthwhile to develop the boundary element model for the scaled barrier to verify this finding if sufficient computational resources are available.

Scale models that were intended to represent highway noise barrier applications were considered. Experiments were performed first to test the post-processing technique that involves windowing in the time domain and filtering in frequency for the straight barrier of the finite length.

The performance of various barrier configurations was experimentally investigated. This investigation shows that a T-shaped barrier does not yield a significant performance improvement over a simple extended barrier. The use of acoustical treatment on the top of the T-shaped was found to improve the insertion loss, but mostly at high frequencies. It was found that sound absorptive treatment placed on the barrier edge is very effective at increasing the insertion loss at receiver locations in the shadow zone behind the barrier. The development of more sophisticated numerical modelling tools is required to predict the performance of noise barriers when sound absorptive treatments without a hard backing are applied to otherwise rigid barrier structures to predict the performance of this configuration and to optimize the shape of porous

material on the edge of the rigid barriers.

This fact can be utilized to design a new noise barrier in a highway application which is more cost effective than traditional reflective barrier. It maybe also possible to design effective treatments that could be retro-fitted to existing barrier installations to improve their effectiveness in a cost-effective manner.

2. INTRODUCTION

Noise, defined as unwanted or excessive sound, is an undesirable by-product of modern life. While noise emanates from many different sources, transportation noise is especially pervasive and difficult to avoid. There are generally three classes of noise control methods that may be applied to deal with traffic noise problems: i.e., one may deal with the noise generated by the vehicles, the noise generated by the interaction between vehicles tires and the pavement or with the propagation path from the source to the receiver. The latter approach was considered in this study.

A recent study of traffic noise from the Indiana Toll Road in Lake and Porter Counties has been conducted by the Indiana Department of Transportation (INDOT) [1]. This study indicated that in several areas, the noise levels at 152.4 m from the road will exceed the residential noise criterion of 67 dBA in the year 2020. The situation is particularly critical near the section starting at the Service Plaza and extending eastward through the Willow Creek Toll Plaza. The Service Plaza on either side of the road near the west end of this segment is an important source of noise due to the acceleration and deceleration of the vehicles that use this facility.

It is pointed out in the INDOT report that the construction of noise barriers appears to be justified in many areas, including the Portage Barrier Plaza. This assessment was based on predictions made using the Federal Highway Administration (FHWA) Highway Traffic Noise Prediction Model, which takes into consideration traffic volume, speed, and truck percentage. INDOT's policy states that the sound reduction needed to justify a noise barrier is 7 dB. The cost of sound barriers per benefited receiver is the key factor in deciding whether a noise barrier is warranted.

Noise barriers are solid obstructions built between a highway and buildings along the highway. They are designed to reflect sound away from specific areas. Effective

noise barriers can reduce noise levels by ten to fifteen decibels within finite regions. They are usually limited to eight meters in height for structural and aesthetic reasons. Noise barriers can be built out of wood, stucco, concrete, masonry, metal, and other materials. Sound barriers have been used extensively to control traffic noise for several decades. Recent developments in acoustic barrier technology include the study of wind and thermal gradients effects on barrier performance, the effects of surface absorption treatments on barrier performance, and the effect of barrier-top geometry in minimizing scattering into the shadow region. The influence of ground and asphalt acoustic properties, and the effects of berms and other features of the surrounding environment on sound propagation are additional factors that play an important role. Many of these aspects have not yet been taken into consideration in the sound barrier performance predictions made as part of the INDOT investigations. The only barrier design parameter considered in the analysis was the barrier height. Non-uniform geometries, optimal placement, and wind and temperature gradient issues have not been considered.

Many suggestions have been made about the effective modification of straight barriers. Complex geometries have been suggested and prototypes have been installed along highway in some countries. The use of sound absorptive material on barriers was also studied as a way of maximizing barrier performance with limited vertical height. The current estimate of barrier cost is $20 per square foot, installed. The INDOT has placed the acceptable cost per benefited receiver in the $20,000 to $30,000 range. The barrier cost and therefore the feasibility of a barrier installation is directly proportional to its height. Noise barriers with improved design may achieve satisfactory performance for lower barrier heights, which would translate into significant cost savings.

The purpose of this study was first to develop reliable boundary element models that could be used to predict the performance of barrier having complex geometries. The boundary element method has significant advantages over methods based on a geometrical diffraction approach. The main advantage of the boundary element

method is its ability to handle arbitrarily-shaped barriers. The boundary element method is also often more accurate than diffraction-based theory since a solution of the governing wave equation to any required accuracy can be obtained: i.e., for practical purpose, a boundary element solution is exact while diffraction-based solutions are always approximate.

The issue of barrier performance metrics was also addressed in this work. In practice, barrier performance is often quantified using the insertion loss: i.e. the sound pressure level behind the barrier relative to the sound pressure level at the same location without the barrier in place. However, the insertion loss should be used with caution when comparisons are made between different barrier shapes since it quantifies the barrier performance at only a single point within the shadow zone. It was shown in the present work that the insertion loss varies significantly from point to point within the barrier shadow zone, and that this variation makes it difficult to judge the relative performance of candidate barrier designs. It was suggested that the sound power propagating through the complete shadow zone behind a barrier could be a useful metric for quantifying and comparing barrier performance.

In the final part of this work, a comparison was made between the performance of a straight barrier, a barrier with a T-shaped top, and one with an absorptive treatment applied to its top. It was found experimentally that for a given barrier height an absorptive treatment is most effective at reducing the sound level in the shadow zone. Thus it is suggested that the design and implementation of absorptive barrier top treatments be pursued in future work. This approach is particularly attractive since it maybe possible to design effective treatments that could be retro-fitted to existing barrier installations to improve their effectiveness in a cost-effective manner.

3. LITERATURE SURVEY

The numerous articles that have appeared in the literature related to noise barrier design and performance may be categorized as: 1) analytical solutions; 2) empirical models; and 3) experimental investigations. Each of these topics is considered in detail below.

3.1 Analytical Solutions for Prediction of Barrier Performance

The first analytical solution for barrier performance was developed late in the 19th century by Sommerfeld [2]. He considered the case of a harmonic plane wave normally incident on a rigid half-plane. MacDonald [3] solved the same problem for cylindrical and spherical incident waves. The solution contains integrals that are related to an integral representation of the Hankel function. For the case of spherical waves incident on a rigid half plane, the solution involves exponential functions instead of Hankel functions. The series solution takes the form of an integral representation with boundaries extended to infinity.

The classical method for solving partial differential equations by separation of variables can be applied to the problem of diffraction by a rigid half plane or a wedge. The solution appears as an infinite series in general. The slow convergence of the infinite series solution at high frequencies in this case is a well-known problem.

The Fresnel-Kirchhoff assumption which is used extensively in optics can lead to an approximate, and hence more easily used analytical solution. In this approach it is assumed that the normal velocity and the pressure on the rear surface of the barrier are both zero. It is also assumed that the pressure and velocity in the acoustic medium above the barrier is the same as they would be without the barrier.

Keller [4] used the geometrical theory of diffraction to address the barrier problem. In addition, Pierce [5] has formulated an approximate solution to the wave equation

for single-edge diffraction by a semi-infinite wedge. Diffraction-based models such as these are usually coupled with an approximation to the spherical wave reflection coefficient at an impedance plane to account for the effect of ground reflections. The sound field behind the barrier is represented as the sum of terms associated with different paths (i.e., edge diffraction with and without ground reflection) and a complex interference spectrum is formed.

Numerical solutions to the barrier problem were primarily developed for the purpose of handling complex barrier geometries. In the case of there being an unbounded acoustic medium surrounding the noise barrier, there has been extensive use of the boundary element method, in particular. To produce predictions for configurations which are complicated in terms of barrier shape and which may also feature absorptive treatments, the boundary element method is essentially the only practical option. This method has important advantages over methods based on a geometrical theory of diffraction. A main advantage is its flexibility, in that, by positioning the boundary elements appropriately, arbitrary barrier shapes and surface acoustic properties can be accurately represented. Secondly, it has the advantage of accuracy in that, provided that the boundary elements are made a small enough fraction of a wavelength, a solution of the governing wave equations can be produced that is correct to any required accuracy. The disadvantage of the boundary element method is that large computing time and storage is required, especially for barrier designs which vary along their length as well as in cross-section. A further limitation which the boundary element method shares with the diffraction-based methods described before, is that atmospheric effects are not considered, so that only predictions for a neutral, quiescent atmosphere can be easily obtained.

Seznec [6] studied the use of the boundary elements techniques which permit the precise evaluation of the acoustic pressure field diffracted by barriers of different shapes on a flat ground. Hothersall [7] also presented numerical results for the two-dimensional diffraction problems. Duhamel [8] suggested how it is possible to calculate the three-dimensional sound pressure from solutions of simpler problems

defined on the two-dimensional domain surrounding the cross-section of the barrier.

Effects of various barrier geometries were studied by Hothersall et al. [9] for barriers with caps having T, Y and arrow shapes following a boundary element approach. It was found that wide T-shaped caps perform best among these possible designs, and that the performance of T-shaped barriers can be further enhanced by placing sound absorbent material on the top surface of the T-top.

Butler [10] suggested lining the region in the immediate vicinity of the edge with absorbent material to reduce the sound pressure level in the shadow zone. Rawlins studied the case where the barrier was treated with strips having both infinitely small impedances [11] and finite impedances [12] based on the Fredholm integral equation. He showed that a one wavelength wide strip of an absorbent material at the edge of a half-plane led to the same diffracted field as that which would be provided by a barrier covered with absorbent material. In 1977, Fujiwara [13] presented a study that dealt with the excess attenuation of sound pressure level provided by an absorptive material placed on the surface of the barrier. He reported in 1991 that the installed absorber reduced the sound pressure level around the edge and improved the sound shielding efficiency of the noise barrier [14]. Moser [15] employed the acoustic intensity near the edge of the barrier as well as the insertion loss in the shadow zone to investigate the influence of the acoustic impedance at the top of the screen. It is interesting to note, however, that Watts and Godfrey [16] reported that the measured effects of applying absorptive materials to a roadside barriers were generally less than 1 dB on the L_Aeq and L_A10 scales and that most recorded changes due to the application of absorptive treatments were not statistically significant.

3.2 Empirical Models for Barrier Performance

Many theoretical barrier diffraction methods are in fact semi-empirical and are based on the application of ray-tracing and geometrical acoustics procedures. The most influential early studies were those of Maekawa [17] and Kurze and Anderson [18], who developed techniques for predicting the insertion loss of reflecting, sharp-edged barriers in terms of the Fresnel number (i.e., the ratio of the difference between

diffracted path length and the direct path length joining the source and receiver and the wavelength). Maekawa used a spherically spreading pulsed tone of short duration and measured the diffraction with a thin rigid barrier in a test room. He measured the sound pressure level in the shadow zone for a variety of frequencies and locations of source and receiver and was able to normalize the insertion loss in terms of the Fresnel number.

Kurze and Anderson derived empirical formulae for the sound attenuation by a thin rigid barrier, utilizing various theoretical and experimental results. The experimental data were taken from the work of Maekawa and Rathe [19] while theoretical results were taken from Keller's theory of diffraction [4]. The resulting empirical formulae have been extensively used in the noise control community.

Traffic noise predictions had been performed using the FHWA approved STAMINA 2.0 highway noise prediction modes, derived from the FHWA Highway Traffic Noise Prediction Model [20]. The barrier calculations within STAMINA are based on the Kurze and Anderson equation. In 1998, the FHWA released its new generation highway traffic noise prediction model called the Traffic Noise Model or TNM [21]. TNM is designed to eventually replace the FHWA's prior pair of computer programs, STAMINA 2.0/OPTIMA. De-Jong's formula for barrier prediction is used in TNM [22].

Lam [23] improved on Maekawa's method by summing the complex pressures instead of the energies travelling along each of the diffraction paths around finite length barriers. Muradali and Fyfe [24] subsequently extended Lam's research by using the Kurze and Anderson formulation as well as Pierce's in combination with Lam's summation procedure with successful results.

3.3 Experimental Studies

Experiments on barrier performance have been performed at various laboratories with the objective of controlling the environmental variables such as wind, temperature gradients, turbulence, and finite impedance ground surfaces. Full-scale outdoor experiments have also been performed at several locations. Despite the inherent

errors associated with environmental factors, the results obtained from full-scale experiments have their own value. But in that case, particular care should be taken when comparisons are made among different barrier designs since inevitably a number of environmental parameters cannot be controlled.

As noted, a number of small scale laboratory experiments have been carried out. Scaled experiments are usually performed indoors with the aim of controlling environmental variables. Atmospheric influences, such as temperature gradients, wind and turbulence can be avoided and the use of a deterministic sound source makes comparison with the results of numerical models easier. Kawai et al. [25] reported very good agreement of the results from model experiments of sound attenuation of a thin half-plane with the theoretically calculated values using the second term of the approximate expression of Macdonald's solution. May et al. [26] reported results from model studies of variously profiled single and parallel barriers in typical highway situations. Rasmussen [27] reported a series of measurements involving an artificial earth berm on a canvas surface simulating grass-covered ground.

Some full-scale measurement have been performed with artificial sound sources. A series of measurement of the performance of full-scale noise barrier of various heights were performed by Scholes and et al. [28]. Experimental results were compared to the empirical model of Maekawa which was found not to account for the effect of ground reflection accurately. More recently Watts et al. [29] conducted full-scale measurements with various barrier shapes. The designs chosen included T-shaped, multiple-edge and double barriers. It was found that multiple-edge and T-shaped barriers gave a consistent improvement in insertion loss over a wide area compared to a simple reflective barrier. Burroughs and Bontomase [30] found experimentally that noise transmission through barriers themselves should not be ignored in the case of a full-scale, wooden barriers.

Much care needs to be taken when designing a full-scale experiment to evaluate the performance of a noise barrier in highway locations. In this case, a traffic noise prediction model must be used to calculate the predicted sound pressure level, unlike

the case of a scale-model or full-scale models in which arbitrary noise sources such as a loudspeaker can be used. Steele [31] reviewed several traffic noise prediction models. In most cases, researchers did not measure the sound pressure level before the barrier was installed. The data without the barrier in place are often calculated by using a prediction model, which can itself be inaccurate. Rochat [32] performed roadside measurements at various locations in the United States and indicated that the calculated sound levels from Traffic Noise Model is within 1.5 dB of the measured levels. Comparison between different traffic noise models used in the United States was performed by Wayson et al. [33].

It can be seen from the literature review that detailed work involving both complex barrier geometry and absorptive treatment has not been performed though some research has been reported about the advantages of complicated barrier top geometry and of sound absorptive treatments applied to the surface of the barrier. In this study, three-dimensional boundary element models combined with scaled barrier experiments in a controlled laboratory environment with a microphone array were employed to evaluate the benefits of various geometries and sound absorptive treatments.

4. THEORETICAL BACKGROUND

4.1 Diffraction-based Models

Two-dimensional analysis

Consider the situation shown in Figure 4.1 in which a source and receiver are separated by a semi-infinite barrier. The pressure at the receiver associated with sound waves travelling along the ith path can be expressed as

$$p_i = A_i e^{j\varphi_i}(-jH_0^1(kd_i)) \tag{4.1}$$

where A_i, φ_i, d_i and H_0^1 are the amplitude, phase change upon diffraction, path length of the diffracted wave and Hankel function of first kind of order zero, respectively. Kurze and Anderson [18] found an approximate solution for the reduction of sound pressure due to the presence of a semi-infinite barrier between a line source and receiver. According to their formulation, the amplitude of the diffracted field is given by

$$A_i = \frac{d_i(1 - cot(\frac{\theta_i - \alpha_i}{2}))}{2\pi(A_i + B_i)\sqrt{\frac{\delta_i}{\lambda}(1 + \frac{d_i}{A_i + B_i})}}. \tag{4.2}$$

The geometrical parameters appearing in this equation are defined in Figure 4.2, and note that the subscript i denotes the parameters associated with the ith path joining the source and receiver. The path length difference between the diffracted and direct paths, $\delta = (A + B - d)$, becomes small for receivers close to the line-of-sight: i.e., near the geometrical shadow boundary. At sufficiently low frequencies, the wavelength, λ, inevitably becomes large enough that the quantity δ/λ becomes very small: under these conditions, equation 4.2 diverges. Thus, this formulation is strictly applicable only at high frequencies and for receivers deep in the shadow zone: these limitations of diffraction-based models will be demonstrated in results presented below. The phase factor in equation 4.1 is usually ignored in the two-dimensional case: i.e., φ_i,

is assumed to be zero. When sound rays propagate to the receiver via different paths (for example, when a barrier is placed on a hard surface, as illustrated in Figure 4.3), the various contributions must be summed at the receiver location to give the total sound pressure. That is, the total pressure, P_R, at the receiver is the sum of the diffracted pressures arriving via the individual paths, and is given by

$$P_R = \sum_i^4 p_i = \sum_i^4 A_i e^{j\varphi_i}(-jH_0^{(1)}(kd_i)) \tag{4.3}$$

for a two-dimensional geometry. The four possible paths that join the source and receiver in the case of a finite-height barrier placed on a reflecting ground surface are shown in Figure 4.3.

Three-dimensional analysis

In a three-dimensional geometry, the sound pressure generated by a point source and arriving at the receiver along the ith path, p_i, is given by

$$p_i = A_i e^{j\varphi_i}(\frac{e^{-jkd_i}}{d_i}) \tag{4.4}$$

and the amplitude of the diffracted field is given by

$$A_i = \frac{d_i}{d_{oi}} \frac{d_i(1 - cot(\frac{\theta_i - \alpha_i}{2}))}{2\pi(A_i + B_i)\sqrt{\frac{\delta_i}{\lambda}(1 + \frac{d_i}{A_i + B_i})}} \tag{4.5}$$

where d_i is the direct distance between the source and receiver and d_{oi} is the path length of the diffracted wave. Pierce has shown that in the three-dimensional case the phase change, φ_i, converges to an asymptotic value of $\frac{\pi}{4}$, and that value has been used in the present calculations. There are eight paths joining the source and the receiver in the case of a finite-length barrier placed on a reflecting ground surface: those paths are shown in Figure 4.4. In comparison with the two-dimensional case, the four additional paths arise from diffraction around the sides of the finite length barrier. It can be seen that when the source is placed near the ground, ground reflections of the side-diffracted components occur on the source side but not the receiver side (i.e., paths 7 and 8 in Figure 4.4). Finally, the total pressure, P_R, at the receiver is the sum of the diffracted pressures arriving via the individual paths, and is thus given by

$$P_R = \sum_i^8 p_i = \sum_i^8 A_i e^{j\varphi_i}(\frac{e^{-jkd_i}}{d_i}) \tag{4.6}$$

for the finite-length barrier placed on a perfectly reflecting surface.

4.2 Boundary Element Method

Boundary element methods are a powerful alternative to finite element and diffraction-based methods. They are particularly useful in cases where the surrounding domain extends to infinity as in the barrier case. The most important feature of boundary element methods is that they require only the discretization of the surface of the structure (i.e., the barrier in this case), and not the volume surrounding the structure. Boundary element methods associated with acoustical problems will be discussed in this section. It is well known that the propagation of acoustic waves is governed by a scalar wave equation. Reflections, scattering and diffractions are characterized by boundary conditions. If a harmonic excitation can be assumed, the acoustic field obeys the Helmholtz equation. Sound radiation or scattering mostly involves solutions of this equation over finite radiators or scatterers in an infinite homogeneous medium. Boundary integral equations are well suited for solving such problems. Some basic concepts behind the boundary element method that plays an important role in barrier applications are summarized in this section. More details can be found in reference [34], [35] and [36].

4.2.1 Helmholtz Equation

Sound waves in fluids involve local changes in the pressure, density and temperature of the media. In regions where the density increases above its equilibrium value, the pressure also increases. The fundamental equations of fluid dynamics for a non-viscous fluid include the linearized continuity equation,

$$\frac{\partial \rho_0}{\partial t} + \rho_0 \frac{\partial v_x}{\partial x} + \rho_0 \frac{\partial v_y}{\partial y} + \rho_0 \frac{\partial v_z}{\partial z} = 0, \tag{4.7}$$

where ρ_0 is fluid density and v_x, v_y, v_z are the particle velocities in the $x-$, $y-$ and $z-$directions, respectively. Euler's equation, or the conservation of momentum in an inviscid fluid, is expressed in linearized form as

$$\rho_0 (\frac{\partial v_x}{\partial t} i + \frac{\partial v_y}{\partial t} j + \frac{\partial v_z}{\partial t} k) + (\frac{\partial p}{\partial x} i + \frac{\partial p}{\partial y} j + \frac{\partial p}{\partial z} k) = 0 \tag{4.8}$$

where i, j, k are unit vectors in $x-$,$y-$ and $z-$directions, respectively. Equation 4.8 is valid for small amplitude sound waves. The propagation of sound waves in air does not generally cause any significant exchange of thermal energy between adjacent air particles, and thus the entropy of the gas is constant. Thus, the propagation of sound waves can be assumed to be nearly adiabatic. In that case, the relationship between pressure and density is

$$p(x,t) = B(\frac{\rho}{\rho_0}) \tag{4.9}$$

where B is the adiabatic bulk modulus or $\rho_0(\frac{\partial P}{\partial \rho})_{\rho_0}$. Equations 4.7 to 4.9 can be combined into a single equation with one variable: i.e., the fluctuating pressure. The result is the linearized, homogeneous acoustic wave equation that is given by

$$\nabla^2 p = \frac{1}{c^2}\frac{\partial^2 p}{\partial t^2} \tag{4.10}$$

where c is the speed of sound. If we assume the variation of pressure with time is sinusoidal, we can assume a solution for Equation 4.10 of the form

$$p(x,t) = Real\{P(x)e^{j\omega t}\}. \tag{4.11}$$

The substitution of Equation 4.11 into Equation 4.10 yields the Helmholtz equation: i.e.,

$$\nabla^2 P(x) + k^2 P(x) = 0 \tag{4.12}$$

where k is the wave number, defined as ω/c and upper case letters are used to indicate a frequency-dependent phasor.

4.2.2 Direct Collocation Method

The aim of the direct collocation method is to determine two acoustic variables; pressure and particle velocity, in the interior or the exterior domain of an object. This method relies on a boundary integral formulation of the Helmholtz equation. The unknowns are the pressure and the normal velocities on the surface of the boundary, which can then be used to calculate the acoustic variables at any point away from the boundary surface. The solution of the wave equation can be simplified by introducing

the notion of an acoustic point source and the corresponding Green's function. The source strength of an ideal point source is defined as

$$q = \rho_0 S \bar{v} \tag{4.13}$$

where ρ_0, S, $\bar{v}$ are the fluid density, the surface area and the mean surface velocity over the surface region. The acoustic field around the point source has to satisfy the Helmholtz equation. At the position of the source, the pressure has to satisfy the following equation,

$$\nabla^2 P(x) + k^2 P(x) = -q\delta(x - y) \tag{4.14}$$

where x, y and $\delta(x - y)$ are the locations of the receivers, the source and the three-dimensional Dirac delta function, respectively. The pressure at point x can be written as

$$p(x, y) = q\frac{e^{-jkr(x,\vec{y})}}{4\pi r(x, y)} \tag{4.15}$$

where $r(x, y)$ is the distance between the receiver and the source. The Green's function $G(x, y)$ for a point source is defined as the solution of the inhomogeneous Helmholtz equation for a point source with unit source strength. For for an unbound fluid, it is given by

$$G(x, y) = \frac{e^{-jkr(x,\vec{y})}}{4\pi r(x, y)}. \tag{4.16}$$

Green's third theorem relates the integral over a surface to the volume integral bounded by the surface for any two functions provided that they are sufficiently smooth and non-singular inside the volume. The use of the pressure and the three-dimensional free space Green function in Green's third theorem leads to an integral expression relating the pressure at any point in a volume to the values of pressure and normal velocity on the surface. This integral equation is called the Helmholtz integral equation and is

$$p(x) = \int (p(y)\frac{\partial G(x, y)}{\partial n} - G(x, y)\frac{\partial p(y)}{\partial n})dS(y). \tag{4.17}$$

4.2.3 Indirect Variational Boundary Element Method

The indirect boundary element method allows the internal and external acoustic radiation and scattering problems to be solved simultaneously. While in the direct collocation method the acoustic surface variables, i.e., the pressure and particle velocity, are assigned to one side of the surface, the indirect representation uses multi-layer potentials expressing the differences between the outer and inner values of pressure and its normal derivative, respectively. The difference between the outer and inner pressure on the surface, μ, is called pressure jump, or double layer potential, and is defined as

$$\mu = p^+ - p^-. \tag{4.18}$$

In addition, σ is the difference between the outer and inner normal derivatives of pressure on the surface and is called the normal derivative pressure jump, or the single layer potential, and can be written as

$$\sigma = \frac{\partial p^+}{\partial n} - \frac{\partial p^-}{\partial n}. \tag{4.19}$$

In the indirect method, the acoustic variables at any point in the volume are computed as functions of these layered potentials. The pressure at an arbitrary point is thus given by

$$p(x) = \int (\mu(y)\frac{\partial G(x,y)}{\partial n_y} - \sigma(y)G(x,y))dS(y). \tag{4.20}$$

This formula can be solved with integral formulations for appropriate boundary conditions using a variational method.

4.3 Acoustic Intensity

The instantaneous acoustic intensity, I, of a sound wave is defined as the rate of flow of energy through a unit area normal to the direction of sound propagation, and it can be expressed as

$$I = p\vec{v}. \tag{4.21}$$

The time average of the instantaneous power flow through a unit area is the mean intensity vector, I, and it is defined as

$$I = \frac{1}{T}\int_0^T p\vec{v}dt. \tag{4.22}$$

The instantaneous intensity can be decomposed into two components: an active component and a reactive component.

The active component corresponds to local net transport of sound energy and the reactive component corresponds to local oscillatory transport of energy. These two intensity components are associated with the components of particle velocity in-phase and out-of-phase with the acoustic pressure, respectively. The active and reactive components of intensity can be readily derived for a one-dimensional, single frequency sound field. The pressure $p(x,t)$ can be expressed as

$$p(x,t) = Real\{P(x)e^{j(\omega t+\phi(x))}\} \tag{4.23}$$

and the pressure gradient as

$$\frac{\delta p(x,t)}{\delta x} = [\frac{dP(x)}{dx} + \jmath\frac{d\phi}{dx}P(x)]e^{\jmath(\omega t+\phi(x))}. \tag{4.24}$$

The particle velocity is given as

$$V = (\frac{j}{\omega\rho_0})\frac{\partial P}{\partial x}. \tag{4.25}$$

The component of particle velocity in-phase with the pressure is associated with the active component of the intensity, which is given by their product as

$$I_a(x,t) = -\frac{1}{\omega\rho_0}[P^2\frac{d\phi}{dx}]\cos^2(\omega t+\phi) \tag{4.26}$$

of which the mean value is

$$-\frac{1}{2\omega\rho_0}[P^2\frac{d\phi}{dx}]. \tag{4.27}$$

The reactive component of intensity is given as

$$I_r(x,t) = -\frac{1}{4\omega\rho_0}[\frac{dP}{dx}]\sin^2(\omega t+\phi) \tag{4.28}$$

and its mean value is zero. It can be seen that the active component of intensity is proportional to the spatial gradient of phase, and the reactive component is proportional to the spatial gradient of mean square pressure. The sound power of an acoustical source is independent of position. The sound power, W, is the integral of the normal intensity over a surface of the source and is given by

$$W = \int I_r dS. \tag{4.29}$$

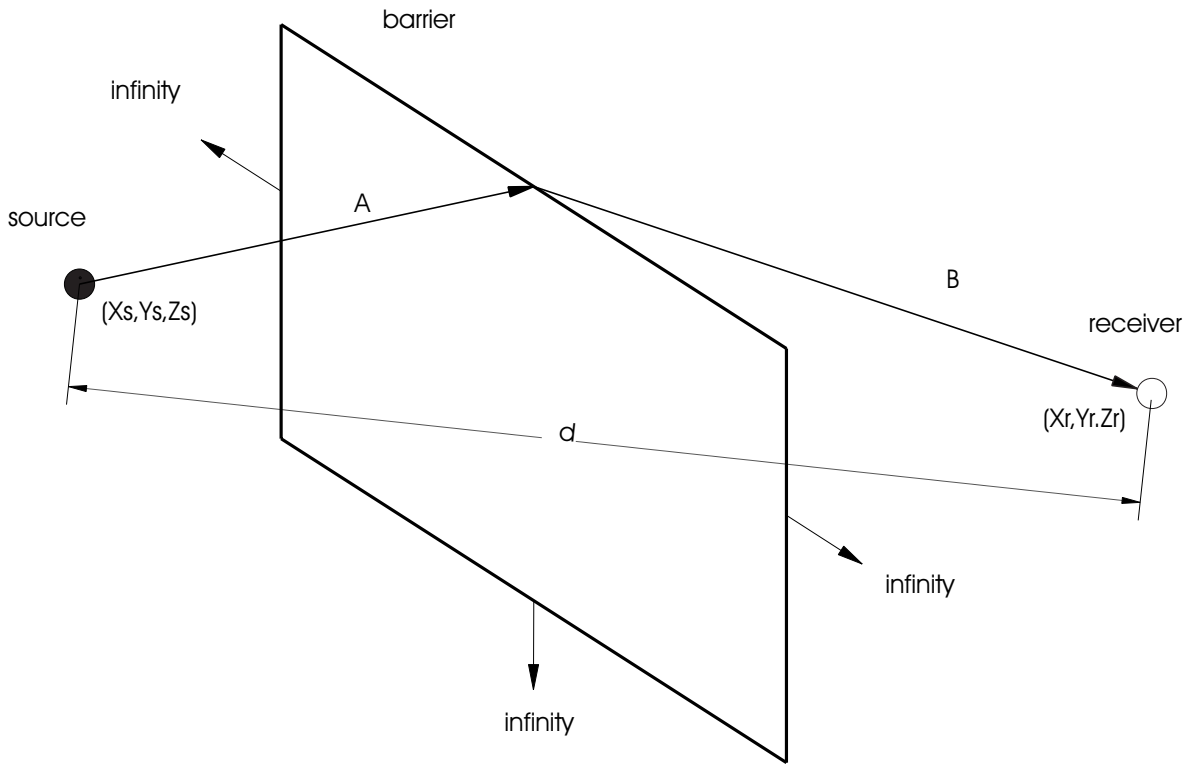

Figure 4.1. Diffraction by a rigid, semi-infinite barrier.

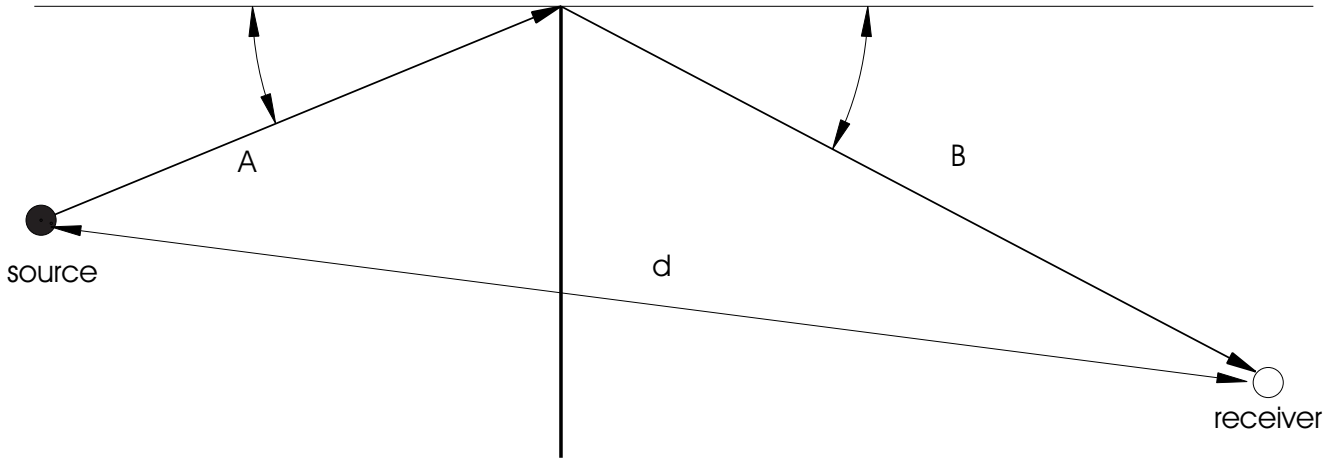

Figure 4.2. Definition of parameters used in Kurze and Anderson formulation.

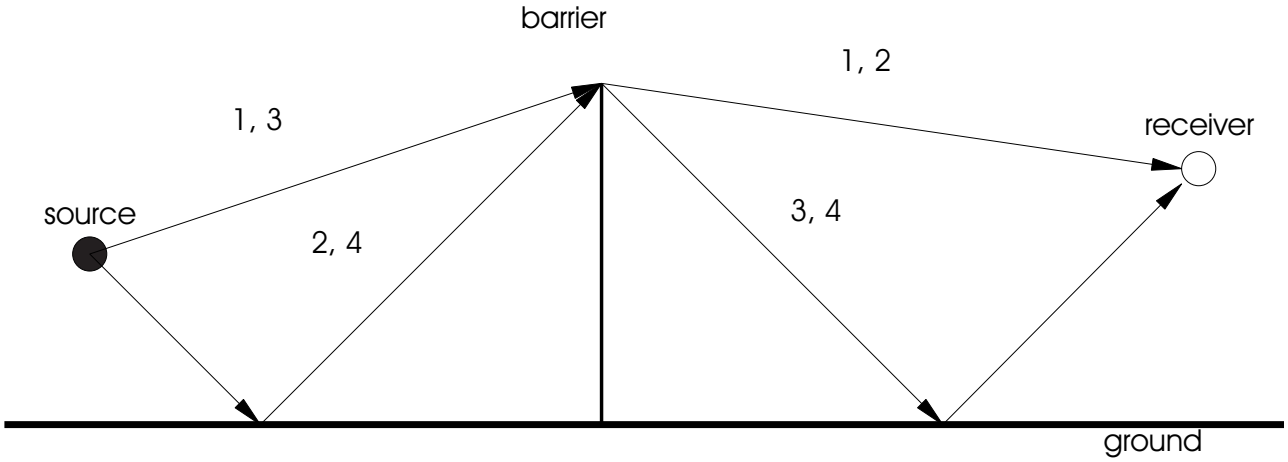

Figure 4.3. Diffraction paths for an infinitely long barrier on the ground.

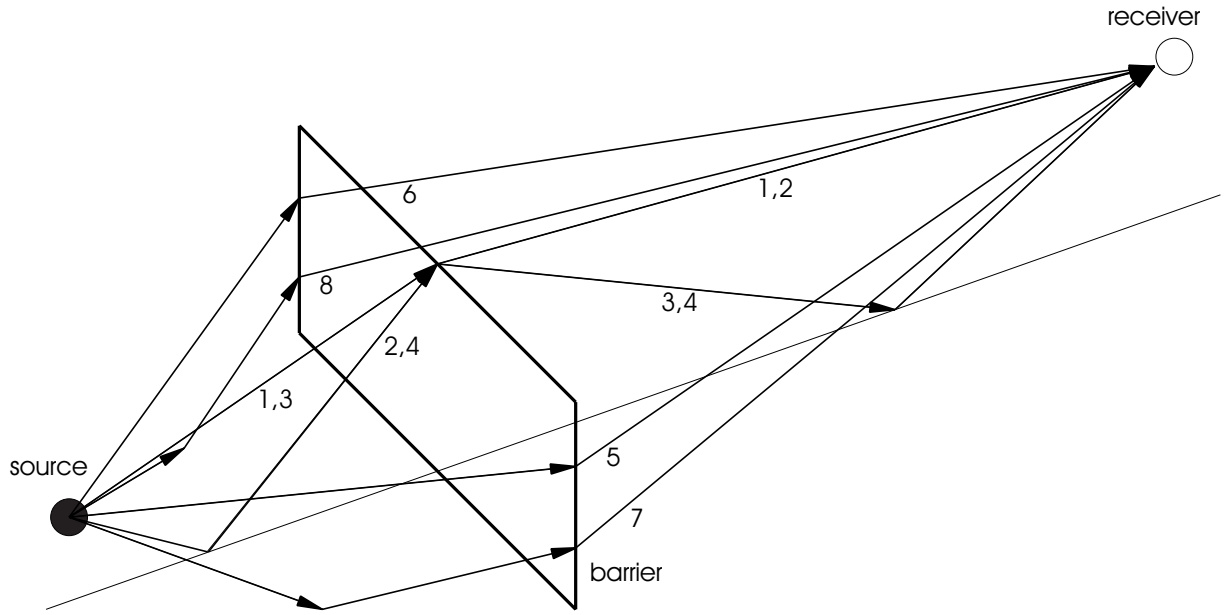

Figure 4.4. Diffraction paths for a finite length barrier on the ground.

5. DIFFRACTION BY A RIGID CIRCULAR DISK

5.1 Introduction

In the present work, sound wave diffraction by a rigid circular disk was studied as a preliminary step before proceeding to the analysis of complex acoustic barriers. A study of the case of a circular disk was also useful as a means of gaining insight into the effects of geometrical factors on the performance of barriers since circular disks are often used to study the effect of complex shapes on diffraction. It has been previously reported that complex disk geometries result in reduced root-mean-square sound pressures at measurement points on the axis compared to those measured in the case of a simple circular disk [37]. The boundary element model is known to be able to solve the case of a complicated geometry more accurately than diffraction-based models. Here, a boundary element model for the simple circular disk case was developed first, and it was validated against results from experiments that were performed in an anechoic chamber.

5.2 Boundary Element Model

Geometry modelling

The commercially available boundary element software SYSNOISE [38] was used to solve the wave-based scattering solution in the present work. SYSNOISE does not feature a pre-processor for creating discretized models, but it offers interfaces to a variety of pre-processors. Here MSC PATRAN [39] was used to generate various models. A two-dimensional model, in which an infinitely thin circular disk was assumed, was first created to reduce the computation time. The effects of disk thickness were considered next, as described in this chapter. The number of elements used here was 842 for a maximum frequency of 10 kHz. A schematic diagram illustrating the

geometry of the problem used for the numerical study is shown in Figure 5.1. A point sound source was located 165 *cm* in front of the circular disk, along the axis normal to the center of the disk. The diameter of the circular disk was 15 *cm*. Seven receivers were located 10 *cm* behind the circular disk, spaced 2.5 *cm* apart, starting from the center axis. The geometrical shadow zone can be defined as the conical zone from the sound source through the annular region along the edge of the obstacle in the sound field. Three receiver locations are in the geometrical shadow zone including one point on the axis. One receiver point was near to the boundary of the shadow zone, and three receivers were in the bright zone.

Numerical considerations

The indirect variational boundary element method requires a greater computational effort than the direct collocation method for the construction of the system matrix. However, the subsequent calculation time for the indirect method is reduced compared to that for the direct collocation method since the matrix is symmetric in the former case. Thus, the indirect method was used here. Recall that the insertion loss is defined as the difference between the sound pressure level without the barrier in place and the sound pressure level at the same location with the barrier in place. Figure 5.2 shows the insertion losses at three different locations in the shadow zone for the present case. In the zone near the central axis the pressure is large: this region is called the "bright spot". Its diameter is approximately one wave-length immediately behind the disk, and increases with increasing distance from the disk. The bright zone very near to the central axis causes there to be a negative insertion loss at receiver locations on the axis as can be seen in Figure 5.2: i.e., the sound pressure level is increased at this point after the circular disk is placed between the sound source and the receivers. In this case the distance between on-axis receiver and any point along the edge of the circular disk is the same and thus constructive interference occurs. The insertion loss values in the remainder of the shadow zone are positive: i.e., the barrier attenuates the sound field. For the receiver 25 *mm* off the axis, the insertion loss increases with frequency up to around 9000 Hz, and reaches a maximum value

of 16.5 dB. The insertion loss reaches a maximum value of 11 dB at about 4500 Hz for the receiver 50 mm off the center axis. It should be noticed that the insertion losses at both receiver locations are still negative at frequencies below 2000 Hz. The acoustic wavelength is about equal to the diameter of the disk at 2000 Hz. This suggests that, below this frequency, the circular obstacle does not significantly affect the sound field. Figure 5.3 shows the insertion loss values at receiver locations outside the shadow region. It can be seen that the insertion losses are very small up to 1000 Hz regardless of the receiver location because of the relatively long wavelength at low frequencies. It can also be seen that the insertion loss tends towards zero as the receiver location is moved away from the shadow region. Thus the insertion loss value measured 150 mm off the axis is the smallest among the values for the three points in the shadow zone.

5.3 Experimental Validation

5.3.1 Experimental Setup

Experiments were performed to verify the results obtained using the numerical model. The experiments were performed in the anechoic chamber at the Ray W. Herrick Laboratories at Purdue University. The dimensions of the anechoic chamber are 3.66 m × 3.66 m × 3.66 m. Figure 5.4 shows the experimental setup used. To simulate a monopole source in the experiments, a small loudspeaker was purchased and installed at one end of a PVC pipe. The diameter of the loudspeaker was 29 mm and the length of the pipe was 80 mm including the cap. Foam was inserted into the pipe to reduce any resonant behavior. It should be noted that, due to its small dimensions, the loudspeaker response at low frequencies was small. To measure the sound pressure level, a B&K 6.35 mm condenser microphone type 4136 was used in conjunction with a B&K microphone amplifier type 5935, and a pistonphone type 4228. A Spectral Dynamics Siglab model 20-42 was used for data acquisition [40]. The Siglab device was controlled using MATLAB and running on a Dell Laptop Inspiron 3200. A random input signal with a 20 kHz bandwidth was generated using the virtual function generator in Siglab, and the sampling frequency was automatically

selected as 2.56 times the bandwidth of interest, resulting in a sampling rate of 51.2 kHz. Here 4096 point records were used for the Fourier transforms which yields a frequency resolution of 12.5 Hz. A circular disk made of bronze with a diameter of 75 mm and a thickness of 10 mm was used as the obstacle between the speaker and microphone. The circular disk was hung using wires attached at four different circumferential positions. The measurements were performed in an anechoic chamber to reduce the effects of any undesirable reflection. The loudspeaker was located at a distance of 165 cm in front of the disk. The centers of the speaker driver and of the circular disk were aligned. A microphone was positioned along a line 10 cm behind the disk and normal to the axis joining the loudspeaker and the disk center. Measurement positions were spaced 2.5 cm apart from the point on the axis up to a distance of 15 cm off axis.

5.3.2 Post-processing of Experimental Data

Continuous random input and transient impulse input

The sound pressure level of the diffracted sound was relatively low. A preliminary study was performed to increase the signal-to-noise ratio. Transient impulse signals have been used in the past as the input for diffraction experiments owing to the convenience with which spurious echoes may be removed [41]. That is, spurious features in the impulse response function can easily be eliminated by simple algebraic operations. However, the impulse input does not have a uniform power spectrum over the entire frequency band of an interest. Figure 5.4 shows the experimental apparatus used to make the diffraction measurements. Figure 5.5 shows the impulse response function in the free field when the microphone was positioned on-axis 60 mm from the loudspeaker. Measurements were repeated three times with a different number of time-domain averages in each case. First, 100 samples were used, and then the number of averages was increased up to 500. In the presence of high signal-to-noise ratios, the results should be the same regardless of the number of averages. In this case, however, some variation of the impulse response with the number of averages when the transient impulse is used. By comparison, the impulse function obtained

by calculating the inverse Fourier transform of the frequency response function measured using a continuous random input does not vary noticeably with the number of averages. Thus it was concluded that it was desirable to use a continuous input for these tests.

Time windowing of the impulse function

Errors associated with sound wave reflection from miscellaneous objects are unavoidable in a test like this, even when experiments are performed inside an anechoic chamber. Here procedures were developed to eliminate the effects of such reflections. The inverse Fourier transform was first used to calculate the impulse response function from measured frequency response data. A time window was then applied to each record to eliminate spurious reflections. The impulse response function shows sound arriving after a certain time delay according to the path length between the sound source and receiver. The sampling frequency was fixed at 51.2 kHz, corresponding to a maximum frequency of interest of 20 kHz. From the symmetry characteristics of the Fourier transform, the data from fs/2 to fs may be constructed using the data from 0 to fs/2. However, the frequency response function was only available up to fs/2.56 in this case, which corresponds to a maximum frequency of 20 kHz: i.e., the frequency response function data from 20 kHz to 25.6 kHz was not available. Figure 5.6 suggests that the amplitude of the frequency response function was small in the frequency range greater than 20 kHz compared to that at other frequencies. A value of zero was assumed for the frequency response function for the frequencies from 20 kHz to 25.6 kHz. The magnitude of the imaginary part of the reconstructed impulse response function was around 10^{-19} which supports the validity of the procedure used to fold the data around the point fs/2. The impulse response function is shown in Figure 5.7. It takes approximately 6 ms for the sound to reach the microphone from the speaker, located 175 cm downstream. Events can also be seen in the impulse response at about 10 and 16 ms in Figure 5.7. These events are likely associated with reflections from the wall, floor, microphone holder or speaker stand. A time window was applied to zero the impulse response after 8 ms seconds. The "cleansed" impulse

response function following the application of the time windowing operation is shown in Figure 5.8

5.3.3 Insertion Loss Results

Influence of time window

A comparison between the insertion loss from the numerical predictions and the experiments without the application of time-domain windowing is shown in Figures 5.9 to 5.13. Five receiver points were considered: one on-axis, two in the shadow zone, one at the boundary of shadow zone and one outside the shadow zone. The general trend of the numerical prediction is in good agreement with the experimental results, except at the point on the shadow boundary (see Figure 5.12). The error at the boundary was believed to come from the assumption of infinitesimal disk thickness in the numerical model. This issue will be addressed later.

Figure 5.9 shows a comparison between insertion losses from the numerical predictions and from experimental data on the central axis. Good agreement can be observed up to 6000 Hz. Above that frequency, some discrepancy can be observed between the two results. This discrepancy is believed to result from experimental error, specially positioning error. At 10 kHz, the wavelength is only 3.4 cm. This means that a positioning error of less than 1 cm can generate a phase difference of more than $\pi/2$. Thus a small receiver positioning error was believed to interfere with the perfect constructive interference that is predicted to occur at the receiver location on the central axis, which results in a positive insertion loss in the experimental results. However, both results show that the insertion loss is small or even negative at this particular receiver location, which confirms the existence of central bright zone.

A comparison between the numerical results and experimental data is shown in Figure 5.10 for one point in the shadow zone. Both results show a positive insertion loss in the frequency range from 2 to 10 kHz. It should be noted that the oscillatory features of the experimental data curves increase as the insertion loss is increased. This was attributed to the low sound pressure level for high insertion loss values and to the resulting decrease in the signal-to-noise ratio in the frequency region of high

insertion loss. Another insertion loss comparison is shown in Figure 5.11 for a point 50 *mm* off-axis. The numerical model successfully predicts the trend of the experimental data. Poor signal-to-noise also can be observed around the frequency region where the peak values of insertion loss occurs.

In contrast with the successful results at the three points in the shadow region, the numerical model fails to predict the experimental result accurately at the shadow boundary as illustrated in Figure 5.12. It is believed that the infinitely thin disk assumption in the numerical model causes this discrepancy. A numerical model with finite thickness was consequently developed, as described in the following subsection. Finally, it can be seen in Figure 5.13 that the numerical model is accurate for the receiver location outside the shadow region. Small oscillatory features can be seen in the experimental result in this case, but otherwise both curves match quite well.

A comparison of the insertion losses after the time windowing operation was performed on the experimental results are shown in Figure 5.14 to 5.18. It can be seen that the time-domain windowing essentially eliminate the small oscillatory features except in the low frequency range, below 500 Hz. The large oscillation of the insertion loss in the low frequency range is due to the poor response of loudspeaker at low frequencies. Figure 5.15 compares the insertion loss between the numerical model and experiment at a point 25 *mm* off axis. There is excellent agreement between 2 and 6 kHz. There are small peaks at 8 and 9 kHz which are believed to result from experimental errors. The insertion loss comparison at the second point in the shadow region, shown in Figure 5.16, is also satisfactory. The insertion loss in Figure 5.17 again illustrates the failure of the numerical model at the shadow boundary, due to the infinitely thin disk assumption. The insertion loss comparison shown in Figure 5.18 demonstrates that the numerical model gives excellent results for receiver locations outside the shadow region.

5.3.4 Effects of Disk Thickness

A three-dimensional boundary element model was developed with MSC PATRAN to represent a finite thickness disk. Unlike the two-dimensional modelling case, an-

other step is necessary when importing a solid model into the boundary element solver SYSNOISE. The pressure and velocity (or single and double layer potentials in the case of indirect boundary element method) need only be known on the surface of the structure, so a so-called skinning process is necessary to delete any internal nodes and element inside the solid model. Figure 5.19 to 5.23 show the comparisons of the insertion losses between the numerical predictions and experimental results when the effects of a finite thickness are considered. It can be seen in these figures that the insertion loss calculated using the actual disk thickness yields better agreement with the experimental results than does the two-dimensional model particularly near the shadow boundary. The results in Figure 5.19 to 5.21 show that the finite thickness disk does not make a large difference in the shadow zone, although the high frequency, on-axis results are somewhat improved (Figure 5.19). More significantly, the insertion losses shown in Figure 5.22 are in much better agreement when the finite disk thickness is accounted for. The insertion loss comparison in Figure 5.23 shows that both numerical models give excellent results for the receiver locations outside the shadow region. The comparisons shown shown here illustrate that the infinitely thin disk model can be used without much error as long as the receiver locations are not very close to the boundary of the shadow region.

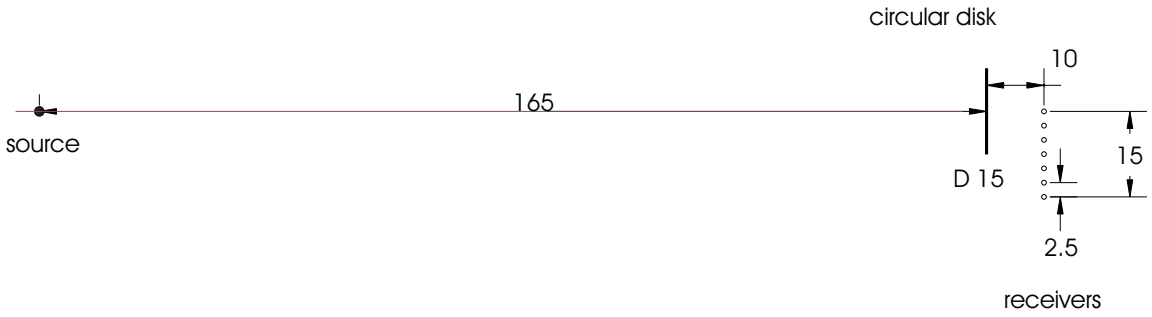

Figure 5.1. Location of the source, the disk and receivers for the circular disk study. Dimensions are in centimeters, unless indicated otherwise.

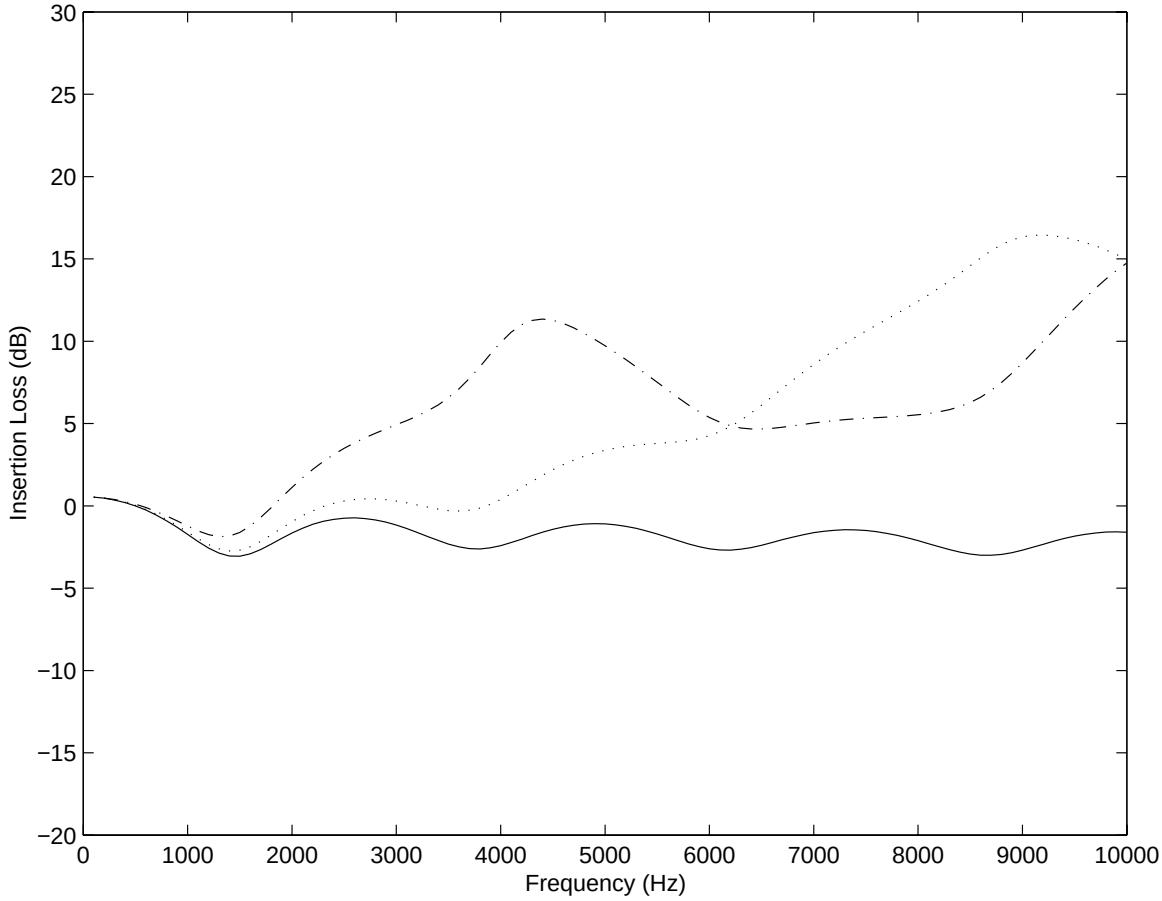

Figure 5.2. Insertion loss of circular disk at three receiver locations inside the shadow zone. '—': receiver on the axis; '· · ·': receiver 25 mm off the axis; '-·-·': receiver 50 mm off the axis.

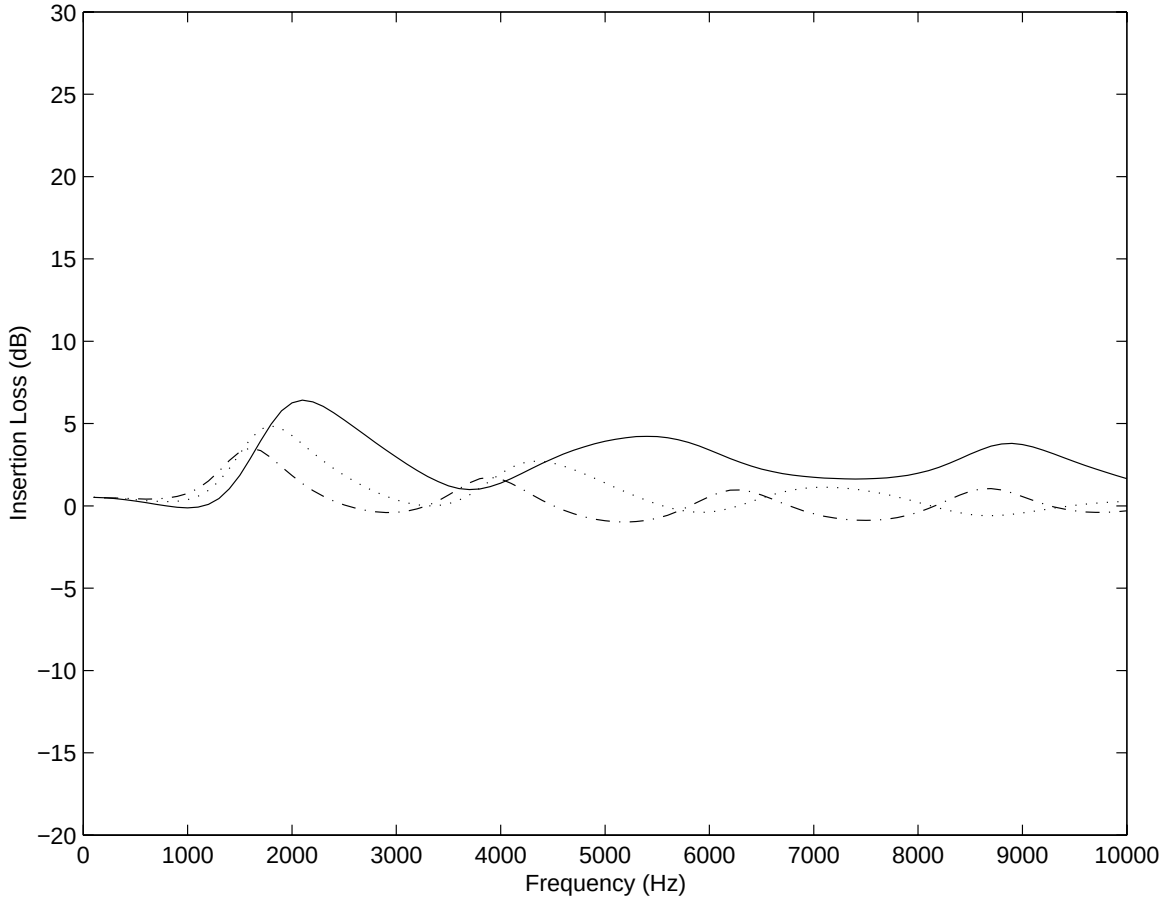

Figure 5.3. Insertion loss of circular disk at three receiver locations outside the shadow zone: '—': receiver 100 mm off the axis; '$\cdots$': 125 mm off the axis; '-·-·': 150 mm off the axis.

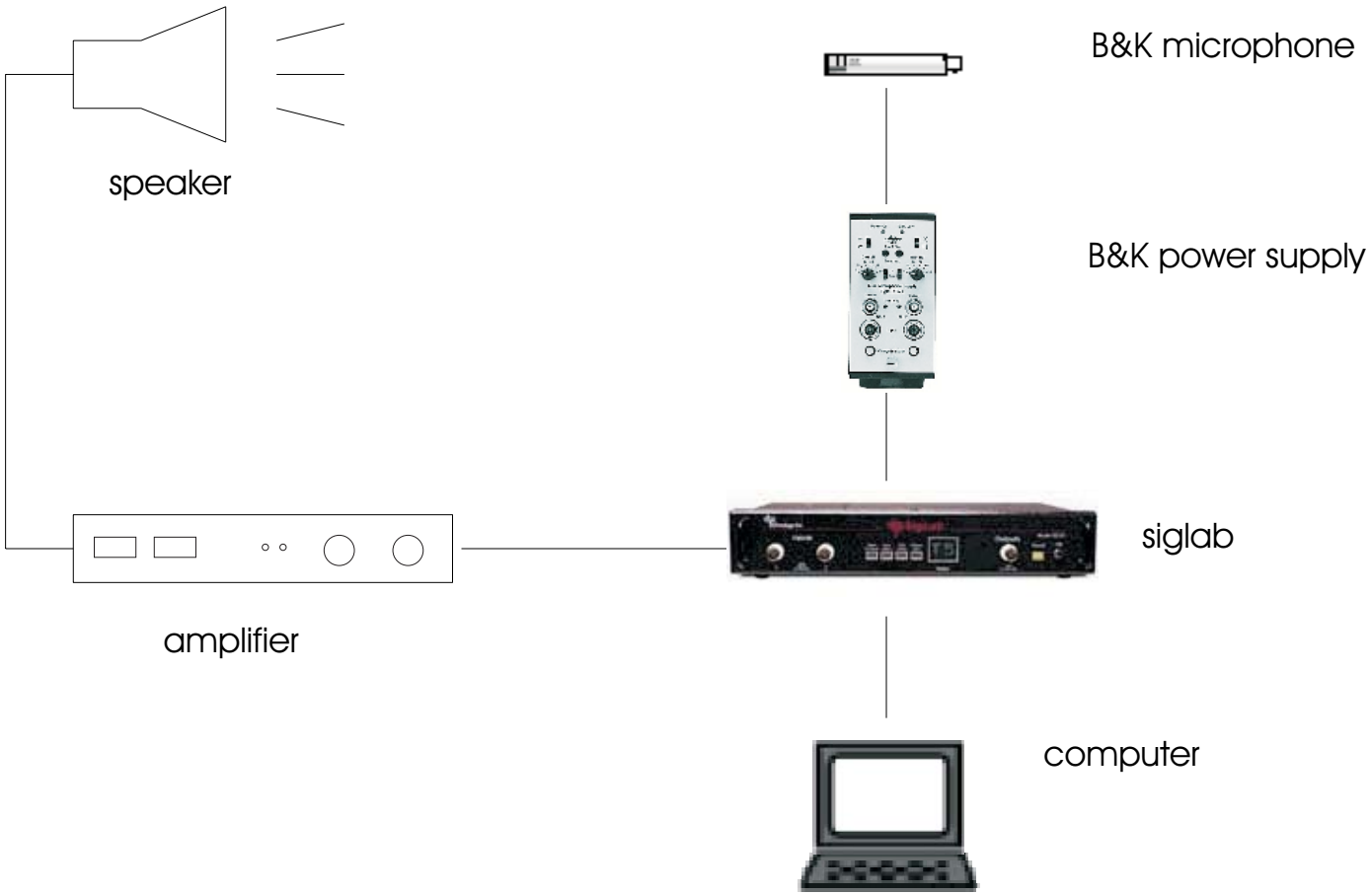

Figure 5.4. Experimental setup for circular disk experimental study.

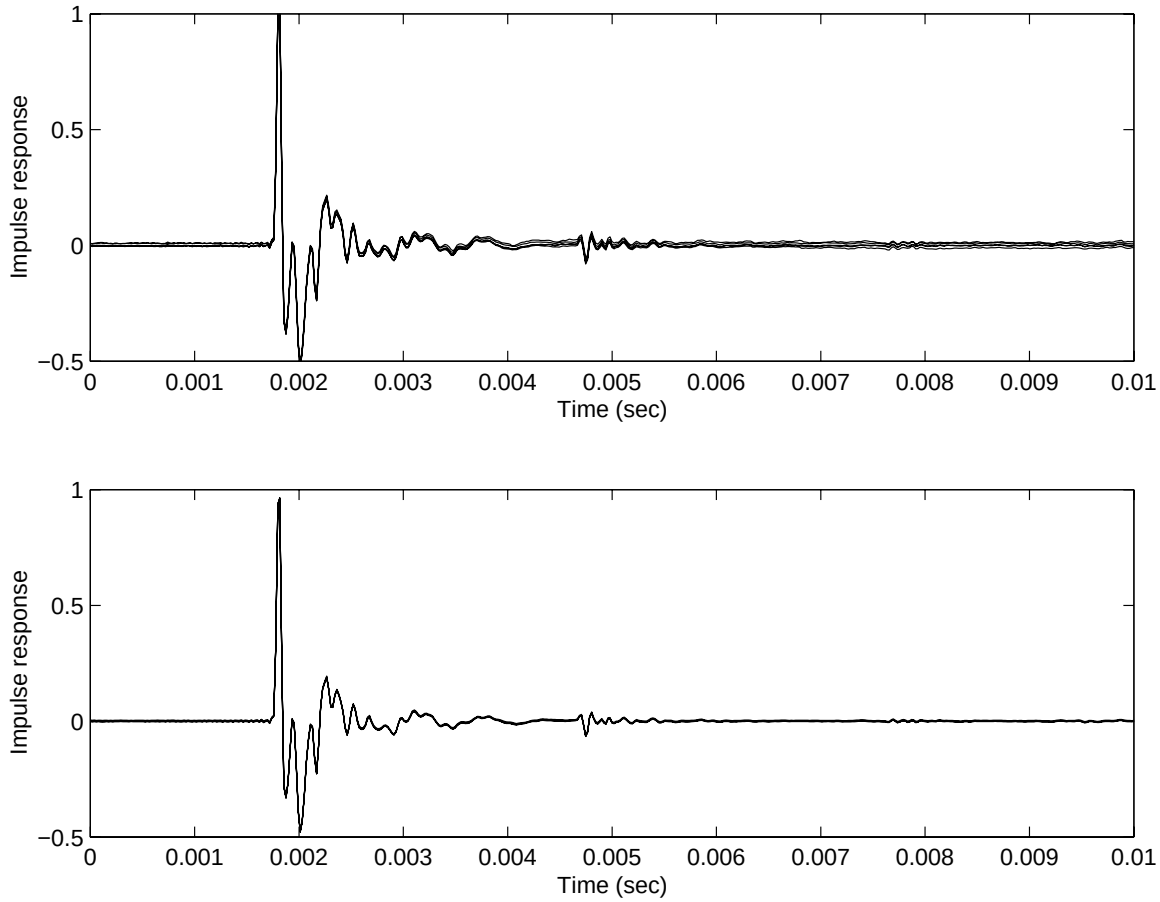

Figure 5.5. a) Impulse response function from impulse input with 100, 300 and 500 averages; b) Impulse response functions from continuous random input with 100, 300 and 500 averages.

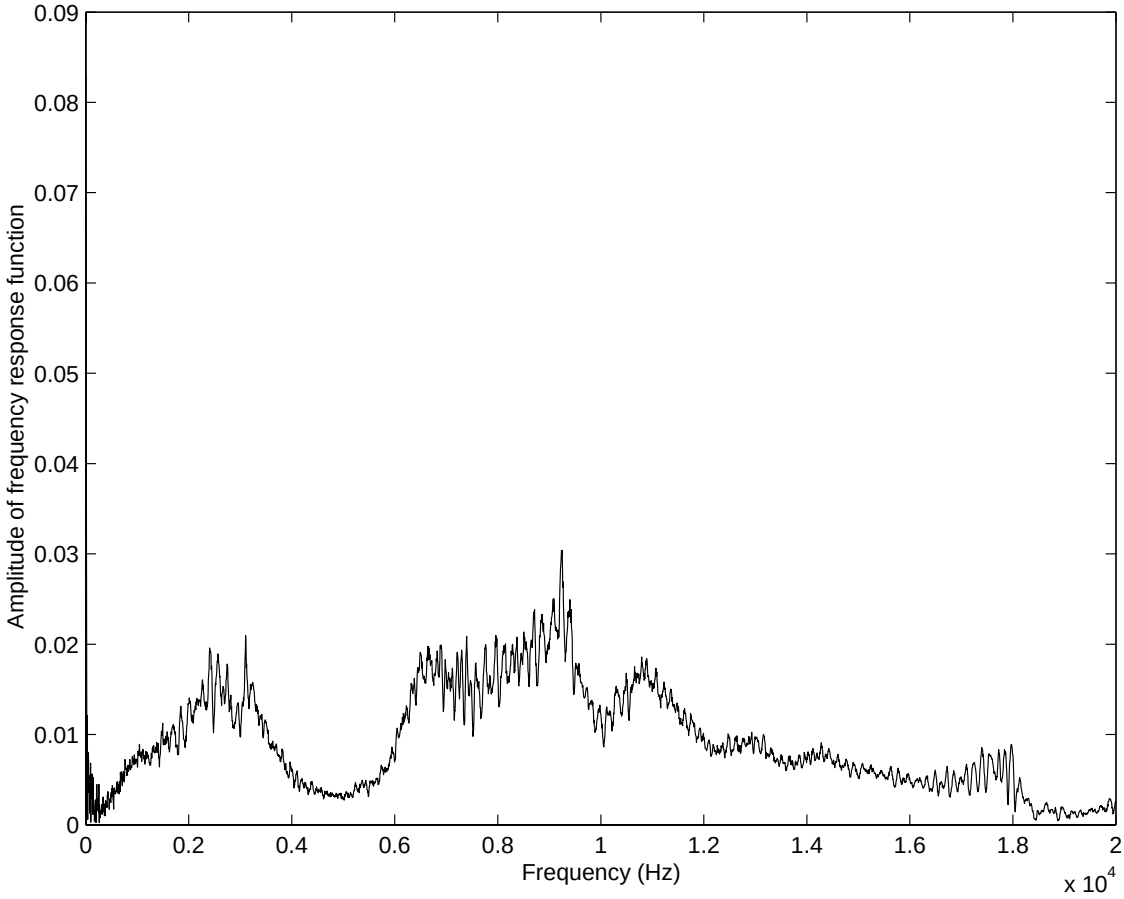

Figure 5.6. Amplitude of frequency response function on the axis.

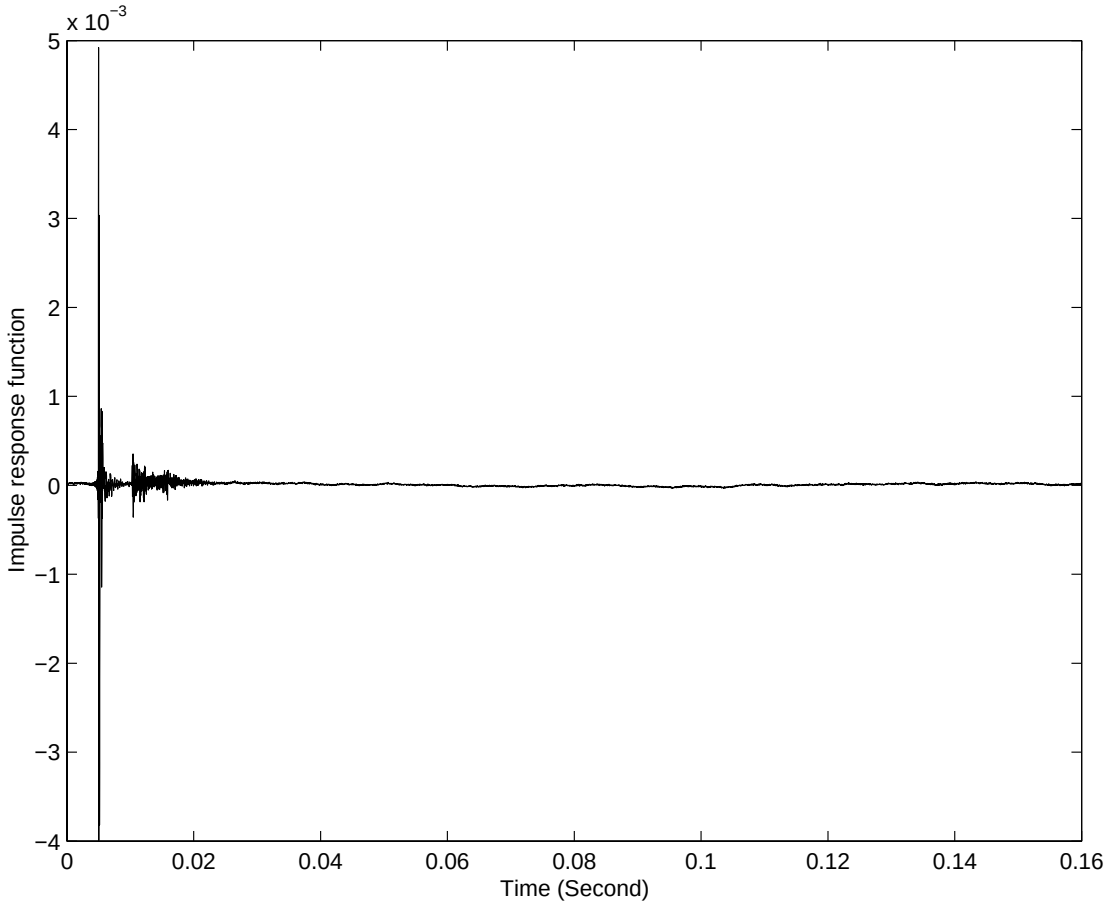

Figure 5.7. Impulse response function calculated at the receiver point on the axis behind the circular disk.

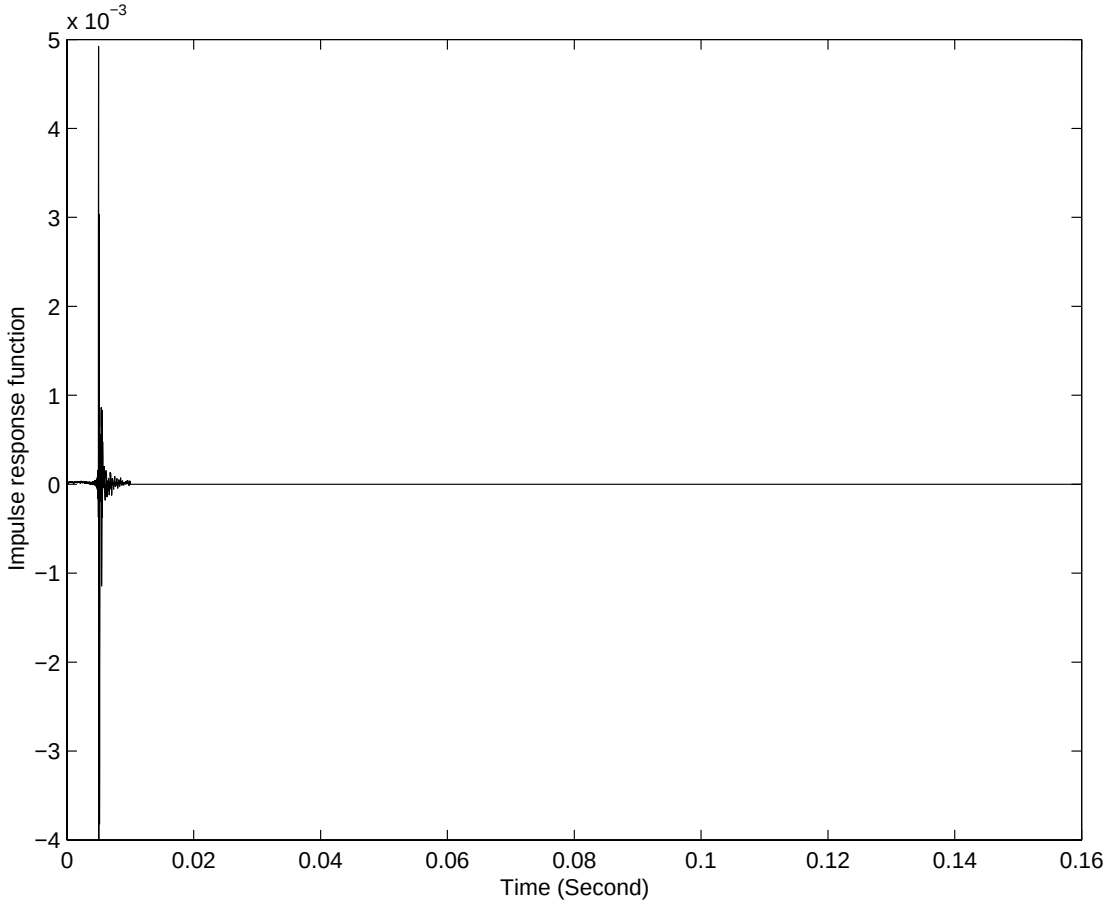

Figure 5.8. Impulse response function calculated at the receiver point on the axis behind the circular disk after time-domain windowing.

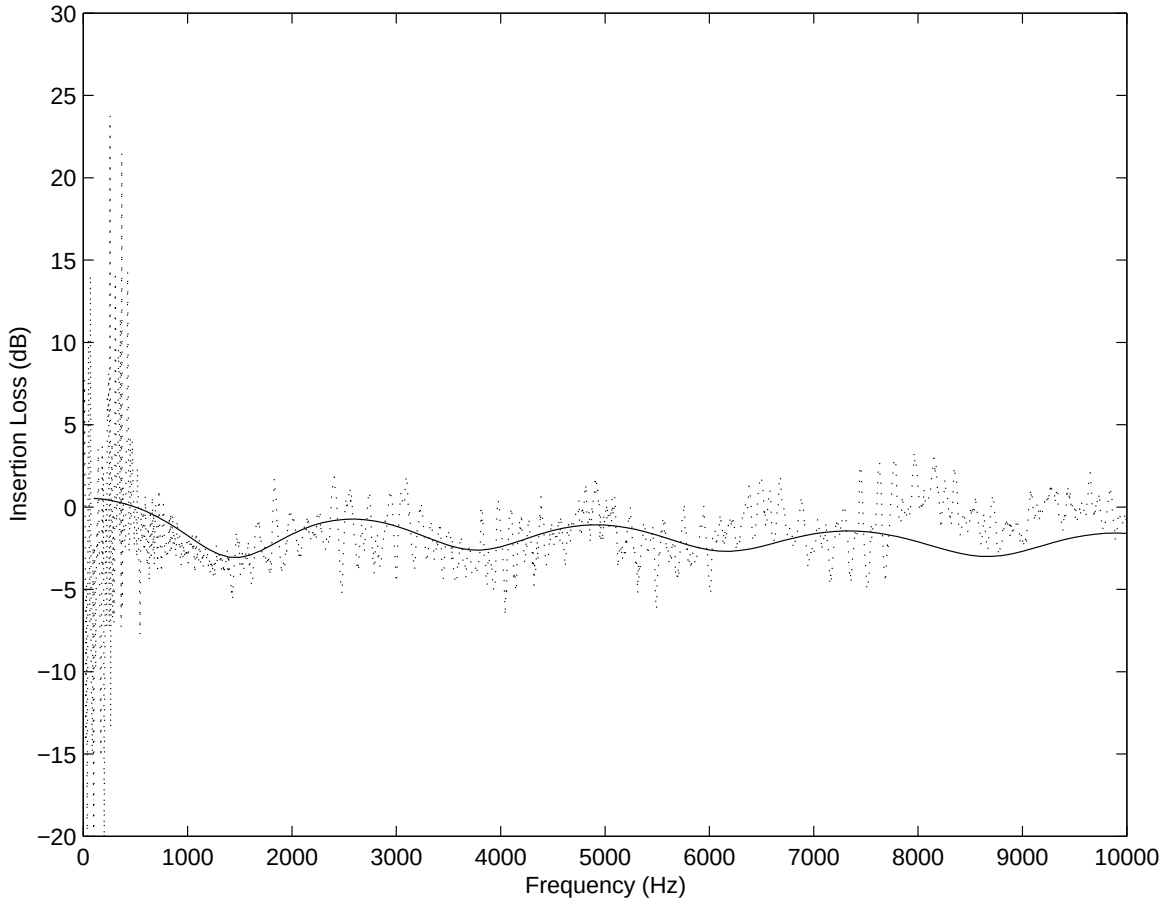

Figure 5.9. Comparison of insertion loss at receiver point on the axis. '···': experimental data; '—': numerical simulation with infinitely thin assumption.

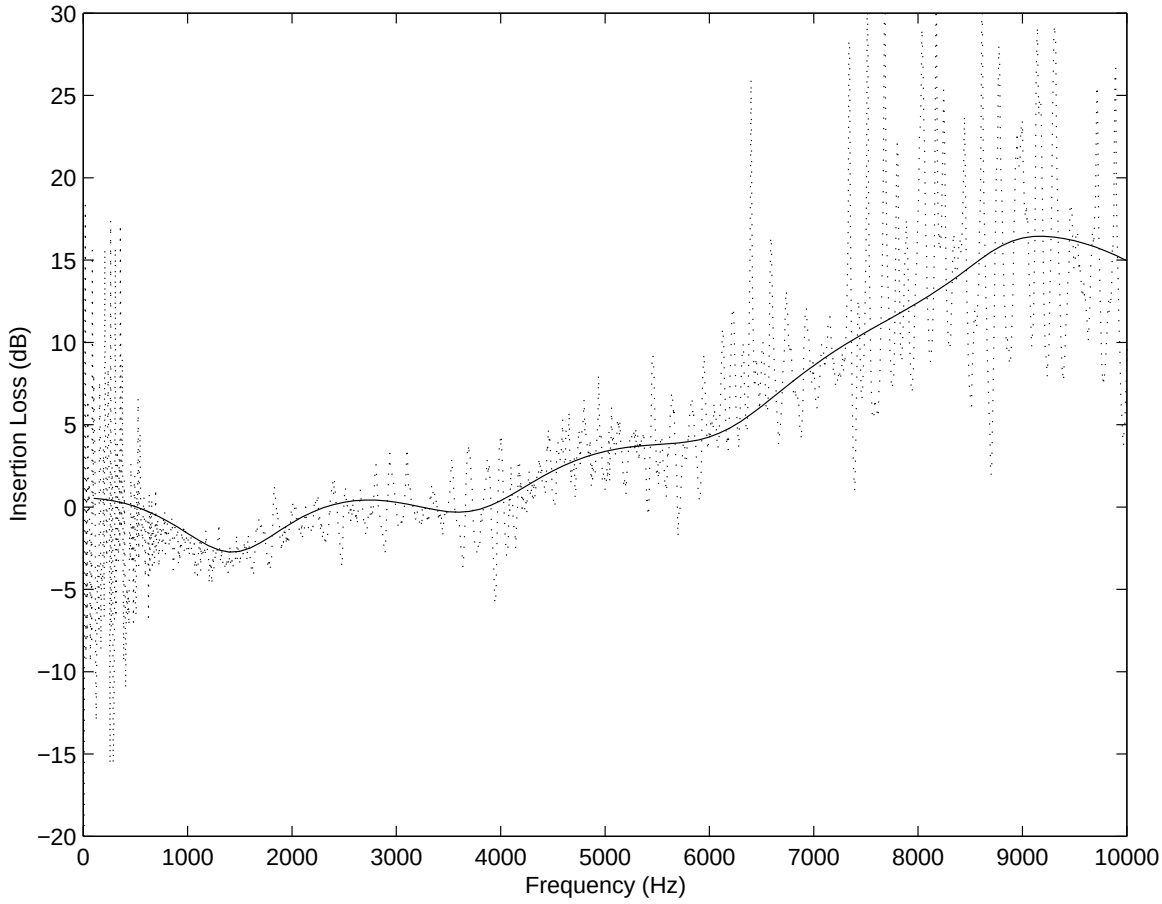

Figure 5.10. Comparison of insertion loss at receiver point 25 mm off the axis. '$\cdots$': experimental data; '—': numerical simulation with infinitely thin assumption.

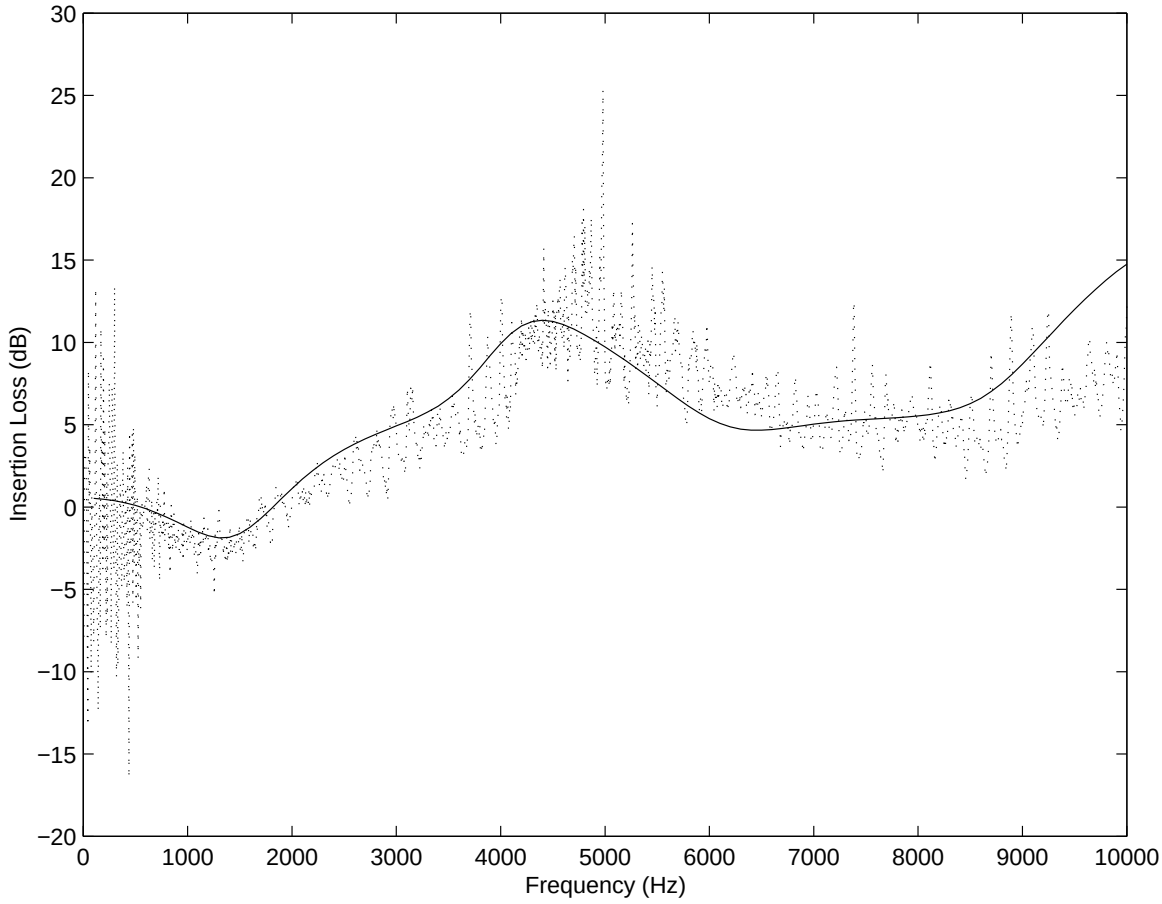

Figure 5.11. Comparison of insertion loss at receiver point 50 *mm* off the axis. '···': experimental data; '—': numerical simulation with infinitely thin assumption.

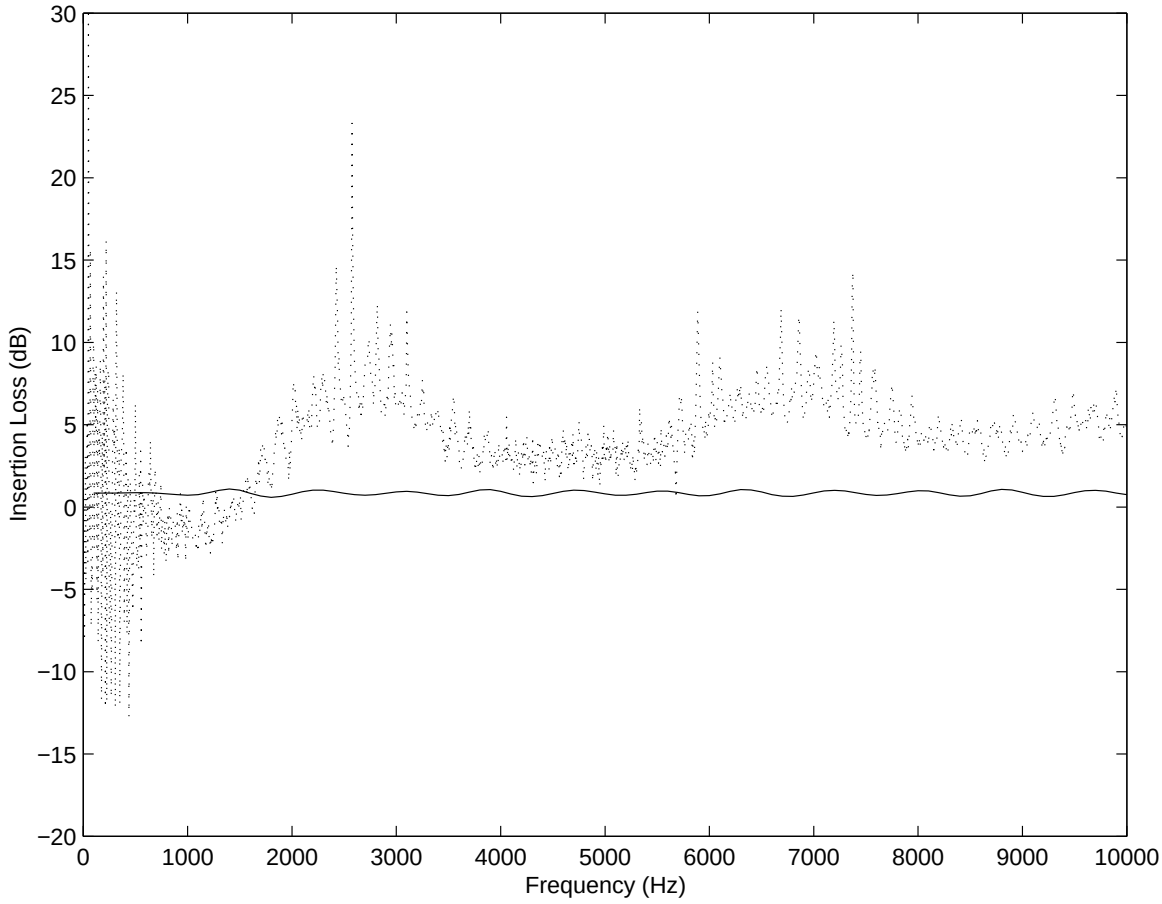

Figure 5.12. Comparison of insertion loss at receiver point 75 *mm* off the axis. '···': experimental data; '—': numerical simulation with infinitely thin assumption.

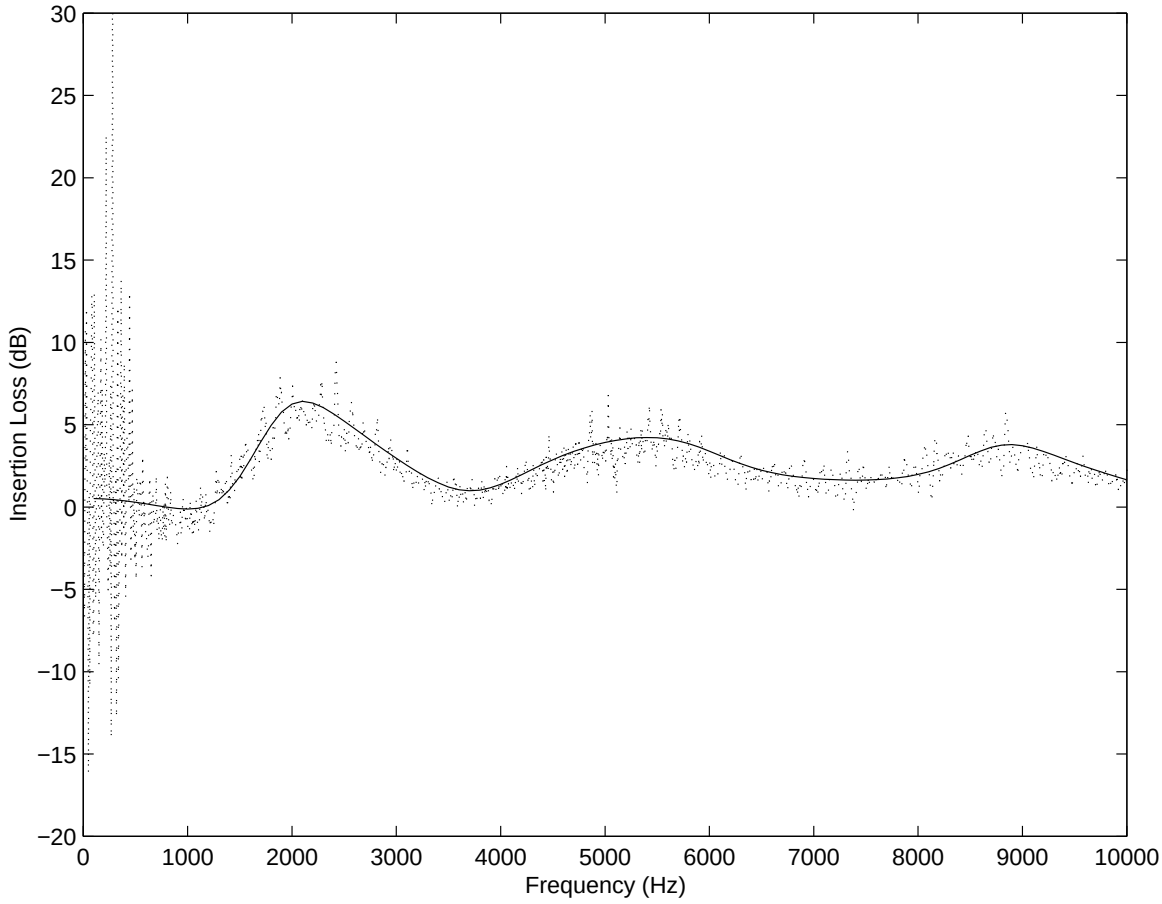

Figure 5.13. Comparison of insertion loss at receiver point 100 mm off the axis. '$\cdots$': experimental data; '—': numerical simulation with infinitely thin assumption.

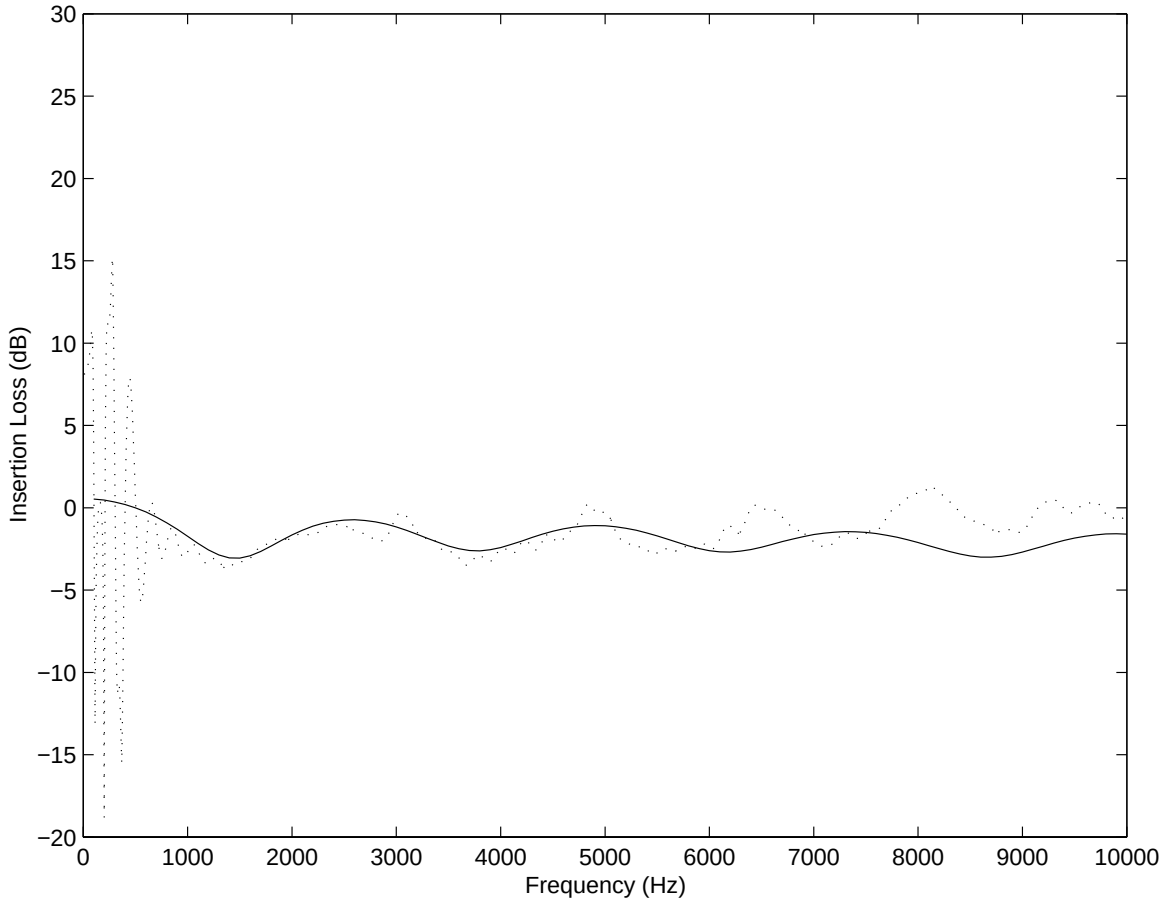

Figure 5.14. Comparison of insertion loss at receiver point on the axis. '···': experimental data with time window technique; '—': numerical simulation with infinitely thin assumption.

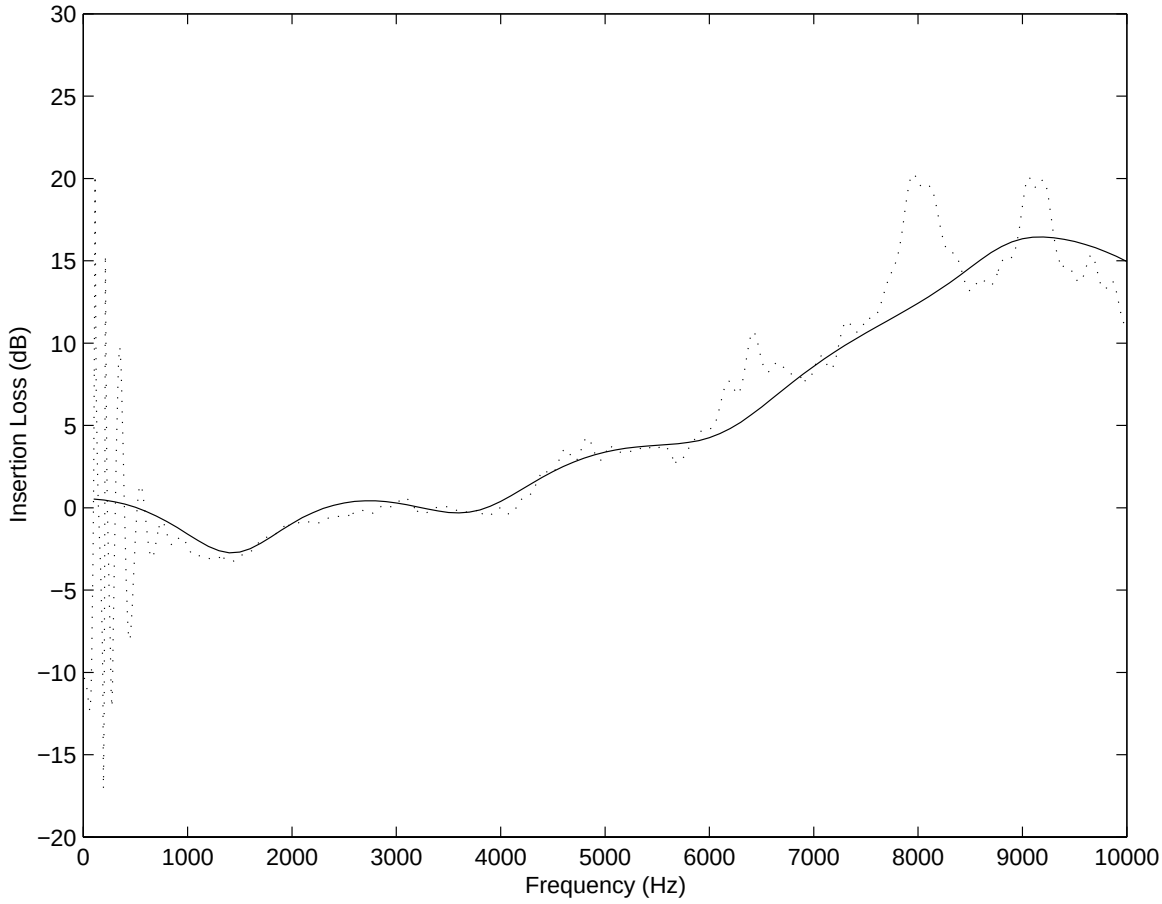

Figure 5.15. Comparison of insertion loss at receiver point 25 *mm* off the axis. '$\cdots$': experimental data with time window technique; '—': numerical simulation with infinitely thin assumption.

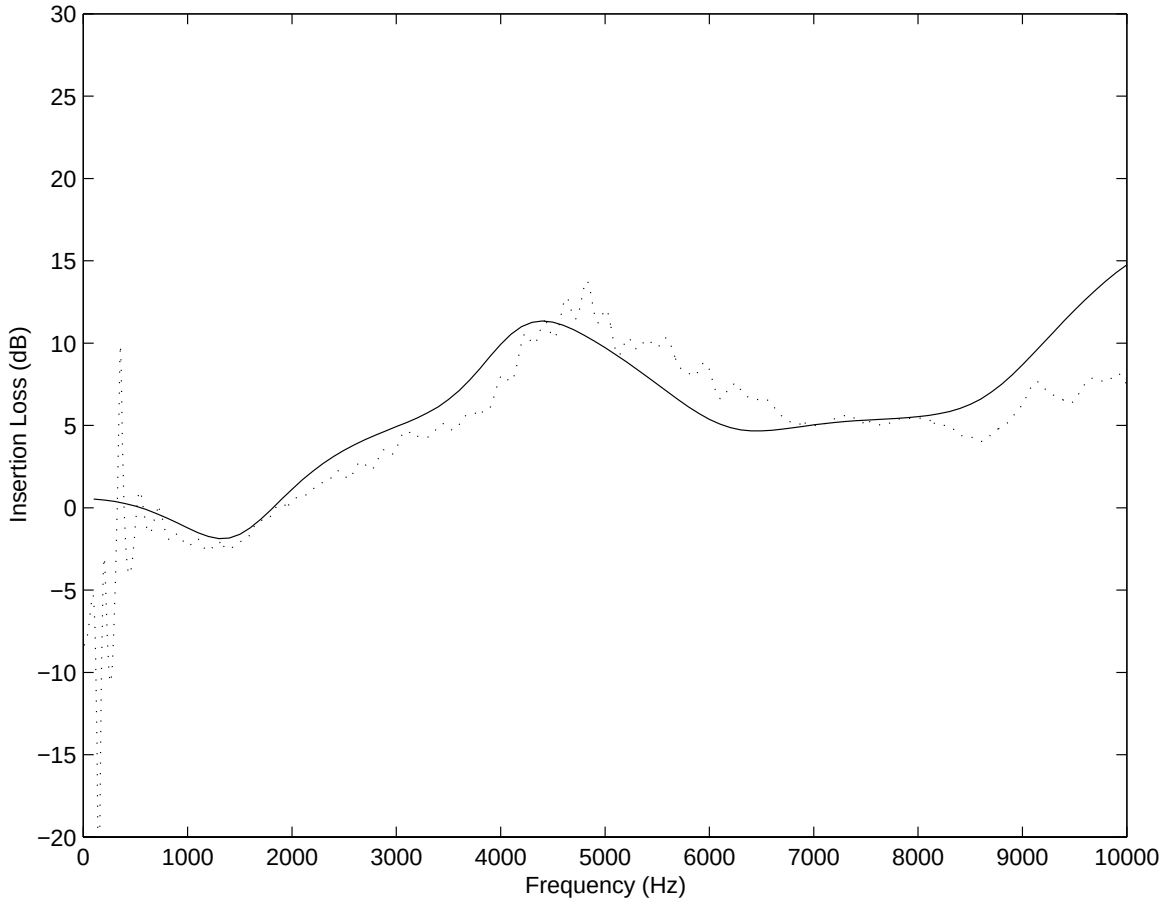

Figure 5.16. Comparison of insertion loss at receiver point 50 *mm* off the axis. '$\cdots$': experimental data with time window technique; '—': numerical simulation with infinitely thin assumption.

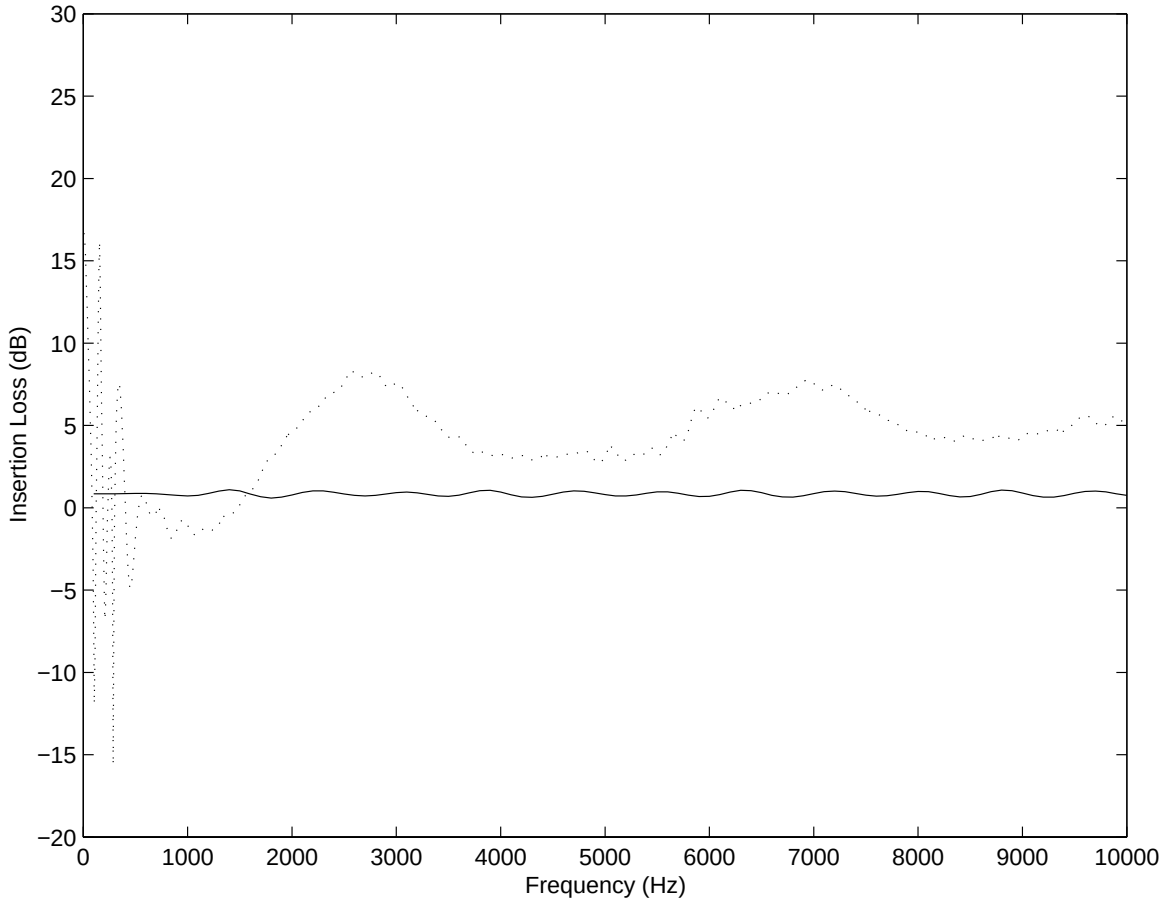

Figure 5.17. Comparison of insertion loss at receiver point 75 mm off the axis. '$\cdots$': experimental data with time window technique; '—': numerical simulation with infinitely thin assumption.

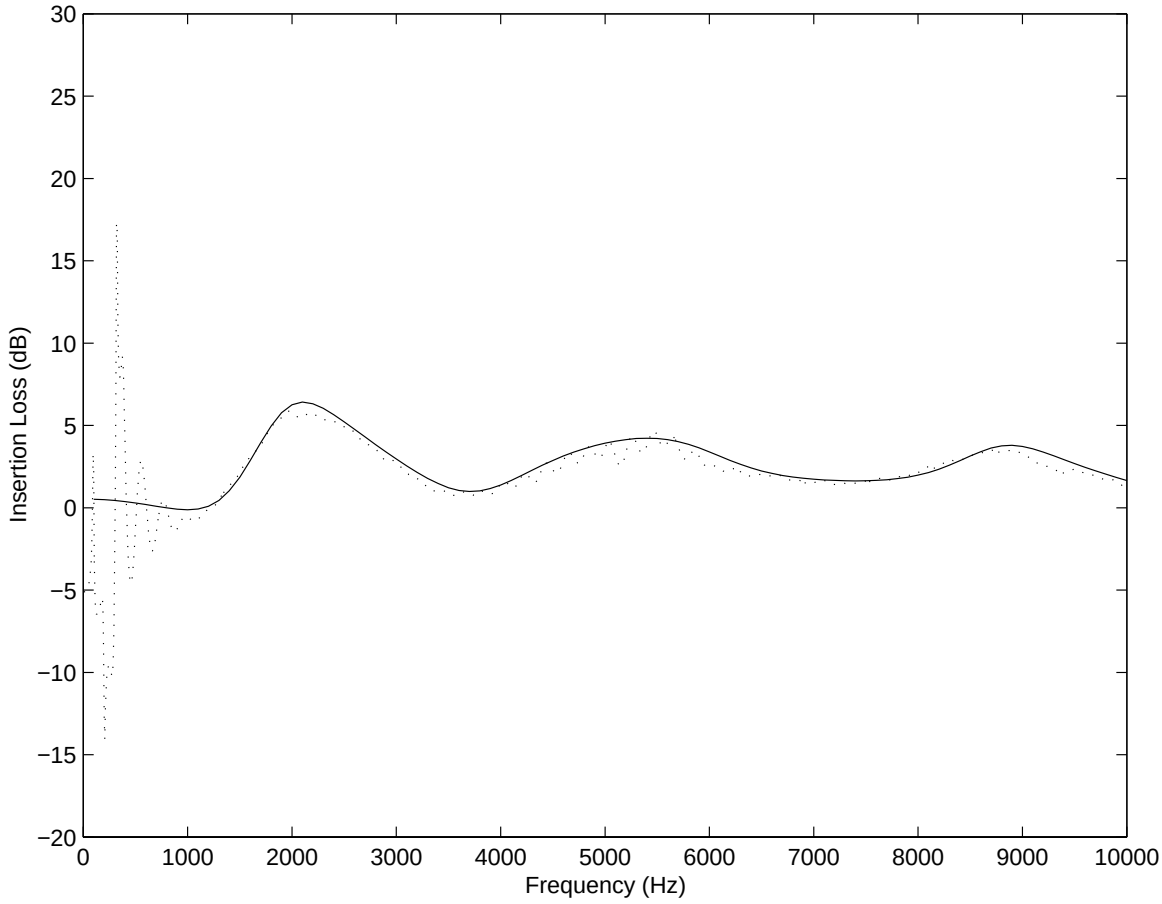

Figure 5.18. Comparison of insertion loss at receiver point 100 mm off the axis. '$\cdots$': experimental data with time window technique; '—': numerical simulation with infinitely thin assumption.

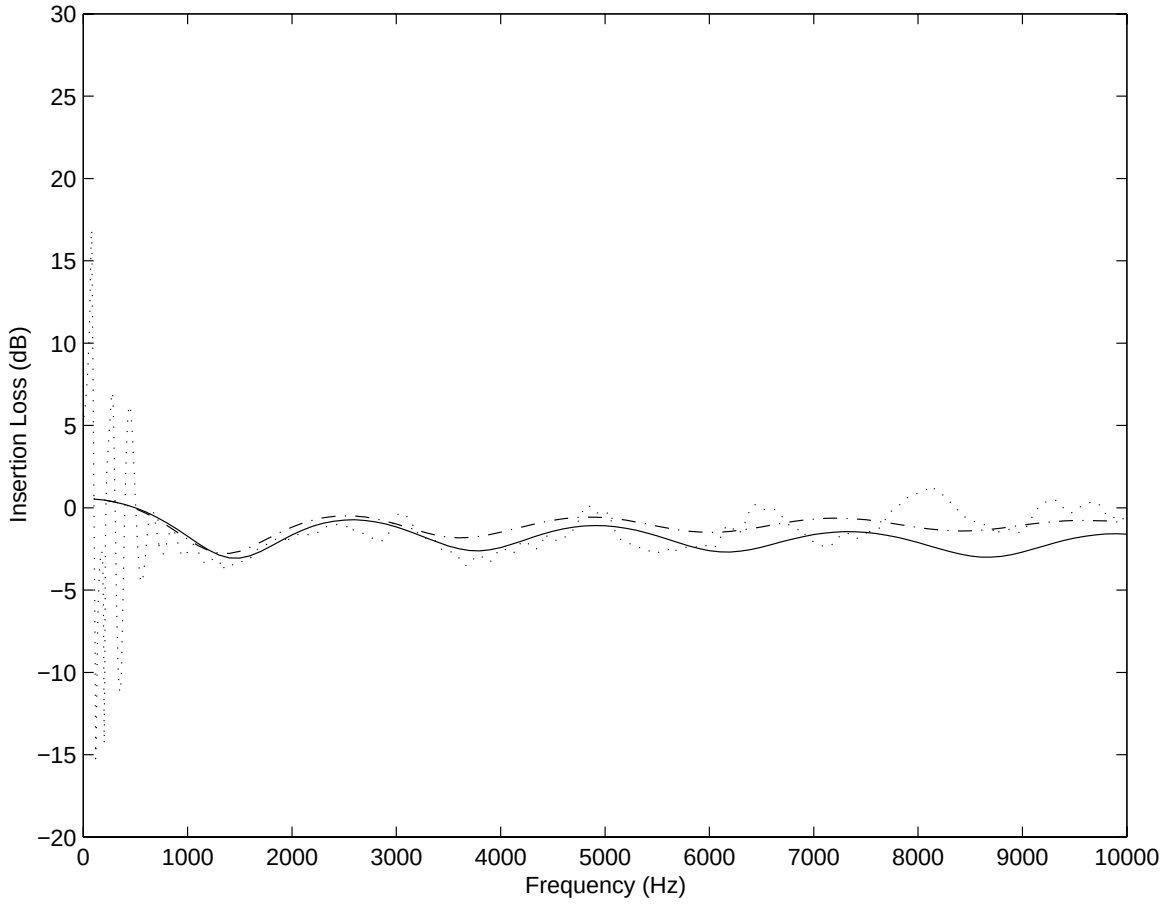

Figure 5.19. Comparison of insertion loss at receiver point on the axis. '· · ·': experimental data with time window technique; '—': numerical simulation with infinitely thin assumption; '-·-·': numerical simulation with finite thickness.

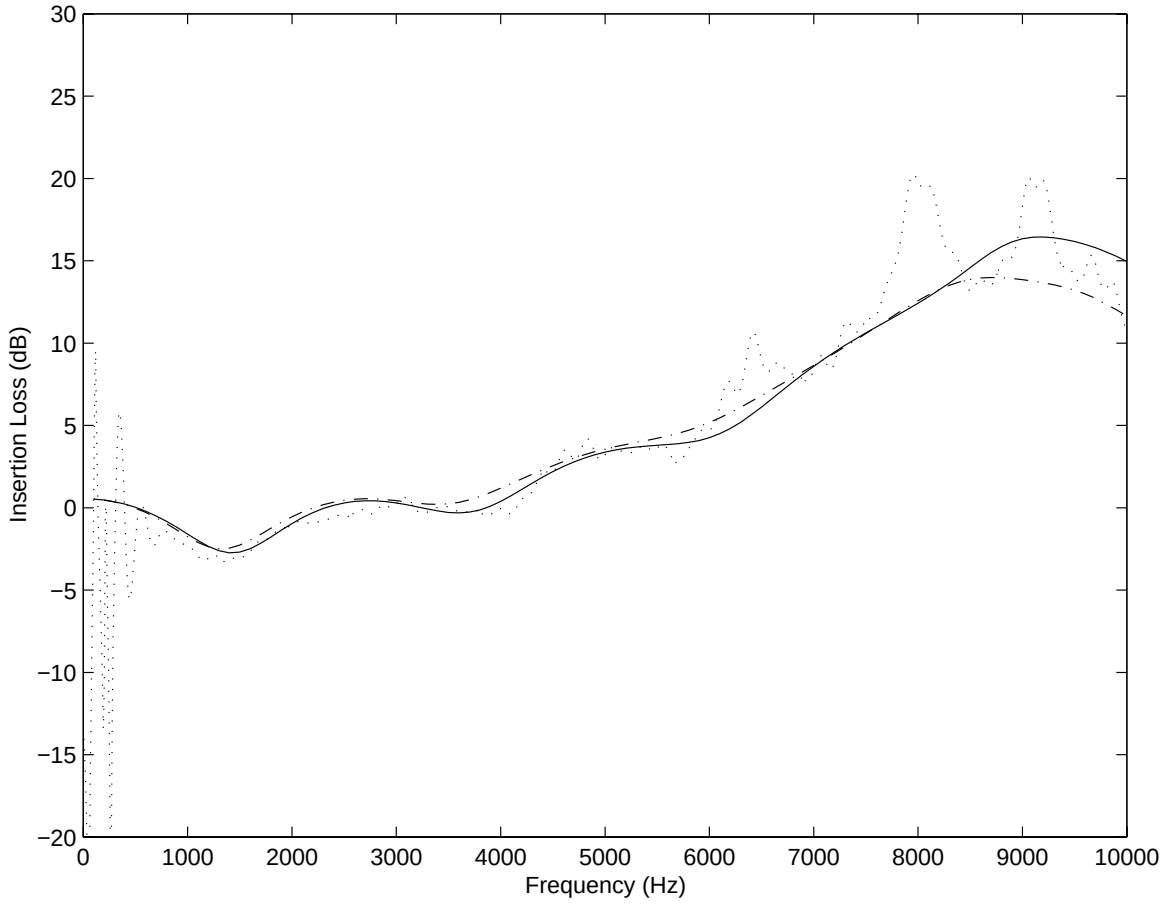

Figure 5.20. Comparison of insertion loss at receiver point 25 *mm* off the axis. '· · ·': experimental data with time window technique; '—': numerical simulation with infinitely thin assumption; '-·-·': numerical simulation with finite thickness.

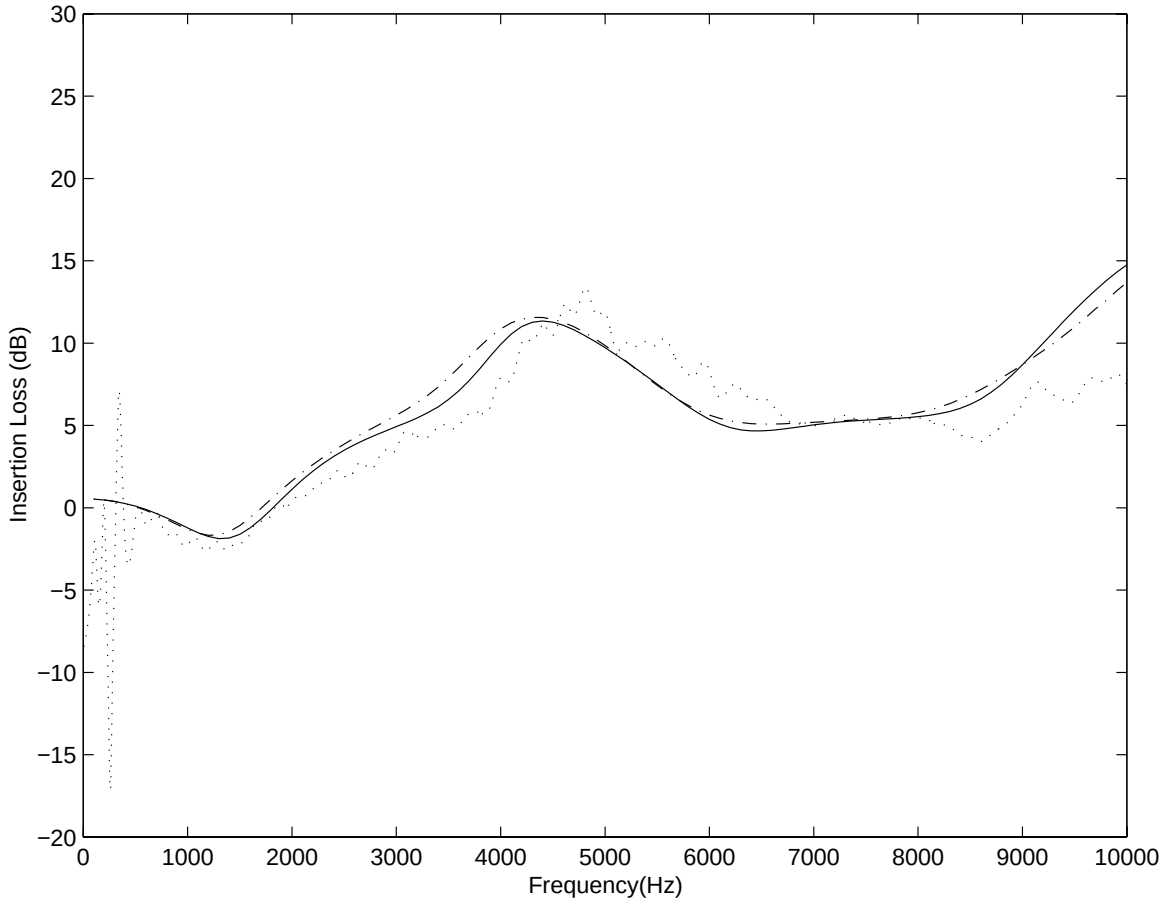

Figure 5.21. Comparison of insertion loss at receiver point 50 mm off the axis. '$\cdots$': experimental data with time window technique, '—': numerical simulation with infinitely thin assumption, '-·-·': numerical simulation with finite thickness.

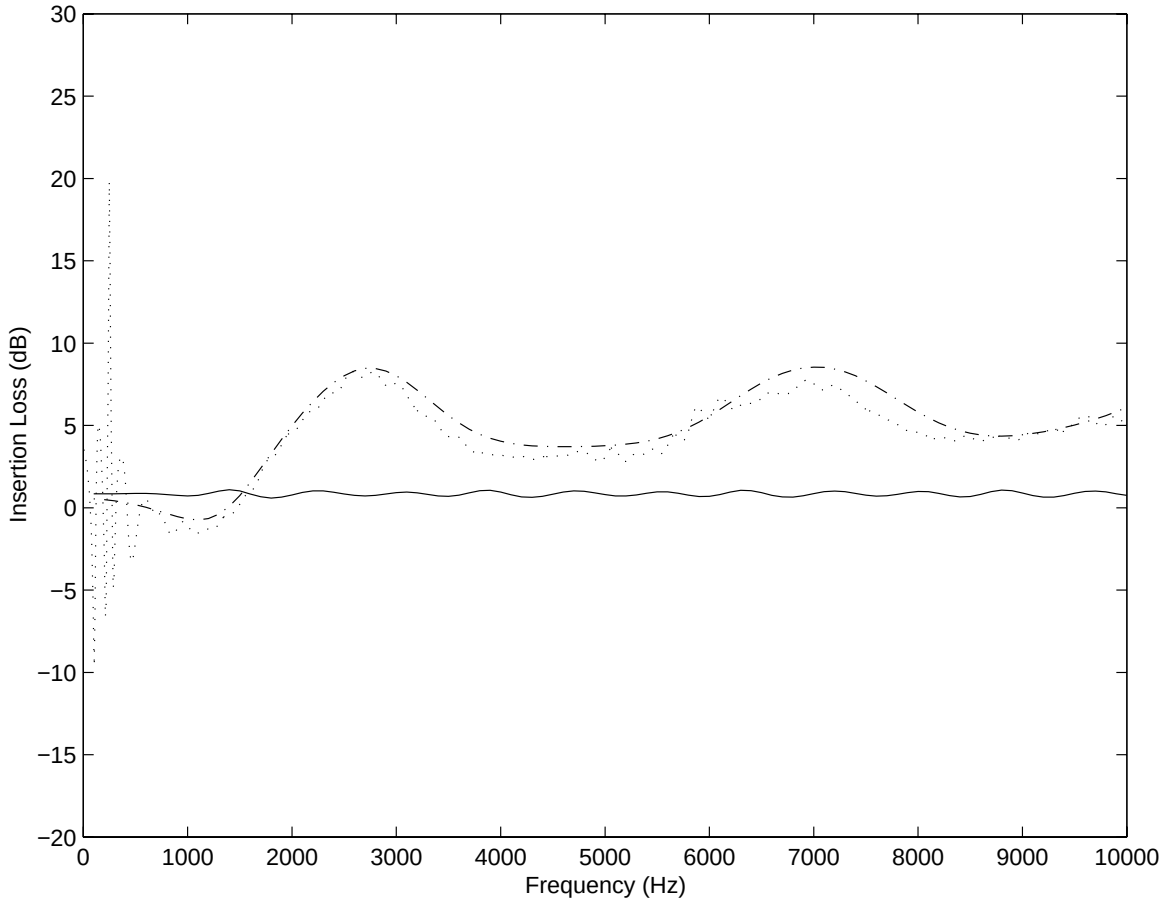

Figure 5.22. Comparison of insertion loss at receiver point 75 *mm* off the axis. '$\cdots$': experimental data with time window technique; '—': numerical simulation with infinitely thin assumption; '-·-·': numerical simulation with finite thickness.

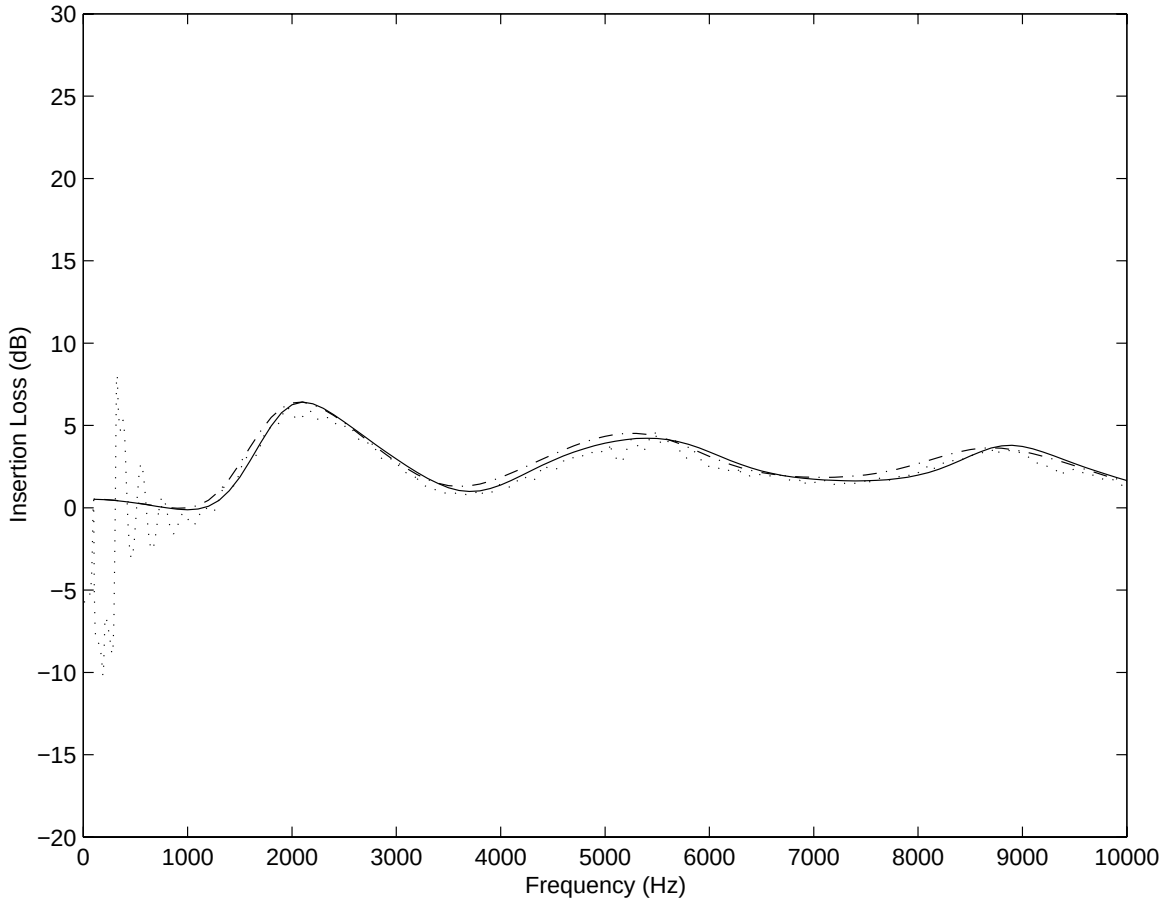

Figure 5.23. Comparison of insertion loss at receiver point 100 mm off the axis. '· · ·': experimental data with time window technique; '—': numerical simulation with infinitely thin assumption; '-·-·': numerical simulation with finite thickness.

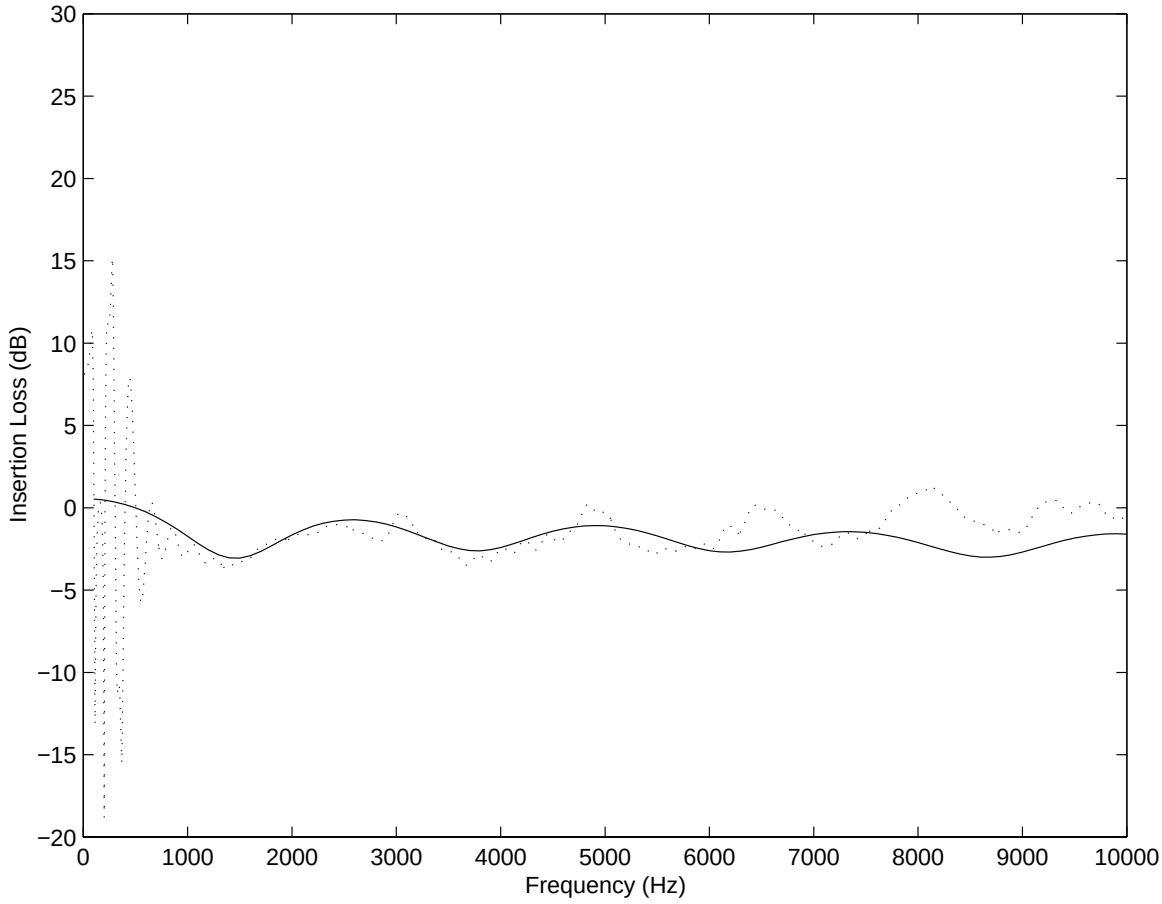

Figure 5.14. Comparison of insertion loss at receiver point on the axis. '···': experimental data with time window technique; '—': numerical simulation with infinitely thin assumption.

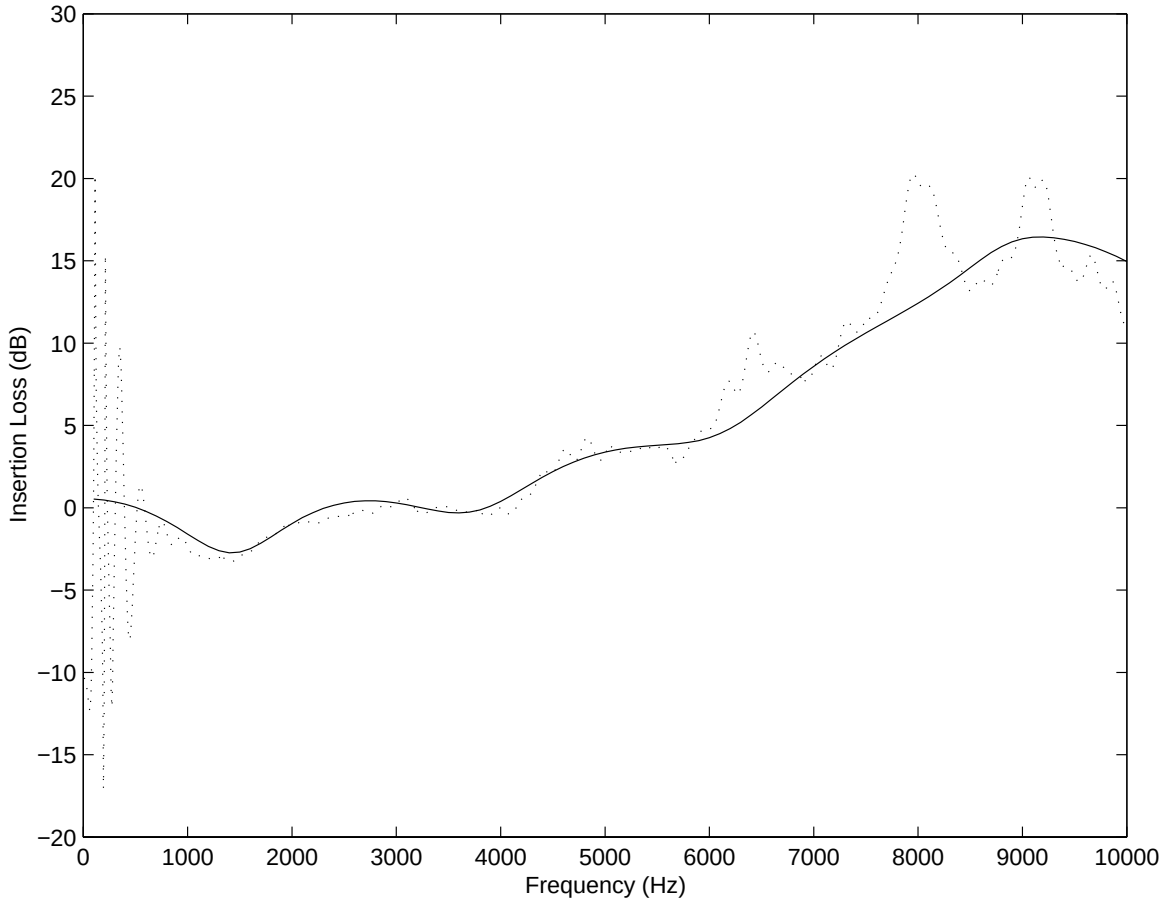

Figure 5.15. Comparison of insertion loss at receiver point 25 *mm* off the axis. '$\cdots$': experimental data with time window technique; '—': numerical simulation with infinitely thin assumption.

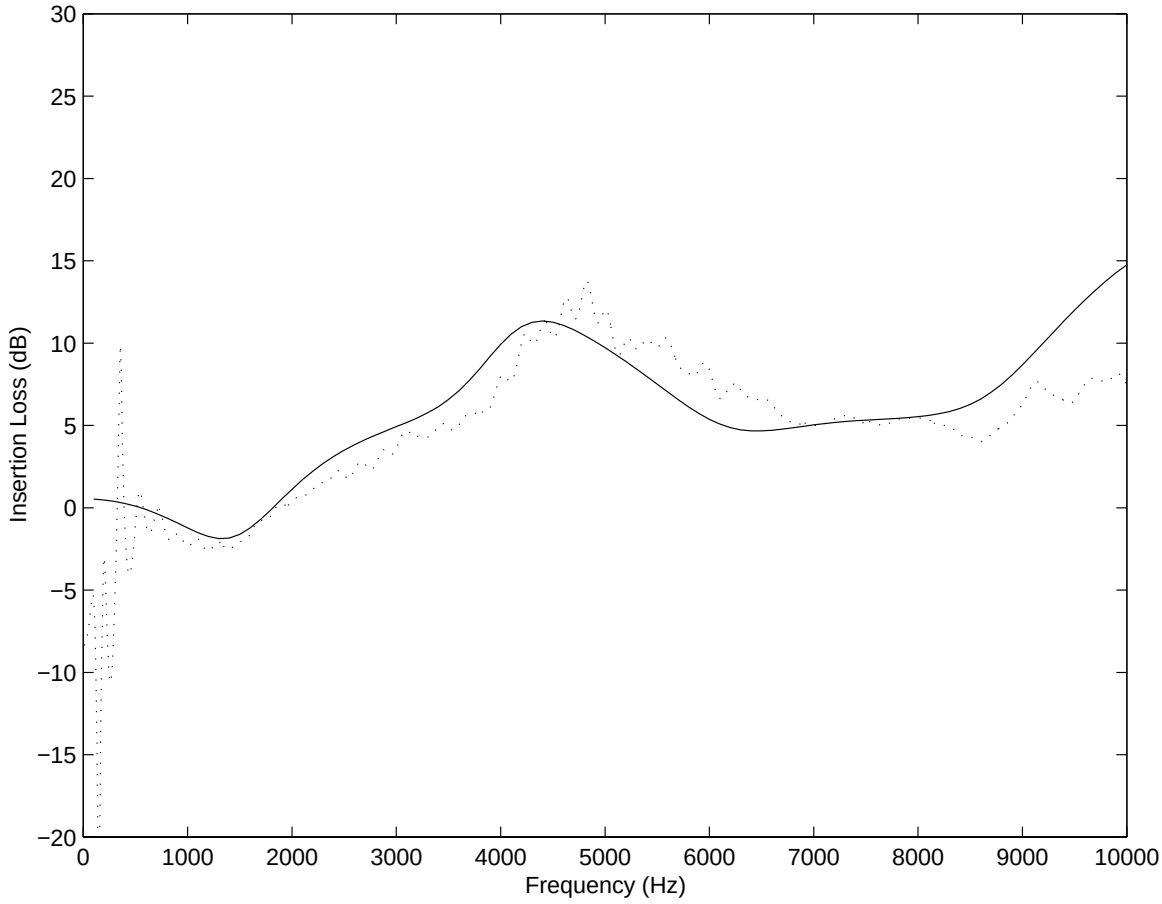

Figure 5.16. Comparison of insertion loss at receiver point 50 *mm* off the axis. '$\cdots$': experimental data with time window technique; '—': numerical simulation with infinitely thin assumption.

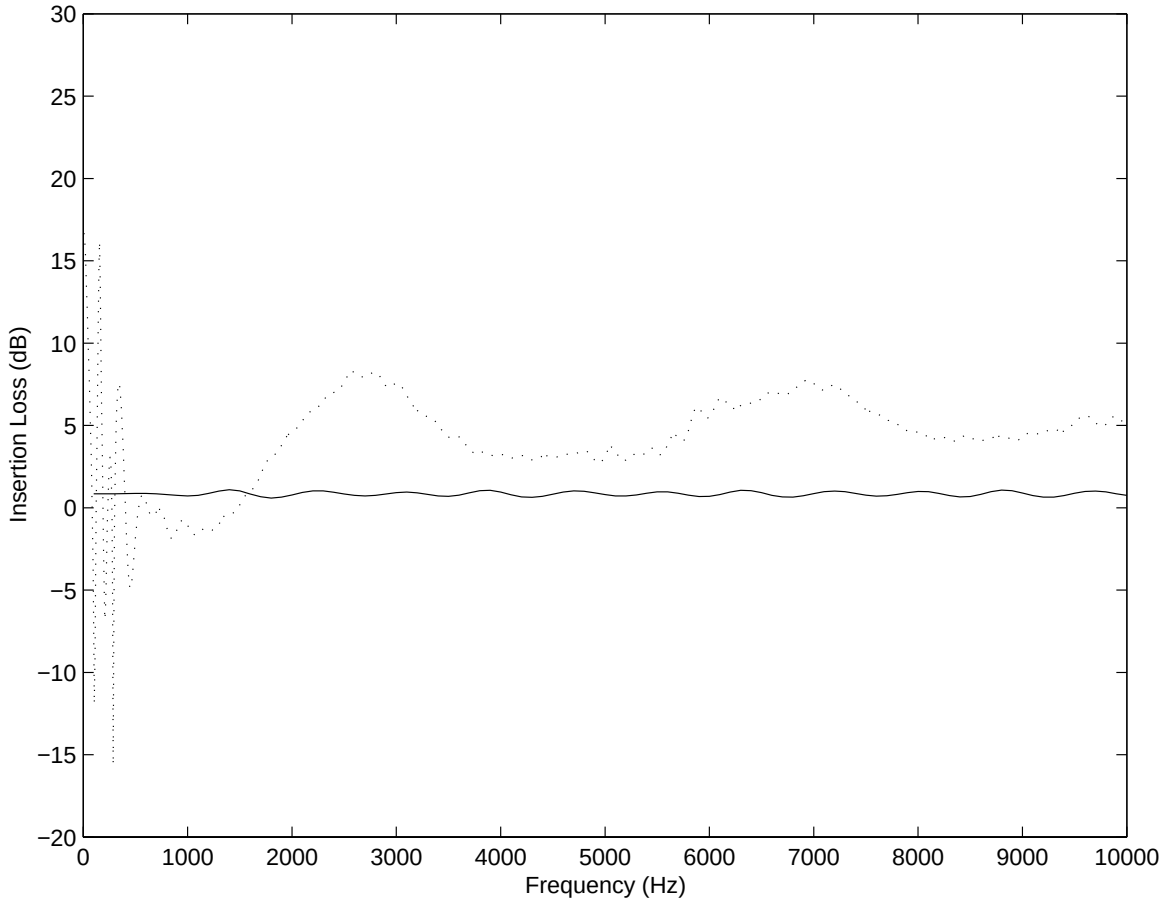

Figure 5.17. Comparison of insertion loss at receiver point 75 mm off the axis. '$\cdots$': experimental data with time window technique; '—': numerical simulation with infinitely thin assumption.

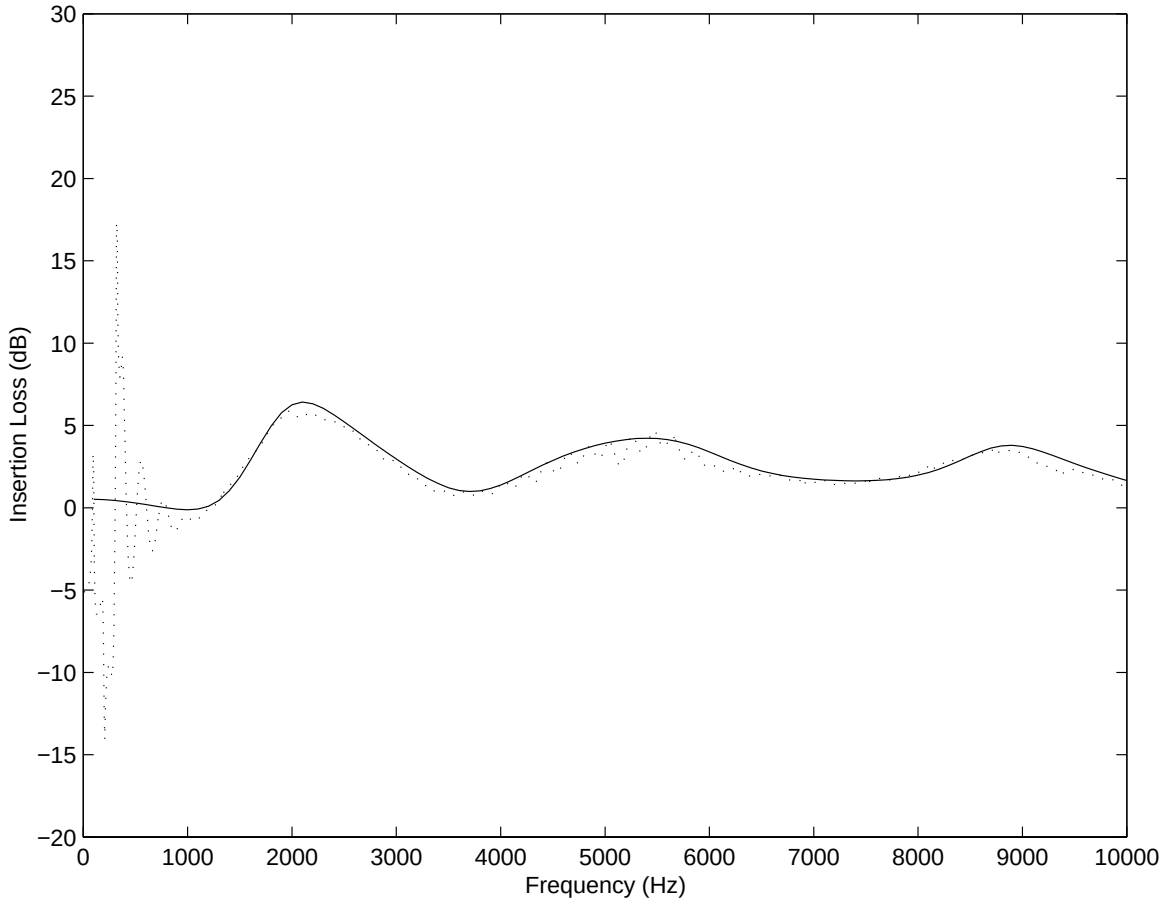

Figure 5.18. Comparison of insertion loss at receiver point 100 mm off the axis. '$\cdots$': experimental data with time window technique; '—': numerical simulation with infinitely thin assumption.

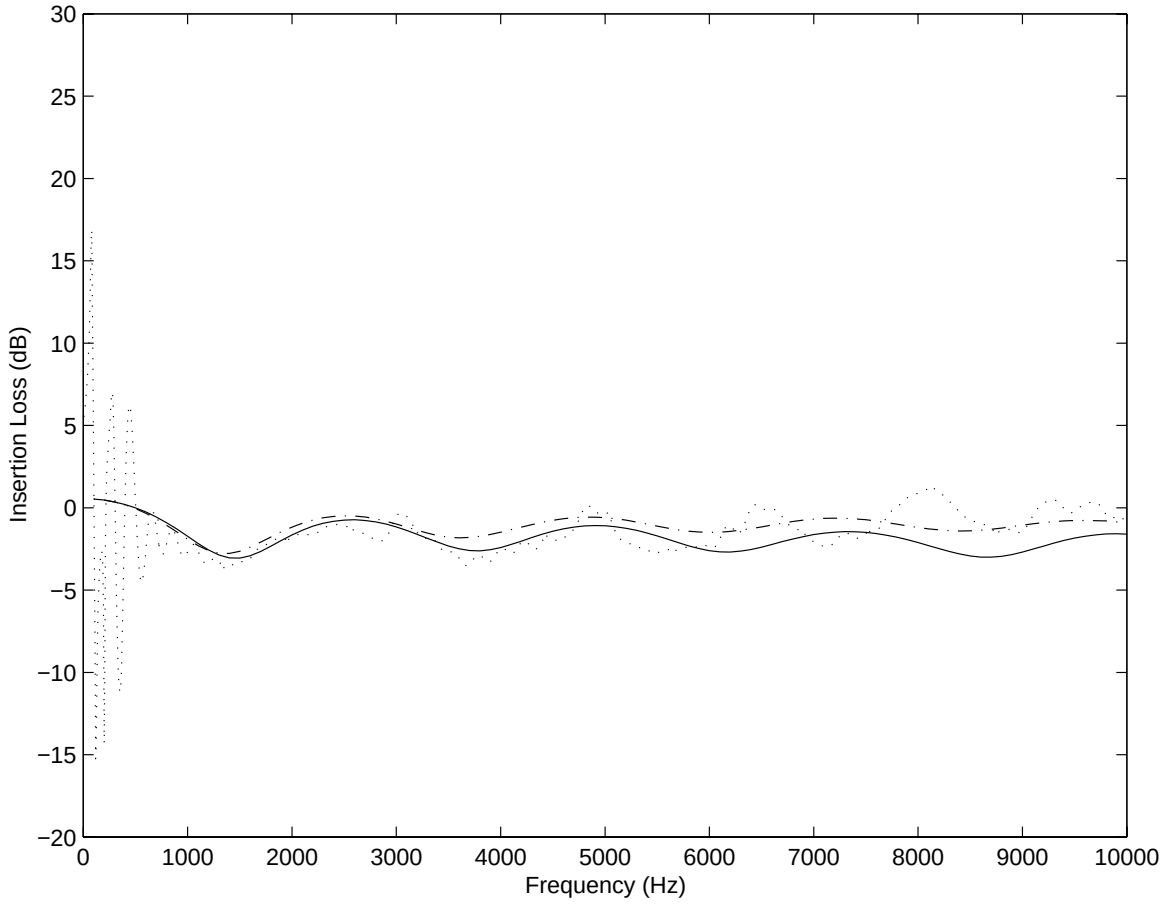

Figure 5.19. Comparison of insertion loss at receiver point on the axis. '· · ·': experimental data with time window technique; '—': numerical simulation with infinitely thin assumption; '-·-·': numerical simulation with finite thickness.

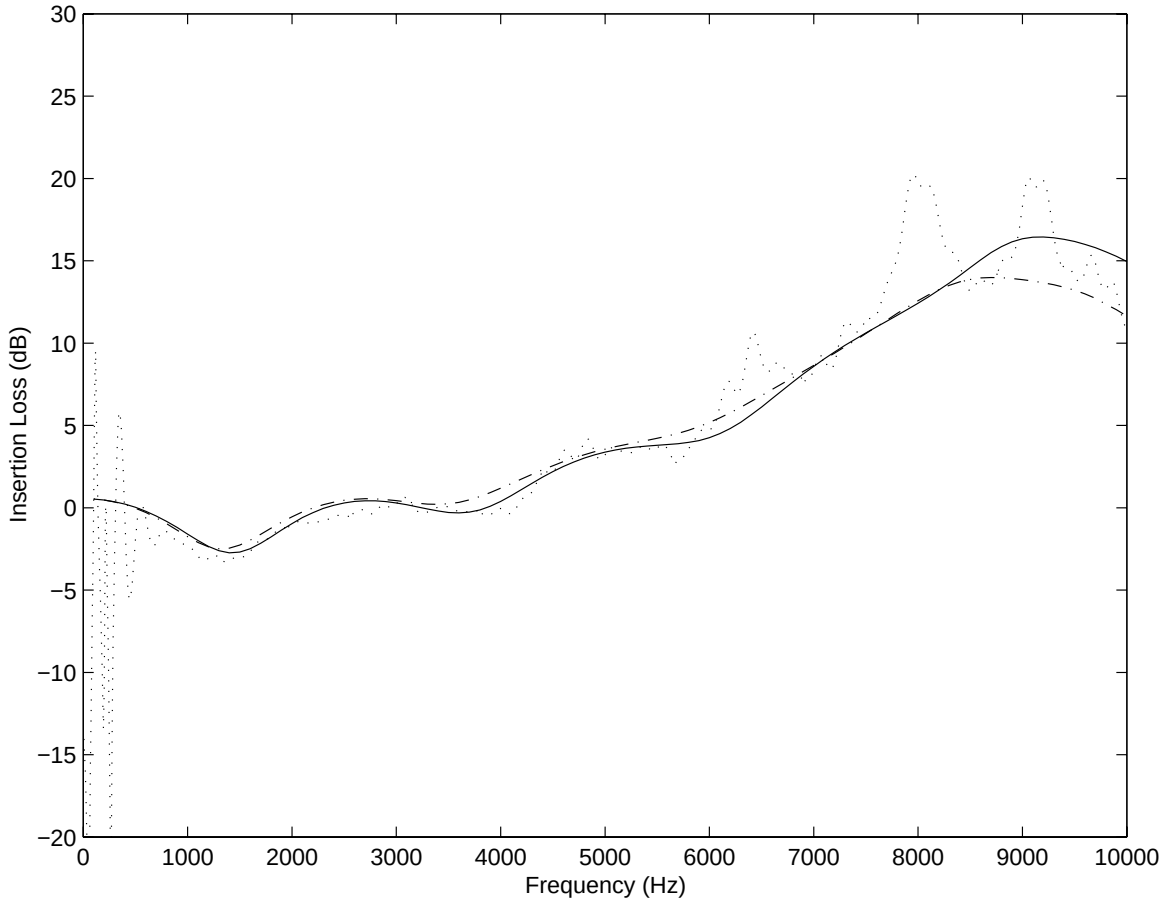

Figure 5.20. Comparison of insertion loss at receiver point 25 *mm* off the axis. '· · ·': experimental data with time window technique; '—': numerical simulation with infinitely thin assumption; '-·-·': numerical simulation with finite thickness.

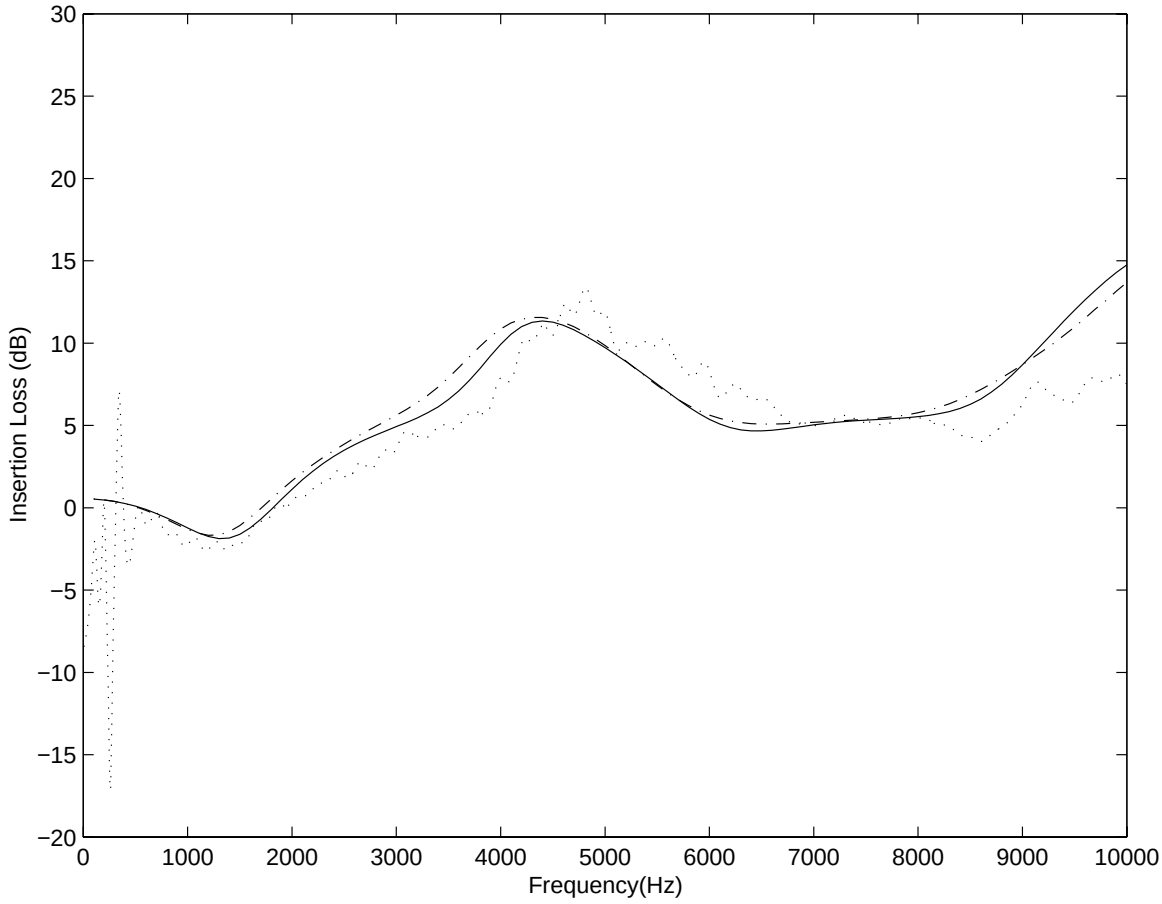

Figure 5.21. Comparison of insertion loss at receiver point 50 mm off the axis. '$\cdots$': experimental data with time window technique, '—': numerical simulation with infinitely thin assumption, '-·-·': numerical simulation with finite thickness.

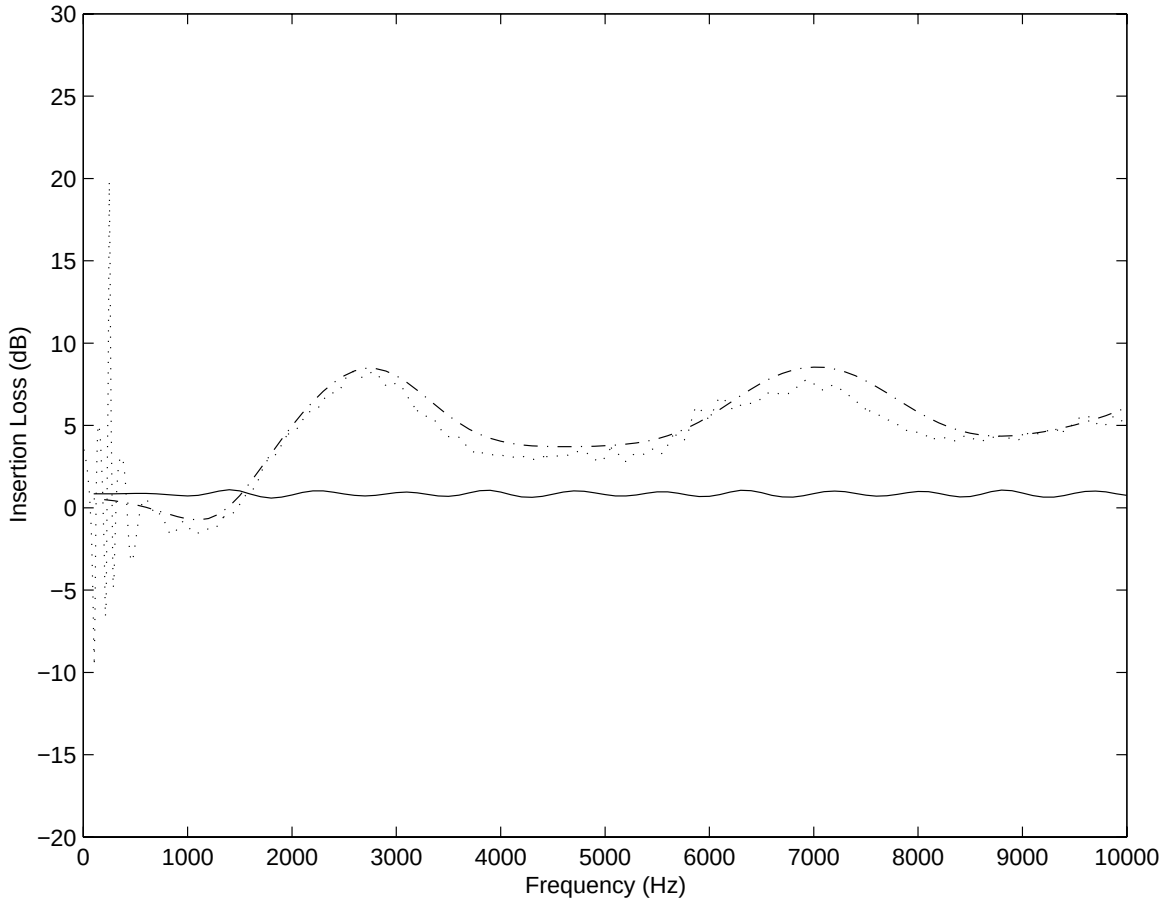

Figure 5.22. Comparison of insertion loss at receiver point 75 *mm* off the axis. '$\cdots$': experimental data with time window technique; '—': numerical simulation with infinitely thin assumption; '-·-·': numerical simulation with finite thickness.

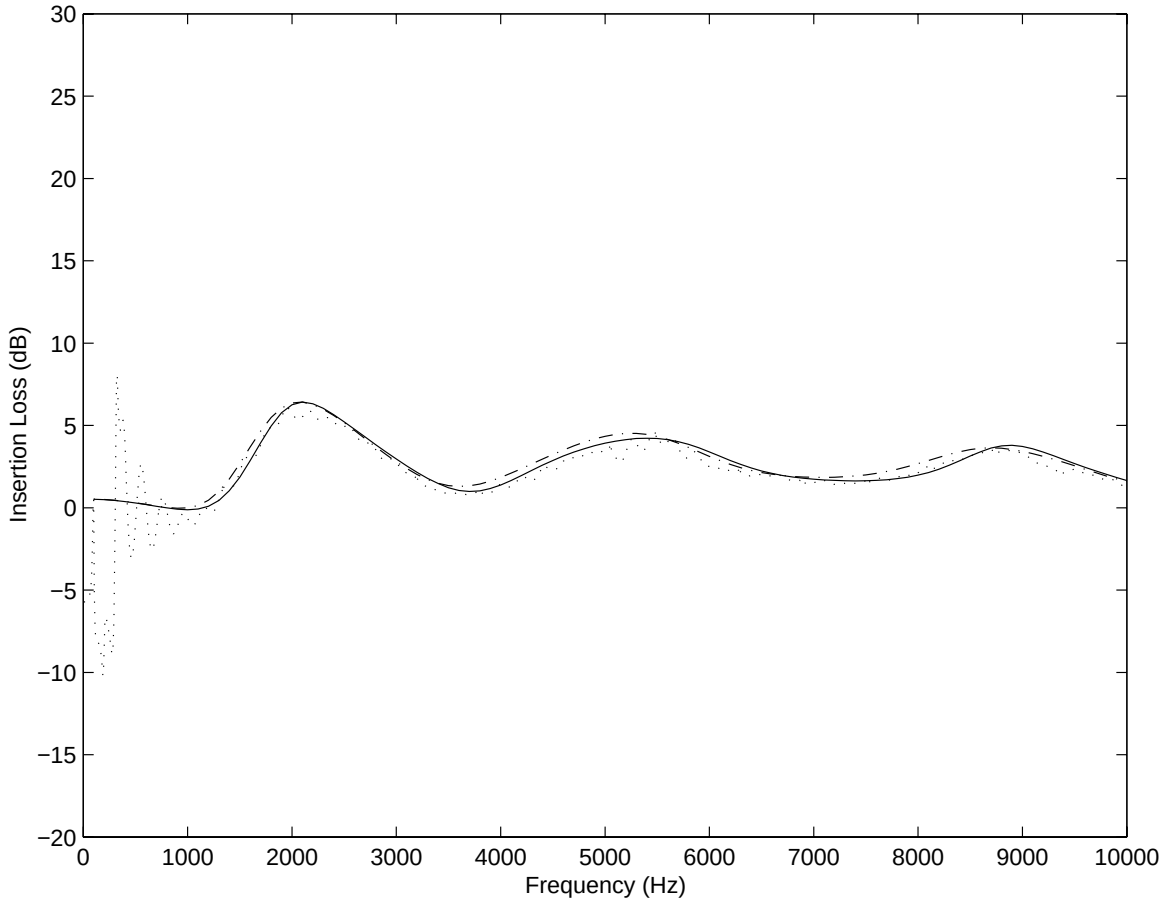

Figure 5.23. Comparison of insertion loss at receiver point 100 mm off the axis. '· · ·': experimental data with time window technique; '—': numerical simulation with infinitely thin assumption; '-·-·': numerical simulation with finite thickness.

6. DIFFRACTION BY OBSTACLES WITH COMPLEX SHAPES

6.1 Introduction

As discussed earlier it has been reported that the use of complex barrier geometries may result in lower root-mean-square sound pressures at measurement points on their central axis compared to the case of simple circular disks [37]. The boundary element model is known to be more accurate for this class of problems than approximate, diffraction-based procedures and the boundary element procedure is used to investigate the effects of barrier shape. Three different shapes were used to study the effects of geometry on rigid barrier performance.

6.2 Boundary Element Models

Geometry modelling

Here the shape of the scattering obstacle was varied while maintaining the same surface area. Figure 6.1 shows the three different shapes that were used to investigate the effects of shape on the diffracted sound field. The uni-radial disk had a radius of 7.5 cm. The bi-radial disk was divided into two halves with radii of 8.25 cm and 6.675 cm. The tri-radial model had three segments of different radii, each being equal in augular extent. The number of surface elements used was 1852, 1949, and 1896 for the uni-radial, bi-radial and tri-radial models, respectively. The locations of the sound source and the receiver were chosen to be the same for all three cases. A schematic diagram illustrating the configuration for the numerical study is shown in Figure 5.1. The point source was located 165 cm in front of the circular disk, along the center axis. The diameter of the circular disk was 15 cm. A linear array of seven receivers was located 10 cm behind the circular disk plane, with a spacing of 2.5 cm, starting from the point on the axis.

6.2.1 Insertion Loss Results

The sound pressure level was calculated using SYSNOISE and results were exported into MATLAB to calculate the insertion loss. Comparisons between insertion losses were performed at four receiver locations: one on-axis, two in the shadow zone, and one at the boundary of the shadow zone. A comparison between the insertion loss for the three disk models is shown in Figures 6.2 to 6.5. Four receiver points were considered; one on-axis, two in the shadow zone, and one at the boundary of the shadow zone.

Figure 6.2 shows the comparison between the insertion losses for the three disk models, on the center axis. It can be seen that the more complicated disk shapes yield slightly higher insertion losses in this case. However, the benefit is only 1-2 dB at high frequencies, and the insertion loss is still negative in this region. The insertion losses for all three disk shapes are the same at low frequencies since at those frequencies the disk is samll compared to a wavelength. For all three cases, the insertion loss is negative at this particular receiver location which confirms the existence of a central bright zone. In Figure 6.3 a comparison between the three disk configurations is presented for the first location in the shadow zone 25 mm off the center axis. For all three cases, the insertion loss is positive in the frequency range between 2 and 6 kHz. At 6 kHz the bi-radial disk insertion loss is 15 dB, which is about 10 dB greater than that of the simple disk. A similar comparison for the location 50 mm off-axis is shown in Figure 6.4. In contrast to the result at 25 mm off axis, the results at this point illustrate that the performance of bi-radial disk is not as good at high frequencies as to that of the uni-radial disk, although it is somewhat better in the frequency range from 1 kHz to 3.8 kHz. The tri-radial disk performance is worse than that of the uni-radial disk at all frequencies.

The insertion loss comparison near the shadow boundary is shown in Figure 6.5. There are not many differences between the insertion loss values for the three configurations at this receiver point, in contrast with the results in the shadow region. It may be noticed in this case that the simple disk barrier performance is more “balanced”

than those of the two barrier designs having more complex shapes.

The results presented here suggest that evaluating the performance of barriers of complex shapes by considering the insertion loss at only certain receiver location can be misleading. A different metric based on sound power was investigated to address this problem.

6.2.2 Sound Power in the Shadow Zone

It was shown in the last sub-section that the insertion loss for the various disks varies significantly as a function of receiver location. This observation suggests that insertion loss might not be a good metric for evaluating the performance of disks having complicated shapes.

The boundary element method makes it possible to compute the sound pressure, the acoustic particle velocity and hence the acoustic intensity, which is the sound power per unit area crossing each receiver surface. By integrating the intensity over various receiver planes, the sound power propagating within the shadow zone can be calculated. The sketch in Figure 6.6 shows how the receiver planes are defined in this case. Note that diffraction causes acoustic energy to scatter from the illuminated zone into the shadow zone in the region behind the obstacle. Thus it is expected that the sound power travelling in the shadow zone should progressively increase with distance behind the barrier. Nevertheless, it has been found that at sufficiently large distances behind the barrier the sound power converges to a nearly stationary limit. The sound power propagating through the shadow zone is then essentially independent of distance far from the barrier.

Figure 6.7 shows the sound power propagating downstream one meter behind the three disks considered here. Note that the receiver plane is based on the shadow region defined by the circular disk in all cases. There are other possible choices of receiver plane since it depends on the shape of the shadow region which in turn is determined by the shape of the obstacle. It was decided to use the shadow zone defined by the simple disk for all three types of geometry since the aim of introducing changes in barrier shapes is to reduce the sound energy in the shadow zone already

defined.

It can be seen clearly in Figure 6.7 that the sound power over the shadow zone has not been reduced by the use of more complex geometries. In particular, there are not any noticeable differences in terms of sound power between the three different geometries in the frequency range 0 to 5 kHz. At higher frequencies, the sound power in fact increases when more complex geometries are used. The increase is only on the order of 2-3 dB which is perhaps not very significant. Nonetheless, at least in the examples considered here, the shaped disks do not show any significant advantage compared to the uniform disk.

It is suggested here that the performance of a barrier having a relatively complicated geometry can be quantified most effectively in terms of the sound power crossing a recovery plane downstream of the barrier as long as the recovery plane is located an appropriate distance behind the barrier. The use of a sound power metric makes it relatively straightforward to compare the relative performance of various designs, and thus may prove to be a useful tool for barrier shape optimization. It has also been found here that shaped barriers do not necessarily offer any net performance benefit when compared with an equivalent uniform barrier.

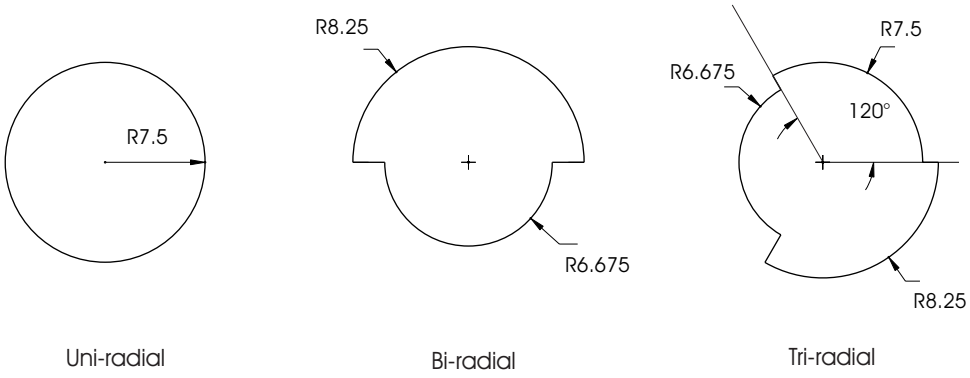

Figure 6.1. Geometry of the three obstacles for the study of the influence of complex shapes.

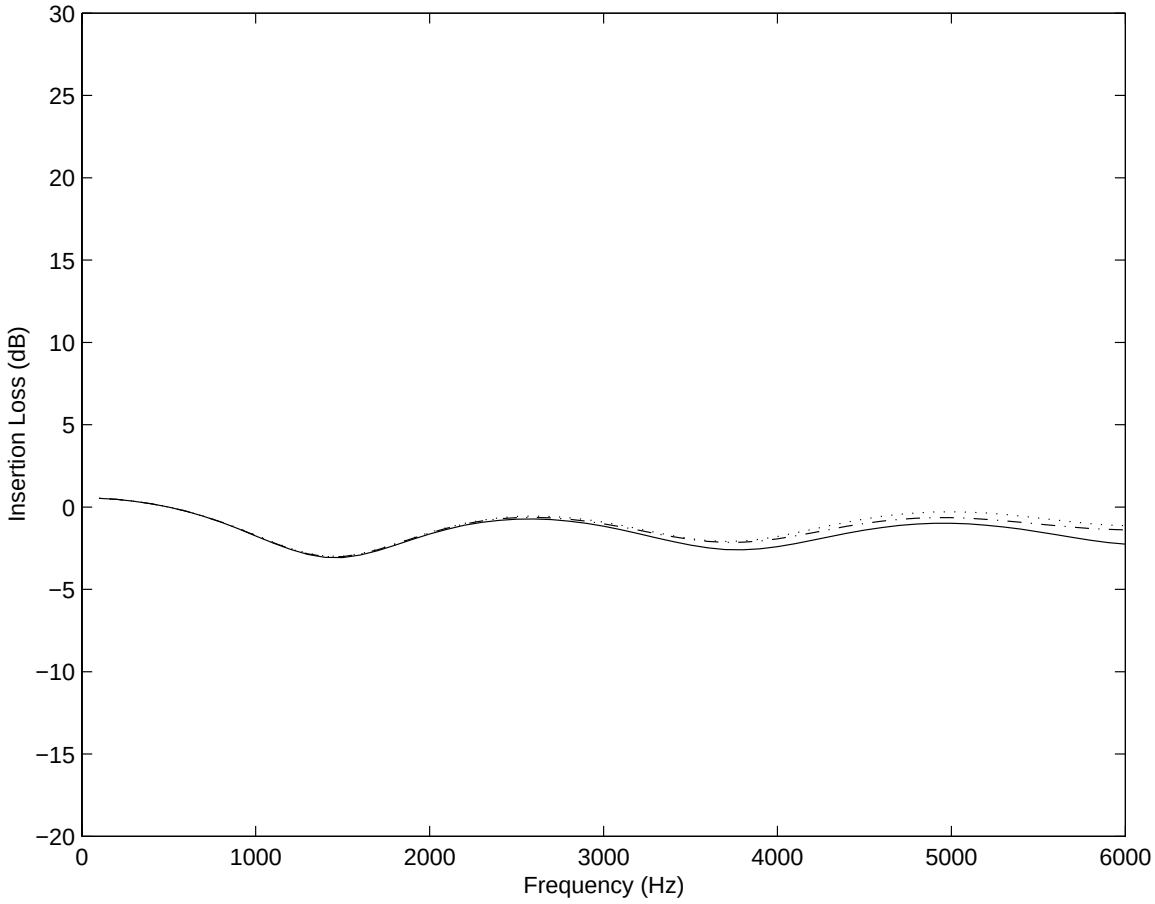

Figure 6.2. Insertion loss vs. frequency. Receiver point on the axis. '—': uni-radial disk; '· · ·': bi-radial disk; '-·-·': tri-radial disk.

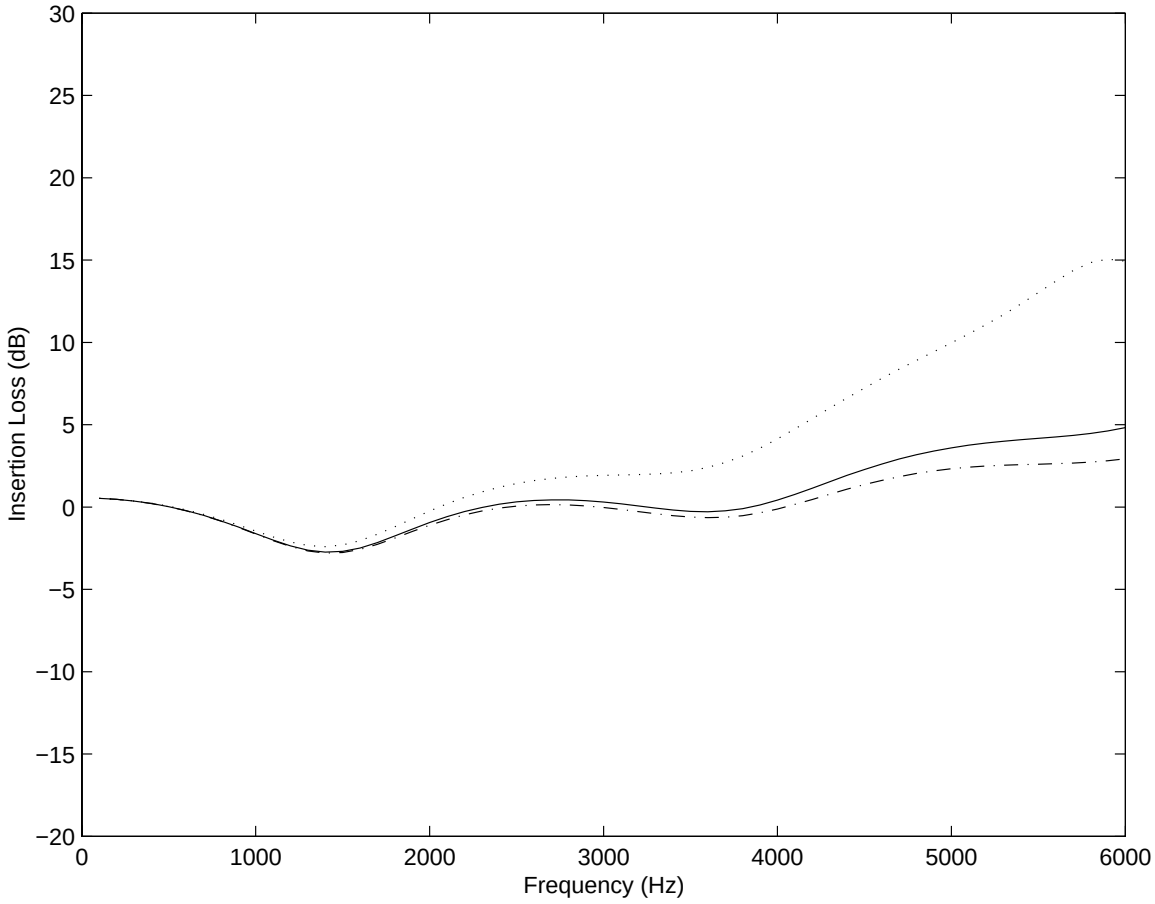

Figure 6.3. Insertion loss vs. frequency. Receiver point 25 mm off the axis. '—': uni-radial disk; '· · ·': bi-radial disk; '-·-·': tri-radial disk.

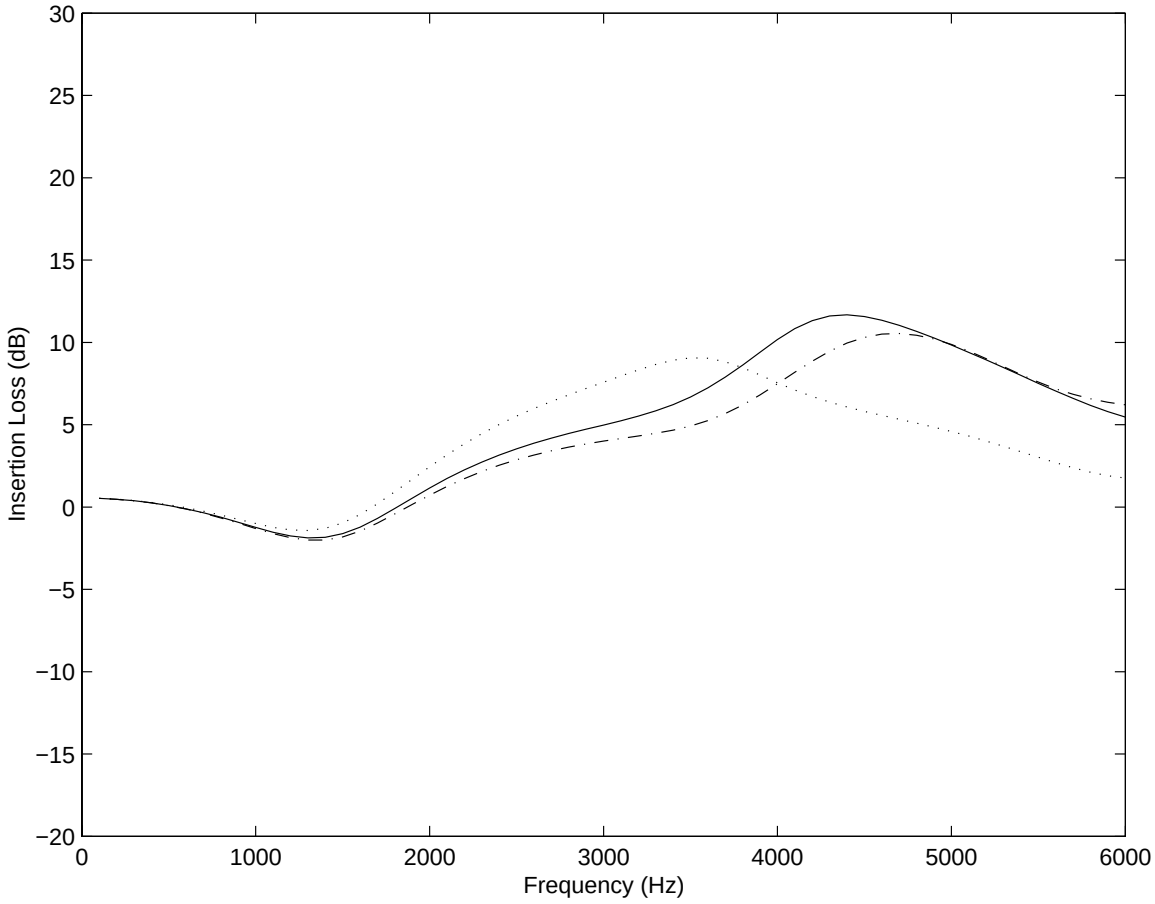

Figure 6.4. Insertion loss vs. frequency. Receiver point 50 mm off the axis. '—': uni-radial disk; '· · ·': bi-radial disk; '-·-·': tri-radial disk.

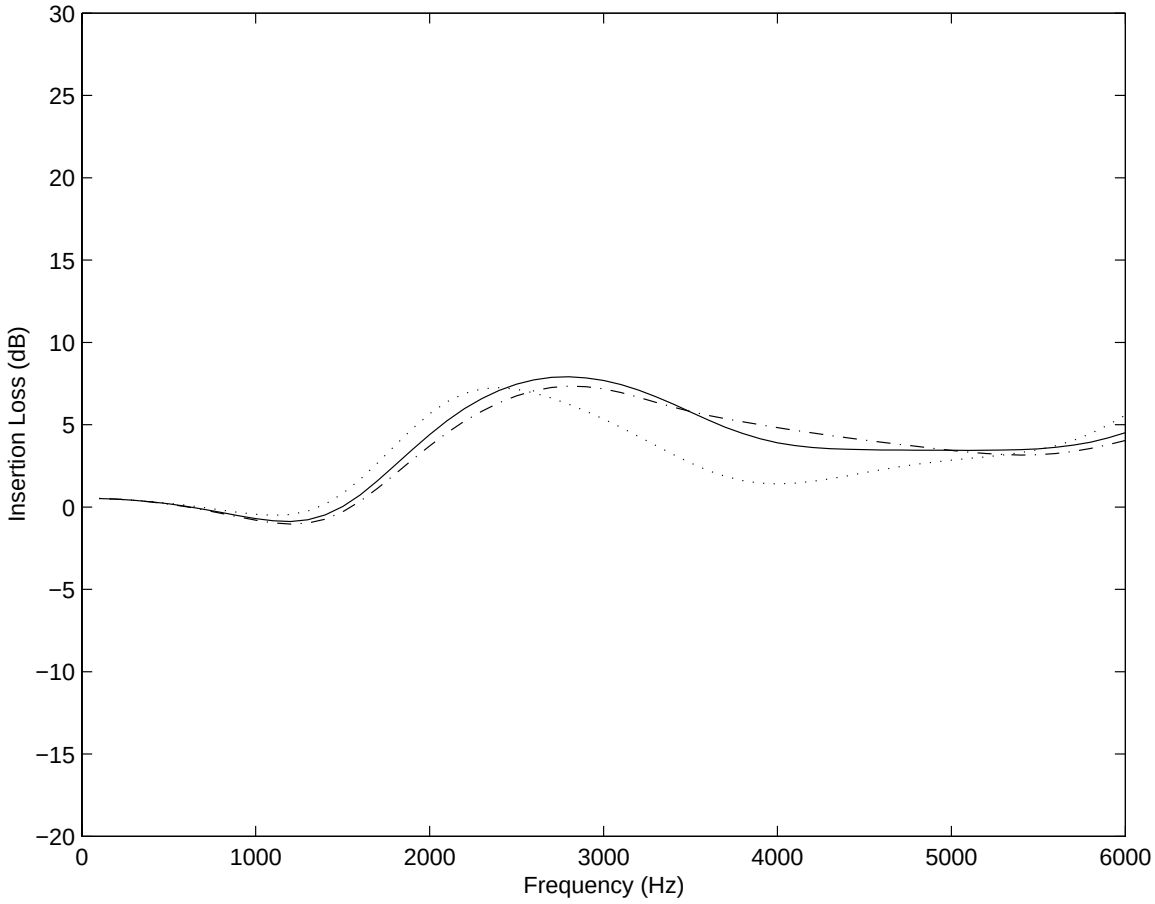

Figure 6.5. Insertion loss vs. frequency. Receiver point 75 mm off the axis. '—': uni-radial disk; '· · ·': bi-radial disk; '-·-·': tri-radial disk.

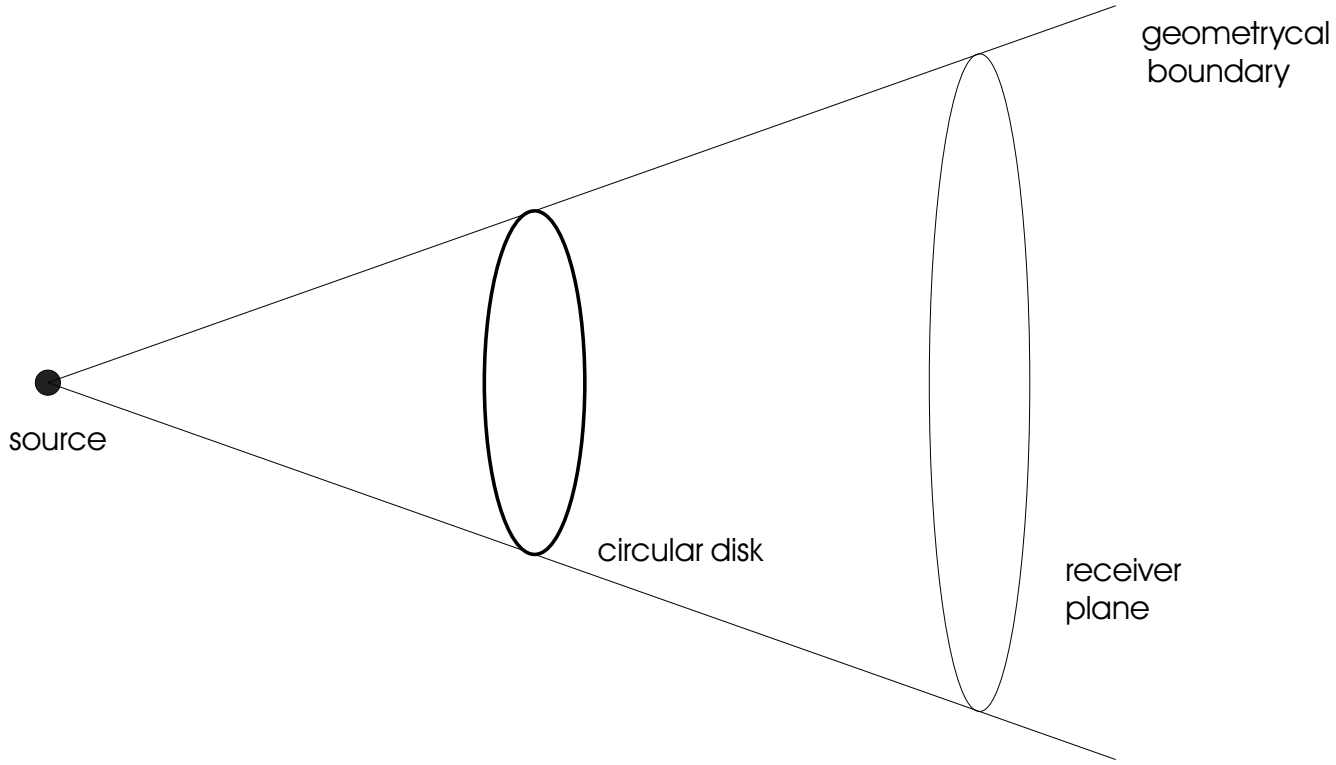

Figure 6.6. The receiver planes defined from the geometrical shadow boundary in case of the circular disk.

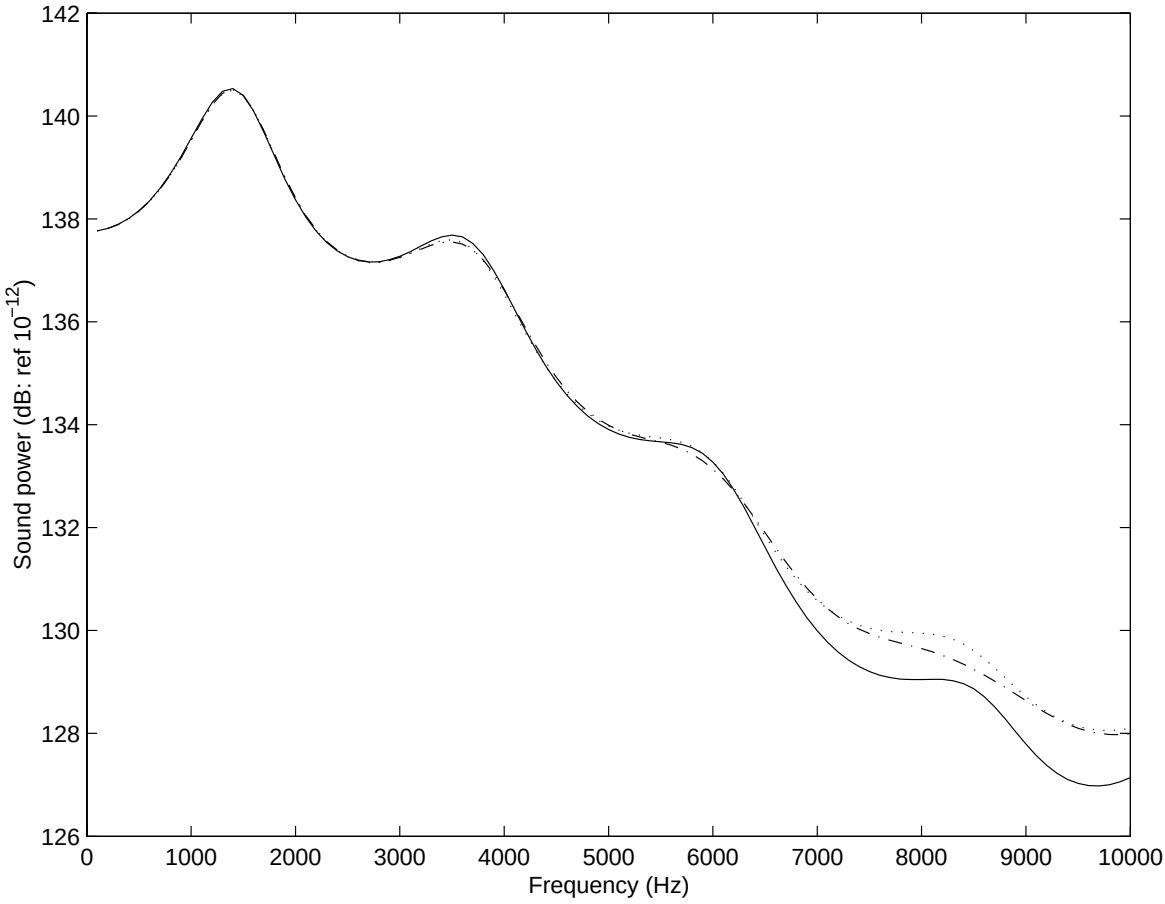

Figure 6.7. Comparison of sound power at receiver plane over the shadow zone 1 m behind the disk. '—': uni-radial disk; '· · ·': bi-radial disk; '-·-·': tri-radial disk.

7. SCALED PHYSICAL MODEL OF RIGID STRAIGHT-EDGE BARRIER

7.1 Introduction

In this chapter we consider scaled barrier models that were intended to represent highway noise barrier applications. The experiments were designed to be performed in an anechoic chamber to eliminate any atmospheric effects which could not be accounted for exactly. A comparison between a diffraction-based model and a boundary element model was first made for the case of an infinite length barrier geometry. The limitations of the widely used diffraction-based model were studied. Experiments were also performed to compare the predictive capability of diffraction-based models and boundary element analysis in the case of a finite length barrier.

7.2 Straight Infinite Barrier

In an ideal case, a boundary element model should be used to predict the performance of a finite size barrier and then should be verified by comparison with experimental results. The calculation load in this case, however, becomes prohibitive because of the so-called six element rule which states that there should be at least six elements per wavelength on the face of the barrier at the maximum frequency of interest. It should be noted that for a real barrier with a length of 10 m and a height of 2 m, the discretization of the rectangular surface with six nodes per wavelength requires 600 / λ^2 unknowns where λ is the wavelength. At 1000 Hz, λ is 0.34 m and a full linear system with about 5000 unknowns need to be solved. Therefore, it is of interest to investigate the accuracy of diffraction-based models that require less computing power.

7.2.1 Diffraction-based Model

The geometry for a semi-infinite barrier without consideration of ground reflection is shown in Figure 7.1. In this case a cylindrical sound source was located 5 meters in front of the barrier and 2.5 meters below its top. The receiver was placed 20 meters behind the barrier and was 1.5 meters below the barrier top. Only diffraction at the top of the barrier was considered since the barrier is considered to be infinitely long with the result that only a single path joins the source and receiver. The insertion loss calculated by using the theory presented in section 4.1, for a semi-infinite barrier without consideration of ground reflection is shown in Figure 7.2. The results shown in Figure 7.2 demonstrate the general characteristics of noise barrier performance, in particular, that a barrier is not effective at low frequencies.

In Figure 7.3 the source and receiver geometry is illustrated for a 3 meter tall barrier placed on a hard ground surface. The insertion loss for that case is shown in Figure 7.4. This result should be compared to the case without ground reflection in Figure 7.2. In this finite-height barrier case, the additional ground reflection paths result in interference between the various diffracted sound rays with the result that a number of peaks and dips appear in the insertion loss. Thus, one result of ground reflection is to cause the performance of a barrier to display a strong dependence on frequency. This dependence on frequency varies according to the source and receiver locations.

7.2.2 Boundary Element Model

The boundary element code SYSNOISE was used to calculate a two-dimensional, wave-based solution for the geometry considered above. MSC Patran was used to generate the various models used here as in the earlier study. In the two-dimensional case, a cylindrical line source was assumed to generate the sound field. In the case of a barrier placed on a hard surface, it is only necessary to discretize the barrier surface since the presence of a uniform reflecting plane can be accounted for automatically in the boundary element calculations. The geometry shown in Figure 7.3 was constructed in the boundary element code SYSNOISE. Note that a typical boundary

element analysis is performed in two steps. First, the Green's function appropriate for the particular sound source and model geometry is computed. Once that calculation is performed, the sound field at arbitrary receiver points can be calculated in a second stage. It is the first step of this procedure that requires the majority of the computation time. To reproduce the diffraction-based calculation of Figure 7.3, 300 surface elements were used to represent the barrier, and the maximum analysis frequency was 5667 Hz based on the requirement that there be at least six elements per wavelength at the highest frequency of interest. To create the results presented here, the analysis was performed from 0 Hz to 2000 Hz in steps of 10 Hz. In the present case, the CPU time required for first step of the boundary element calculation was 431 seconds on an IBM RS-6000 workstation.

7.2.3 Comparison of Diffraction-based and Boundary Element Models

A comparison of the insertion losses calculated by using both the diffraction model and the boundary element model is shown in Figure 7.5 for a receiver point located at (x,y)=(20, 1.5): i.e., for a point 20 meters behind the barrier and 1.5 m above the ground. It can be seen that there is generally good agreement between the two models except in the vicinity of the insertion loss peaks, which are systemically under-estimated by the diffraction model, particularly at low frequencies. The latter behavior is characteristic of diffraction-based models.

It was noted earlier that one disadvantage of diffraction-based models is their inability to handle receiver points near the line-of-sight: i.e., close to the shadow boundary. Figure 7.6 shows the locations of several receiver points for the case of a 3 meter tall barrier when the sound source is placed 5 meter in front of the barrier at the height of 0.5 meter. The model geometry was otherwise the same in this case as in the case illustrated in Figure 7.3, except that the receiver was moved progressively closer to the shadow boundary as illustrated. The results shown in Figures 7.7 to 7.9 demonstrate that the accuracy of the diffraction-based predictions does indeed deteriorate as the receiver point approaches the shadow boundary. The diffraction model error is greater at lower frequencies as expected.

7.3 Straight Barrier of Finite Length

The difference between the performance of a finite size barrier and an infinite length barrier comes from diffraction around the sides of the finite size barrier. That is, the finite size barrier has four additional paths from the sound source to the receiver due to the diffraction around its ends. If the width of the finite size barrier is much greater than the barrier height, the amplitude of the diffraction from the two sides of the barrier is small compared to the diffraction from the top of the barrier. A comparison of two- and three-dimensional diffraction models was performed before the three-dimensional boundary element model was validated by comparison with experimental results. The height of the barrier was 3 meters and the receiver was placed 20 meters behind the barrier at a height of 1.5 meters midway along the barrier's length: Figure 7.10 shows the configuration for this comparison. The insertion loss for a 20 meter long barrier is shown in Figure 7.11 where it is compared with an equivalent result for an infinitely long barrier. It can be seen in that figure that the insertion loss of a finite-length barrier is reduced compared to that of an infinitely long barrier as a result of diffraction around the barrier edges. The insertion loss of the finite length barrier is also very frequency-dependent owing to the diffraction around the ends of the barrier.

7.3.1 Boundary Element Model

MSC PATRAN was then used to generate a model of a three dimensional geometry that could be directly compared with experimental results. Linear rectangular elements in MSC PATRAN were used to generate the 9065 elements for the straight barrier which had dimensions of 37 cm $\times$ 244 cm. The thickness of the plate was not considered in the numerical model. The point sound source was assumed to be located 100 cm in front of the barrier on the ground and midway along the barrier's length. The 17 receivers were located 116 cm behind the barrier and spanned the space from the ground plane to the boundary of the shadow zone which was 80 cm above the ground plane at this distance behind the barrier. The analysis was preformed from 200 to 6000 Hz in steps of 200 Hz. In this instance, the calculation took

137637 seconds on an IBM-RS 6000.

7.3.2 Experimental Methods

Note that when the source is situated on the ground the insertion loss of a barrier situated on a perfectly reflecting plane is equal to the insertion loss of a screen in free space that is twice the height of the original barrier. This equivalence is illustrated in Figure 7.12 using the mirror image method. The use of this configuration eliminates the necessity of creating a perfectly reflecting plane and thus the errors associated with finite impedance values of the material used for the reflecting plane. Experiments were performed for the case of a straight barrier of finite length in order to verify the numerical model. The dimensions of the steel plate used in the experiment were 74 $cm \times 244\ cm \times 3\ mm$. The scale factor to a realistic highway barrier is about 10 and thus the frequency is also scaled by approximately a factor of 10. To reinforce the plate, two L-shape channels were bolted to the rear of the plate, as shown in Figure 7.13. Four holes at each corner of the plate were made to allow the plate to be hung using steel wires. The experiments were performed in the anechoic chamber. A small driver installed at one end of a 10 mm PVC pipe was again used as the sound source. To measure the sound field, 17 microphones were used to measure the sound pressure level simultaneously at various locations within the geometrical shadow zone. The geometry for this case is shown in Figure 7.14. The microphones were inserted into 6 mm diameter holes in a 1.27 cm diameter wooden rod. The circular cross section of the wooden rod was chosen to minimize diffraction off the microphone holder. Modal Shop T130C21 microphones were used with PCB model 442B119 ICP sensor signal conditioners with 0 dB gain. A G.R.A.S. Sound & Vibration Pistonphone type 42AA with octopus coupler type RA0025 designed to work with the microphone array was used for calibration. The LMS CADA-X system was used to acquire multichannel data in combination with an Agilent E8403A VXI mainframe.

7.3.3 Post-processing of Experimental Data

Typically, diffraction experiments have been performed using impulsive input signal to facilitate the identification of the desired response. Since the distance between

the sound source and receiver is known, simple algebraic calculations yield the time necessary for sound waves to travel from the source to the receiver. Spurious events which occur at different time delays can be easily identified and eliminated by a time domain editing method. However, the impulse input method could not be implemented in this case because of the speaker's limited frequency response and dynamic range: i.e., the experimental signal-to-noise ratio was not acceptable over a wide frequency range when an impulsive signal was used. As a result, a continuous random input signal was chosen. The use of random signals yielded better signal-to-noise ratios compared to impulsive signals as explained in section 5.3.2. The disadvantage of using a continuous input random signal is the difficulty of identifying spurious reflective effects. This problem can be avoided by adopting post-processing techniques involving the use of the inverse Fourier transform. The time domain impulse response function can be calculated from the measured frequency domain transfer function with a knowledge of the sampling frequency, the frequency resolution and the total bandwidth. A time window can then be employed to eliminate spurious reflection and diffraction features from the impulse response function. Unlike the circular disk experiments described in chapter 5.3.2, different time windows were used for the measurements performed with and without the scaled barrier in place between the sound source and receiver. This was necessary because of the differences in the dimensions of the two obstacles in the two experiments. For the circular disk case, the distance between the sound source and receiver was much larger than the dimension of the circular disk. Note that the distance between the speaker and the microphone was 2.16 m while the radius of circular disk was only 7.5 cm. Thus, it was not necessary to modify the path length when the circular disk was present between the sound source and microphone. In contrast, the size of the rectangular barrier was comparable to the distance between the sound source and the receiver and it was necessary to account for the relatively large difference between the direct and diffracted path lengths in this case.

Note also that the 2.86 cm driver that was used for this experiment had a very low

sensitivity at frequencies below 500 Hz because of its small size. Thus the signal-to-noise ratio is very poor at low frequencies. The calculation of the insertion loss involves a division of transfer functions in the frequency domain. This division becomes very unstable at frequencies at which the signal is contaminated with noise.

Figure 7.15 illustrates the post-processing procedure used here. In the diagram, TF1 is the measured transfer function without barrier, IRF1 is the impulse response function associated with TF1, wIRF1 is the windowed time domain impulse response function and wTF1 is the transfer function in the frequency domain calculated from wIRF1. TF2 is the measured transfer function with the barrier in place, TF3 is the transfer function resulting from the division of TF2/wTF1, and IRF3 is the impulse transfer function associated with TF3. fIRF3 is the impulse response function after a high pass filter operation. Windowing fIRF3 in the time domain gives wfIRF3. wfTF3 is the transfer function after the filtering in the frequency domain and the windowing operation in the time domain which eliminates errors related to the experiment. Finally, nTF2 is the transfer function with the barrier between the sound source and microphones and it can be used to calculate the insertion loss which is designated as IL in the diagram. Therefore, TF1 should represent the system characteristic of the loudspeaker including the time delay resulting from the spatial separation between the sound source and the receivers. TF2 involves the loudspeaker characteristic and includes the effects of the time delay and diffraction phenomena at the edges of the scaled barrier. The operation TF2/TF1 is performed to eliminate the loudspeaker frequency response and the time delay from TF2. These procedures allow the isolation of the signal components related to the diffraction effects of interest.

Figure 7.16 shows a measured transfer function without the scaled barrier model in place. The inverse Fourier transform was used to obtain the impulse response function in the time domain which helps to identify the reflection from the walls, ceiling and floor. Algebraic calculations show that sound should take 6 ms to reach the microphone when there is no obstacle between the sound source and the microphone. However, the results in Figure 7.17 show that there are many small features after the

6 ms which are believed to result from spurious reflections from various components of the experimental apparatus. Care must be taken when the time domain window is applied. Any abrupt discontinuity in the windowing function results in lightly damped oscillations in the frequency domain data. The time domain window shown in Figure 7.18 was designed to remove the trailing component from the impulse response function in a smooth way. The impulse response function after the windowing operation is shown in Figure 7.19. A Fourier transform was then employed to obtain the transfer function associated only with the response of the loudspeaker and wave propagation between the sound source and the receiver. This transfer function is shown in Figure 7.20. Sound takes approximately 6 ms to reach the microphone after hitting the top and bottom of the plate when the barrier is present for a receiver location in the middle of the barrier height 1 m behind the barrier. The 2.44 meter width of the scaled barrier gives a time delay of 10 ms. However, the impulse response function measured with the scaled barrier model in place shows a much longer response. These additional features are reflections of other objects in the anechoic chambers. To remove the effects of those features correctly, one further intermediate step is necessary. Transfer function TF2 shown in Figure 7.21 represents three physical effects: the loudspeaker response, the wave propagation between the loudspeaker and the receiver locations, and any diffraction phenomenon at the edges of the scaled barrier. The division of the transfer function with the barrier by the transfer function measured without the barrier was done to eliminate the effect of the loudspeaker frequency response and the time delay related to wave propagation. The result is shown in Figure 7.22.

The problem now is the low amplitude and poor signal-to-noise ratio at low frequencies which makes this division very unstable. It can be seen in Figure 7.23 that an apparent oscillation at low frequency exists in the impulse response function. A highpass filter was designed to cut off signal components below 400 Hz in MATLAB to deal with this problem. A Chebyshev type I filter of order 1 with a specification of 0.5 dB ripple in the passband and 1.0 dB attenuation in the stop band was used.

the resultant impulse response function is shown in Figure 7.24. In addition, a time window was utilized to remove any signals after 4 ms. Note that the time delay associated with the wave propagation from the sound source to the receivers has been removed by the division operation of TF2/wTF1. So the impulse response function fIRF3 should start at 0.4 ms second which accounts for the difference in time taken for sound to travel via the top of the barrier and the direct path without barrier. The path length when the barrier is present is 107 cm from the sound source to the top of the barrier and 122 cm from the top of the barrier to the receiver location for the microphone 116 cm behind in the middle of the plate. This gives an indirect path length of 229 cm which is 13 cm longer than the direct path which connects the locations of the sound source and the receiver. The resulting impulse response function is shown in Figure 7.25. The final processed version of the transfer function TF3 is shown in Figure 7.26. The transfer function for the case with barrier present between the sound source and receiver after appropriate post-processing is shown in Figure 7.27.

A comparison between the insertion loss calculated with and without the use of the post-processing techniques at selected receiver points are shown in Figures 7.28 to 7.31. Many spurious peaks in the insertion loss are removed by the time domain windowing and high pass filtering, at least above 500 Hz. The apparently increased insertion loss in this low frequency region is due to the very low sensitivity of the loudspeaker.

Figure 7.28 shows that the insertion loss increases with frequency, following a trend similar to the performance of the semi-infinite barrier shown in Figure 7.2. Note that the microphone located at the midpoint of the barrier gives the same result that would be measured if the receiver were located on the ground behind a finite height barrier placed on the ground. When the receiver is on the ground there is no complicated interference from the ground reflection on the receiver side. It should also be noted that the sound source is located at the midpoint of the barrier height. Thus, there is no ground reflection on the source side, either. The small dips and

peaks in the insertion loss for the receiver in this location can be explained by the effect of diffraction from the sides of the barrier.

The insertion loss data 10.16 *cm* above the ground and 116 *cm* behind the 37 *cm* barrier is shown in Figure 7.29. The insertion loss reaches its maximum values at 1600 Hz and 4700 Hz. For receiver locations deep in the shadow zone, insertion loss values greater than 20 dB can be achieved. Figure 7.30 shows that the insertion loss is decreased when the receiver is moved towards the shadow region. More complicated interference effects from ground reflections occurs in this case, which create the peaks and dips in the insertion loss. When the receiver point is located 30.48 *cm* from the middle of the barrier height, the insertion loss is only 5 dB at several frequencies as illustrated in Figure 7.31.

7.3.4 Comparison between Boundary Element Model Predictions and Experimental Results

In general, the numerical predictions are in relatively good agreement with the experimental results except at frequencies greater than 5000 Hz. Direct comparisons between numerical predictions and experimental data are shown in Figures 7.32 to 7.35, for five receiver locations (shown in Figure 7.14). The comparison of the insertion loss for the midpoint receiver shown in Figure 7.32 shows very good agreement between the experiment and numerical prediction. The numerical model correctly predicts the increase in insertion loss with the frequency. The numerical prediction in Figure 7.33 shows a good agreement for a receiver location deep in the shadow zone. The frequencies where the insertion loss is a maximum are predicted with good accuracy. Figure 7.35 illustrates acceptable agreement between the numerical and experimental results close to the edge of the shadow zone.

Note that the computations were performed only for a limited number of frequencies to limit the computational costs. The solid lines connecting the predicted insertion loss values are shown only as a guide. The frequency resolution of the numerical data was much smaller than that of the experimental data, making the two curves appear at fist glance different. But the computed insertion losses in most cases

are close to the measured values.

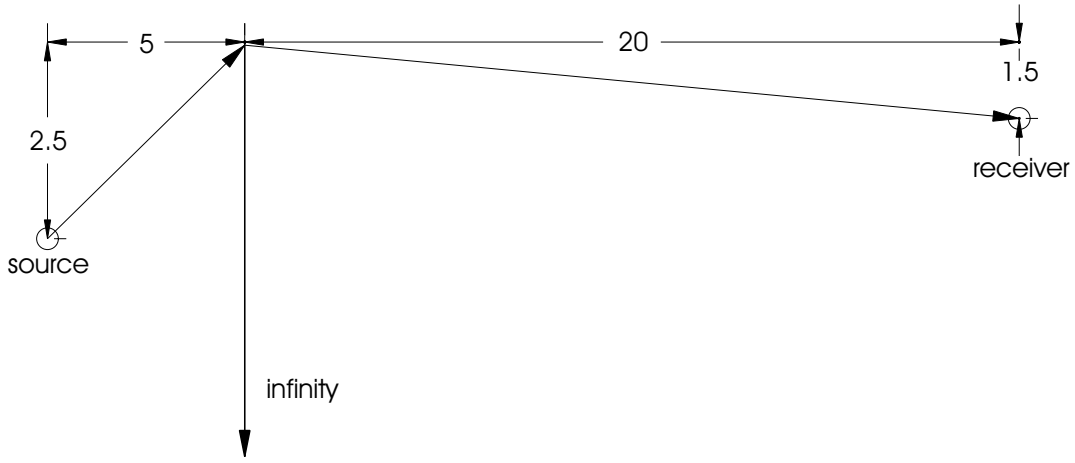

Figure 7.1. Geometry for semi-infinite barrier. All dimensions are m.

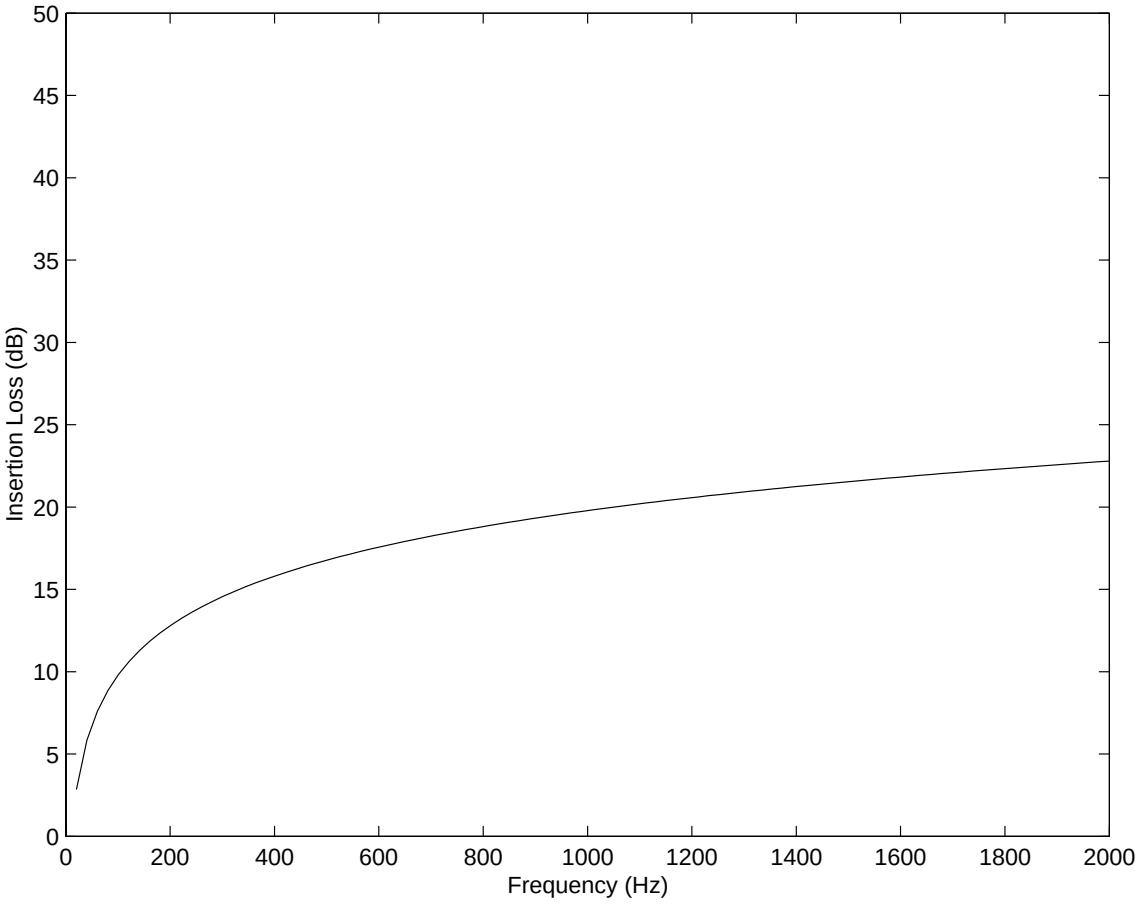

Figure 7.2. Insertion loss vs. frequency. Semi-infinite barrier. Prediction obtained using Equation 4.1 and 4.2

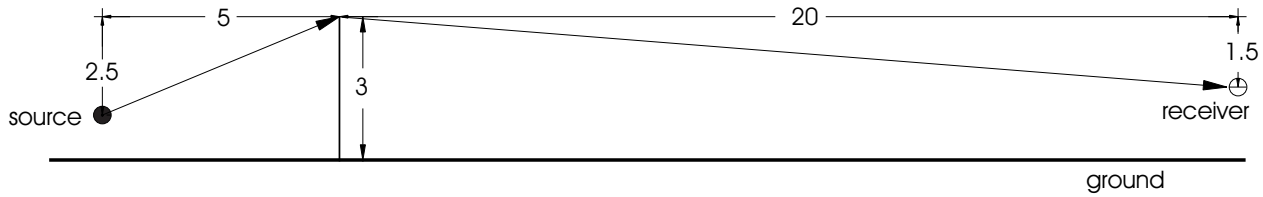

Figure 7.3. Geometry for infinite length barrier on the hard ground. All dimensions are m.

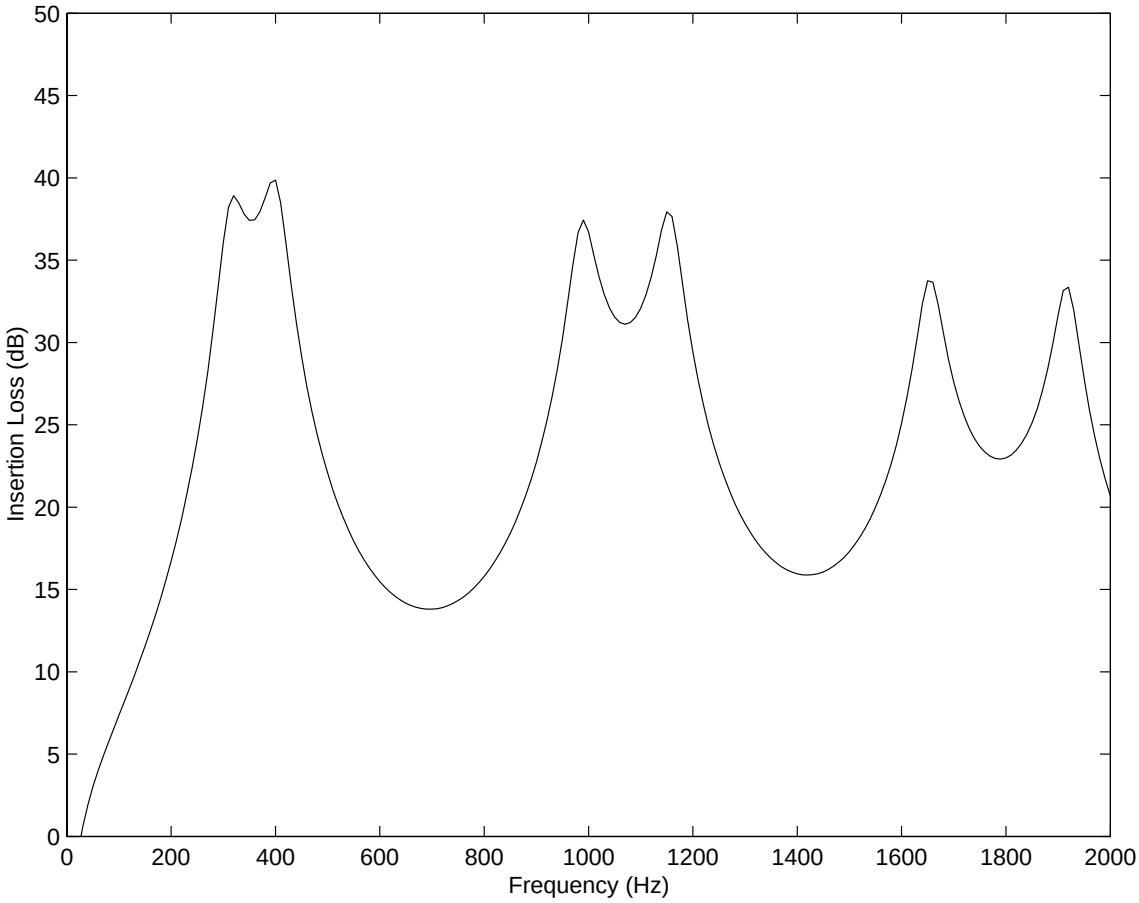

Figure 7.4. Insertion loss vs. frequency. Infinite length barrier on a hard ground. Prediction from diffraction-based model.

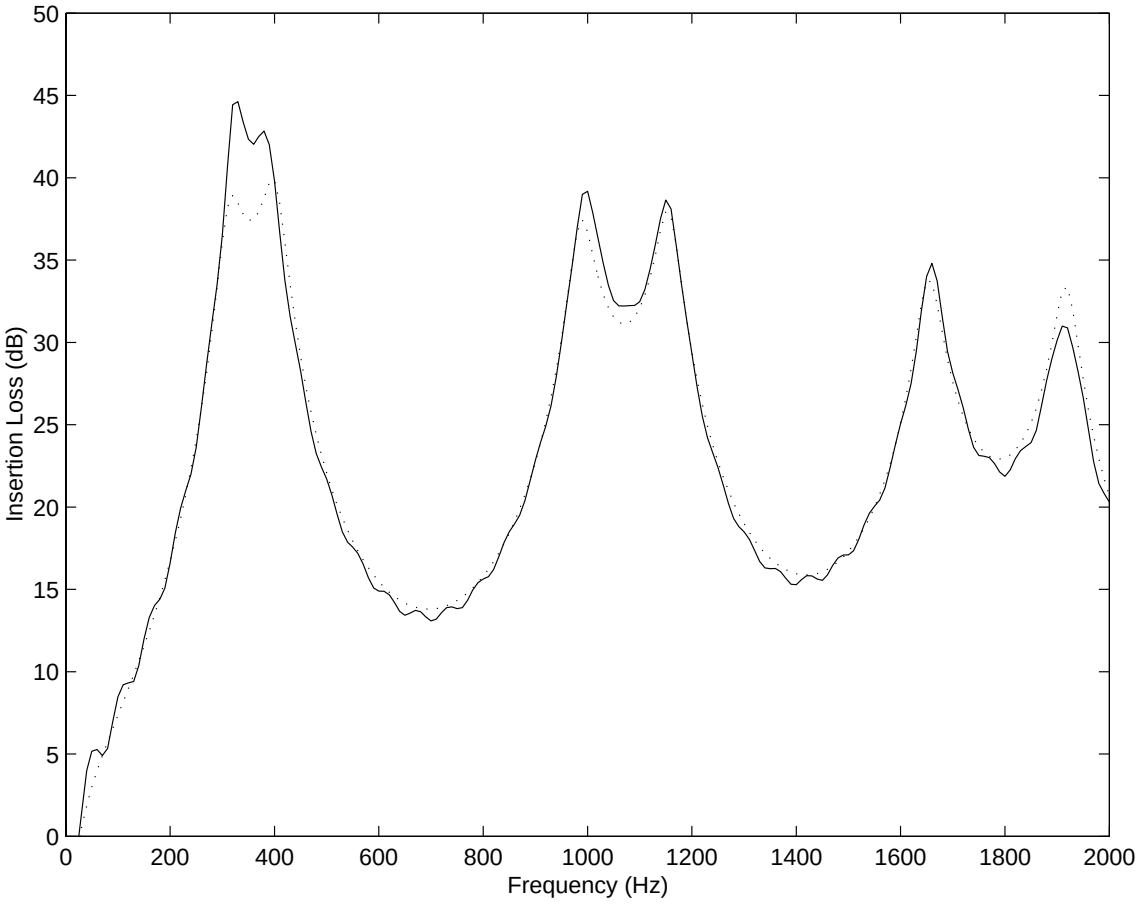

Figure 7.5. Comparison of insertion loss between the diffraction model and boundary element model. '—': Boundary element model; '· · ·': Diffraction Model.

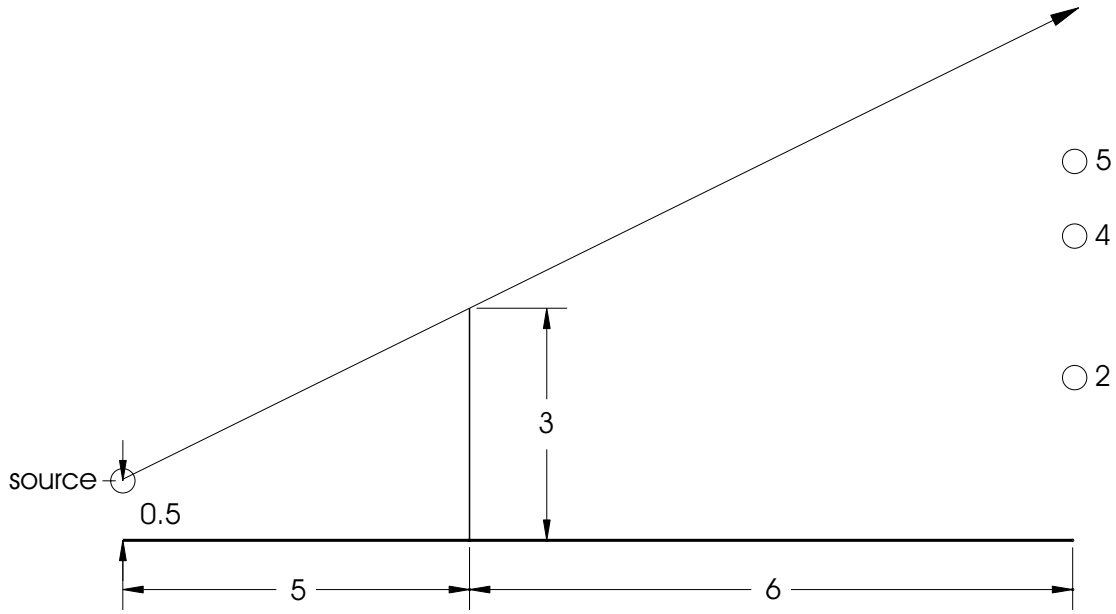

Figure 7.6. Three different receiver points in the shadow zone. All dimensions are m.

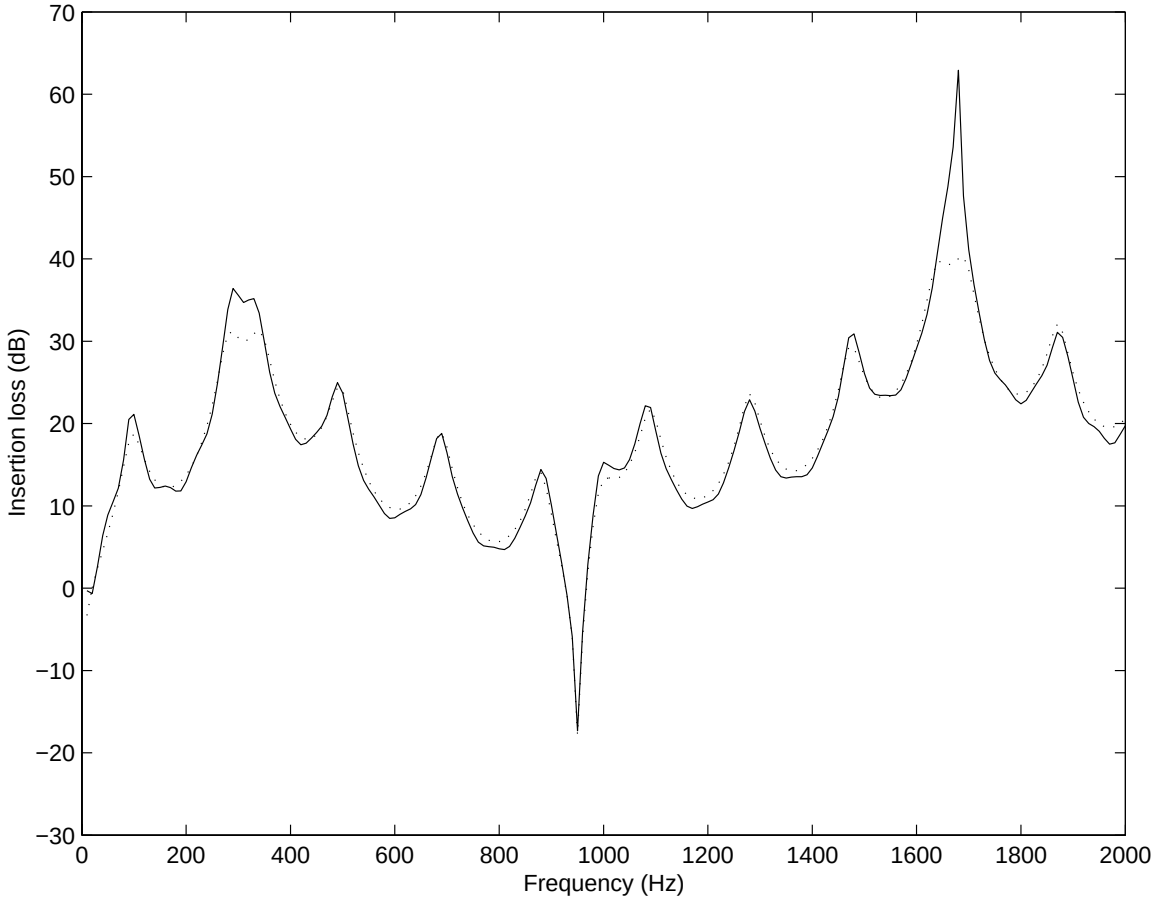

Figure 7.7. Comparison of insertion loss calculated using the diffraction and the boundary element model at receiver point (6,2). '—': Boundary element model; '···': Diffraction Model.

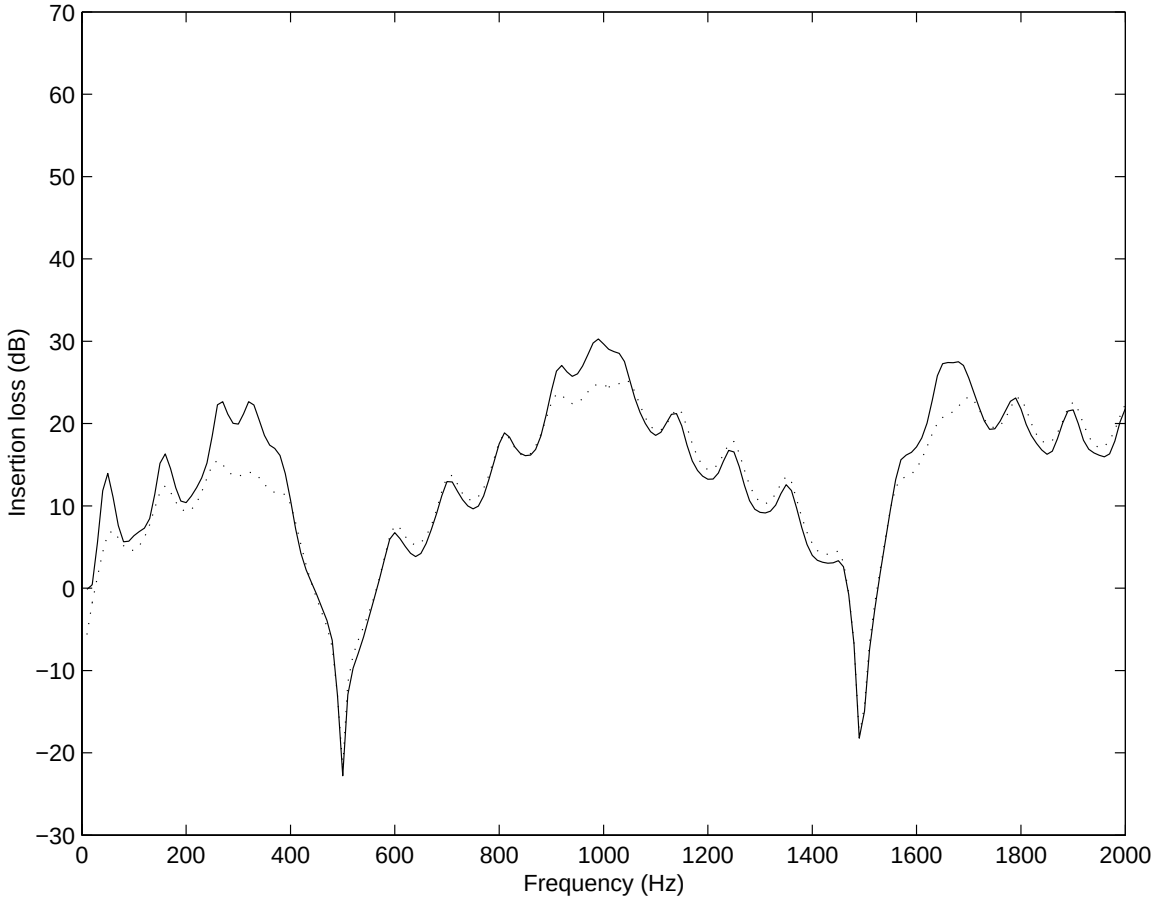

Figure 7.8. Comparison of insertion loss calculated using the diffraction and the boundary element model at receiver point (6,4)'—': Boundary element model; '···': Diffraction Model.

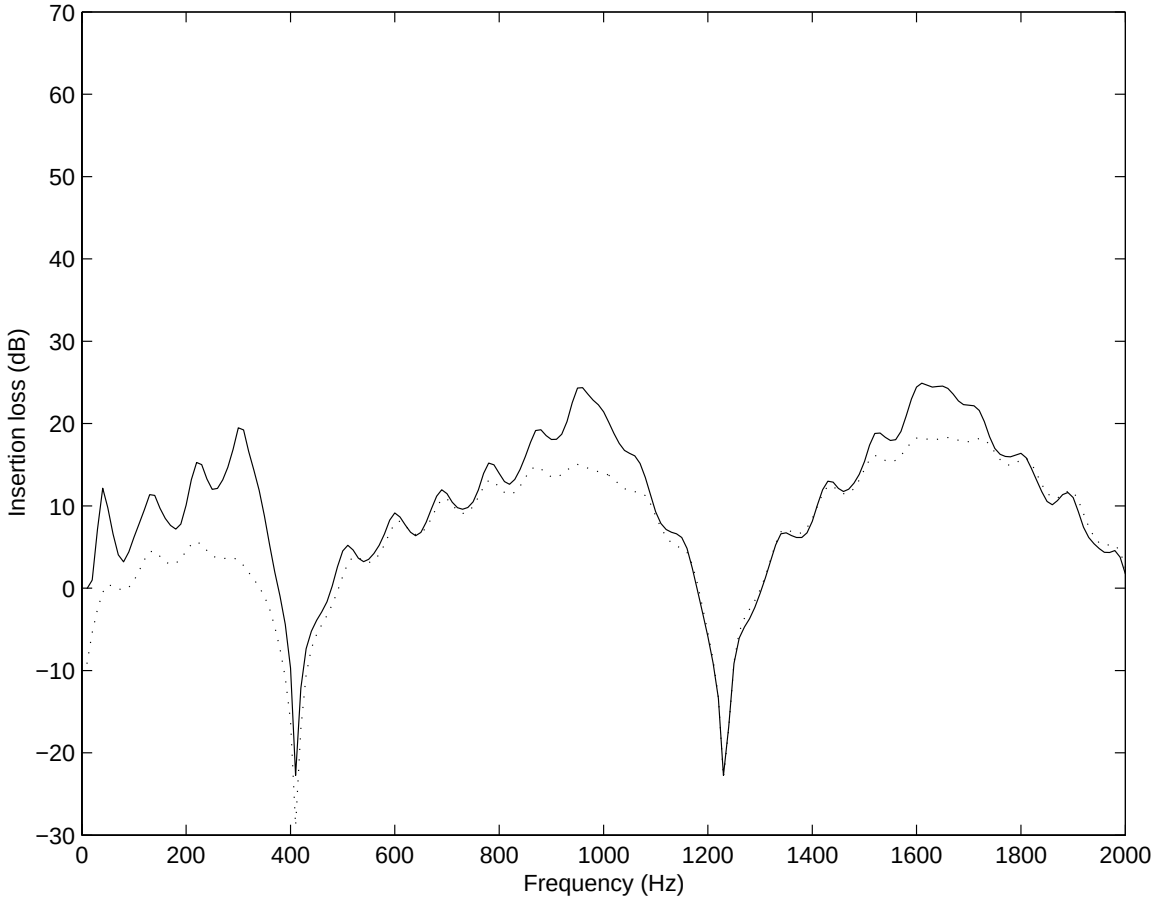

Figure 7.9. Comparison of insertion loss calculated using the diffraction and the boundary element model at receiver point (6,5). '—': Boundary element model; '...': Diffraction Model.

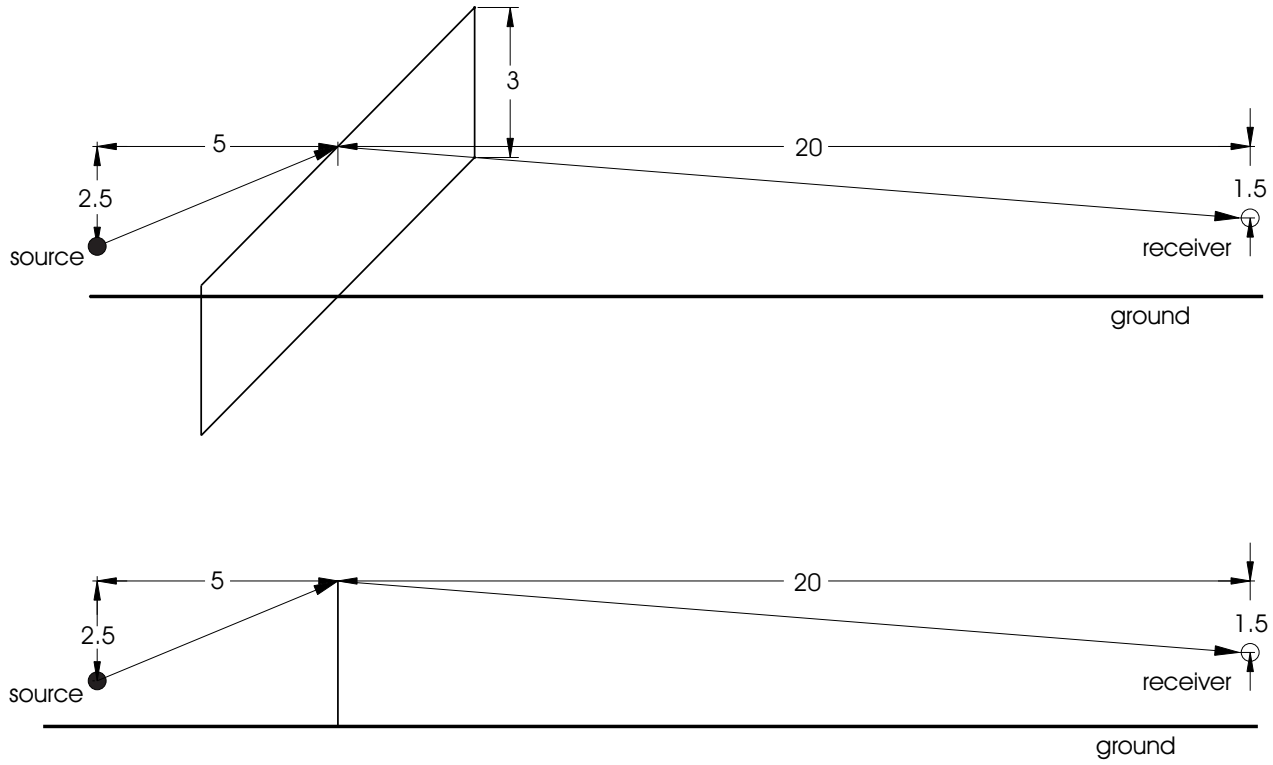

Figure 7.10. Geometry of infinite length and finite length barrier. All dimensions are m.

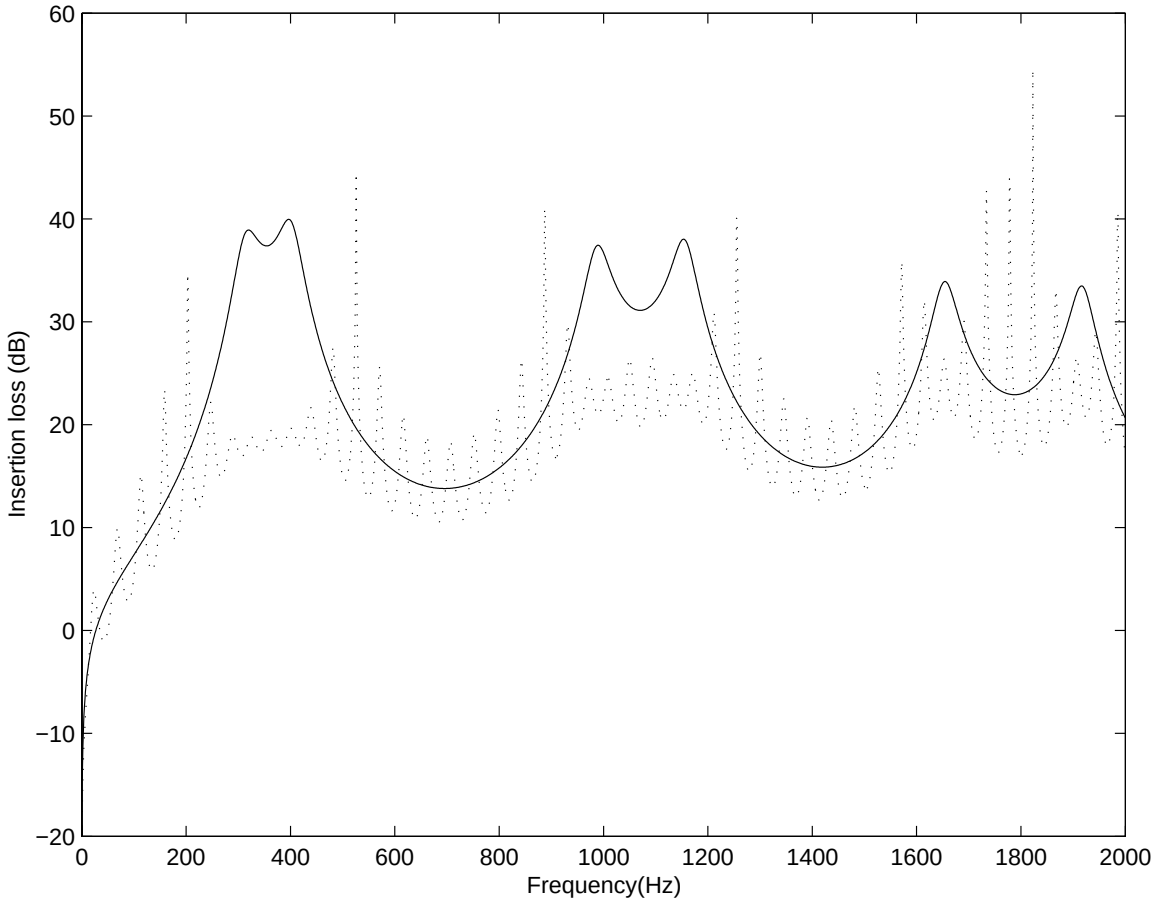

Figure 7.11. Comparison of insertion loss of an infinite length barrier and a finite length barrier. '—': infinite length barrier, '· · ·': finite length barrier.

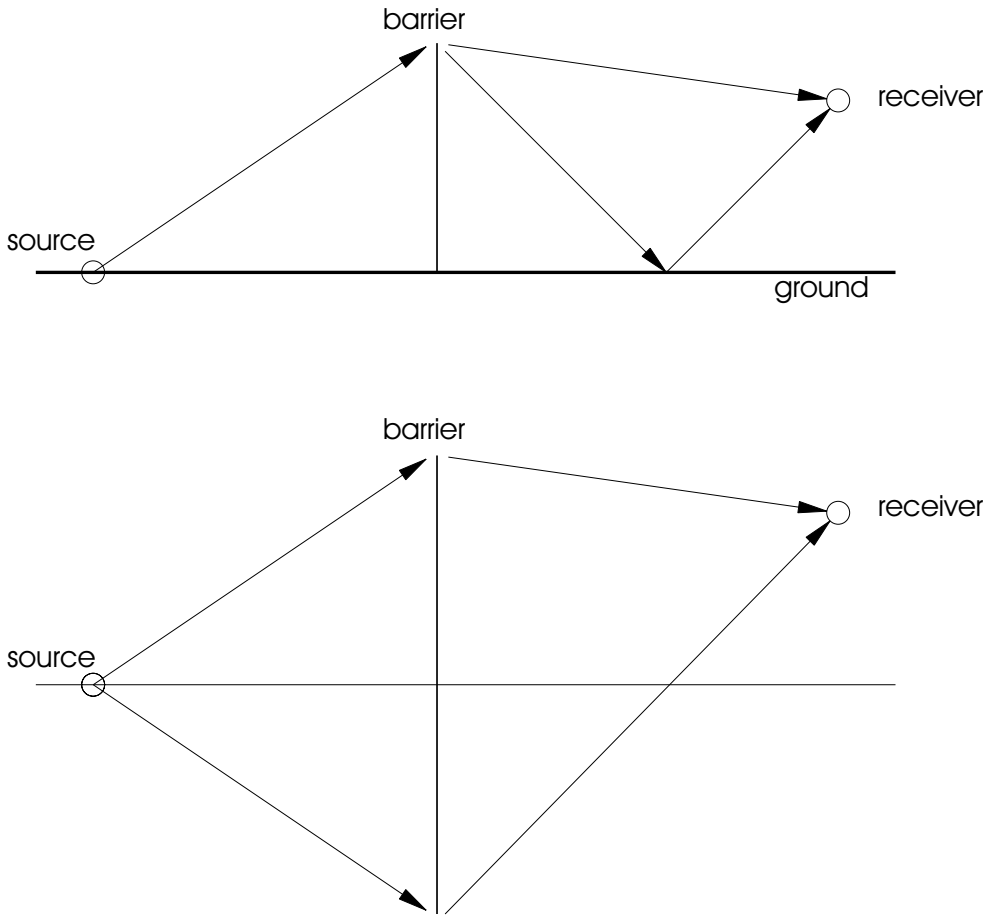

Figure 7.12. Barrier experimental setup taking advantage of symmetry conditions.

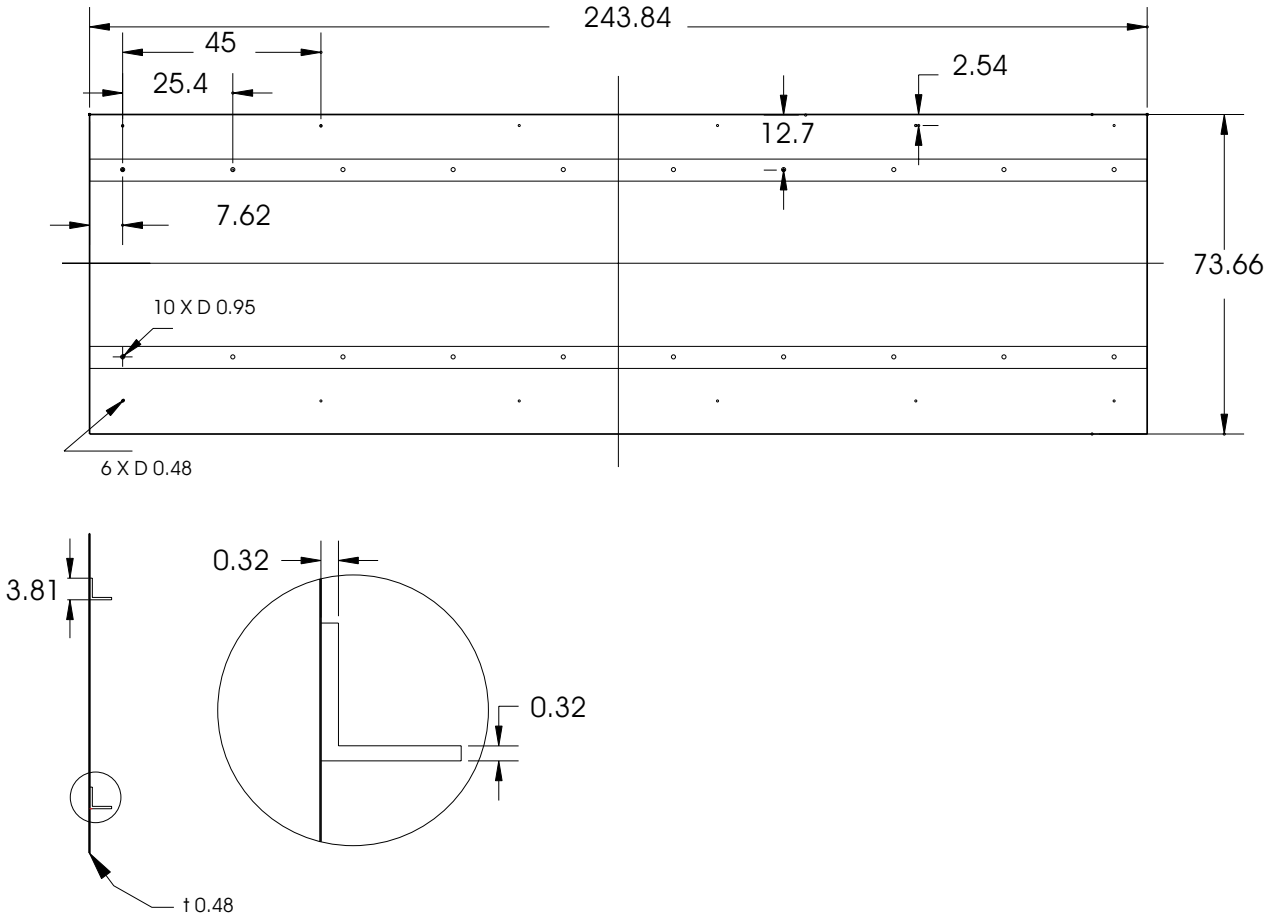

Figure 7.13. Schematic of the plate assemblage used for the experimental studies of sound diffraction by straight-edge barrier.

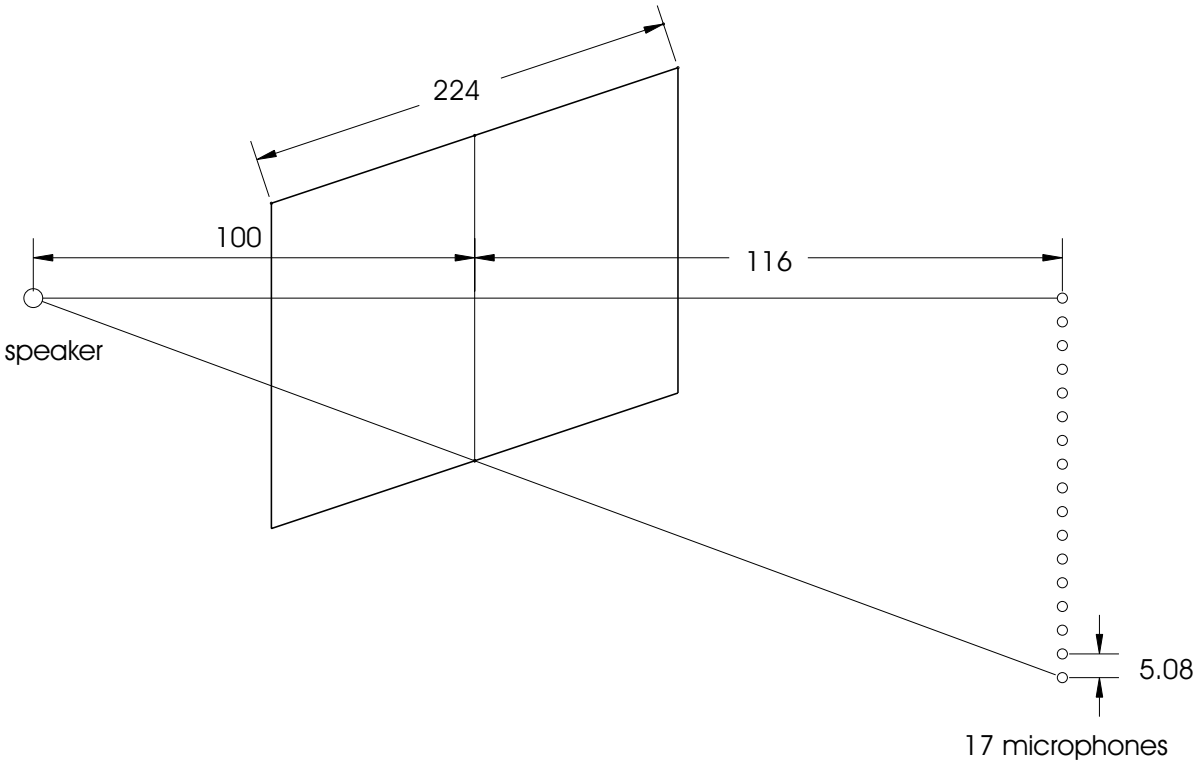

Figure 7.14. Source and receiver locations for the straight barrier experimental studies.

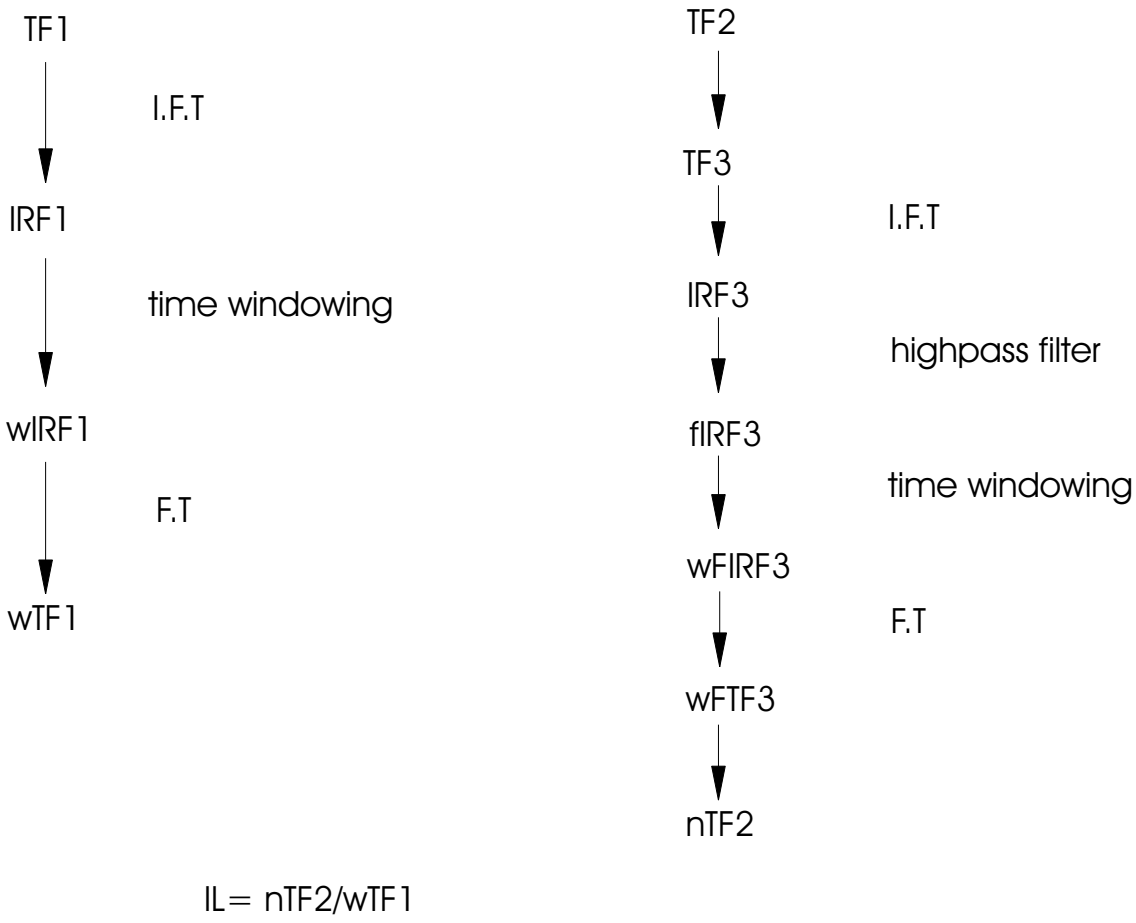

Figure 7.15. Procedure for post-processing experimental data.

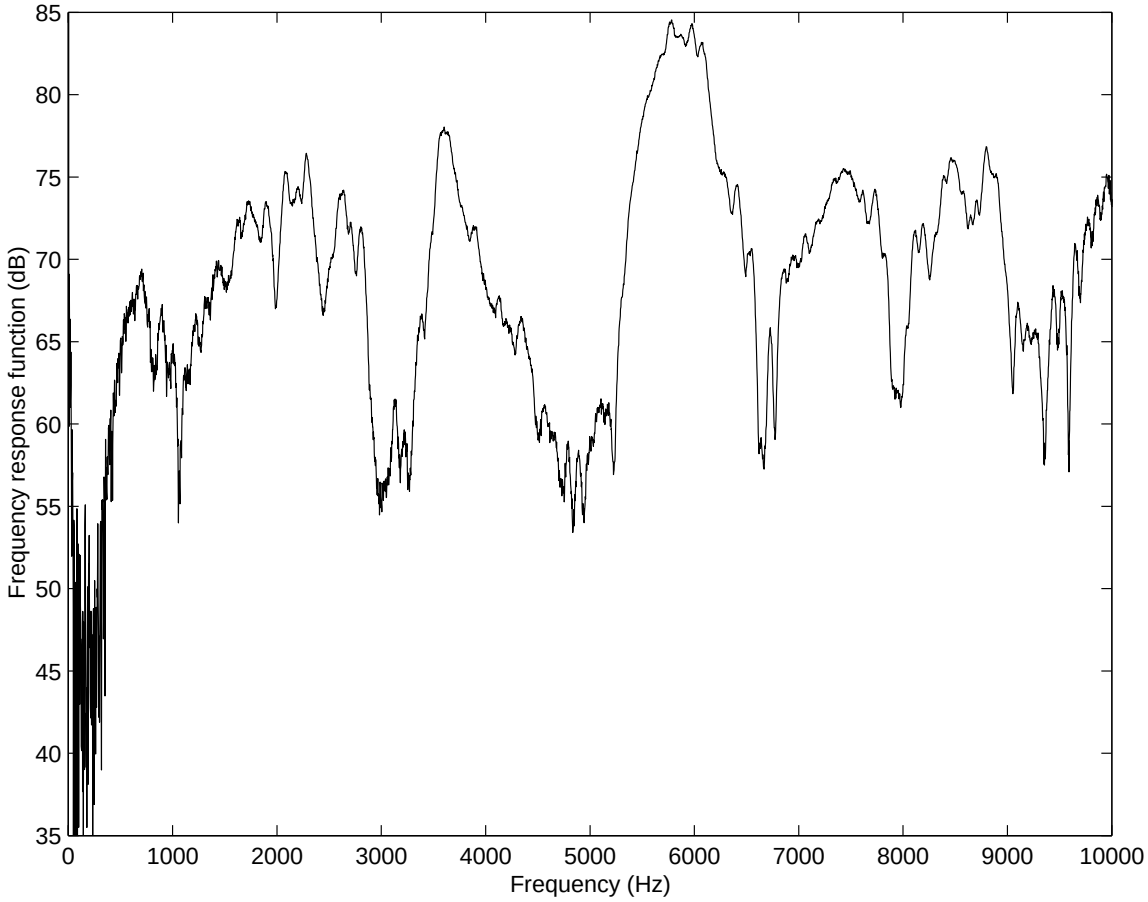

Figure 7.16. Transfer function without rectangular barrier in place. TF1.

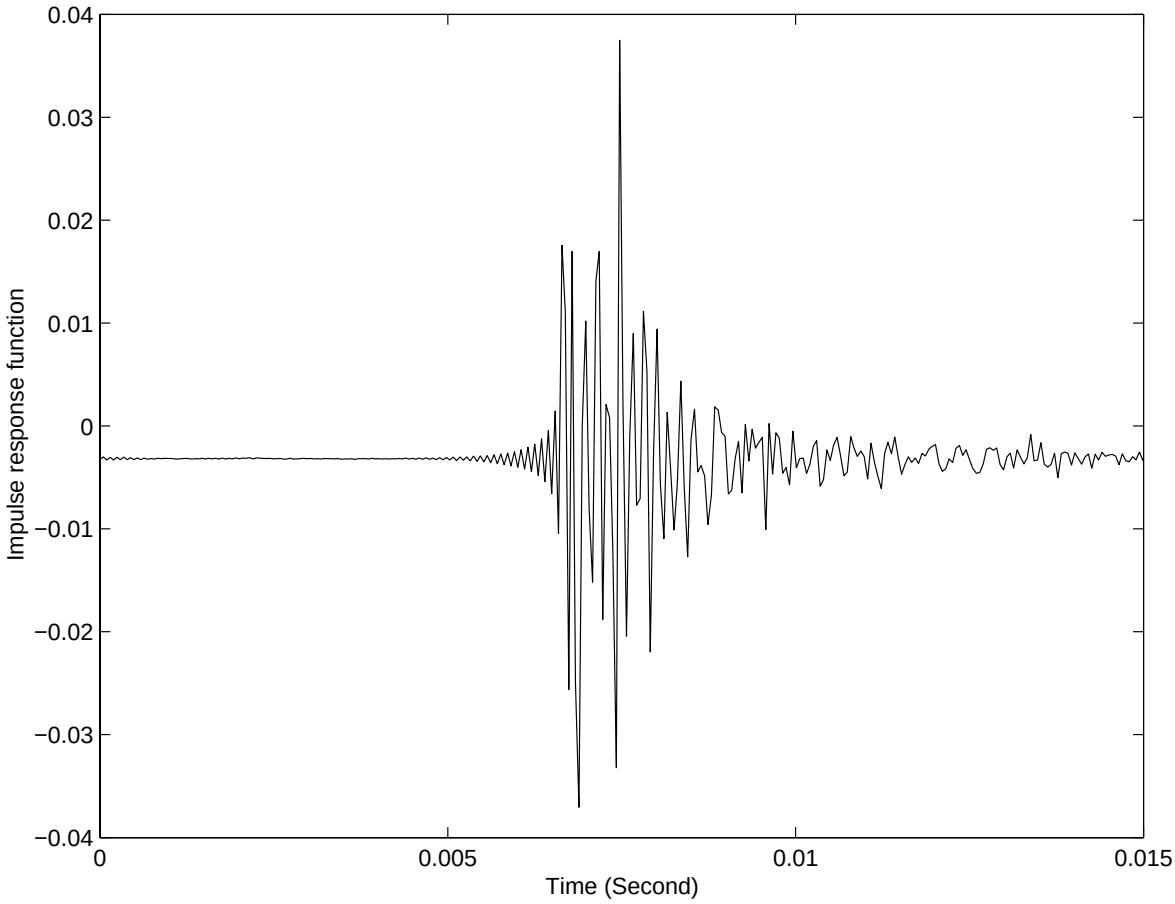

Figure 7.17. Impulse response function without barrier. IRF1.

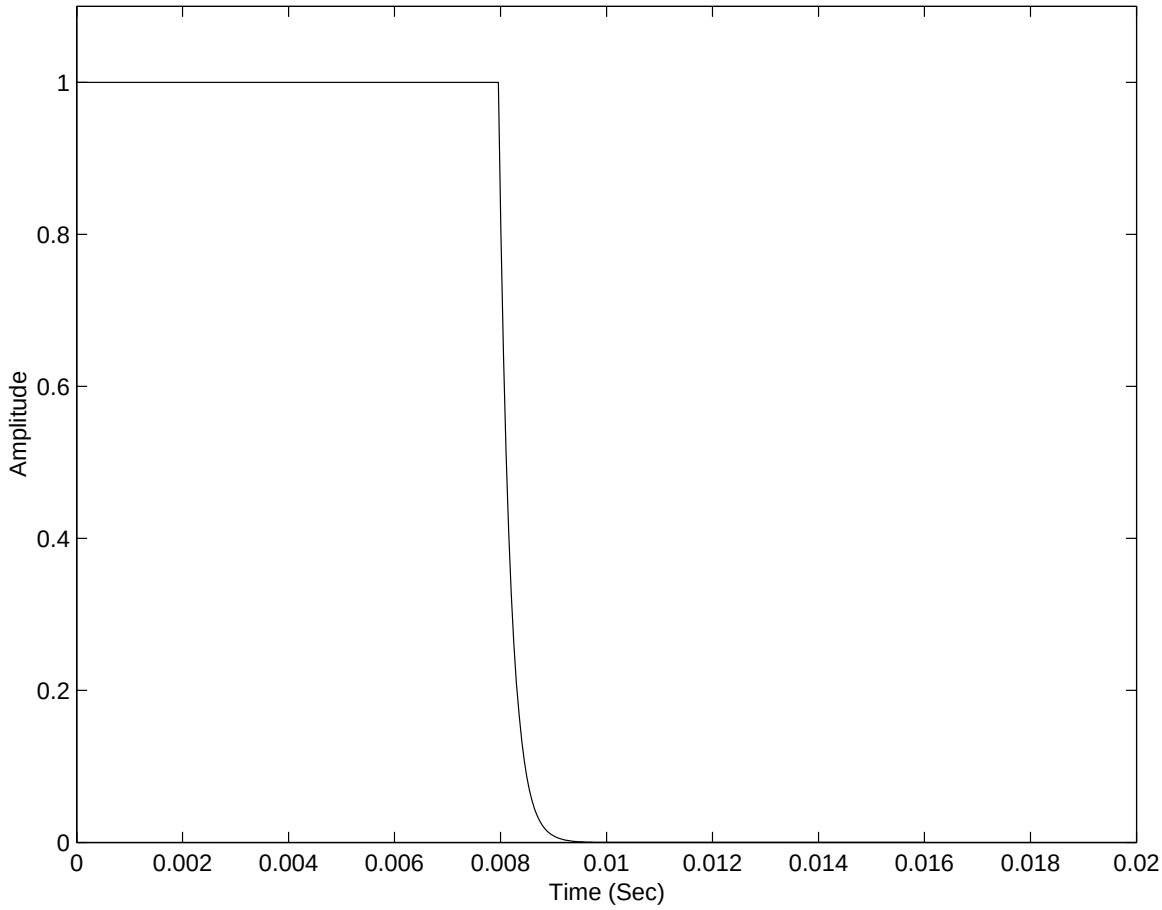

Figure 7.18. Window function applied to the impulse response function without barrier.

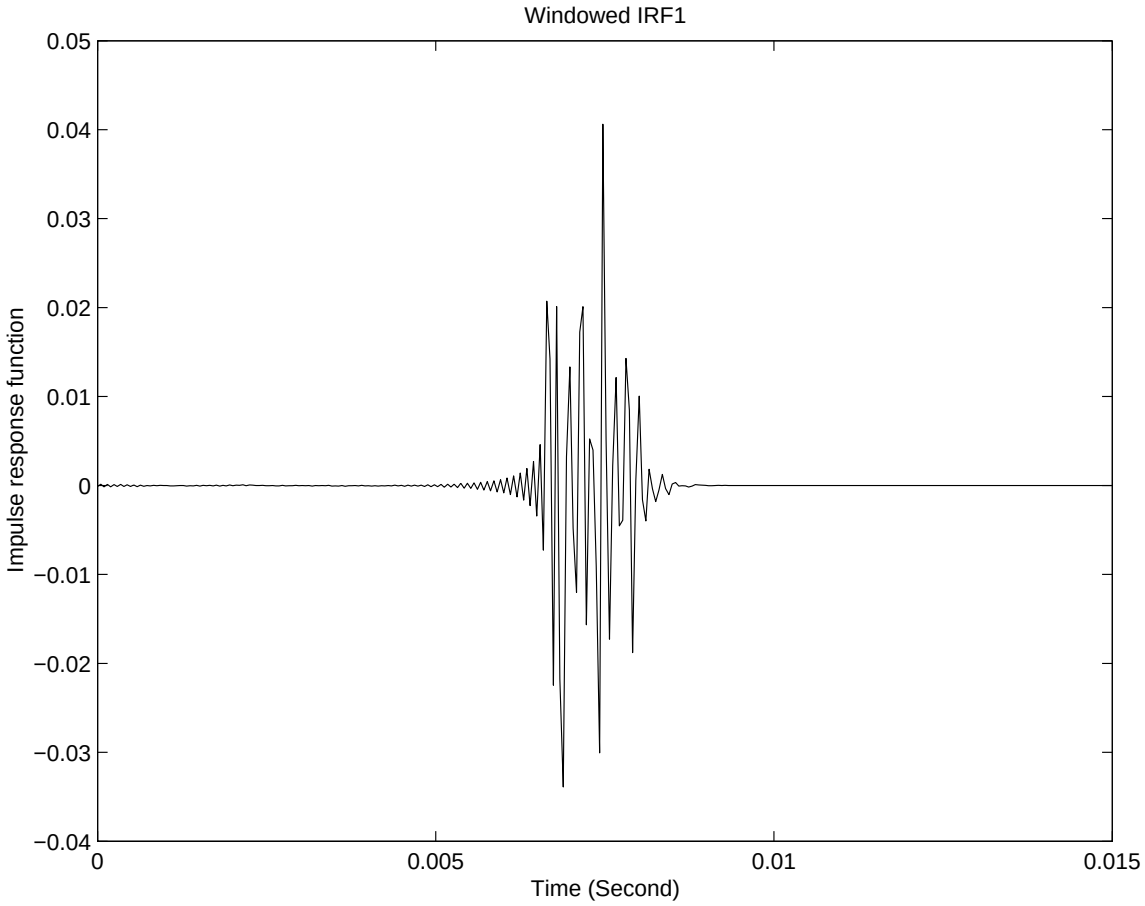

Figure 7.19. Time-windowed impulse response function without barrier. wIRF1.

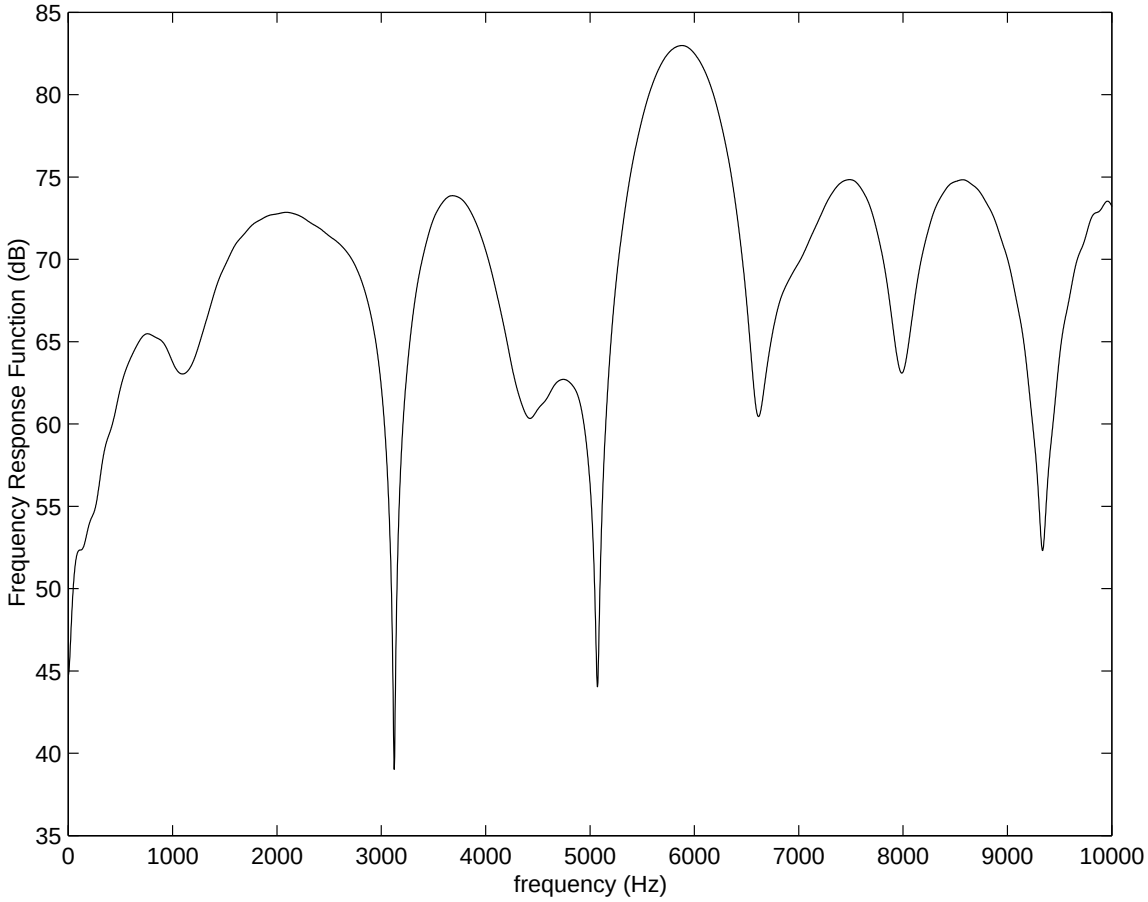

Figure 7.20. Time-windowed transfer function without the barrier. wTF1.

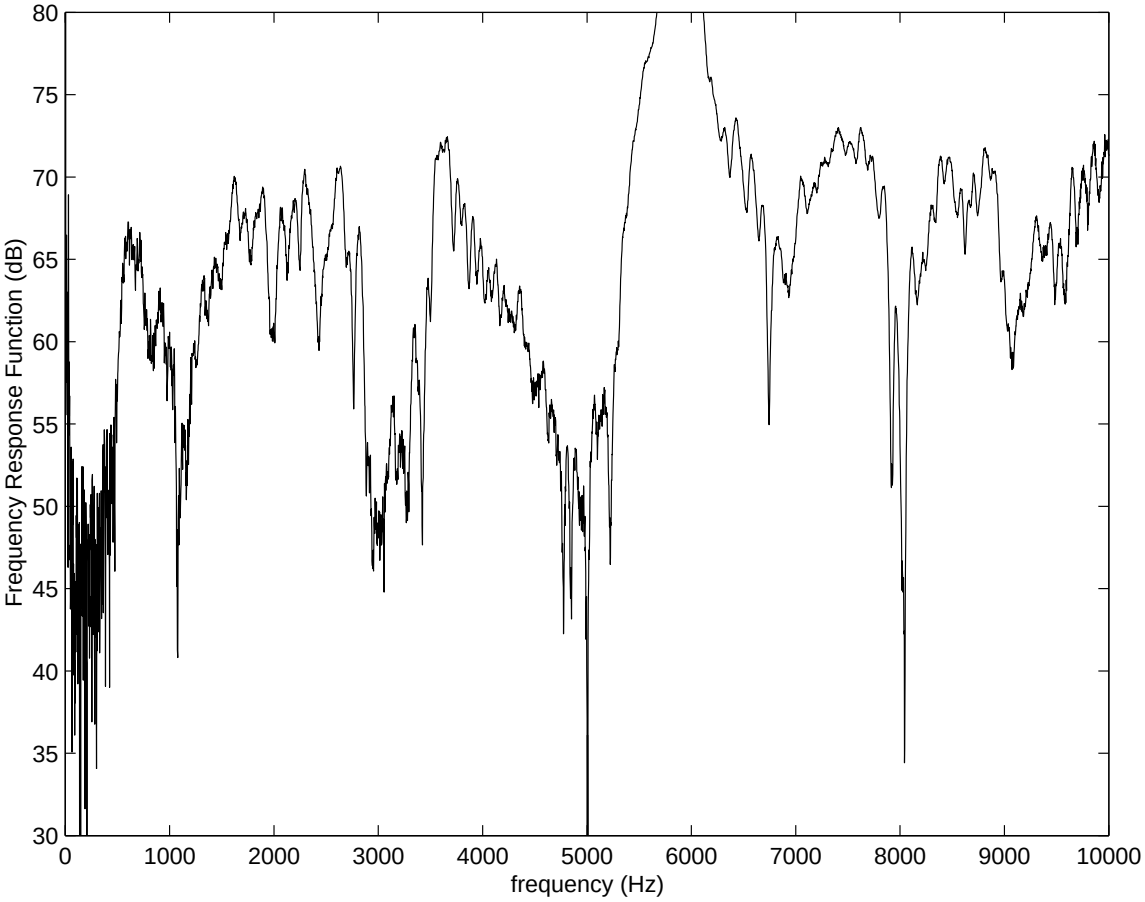

Figure 7.21. Transfer function measured with the barrier in place. TF2.

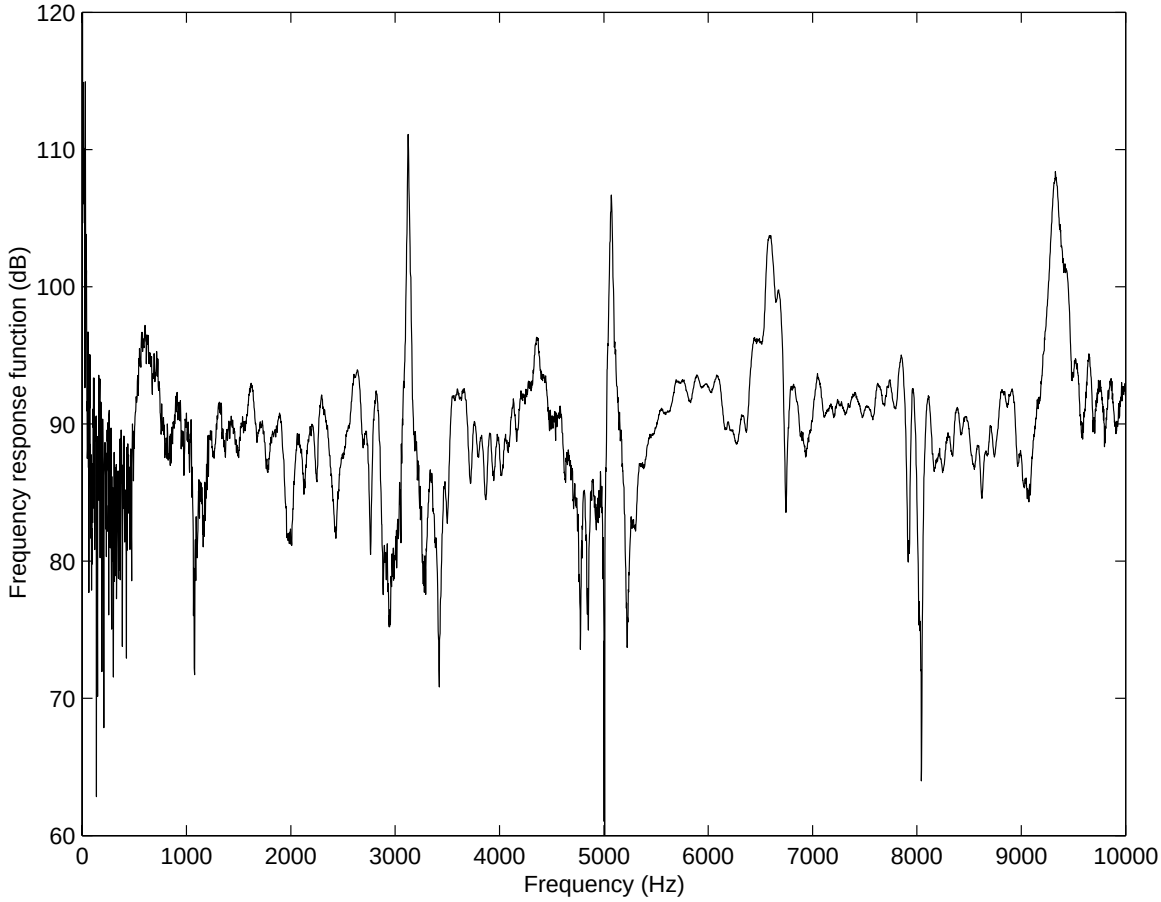

Figure 7.22. Transfer function of diffraction phenomena. TF3.

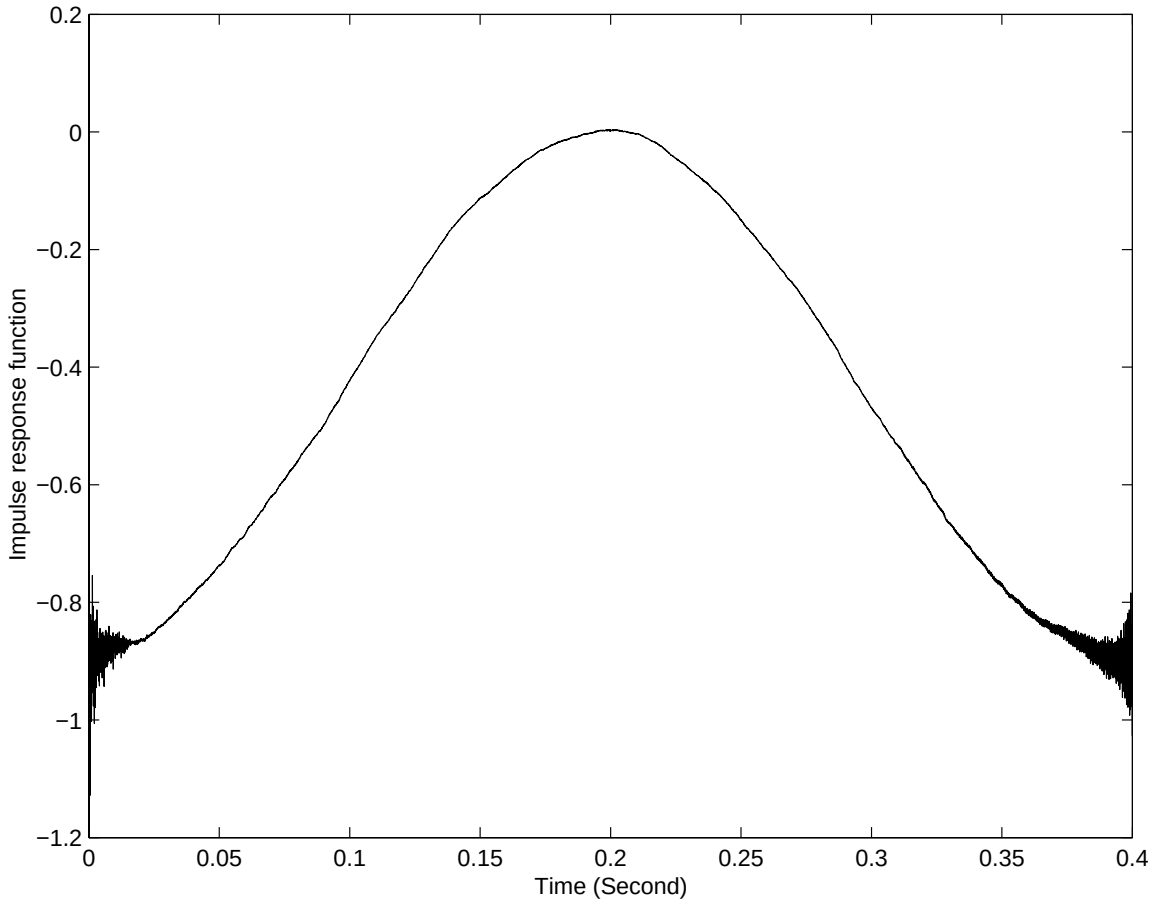

Figure 7.23. Impulse response function accounting for the diffraction. IRF3.

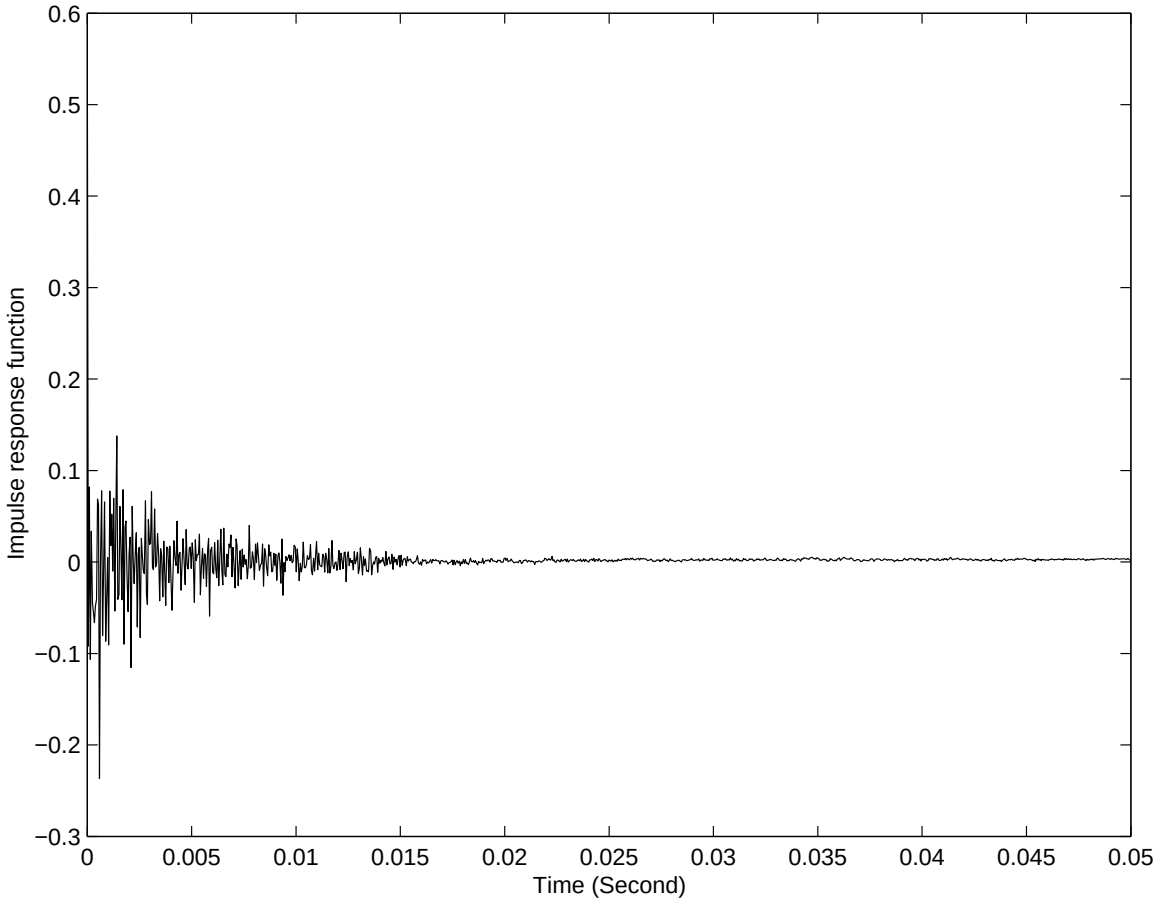

Figure 7.24. Impulse response function accounting for the diffraction after filtering. fIRF3

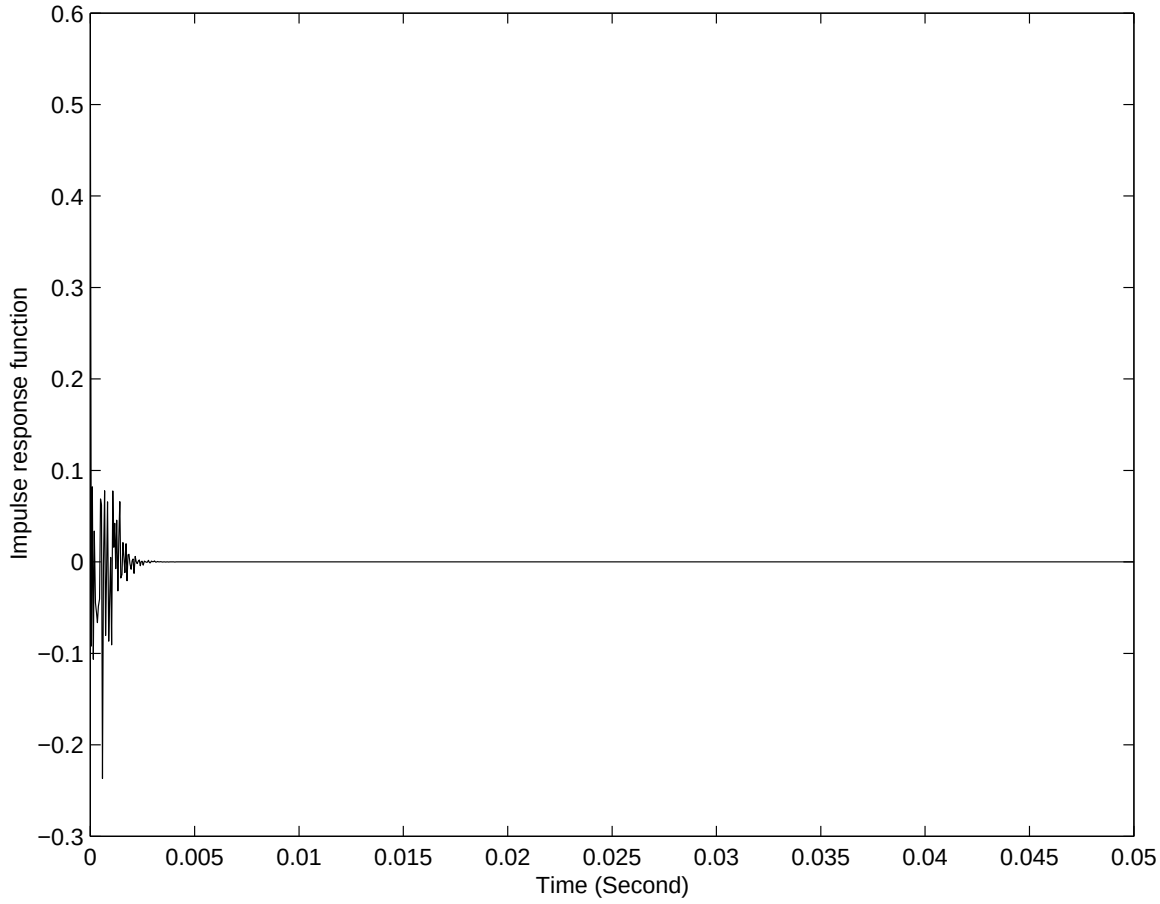

Figure 7.25. Impulse response function accounting for the diffraction after filtering and windowing. wfIRF3.

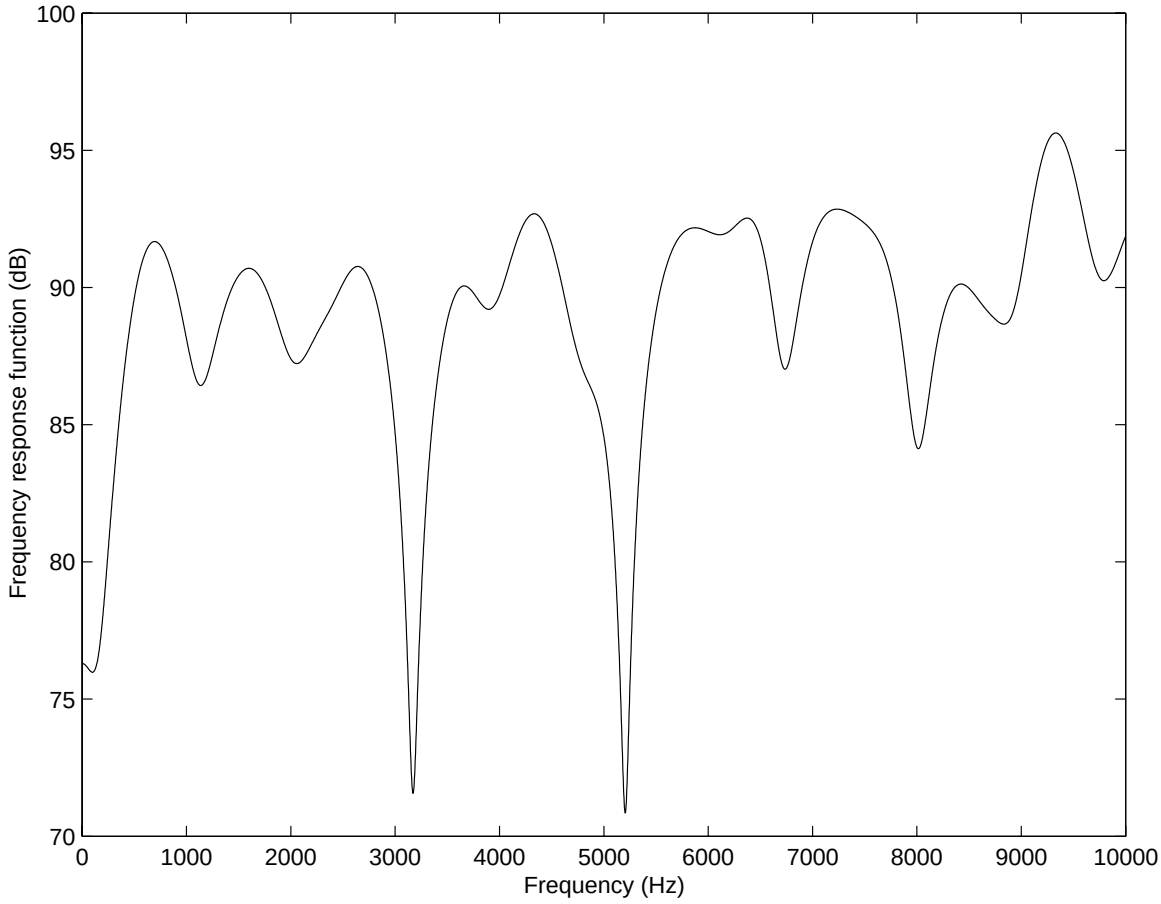

Figure 7.26. Transfer function accounting for diffraction after filtering and windowing. wfTF3.

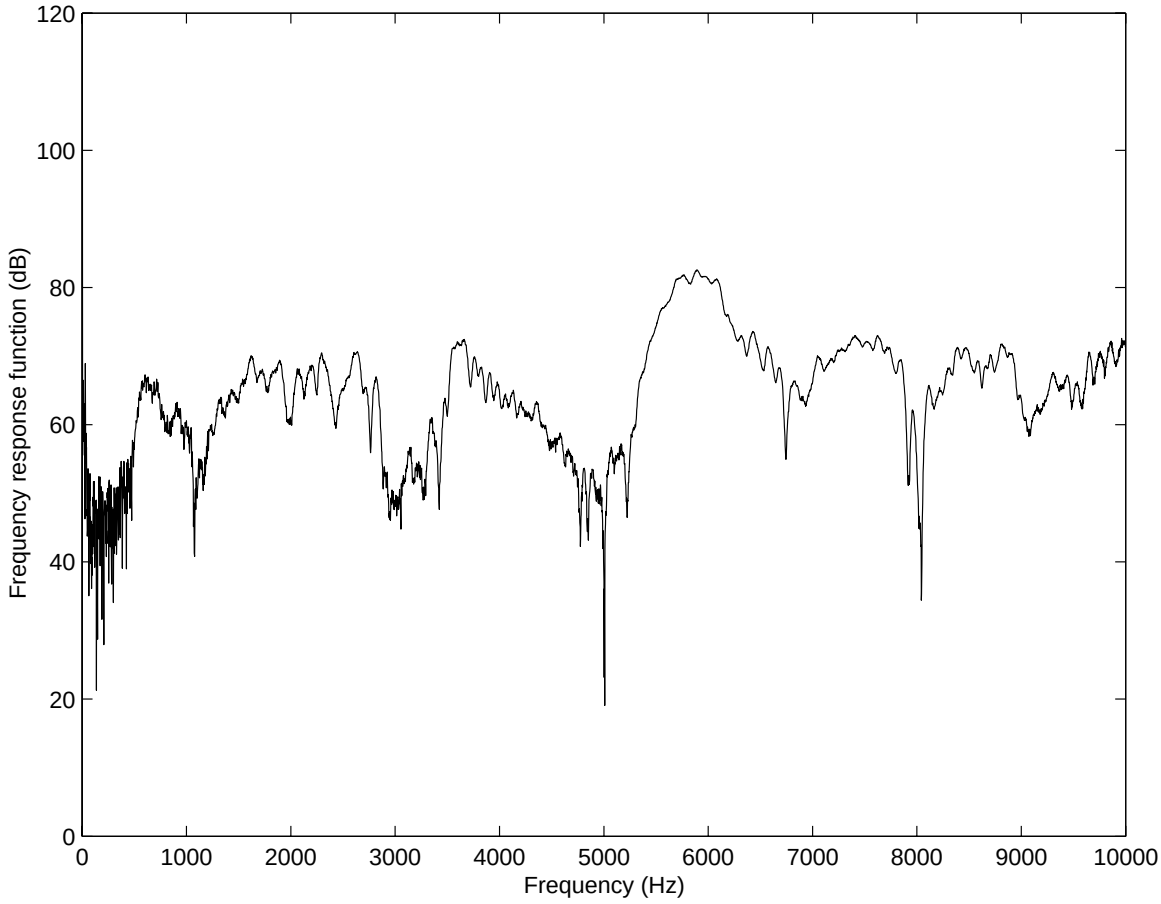

Figure 7.27. Transfer function with the barrier in the sound field after the post-processing. nTF2.

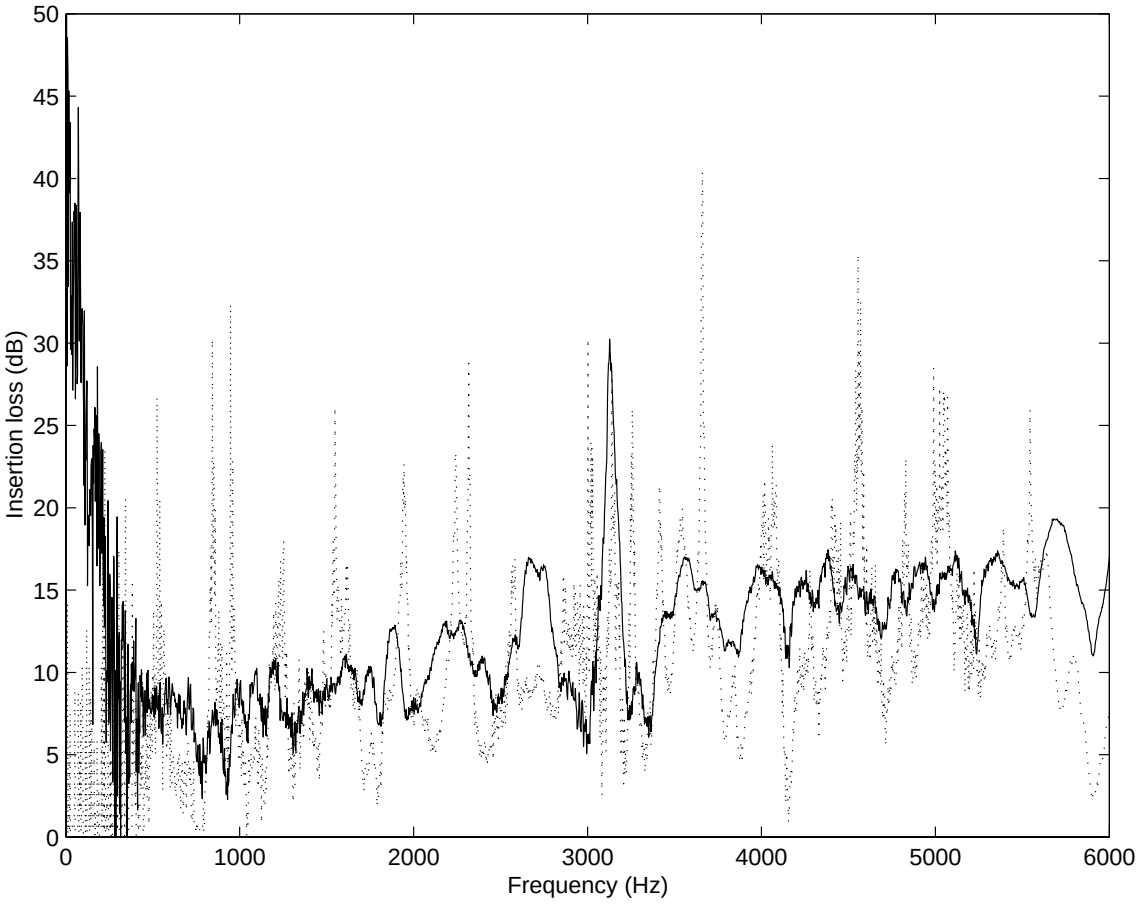

Figure 7.28. Comparison of insertion loss between the experimental data with and without post-processing at the receiver point at the midpoint of the barrier height: '—' after the post post-processing, '···' without post-processing.

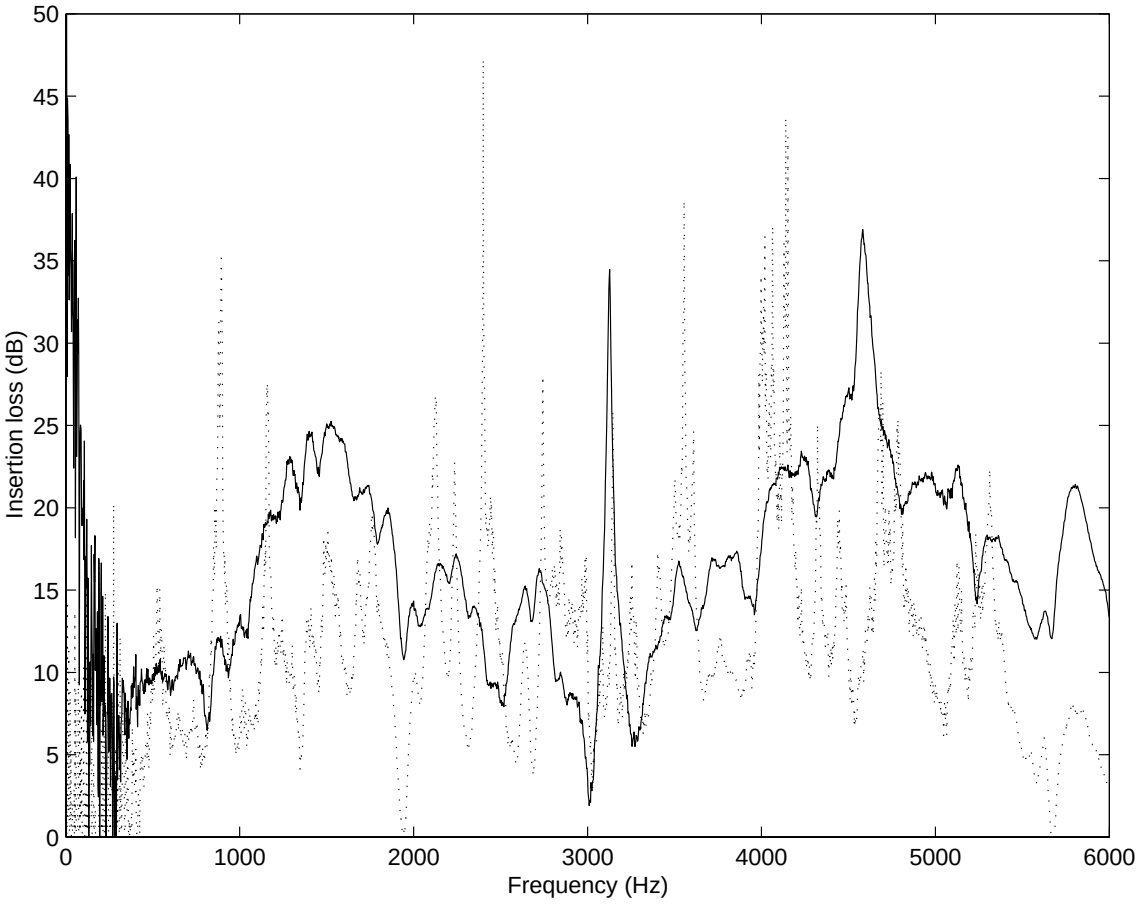

Figure 7.29. Comparison of insertion loss between the experimental data with and without post-processing at the receiver point 10.16 *cm* off the midpoint of the barrier height: '—' after the post post-processing, '· · ·' without post-processing.

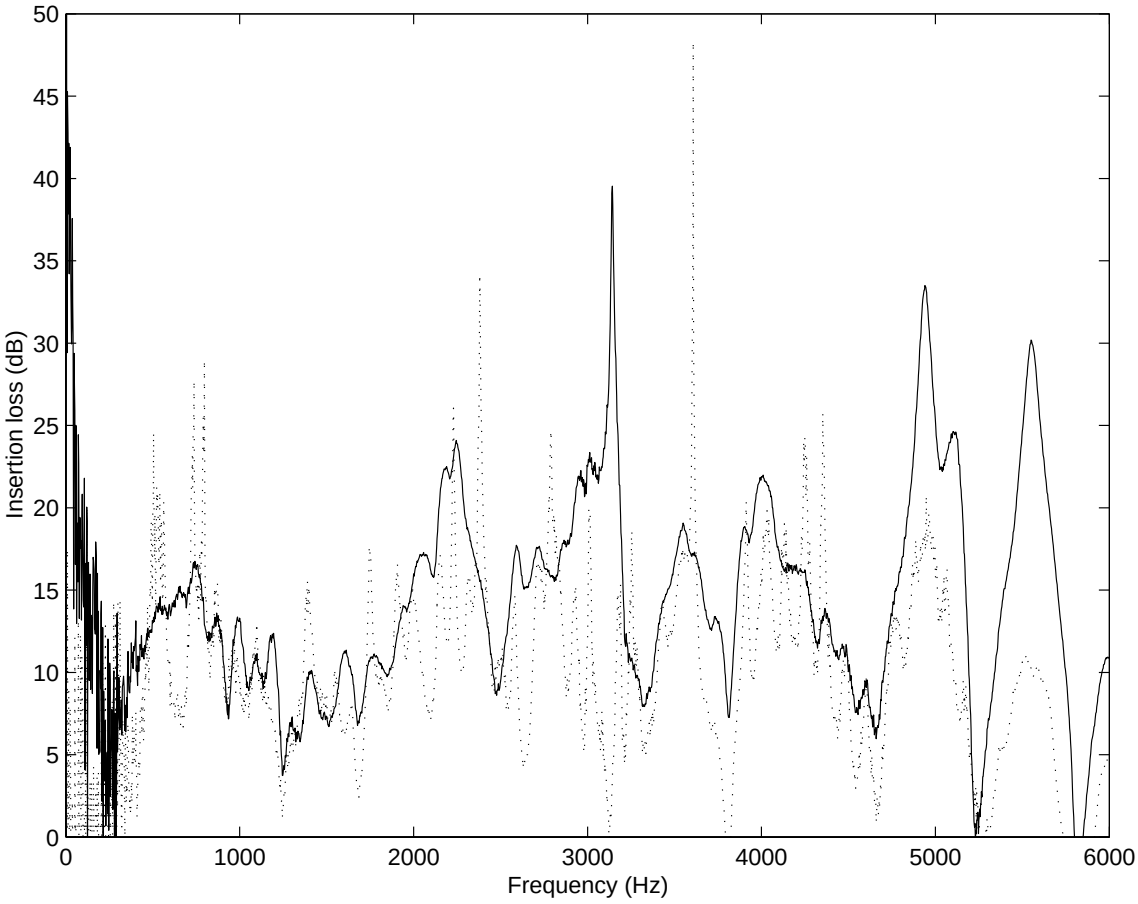

Figure 7.30. Comparison of insertion loss between the experimental data with and without post-processing at the receiver point 20.32 *cm* off the midpoint of the barrier height: '—' after the post post-processing, '· · ·' without post-processing.

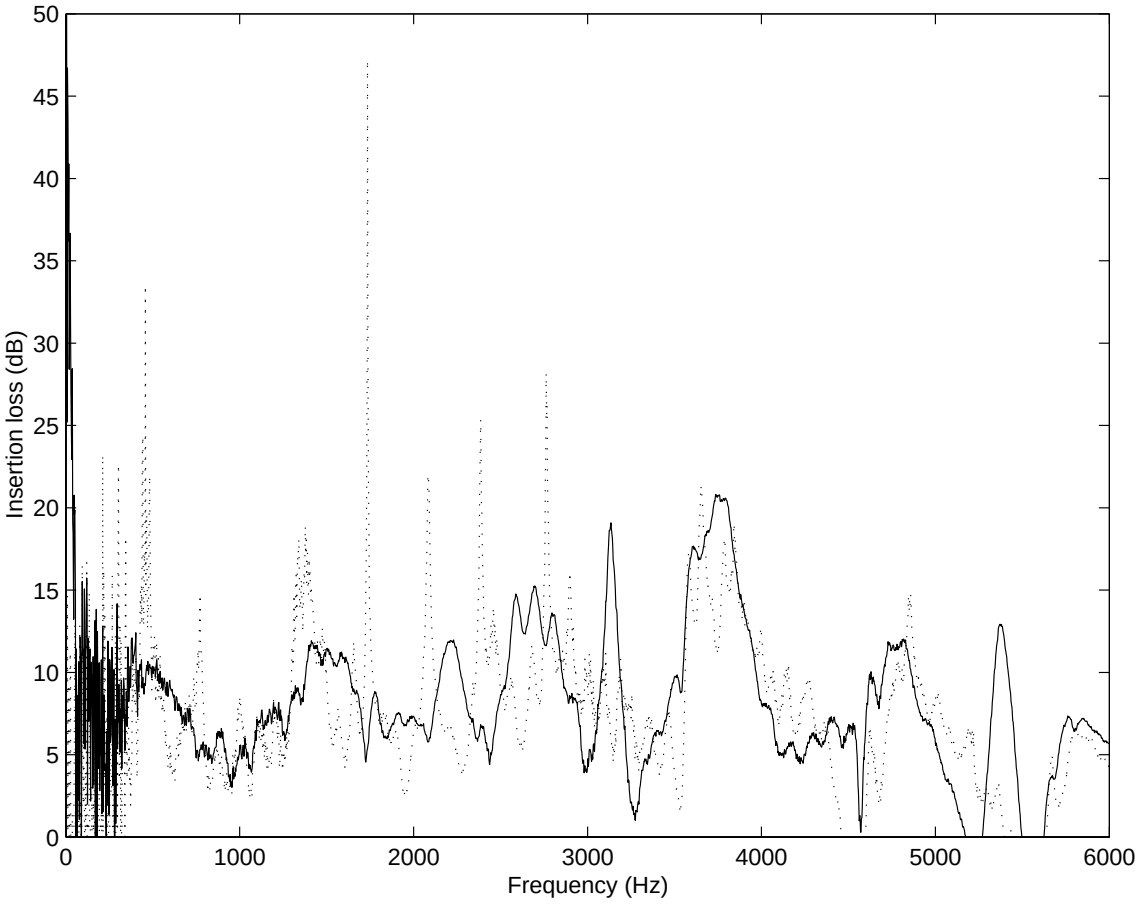

Figure 7.31. Comparison of insertion loss between the experimental data with and without post-processing at the receiver point 30.48 *cm* off the midpoint of the barrier height: '—' after the post post-processing, '· · ·' without post-processing.

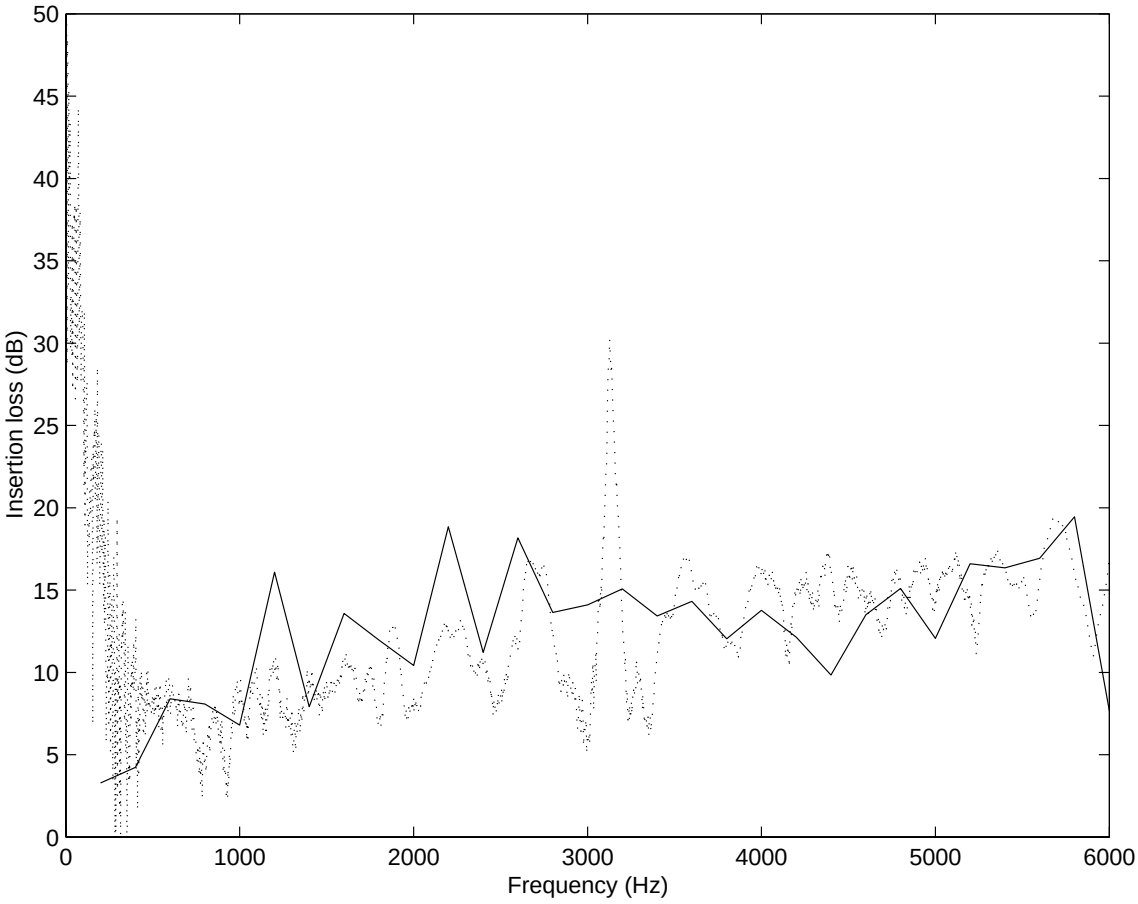

Figure 7.32. Comparison of insertion loss between the boundary element model and experiment with post-processing at the receiver point at the midpoint of the barrier height: '—' boundary element model, '· · ·' experiment.

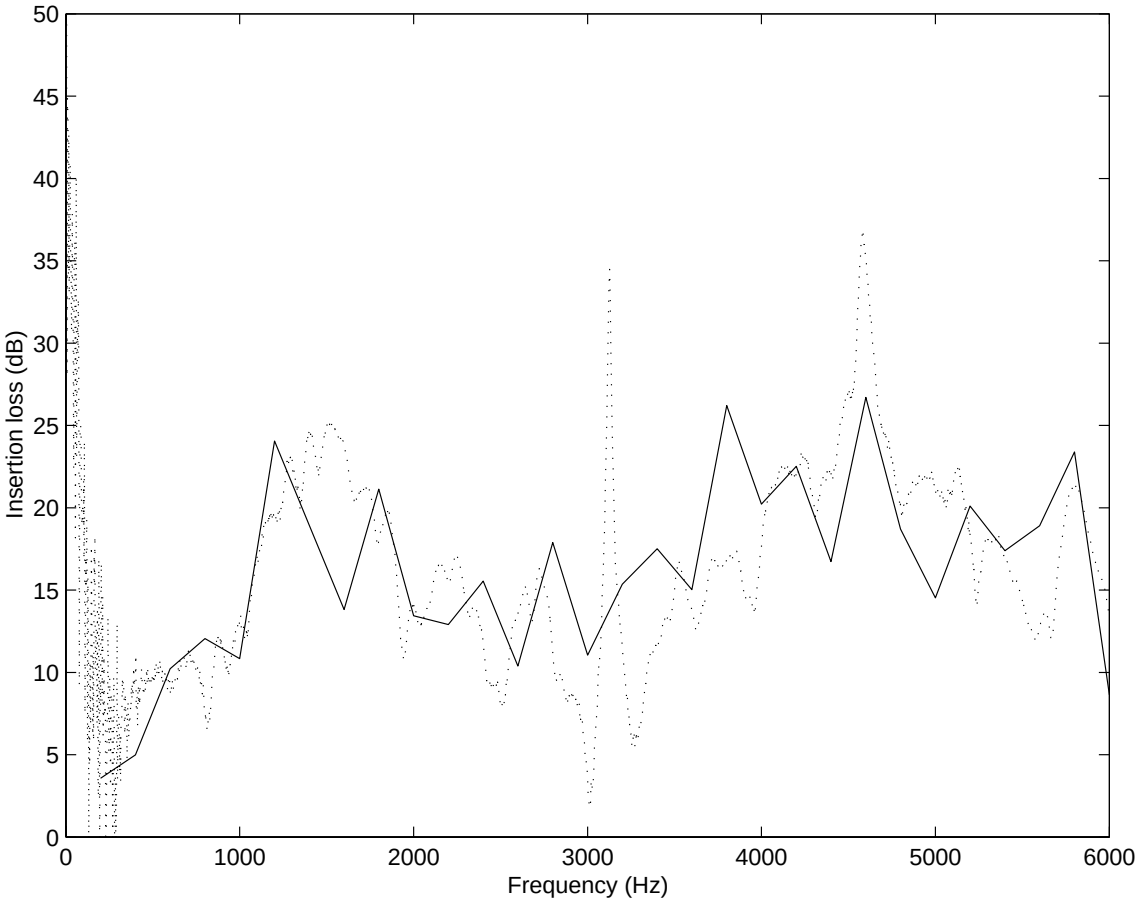

Figure 7.33. Comparison of insertion loss between the boundary element model and experiment with post-processing at the receiver point 10.16 *cm* off the midpoint of the barrier height: '—' boundary element model, '· · ·' experiment.

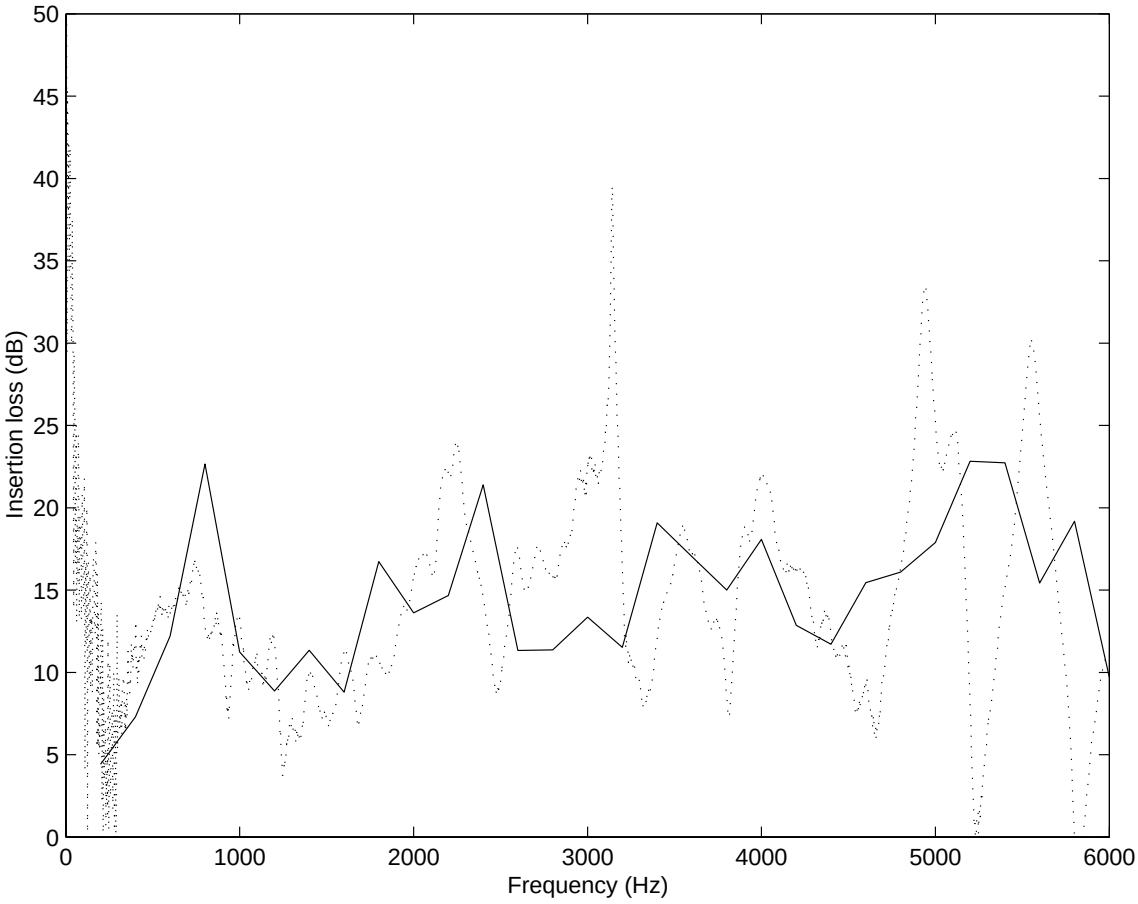

Figure 7.34. Comparison of insertion loss between the boundary element model and experiment with post-processing at the receiver point 20.32 *cm* off the midpoint of the barrier height: '—' boundary element model, '· · ·' experiment.

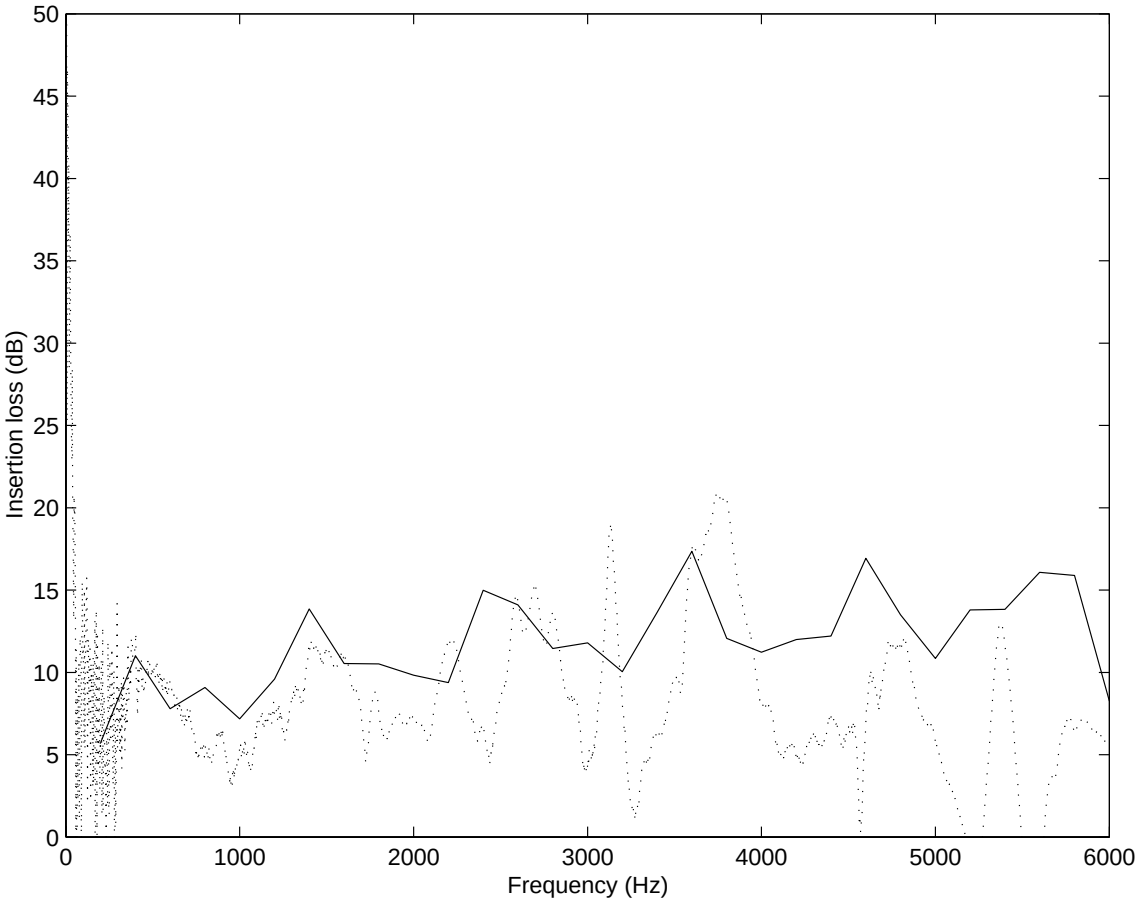

Figure 7.35. Comparison of insertion loss between the boundary element model and experiment with post-processing at the receiver point 30.48 *cm* off the midpoint of the barrier height; '—': boundary element model; '$\cdots$': experiment.

8. PERFORMANCE OF OTHER BARRIER CONCEPTS

8.1 Introduction

Much research has been performed with the intention of improving the performance of barriers without rasing their height. In particular, various barrier-top geometries have been suggested to improve sound barrier performance: e.g., T-shaped and Y-shaped barrier top treatments. The performance of several different barrier top treatments, both absorptive and non-absorptive are compared to the corresponding straight barrier in the experimental work described in this chapter.

8.2 Straight Barrier with Extended Height

A preliminary study was performed to study the improvement of insertion loss that can be obtained simply by extending the height of a barrier. The results presented here give a first insight into the performance improvement that can be expected by raising barrier height. These results also provide a reference against which the performance of various other types of barriers can be compared. An experimental study was performed for the straight barrier having an initial effective height of 36.83 cm along with 2.54 cm, 5.08 cm and 7.62 cm extensions. Experiments were first performed for a straight barrier which was 204 cm in length by 76 cm high with a thickness of 10 mm. For the next step, 2.54 cm, 5.08 cm and 7.62 cm wide metal strips, 204 cm long were attached to the top and bottom of the straight barrier. Note that this is same as raising the barrier height from 38 cm to 39.39, 41.91 and 44.45 cm, respectively when the barrier is placed on the ground as described in the last chapter.

8.2.1 Experimental Methods

In the work described in the last chapter, 17 receiver locations were used to evaluate the performance of the straight barrier. A more complicated top geometry creates more complex interference patterns behind the barrier. Therefore, to help evaluate the performance of the various acoustic barriers more accurately, 60 receiver locations were used on a plane parallel to the barrier in the shadow region. A knowledge of the sound pressure level at those receiver locations enables the calculation of the spatial insertion loss distribution over the receiver plane at selected frequencies. In addition, 2.54 *cm*, 5.08 *cm* and 7.62 *cm* wide metal strips were attached to the top and bottom of the straight plate to extend it to the desired heights. The source loudspeaker was located 73.66 *cm* in front of the barrier midway along the barrier's height and length. The 60 receivers were located 68.58 *cm* behind the barrier and spread from the midpoint of the barrier height to the boundary of the shadow zone which is 71.12 *cm* above the midpoint of the barrier height at this distance behind the barrier. The experimental apparatus used to make the diffraction measurements in this case is shown in Figure 8.1, and Figure 8.2 illustrates the dimensions of the microphone array used in this study. The various barrier dimensions are shown in Figure 8.3. Note again that the height of the steel plate used here is twice of that of the equivalent barrier on the ground because of the symmetry conditions that apply.

8.2.2 Comparison of Experimental Results

First, the insertion loss was compared at selected receiver locations over the frequency range up to 8000 Hz. To facilitate the comparison between various barrier designs, narrow band experimental insertion loss results were averaged into the 1/3 octave band results. One receiver location was selected to be on the virtual ground which is midway up the barrier height; a second microphone was located near the midpoint of the shadow zone of the equivalent barrier height: i.e., at 17.78 *cm* above the barrier midpoint. Both microphones were located midway along the barrier's length.

The effect of increasing the barrier height is shown in Figures 8.4 and 8.5 in

terms of insertion loss against frequency at one receiver location. A comparison of the insertion loss at the midpoint of barrier height (Figure 8.4) shows a monotonic insertion loss increase for all four configurations. This simple result follows from the fact that the receiver is located on the "ground" behind the barrier. Thus, there were no ground reflection interference effects. The 2.54 *cm* extended barrier gives an improvement of about 2 dB over all frequencies while the barrier with a 5.08 *cm* extension gives an insertion loss gain of 2 to 5 dB depending on frequency. It can be seen that extending the barrier by 7.62 *cm* gives an increase of insertion loss from 2 to 10 dB compared to the basic barrier at this particular receiver location. Figure 8.5 shows the insertion losses at the point in the middle of the shadow region. Compared to the insertion loss curves shown in Figure 8.4, the ground reflection effects in this case cause the insertion loss gain to be dependent on frequency. The three extended barrier designs do give better protection for the receiver at this point compared to the basic barrier; there were insertion loss increases of up to 7 dB. These results confirm the fact that a barrier's height is the single most important factor in determining its insertion loss.

Figures 8.4 and 8.5 clearly illustrate that the insertion loss increases with barrier height. However, since the cost of building a noise barrier usually depends on its height, it is of interest to keep the barrier height as small as possible while maintaining a given level of noise control performance. The idea of shaping the top of the barrier to improve the insertion loss for a given barrier height is considered next.

8.3 T-shape Barriers

One of many possible barrier top shapes was selected in order to evaluate the potential improvements in insertion loss that can be obtained by modifying the barrier top geometry. The height of the barriers considered was 73.66 *cm*, but the top of the barrier was given different horizontal widths: i.e., the barrier was T-shaped. T-shaped barriers with different top widths were created by adding 5.08, 10.16 and 15.24 *cm* wide metal strips to the barrier top. The dimensions of the three barrier configurations are shown in Figure 8.6, along with the corresponding straight barrier design. The

loudspeaker was located 73.66 *cm* in front of the barrier midway along the barrier's height and length as before. The 60 receivers were located 68.58 *cm* behind the barrier from the midpoint of the barrier height to the boundary of the shadow zone which is 71.12 *cm* above the midpoint of the barrier height at this distance behind the barrier.

8.3.1 Comparison of Experimental Results

First, the insertion loss was compared at selected receiver locations over the frequency range up to 8000 Hz. The receiver locations were the same as described previously for the straight barrier with extended heights. The effect of adding horizontal widths on the top of the barrier is shown in Figures 8.7 and 8.8 in terms of insertion loss over frequency at one receiver location.

Figure 8.7 illustrates the insertion losses of the three different T-shaped barriers along with the insertion loss of the straight barrier at the midpoint of the barrier height. At this point the increase of insertion loss was considerably larger than that provided by the straight extension cases considered in the last subsection. The 5.08 *cm* wide T-top shows a monotonic increase in insertion loss with frequency while the two other configurations show a frequency-dependent increase. At the middle of the shadow region, the insertion loss increases more smoothly with frequency, compared to the receiver on the virtual ground, as shown in Figure 8.8. One noticeable feature of all three T-shapes is the insertion loss increase of up to 5 dB in the relatively low frequency range up to 1600 Hz: but the relative benefits of T-shapes compared to a simple extension decrease as the frequency is increased.

Although T-shaped barriers with various configurations yielded better performance than a straight barrier of the same height, it cannot be thought of as a valid comparison since those three T-shaped barriers involve the use of more material than do straight barriers. Thus, a fairer comparison was made here to see the benefit of the T-shaped top: a comparison was made between 5.08 *cm* straight extension and 5.08 *cm* wide T-shape barrier. Figures 8.9 and 8.10 shows comparisons of the insertion losses in these two cases. It is apparent from the figures that the T-shape configuration does not result in a significant overall benefit when compared against

the corresponding linearly extended barrier.

8.4 Influence of Sound Absorbing Materials Placed on T-shaped Barriers

It is known that sound absorptive materials can be used to enhance barrier performance. In particular, sound absorptive treatments have been widely used in the parallel barrier situation. It has also been suggested that sound absorptive material should be placed on the edge of a barrier to reduce the diffraction from the top. Here, experiments were performed to measure the increase in insertion loss when glass fiber was attached to the top of the horizontal plate of the T-shaped barrier. In this case, 5.08, 10.16 and 15.24 *cm* width glass fiber pieces having a 2.54 *cm* thickness were added to the top of the corresponding three different types of T-shapes. Figure 8.11 shows the dimensions of the T-shape barriers with acoustic treatment.

The loudspeaker and 60 receivers were located as in the previous tests. First, comparisons were made for each particular T-shaped barrier with and without sound absorptive treatment. Figures 8.12 and 8.13 show the improvement at two different positions in insertion loss resulting from the application of a sound absorptive treatment to the 5.08 *cm* wide T-shape barrier. The increase in insertion loss at the midpoint is mostly in the high frequency region and the magnitude of the increase is not large as shown in Figure 8.12. Figure 8.13 also shows the same trend.

The same comparison was made for the 10.16 *cm* T-shaped barrier with and without sound absorptive treatment. The results in this case are shown in Figure 8.14 at the midpoint of the barrier height. It can be seen that application of the sound treatment to the top of the T-shape smooths out the peaks and dips in the insertion loss. It can also be observed that there is an overall improvement in performance in the frequency range from 4000 - 8000 Hz. An increase in the frequency bands from 3150 Hz to 8000 Hz can be seen in Figure 8.15 when the insertion loss was measured at the midpoint of the barrier height. The last comparison was made for a 15.24 *cm* wide T-shape barrier. Figures 8.16 and 8.17 show that the insertion loss is increased as frequencies above 2000 Hz at both measurement locations after application of the absorptive material.

8.5 Effective Use of Sound Absorbing Treatment

It has been suggested that positioning sound absorptive material on the edge of a barrier reduces the diffraction from the top of the barrier and increases the insertion loss behind the barrier. However, optimal positioning of porous materials has not been studied extensively. The modelling of porous material is relatively complicated when the porous material is used without a solid structure behind it. Calculation of acoustic impedance in this case requires finite element modelling of the micro-structure of the porous material. The techniques for including calculated impedance values from a finite element model into the acoustic boundary element model have not yet been fully verified. Thus an experimental study was performed for various barrier configurations to identify the most effective way of using porous material. The loudspeaker was located 73.66 *cm* in front of the barrier midway along the barrier's height and length. The 60 receivers were located 68.58 *cm* behind the barrier from the midpoint of the barrier height to the boundary of the shadow zone which is 71.12 *cm* above the midpoint of the barrier height at this distance behind the barrier.

Effective Positioning of Porous Material

Fiberglass pieces of 10.16 *cm* width and 2.54 *cm* thickness were used to study the effects of positioning absorptive material at the edge of the barrier. In the first case, a 10.16 *cm* wide glass fiber strip was pasted on the front side of the barrier with a 5.08 *cm* overlap on the rigid barrier. This arrangement gave a 5.08 *cm* extension of the barrier without a hard backing. In the second case, the fiberglass was placed on the back of the barrier with the same overlap of 5.08 *cm*. Finally a measurement was performed with two 10.16 *cm* wide fiber glass pieces attached on both sides of the barrier with an overlap of 5.08 *cm*. The geometries for these cases are shown in Figure 8.18.

A comparison is shown in Figure 8.19 between the performance of the three barriers with sound absorptive treatments and a straight barrier with no acoustic treatment for a the receiver located at the midpoint of the barrier height. All three sound absorptive configurations result in a considerable increase in the insertion loss for

this receiver location. The experimental result suggests that when the fiberglass was attached on both sides of the rigid barrier the performance of barrier was worse than when a single piece of fiberglass was placed on either side of the barrier. This result needs more investigation at this point.

It can be seen in Figure 8.20 that better performance is obtained by placing the sound absorptive material on the front side of the barrier rather than the rear side when the receiver is at the midpoint of the shadow zone. As before, the configuration with sound absorptive treatment on both sides of the barrier performs worse than the case where absorptive treatment was placed on the front of the barrier.

Effects of Overlap on the rigid wall

Next, the 10.16 *cm* inch wide and 2.54 *cm* thick fiberglass was used to see the effect of positioning the absorptive material on the top of the barrier. In the first case, the 10.16 *cm* wide fiberglass was pasted on the front side of the barrier with a 5.08 *cm* overlap on the rigid barrier. This configuration gave a 5.08 *cm* extension of the barrier without hard backing. The second case featured a 2.54 *cm* wide overlap with the rigid barrier. The sound absorptive treatment was applied on the source side of the barrier based on the earlier results. Figure 8.21 illustrates the geometries of two sound absorptive treatments.

The effect of the size of the overlapped region at the edge of the barrier is shown in Figure 8.22. At this receiver location, the additional 2.54 *cm* wide fiberglass of 2.54 *cm* thickness gave an additional 5 dB increment in the insertion loss from 4000 to 8000 Hz. Note that there is no noticeable difference in insertion loss curves in the low frequency region up to 1600 Hz since the characteristic of sound absorptive material used in this study does not give any significant sound absorption at those low frequencies. Figure 8.23 shows that the 2.54 *cm* of additional overlap does not make a noticeable difference at the midpoint of the shadow zone. In this case the increased overlap gives only slightly better performance in the frequency band 2000 Hz to 5000 Hz. It can again be seen that there is no difference in insertion losses in the low frequencies.

8.6 Comparison of Various Barrier Configurations

To assess the relative performance of the various configurations considered in this chapter, three cases were compared: the 5.08 *cm* linear extension on the basic barrier; the T-shaped barrier with a 5.08 *cm* wide top; and a 7.62 *cm* sound absorptive treatment with 2.54 *cm* overlap with the rigid barrier. Figure 8.24 shows those configurations. Note that the 7.62 *cm* wide fiber glass was positioned on the front side of the rigid barrier based on the discussion earlier about the positioning of sound absorptive treatments.

Figure 8.25 shows that the absorptive treatment on the top edge of the barrier has a significant advantage over the other two configurations. Especially in the frequency band from 3150 Hz to 6300 Hz, the performance enhancement produced by the absorptive extension was more than 10 dB compared to a straight barrier with the same height. The benefit of the sound absorptive treatment also can be seen in Figure 8.26. At this receiver point, much smooth insertion loss was obtained and dips in the insertion loss were eliminated. Figure 8.27 and Figure 8.28 shows that the sound absorptive extension raise the insertion loss particularly in the frequency band from 4000 to 8000 Hz. It can be observed that the benefit of soft extension decreases as the receiver location approaches the shadow boundary as shown in Figure 8.29. However, still fiber glass extension slightly works better than other designs at this receiver location.

In this section, the improvement of the insertion loss associated with increased barrier height were addressed. The performance of the T-shape barrier was compared against the corresponding straight barrier. The effective use of sound absorptive material was also considered. Finally, it was found that it is more efficient to use porous material without any rigid backing structure when the porous material is added to the top edge of the barrier when an improvement in the insertion loss is desired at receiver locations deep in the shadow region.

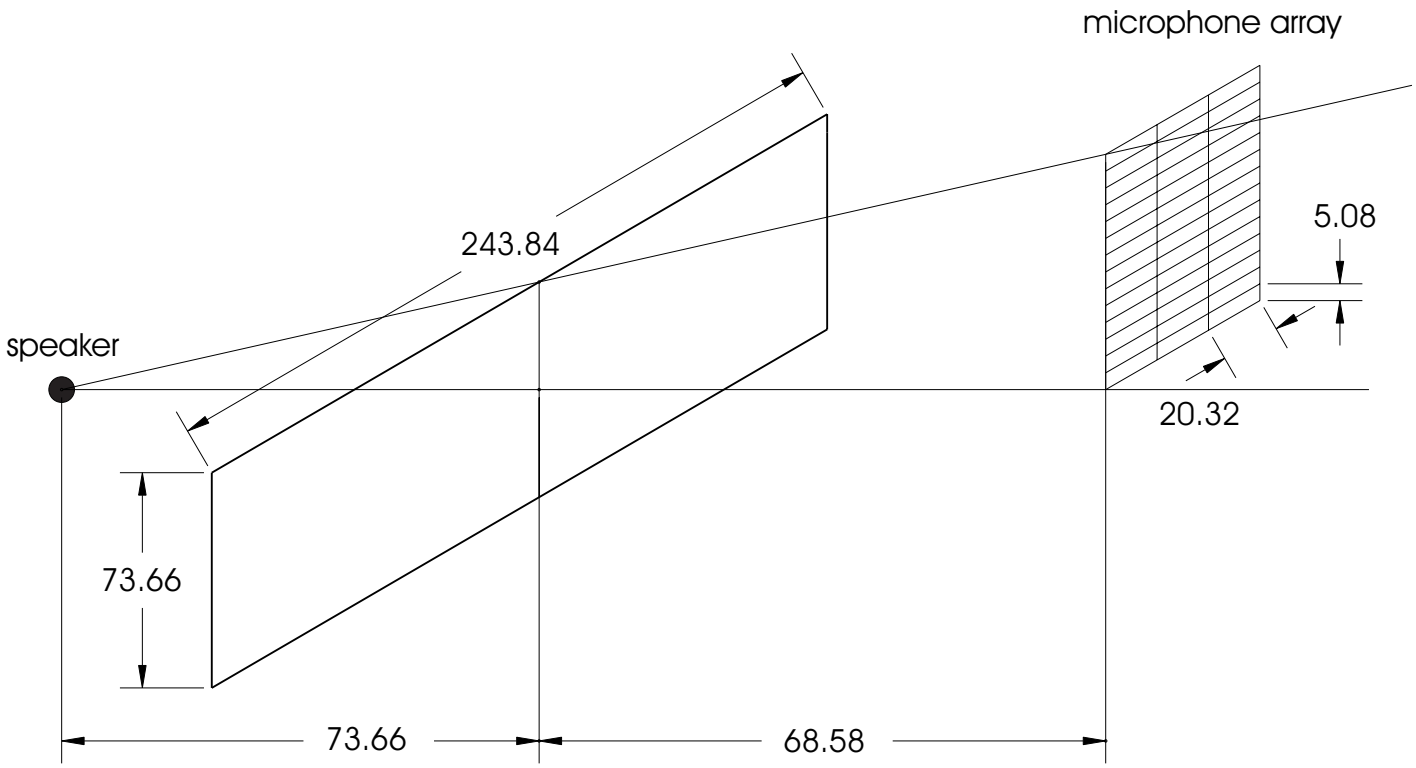

Figure 8.1. Geometry for finite length barrier analysis with microphone array.

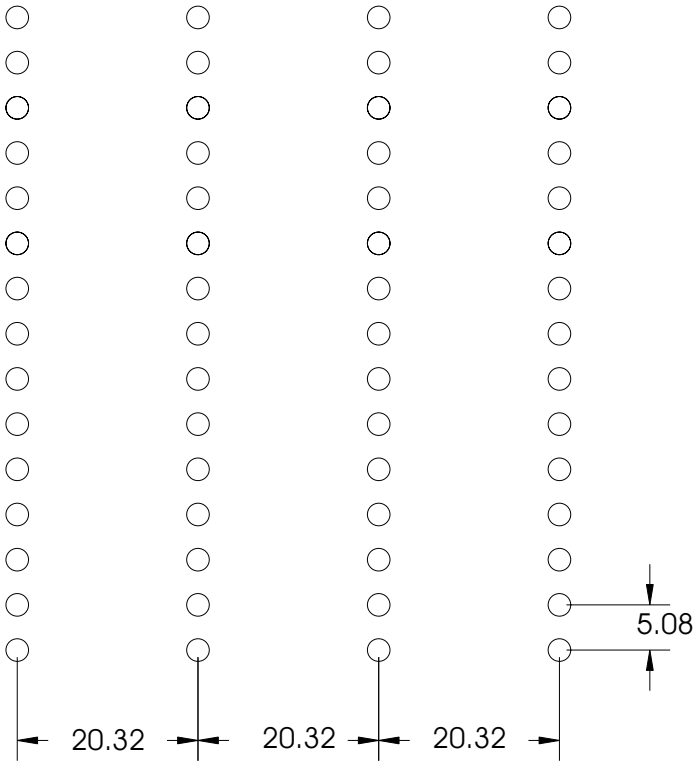

Figure 8.2. Dimension of the microphone array.

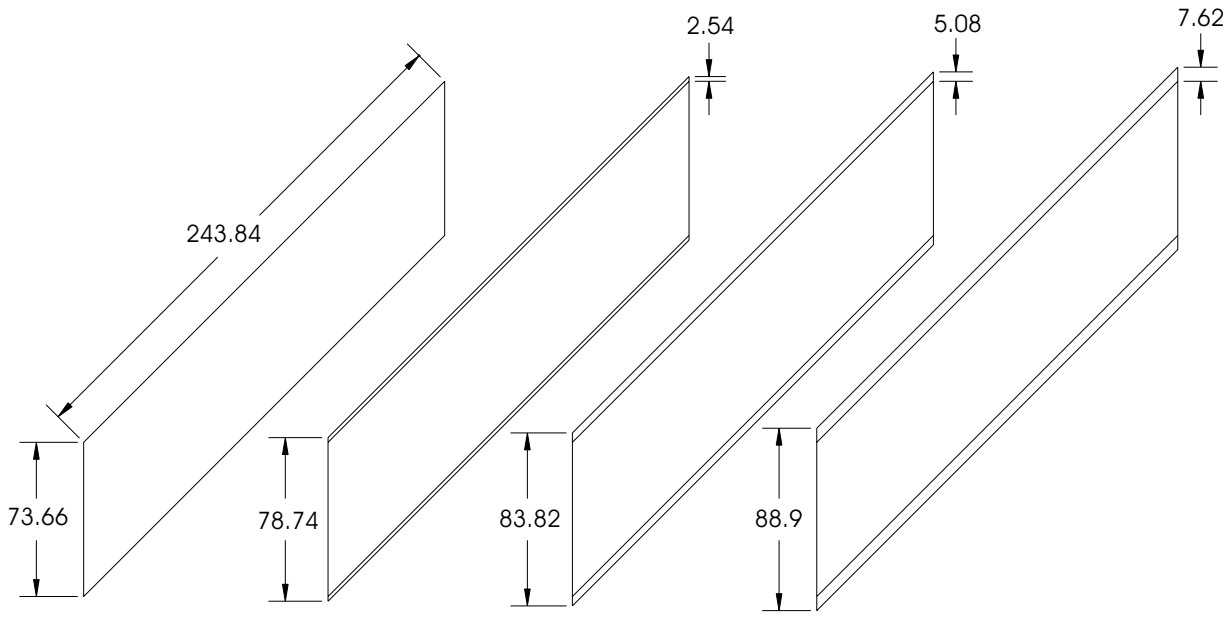

Figure 8.3. Geometry of the straight barrier and extended barriers with different heights.

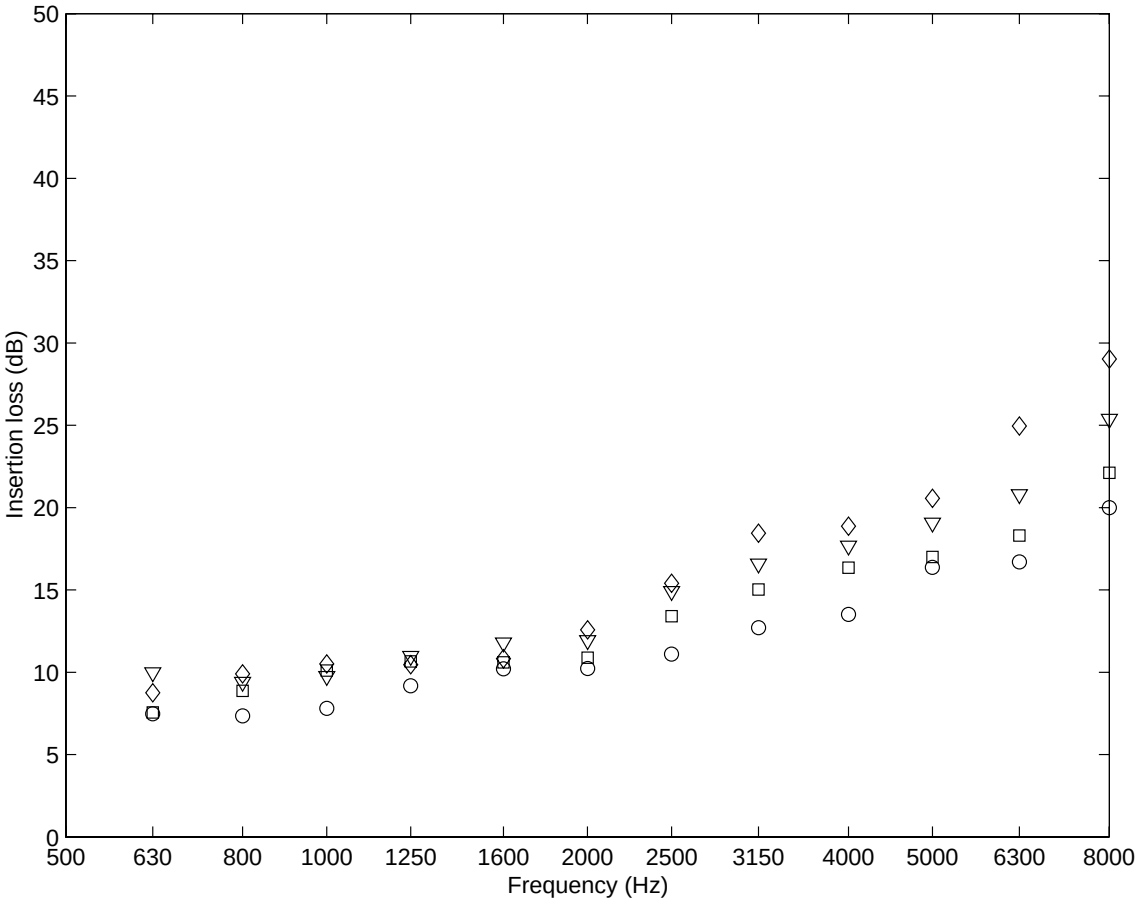

Figure 8.4. Comparison of insertion loss at the midpoint of the barrier height. '*bigcirc*': basic barrier without extension; '□': straight barrier with 2.54 *cm* extension; '◇': straight barrier with 5.08 *cm* extension; ' ': straight barrier with 7.62 *cm* extension.

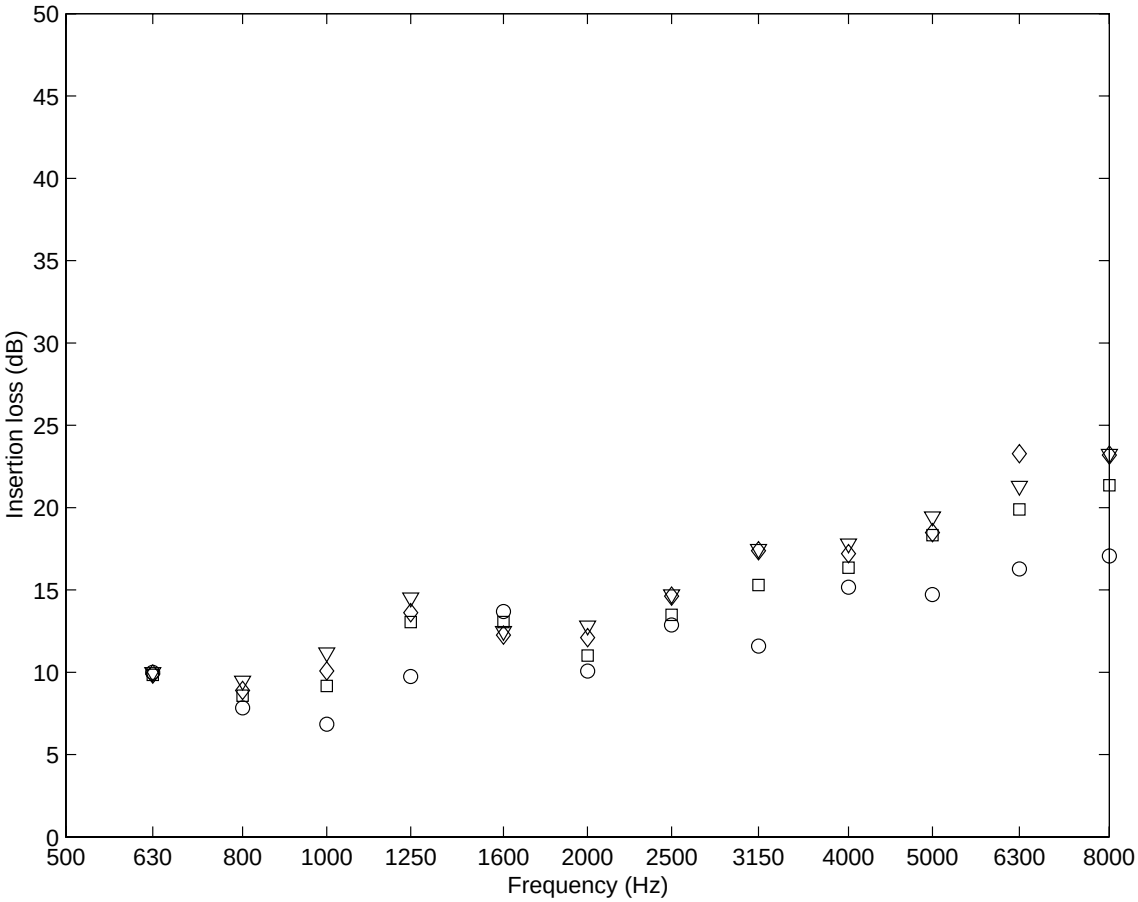

Figure 8.5. Comparison of insertion loss at the 17.78 *cm* off the midpoint of the barrier height. ‘ ’: basic barrier without extension; ‘□’: straight barrier with 2.54 *cm* extension; ‘◇’: straight barrier with 5.08 *cm* extension; ‘ ’: straight barrier with 7.62 *cm* extension.

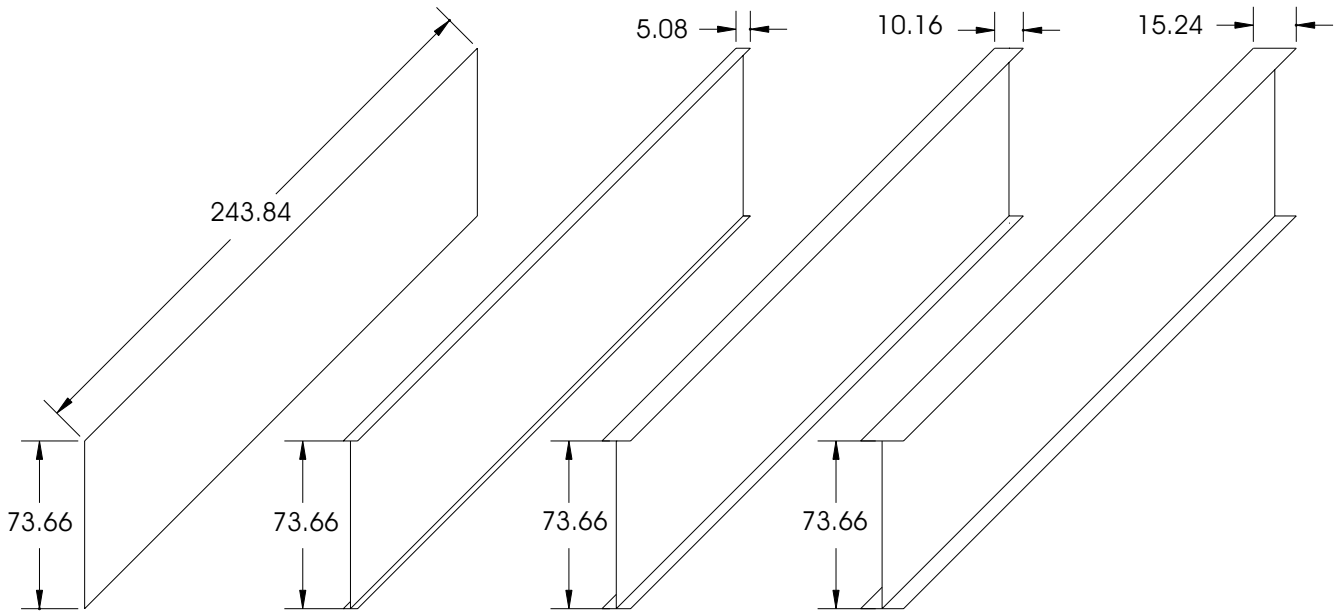

Figure 8.6. Geometry of the T-shape barrier designs.

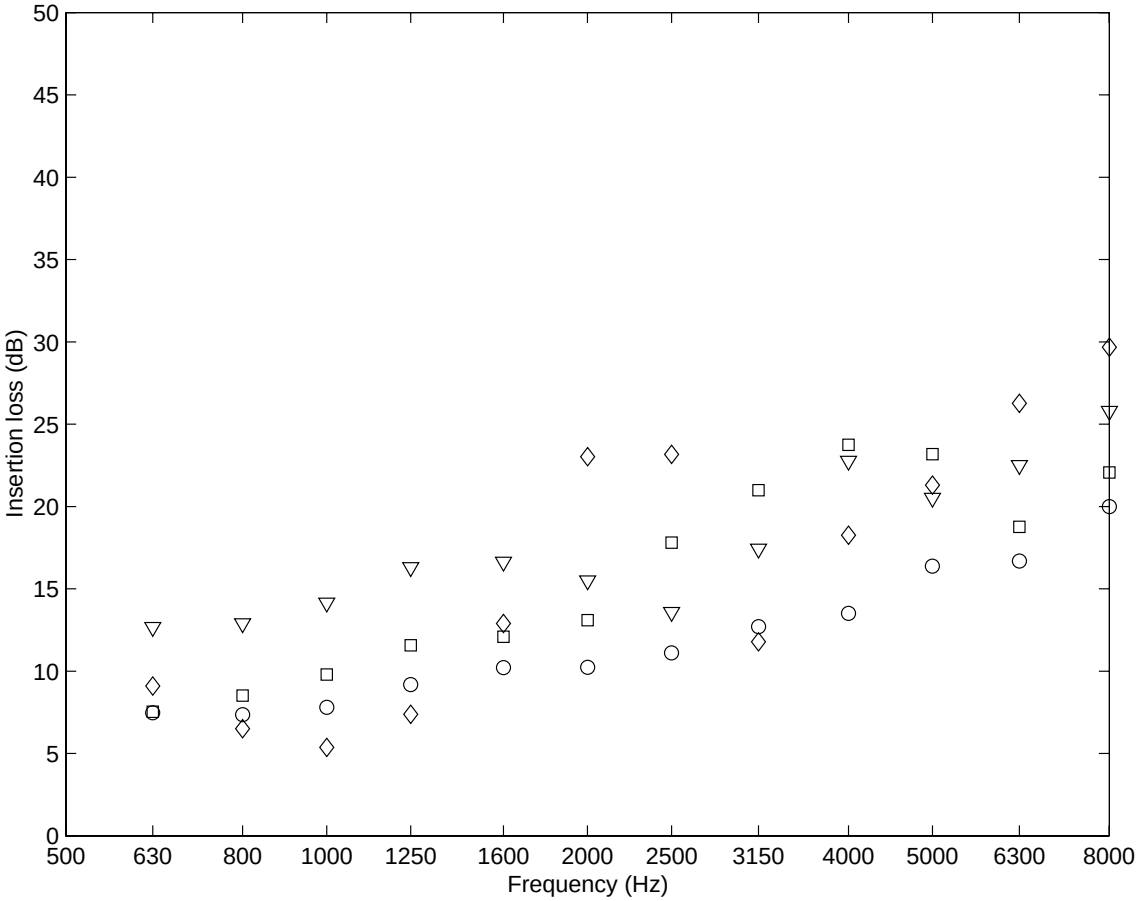

Figure 8.7. Comparison of insertion loss at the midpoint of the barrier height. ': basic barrier without extension; '□': T-shape barrier with 5.08 *cm* wide top; '◇': T-shape barrier with 10.16 *cm* wide top; ' ': T-shape barrier with 15.24 *cm* wide top.

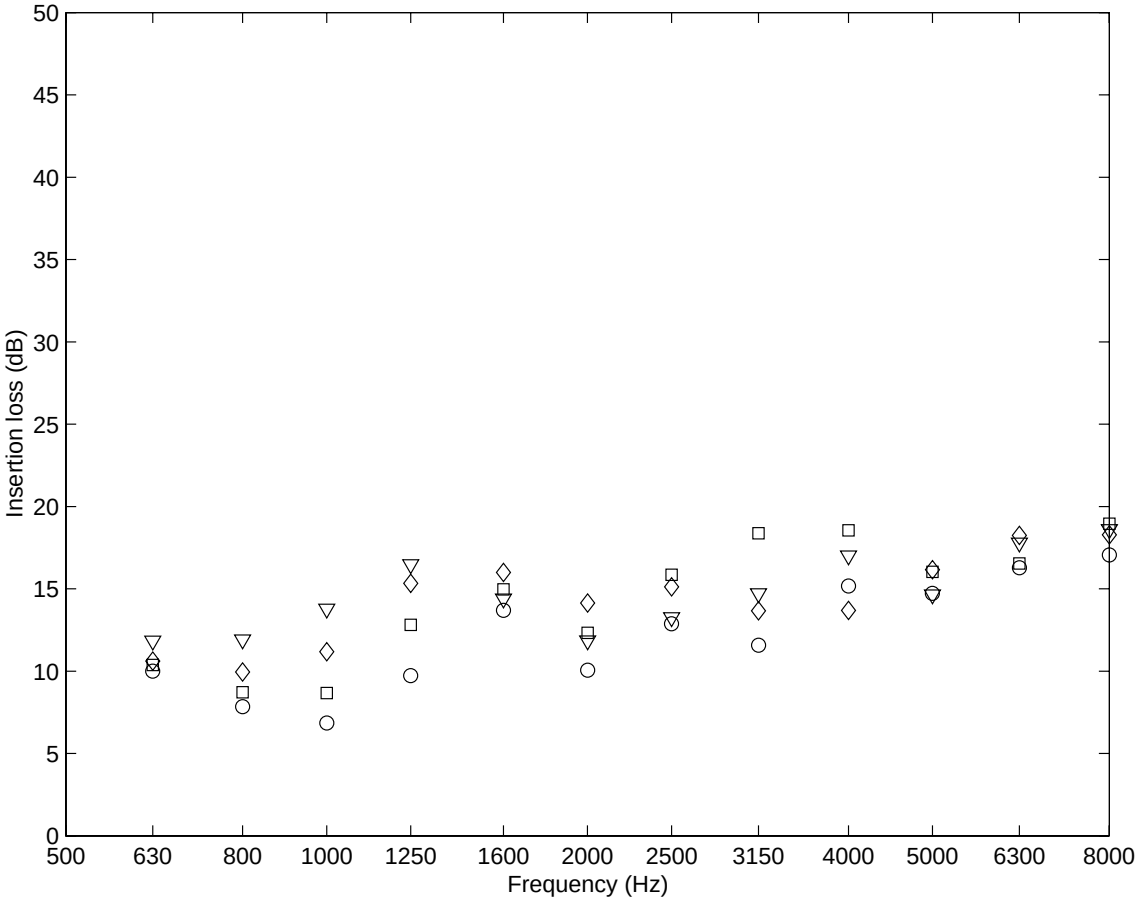

Figure 8.8. Comparison of insertion loss at the 17.78 *cm* off the midpoint of the barrier height. ‘ ’: basic barrier without extension, ‘□’ T-shape barrier with 5.08 *cm* wide top; ‘◇’: T-shape barrier with 10.16 *cm* wide top; ‘ ’: T-shape barrier with 15.24 *cm* wide top.

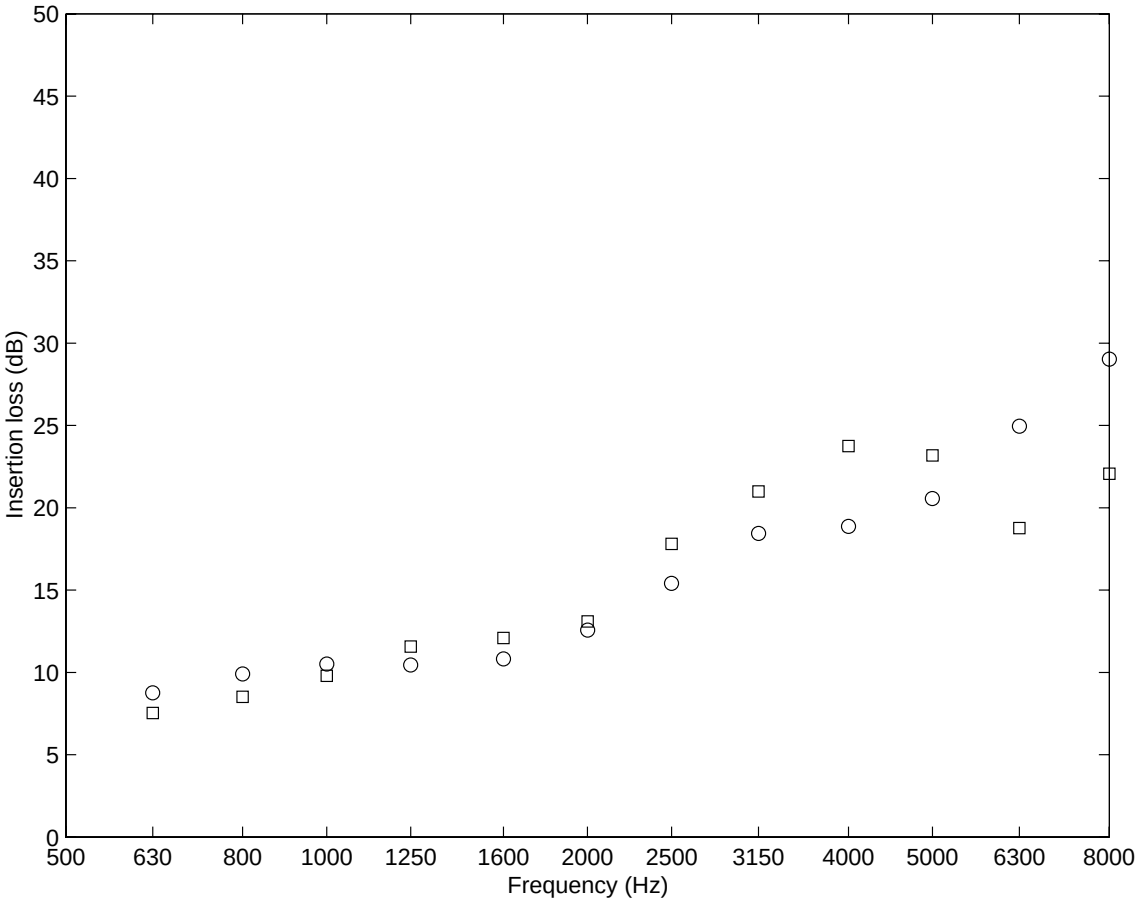

Figure 8.9. Comparison of insertion loss at the midpoint of the barrier height. ‘ ’: straight barrier with 5.08 *cm* linear extension; ‘□’: T-shape barrier with 5.08 *cm* wide top.

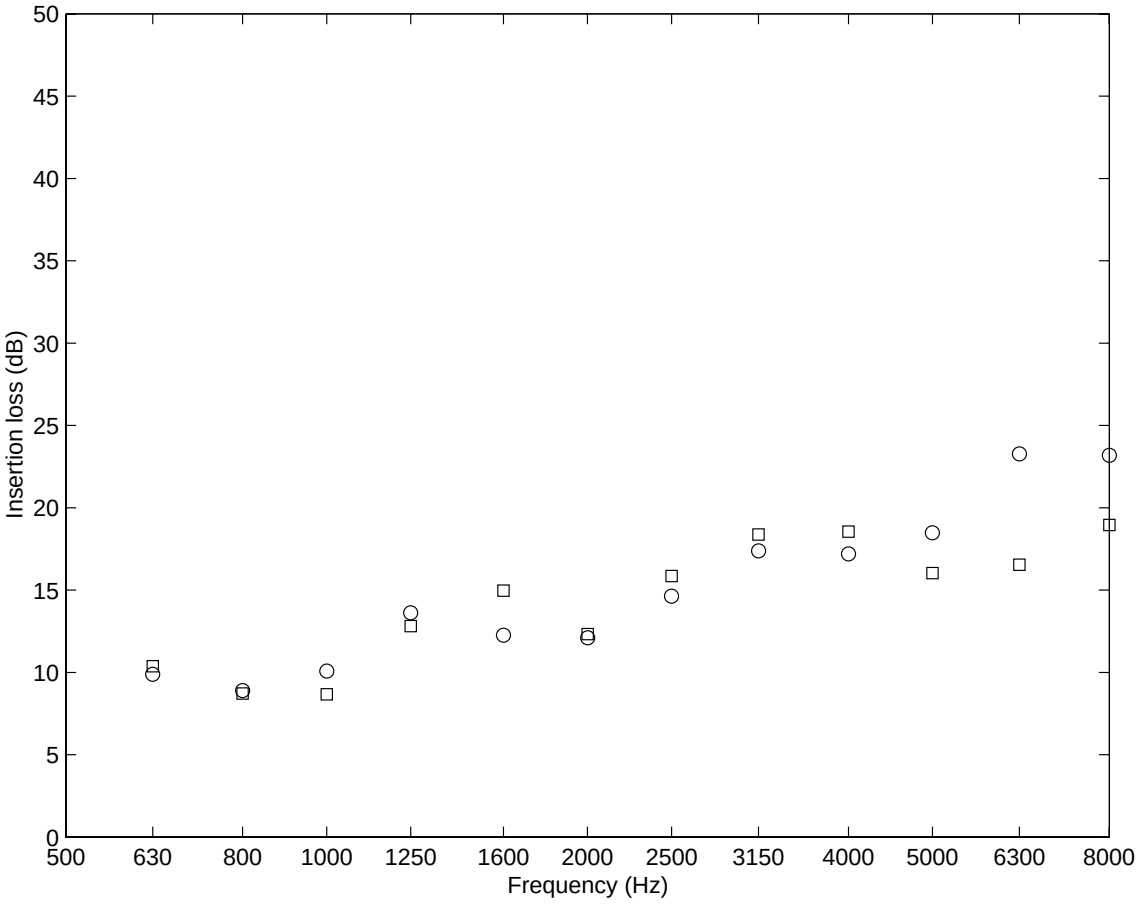

Figure 8.10. Comparison of insertion loss at the 17.78 *cm* off the midpoint of the barrier height. ‘ ’: straight barrier with 5.08 *cm* linear extension; ‘□’: T-shape barrier with 5.08 *cm* wide top.

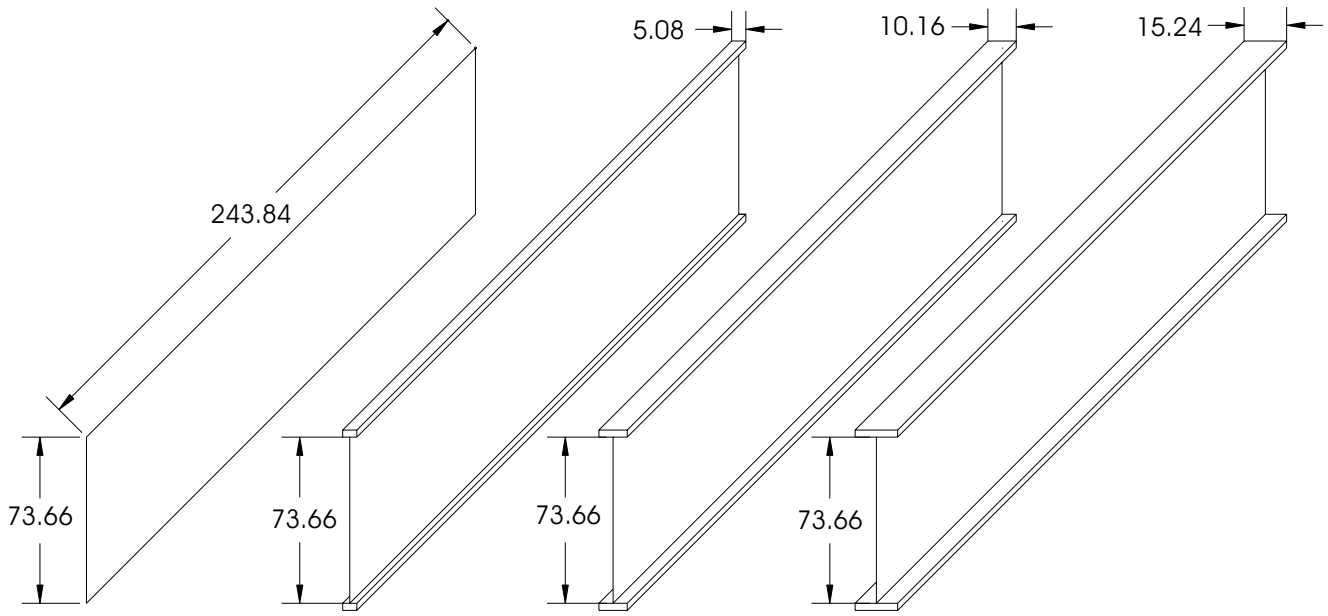

Figure 8.11. Geometry of the T-shape designs with sound absorptive treatment.

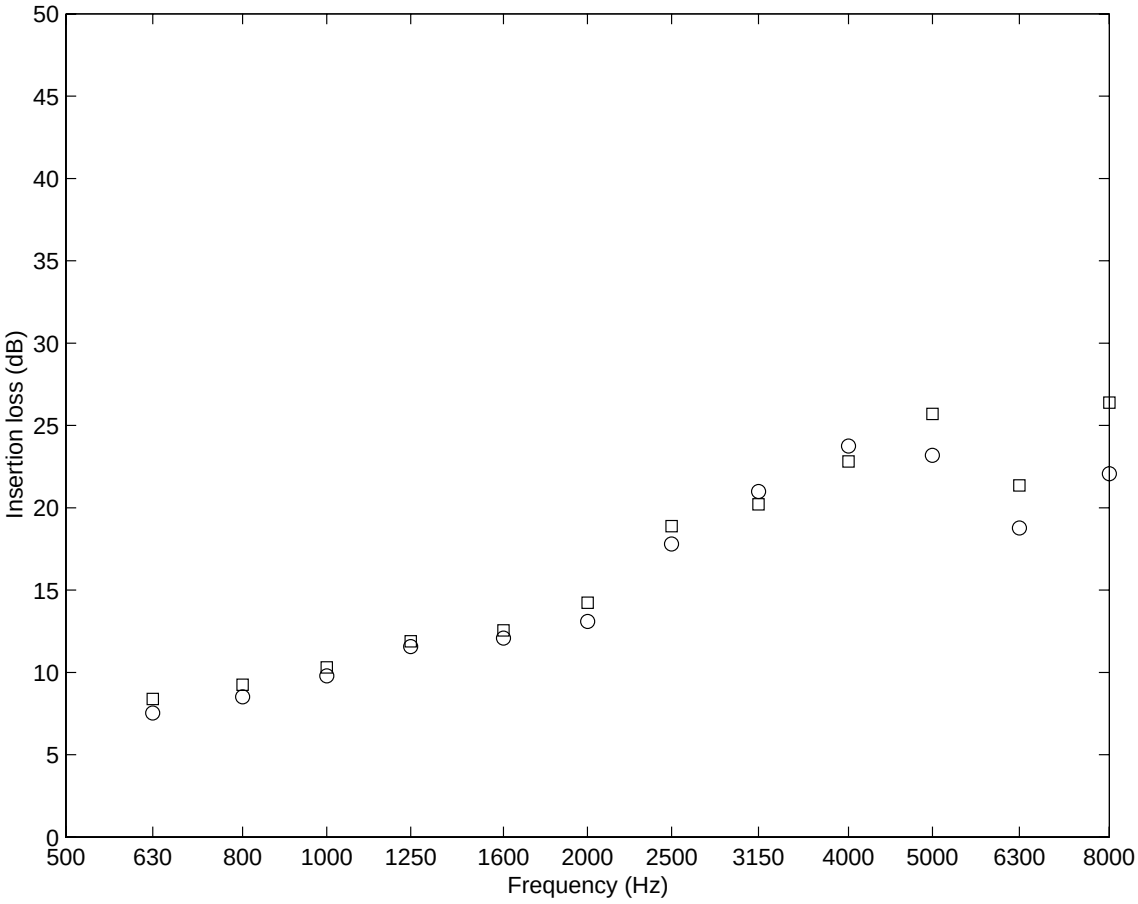

Figure 8.12. Comparison of insertion loss at the midpoint of the barrier height. ‘ ’: T-shape barrier with 5.08 *cm* wide top; ‘□’: T-shape barrier with 5.08 *cm* wide top with sound absorptive treatment.

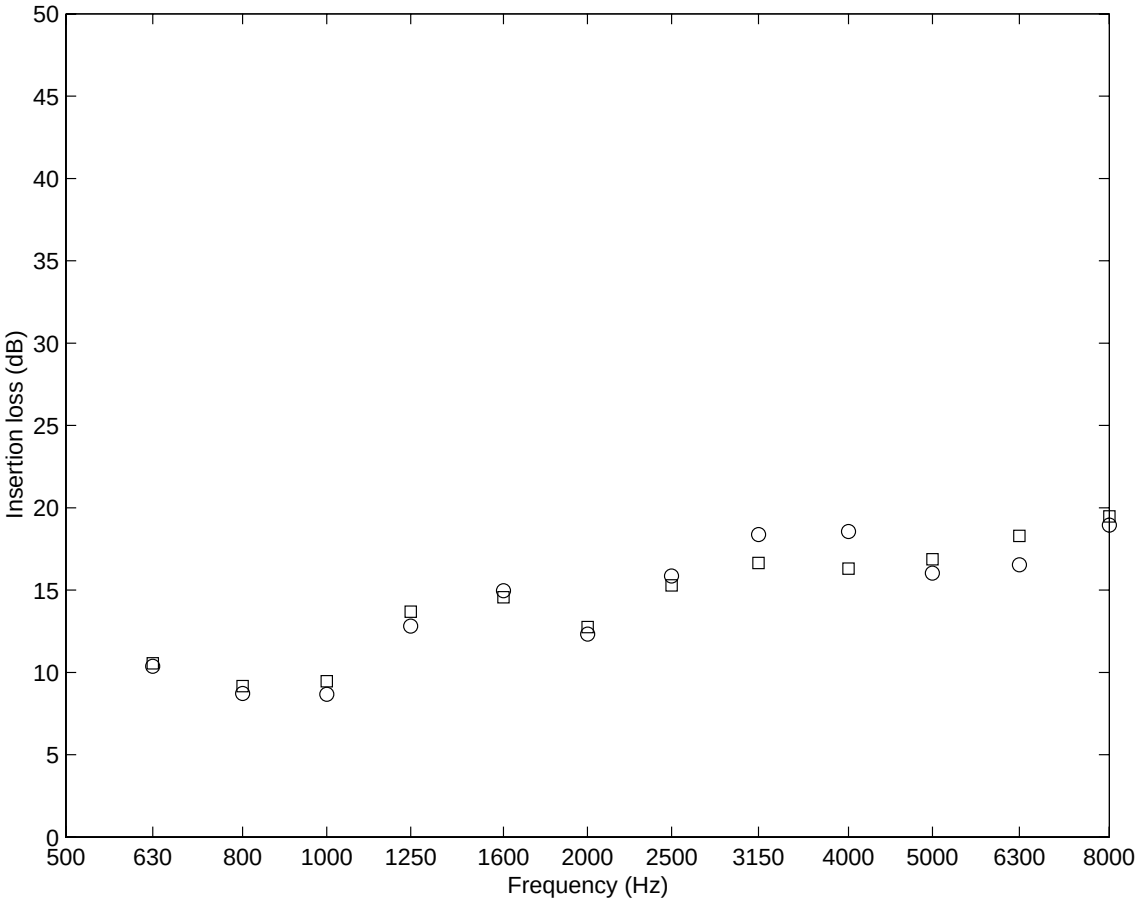

Figure 8.13. Comparison of insertion loss at the 17.78 *cm* off the midpoint of the barrier height. ‘ ’: T-shape barrier with 5.08 *cm* wide top; ‘□’: T-shape barrier with 5.08 *cm* wide top with sound absorptive treatment.

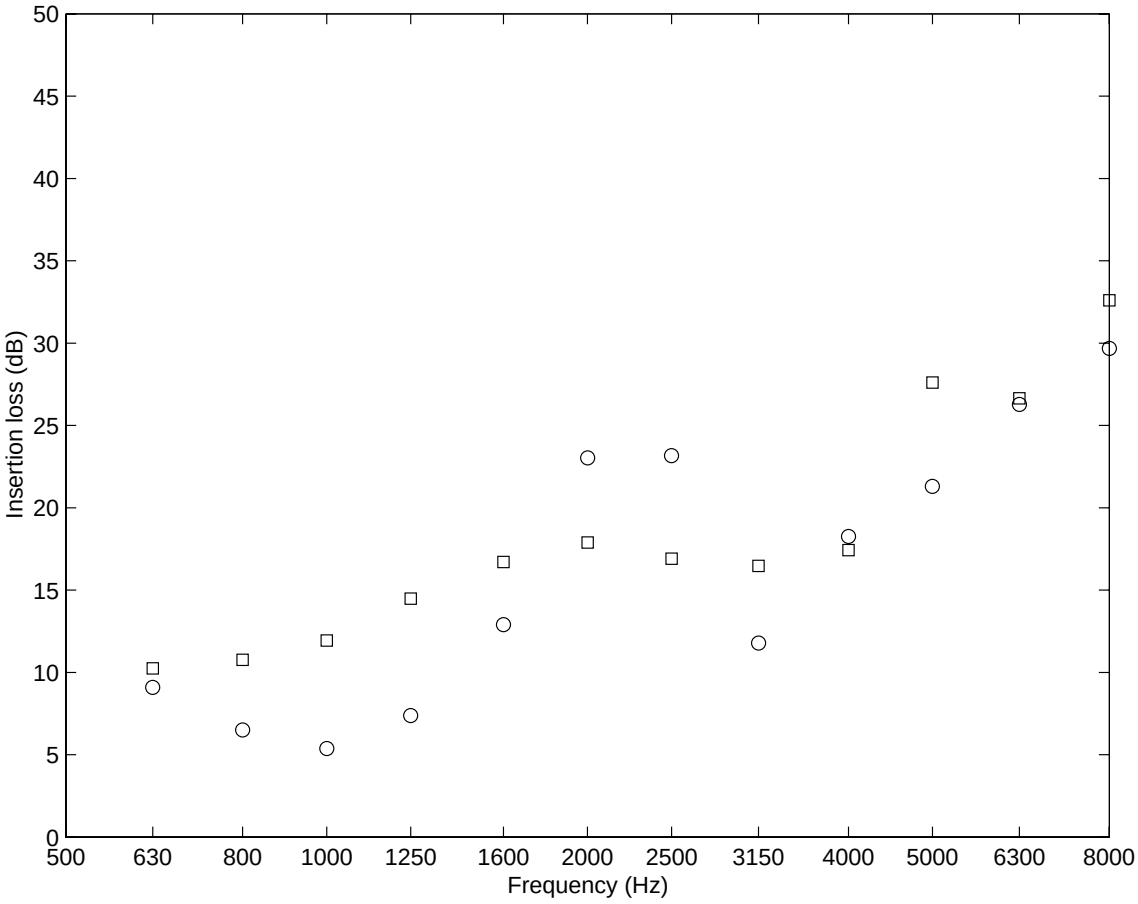

Figure 8.14. Comparison of insertion loss at the midpoint of the barrier height. ‘ ’: T-shape barrier with 10.16 *cm* wide top; ‘□’: T-shape barrier with 10.16 *cm* wide top with sound absorptive treatment.

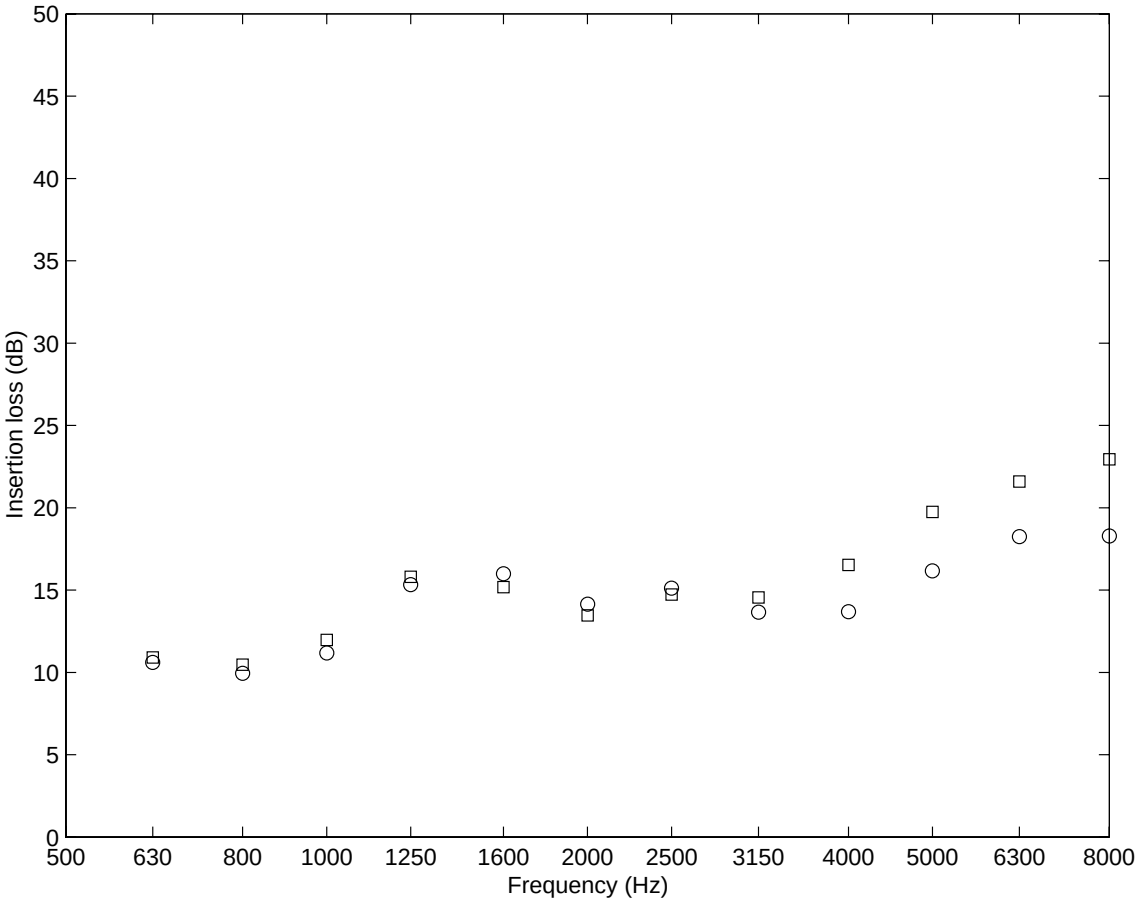

Figure 8.15. Comparison of insertion loss at the 17.78 *cm* off the midpoint of the barrier height. ‘ ’: T-shape barrier with 10.16 *cm* wide top; ‘□’: T-shape barrier with 10.16 *cm* wide top with sound absorptive treatment.

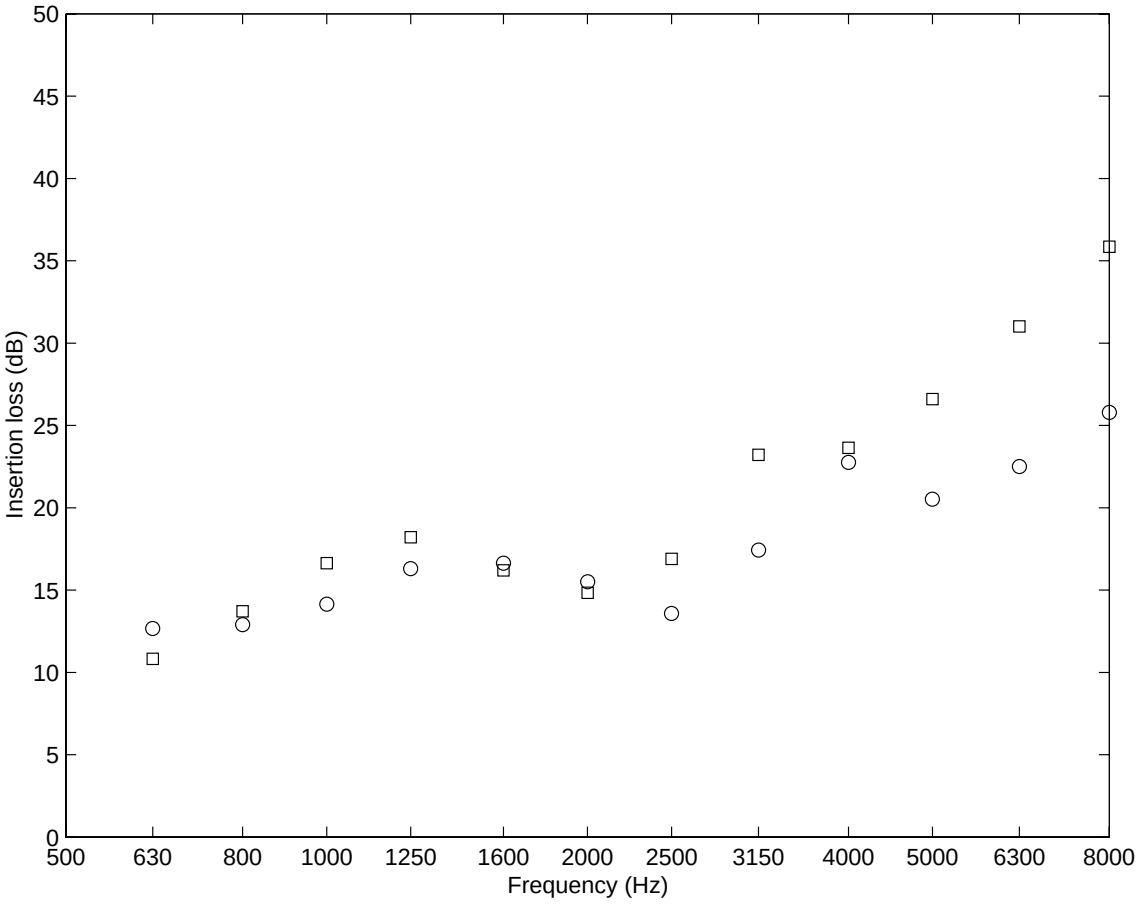

Figure 8.16. Comparison of insertion loss at the midpoint of the barrier height. ‘ ’: T-shape barrier with 15.24 *cm* wide top; ‘□’: T-shape barrier with 15.24 *cm* wide top with sound absorptive treatment.

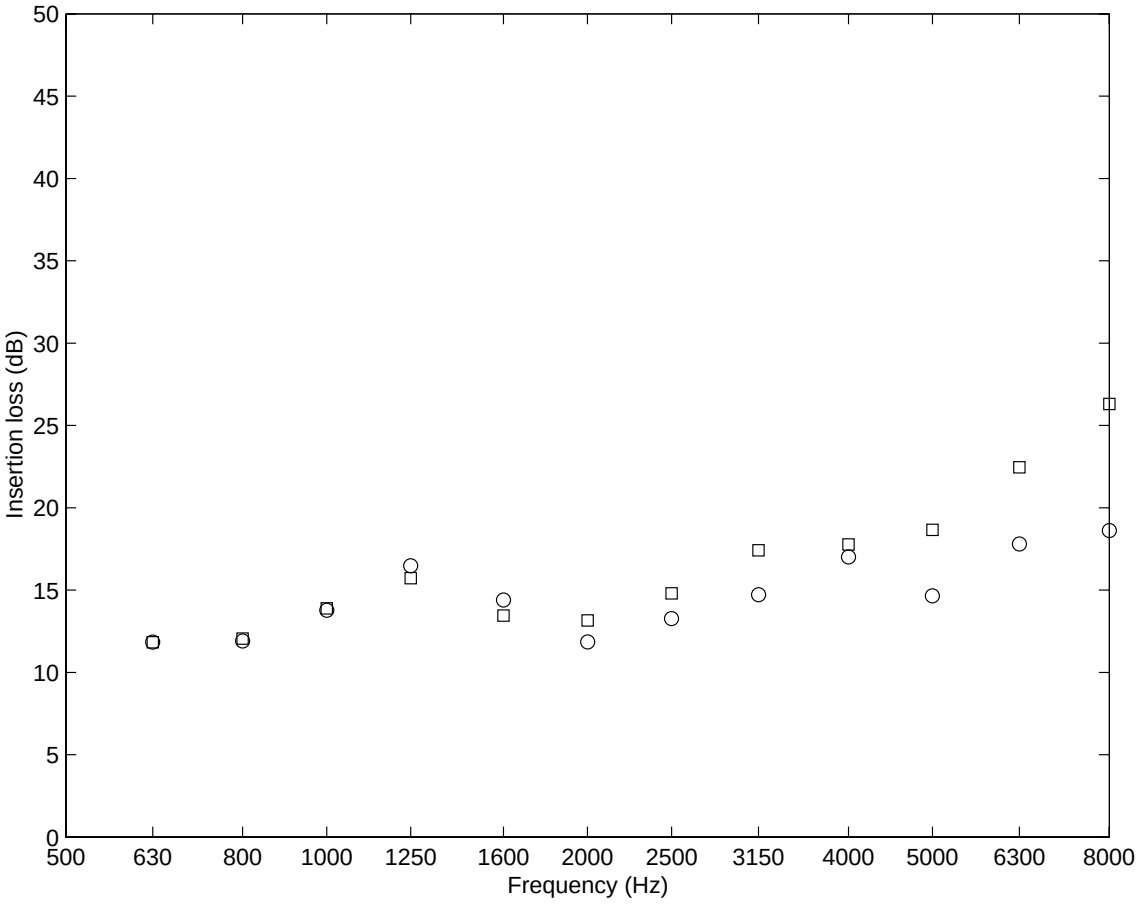

Figure 8.17. Comparison of insertion loss at the 17.78 *cm* off the midpoint of the barrier height. ‘ ’: T-shape barrier with 15.24 *cm* wide top; ‘□’: T-shape barrier with 15.24 *cm* wide top with sound absorptive treatment.

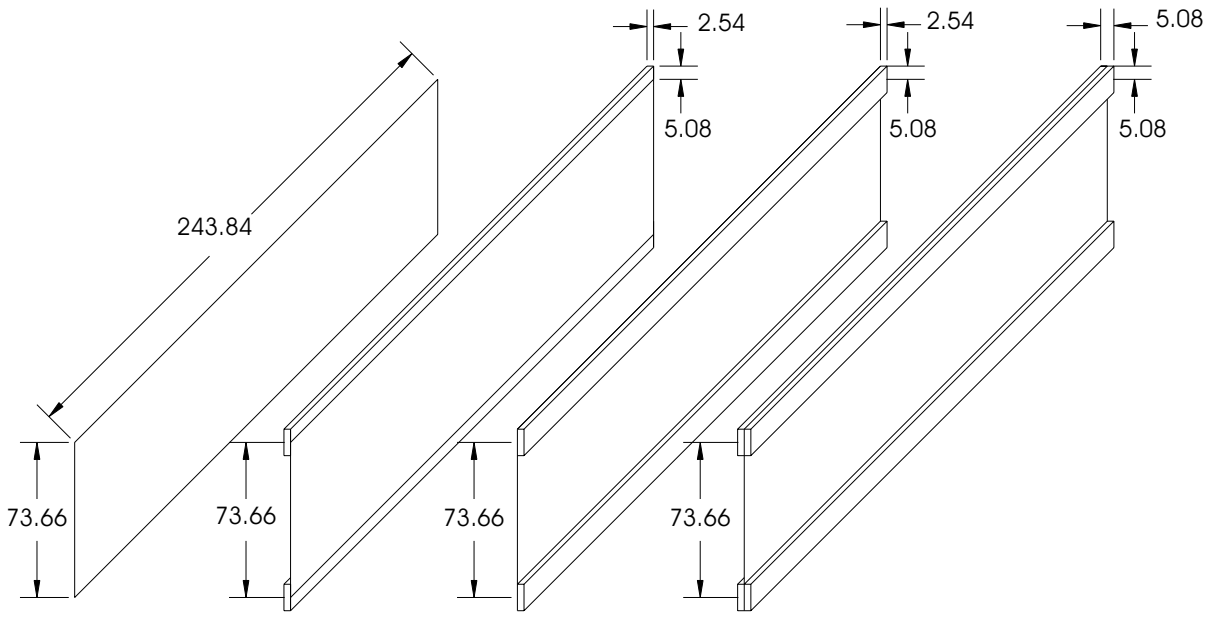

Figure 8.18. Geometry of the extended sound absorptive material on the barrier edge.

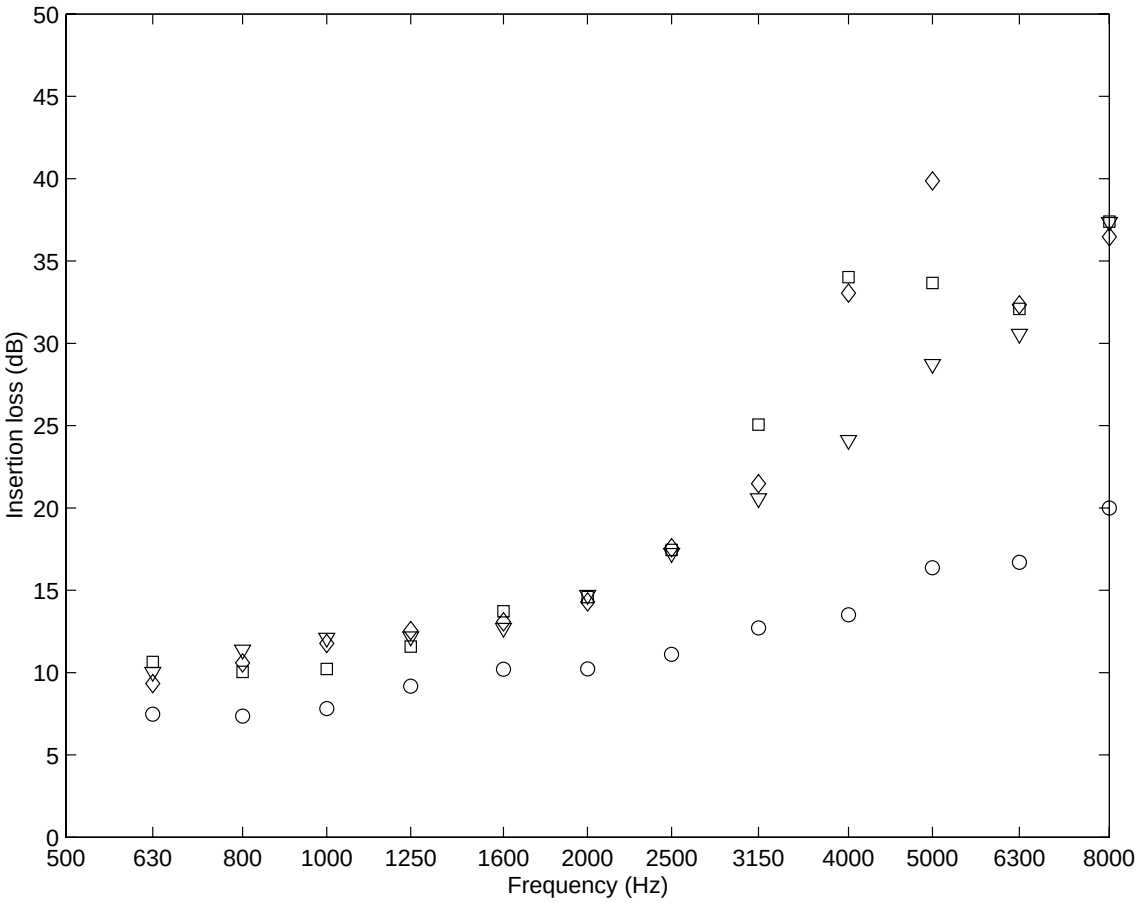

Figure 8.19. Comparison of insertion loss at the midpoint of the barrier height. ‘ ’: basic straight barrier; ‘□’: straight barrier with 10.16 *cm* wide and 2.54 *cm* thick fiberglass on the front with 5.08 cm overlap with the rigid barrier; ‘◇’: straight barrier with 10.16 cm wide and 2.54 cm thick fiberglass on the rear with 5.08 cm overlap with the rigid barrier straight; ‘ ’: straight barrier with 10.16 cm wide and 2.54 cm thick fiberglass on both sides with 5.08 cm overlap with the rigid barrier.

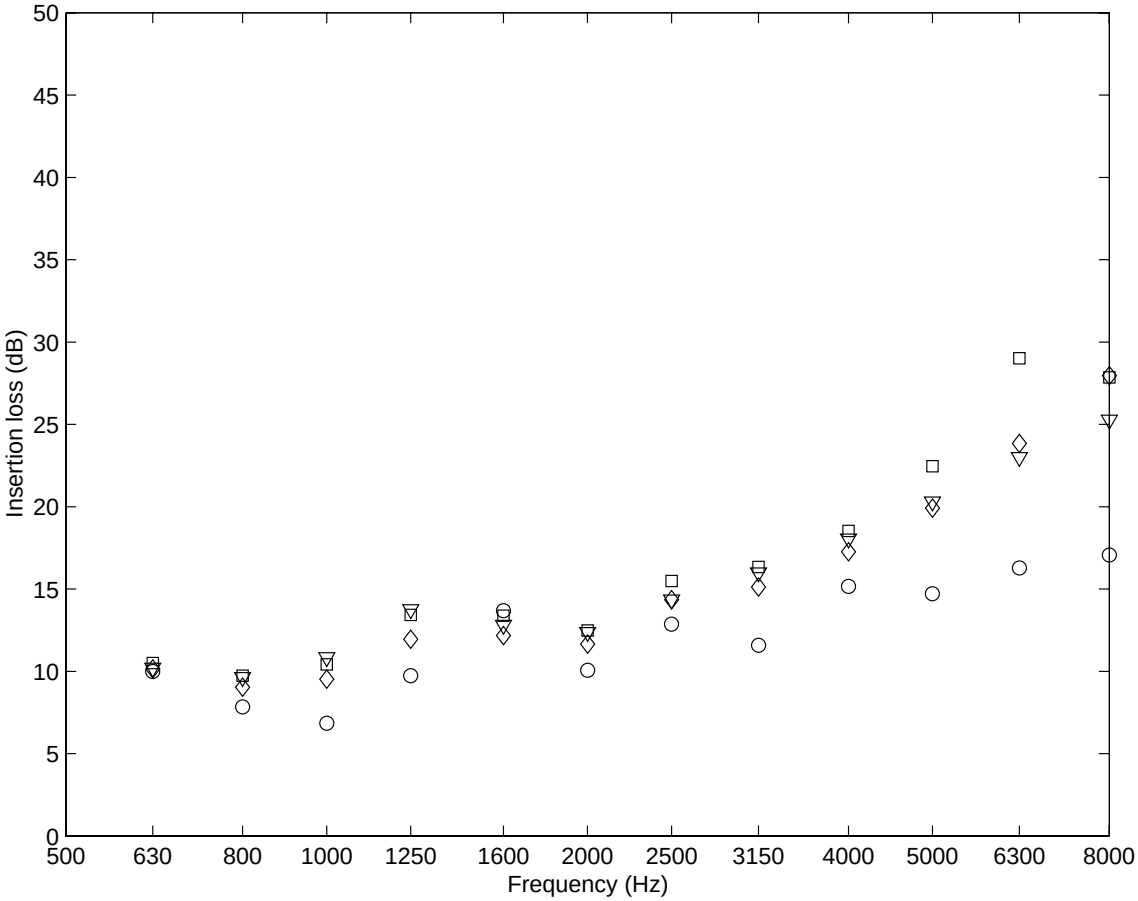

Figure 8.20. Comparison of insertion loss at the 17.78 *cm* off the midpoint of the barrier height. ‘ ’: basic straight barrier; ‘□’ straight barrier with 10.16 cm wide and 2.54 cm thick fiberglass on the front with 5.08 cm overlap with the rigid barrier; ‘◇’: straight barrier with 10.16 cm wide and 2.54 cm thick fiberglass on the rear with 5.08 cm overlap with the rigid barrier straight; ‘ ’: straight barrier with 10.16 cm wide and 2.54 cm thick fiberglass on both sides with 5.08 cm overlap with the rigid barrier.

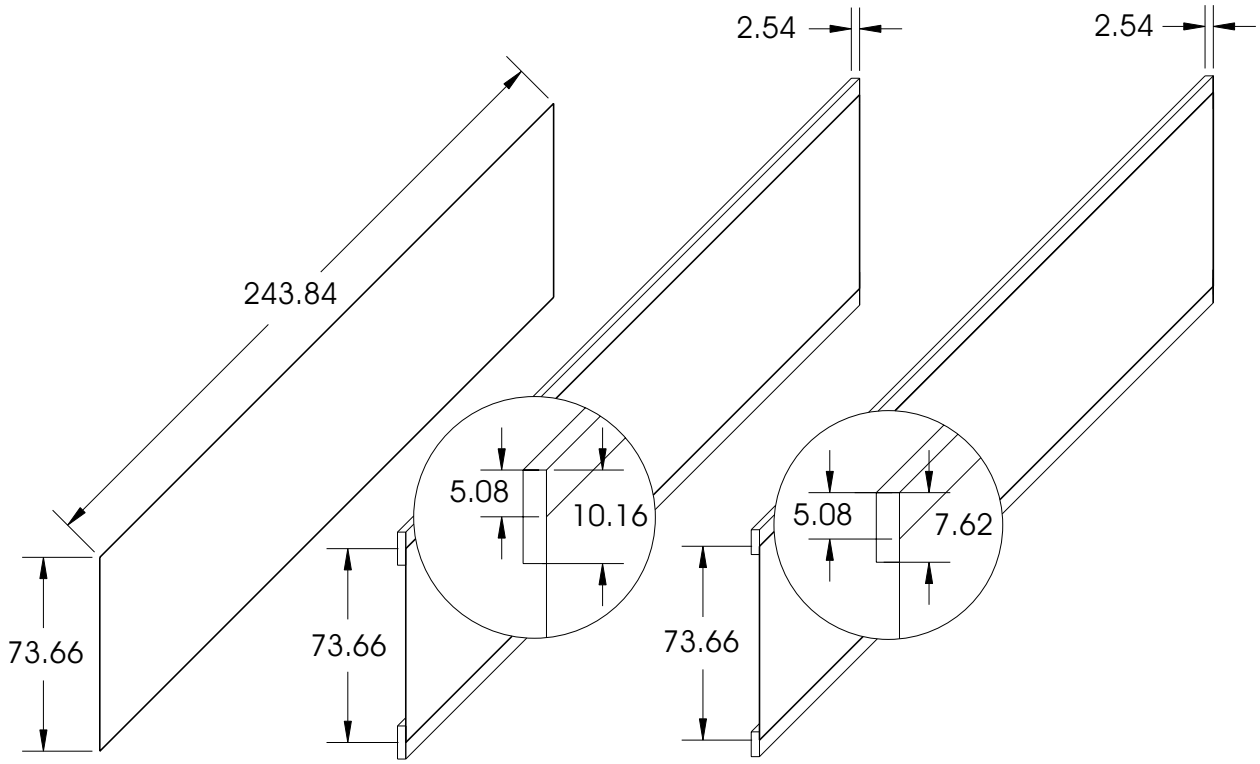

Figure 8.21. Geometry of the overlapped sound absorptive material on the barrier edge.

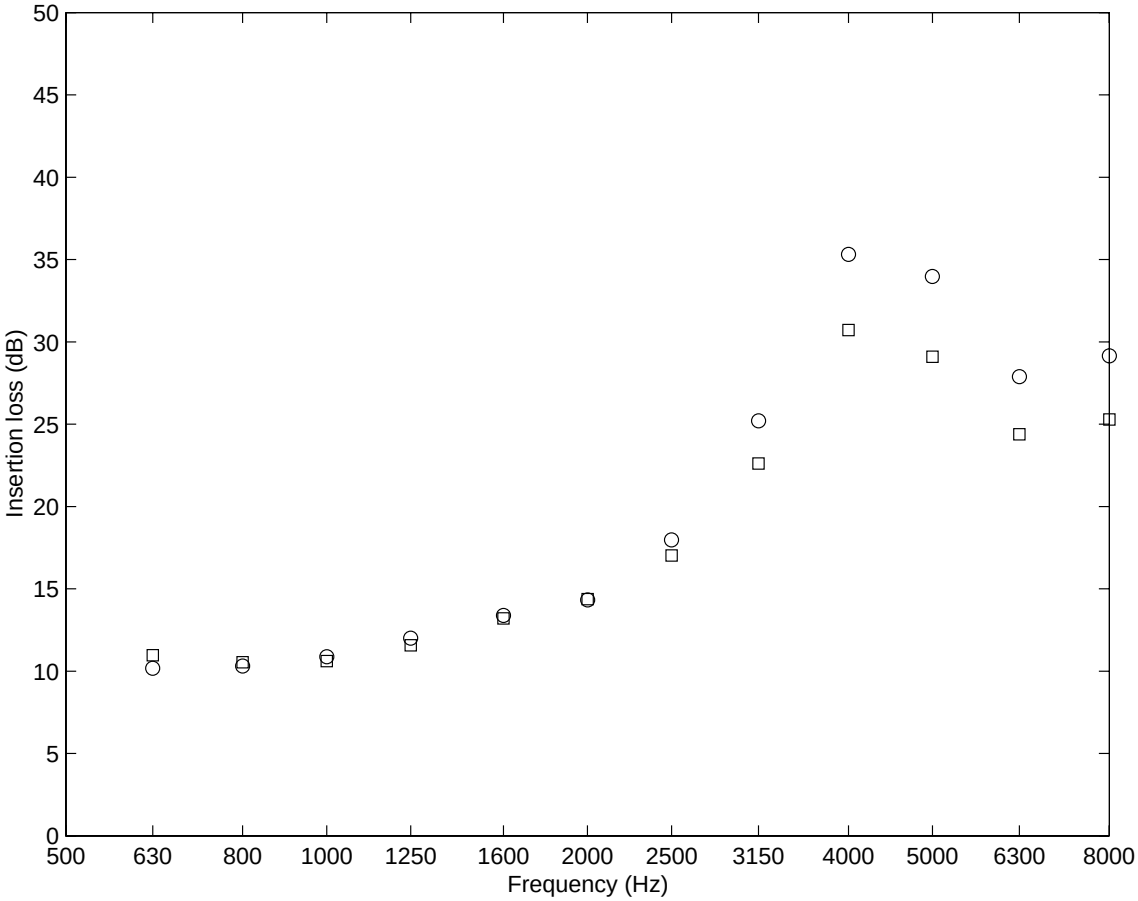

Figure 8.22. Comparison of insertion loss at the midpoint of the barrier height. ‘ ’: straight barrier with 10.16 *cm* wide and 2.54 *cm* thick fiberglass with 5.08 cm overlap with the rigid barrier; ‘□’: straight barrier with 7.62 *cm* wide and 2.54 cm thick fiberglass with 2.54 cm overlap with the rigid barrier.

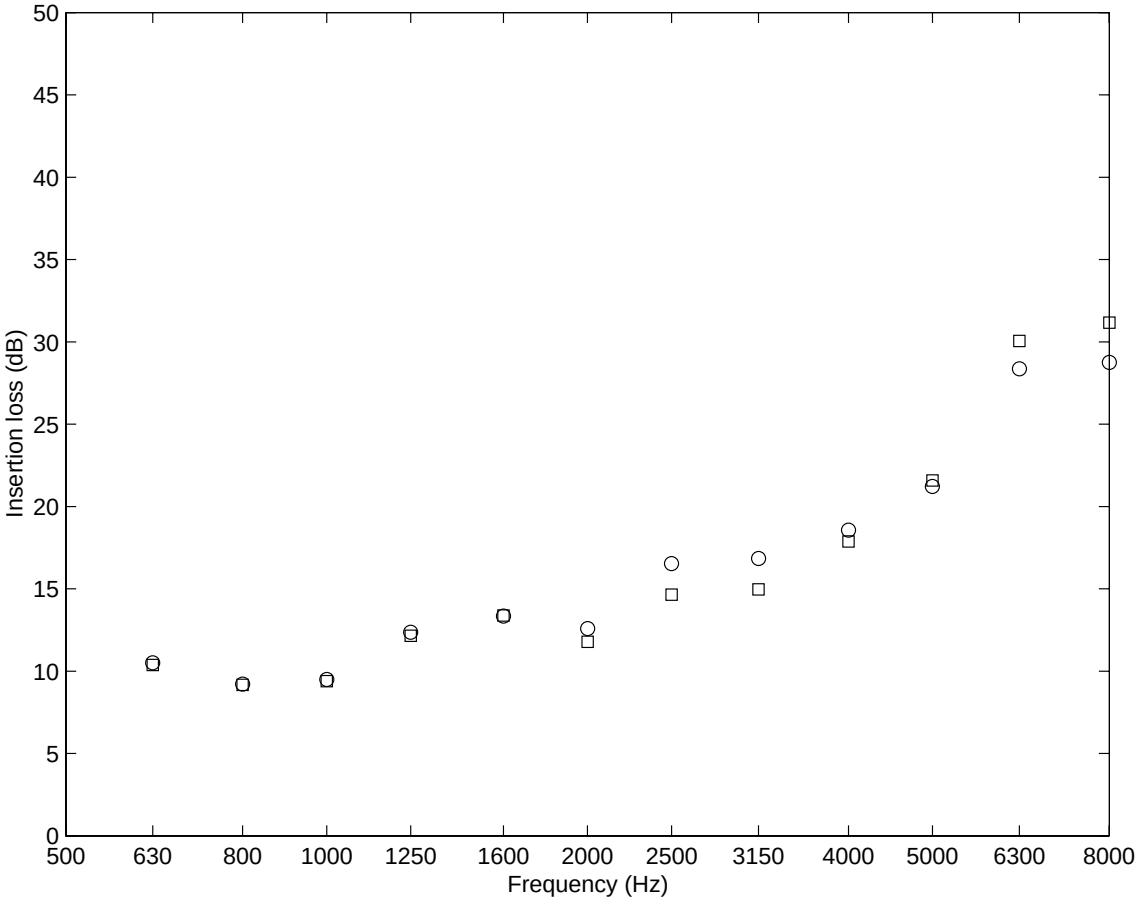

Figure 8.23. Comparison of insertion loss at the 17.78 *cm* off the midpoint of the barrier height. ‘ ’: straight barrier with 10.16 cm wide and 2.54 cm thick fiberglass with 5.08 cm overlap with the rigid barrier; ‘□’: straight barrier with 7.62 *cm* wide and 2.54 cm thick fiberglass with 5.08 cm overlap with the rigid barrier.

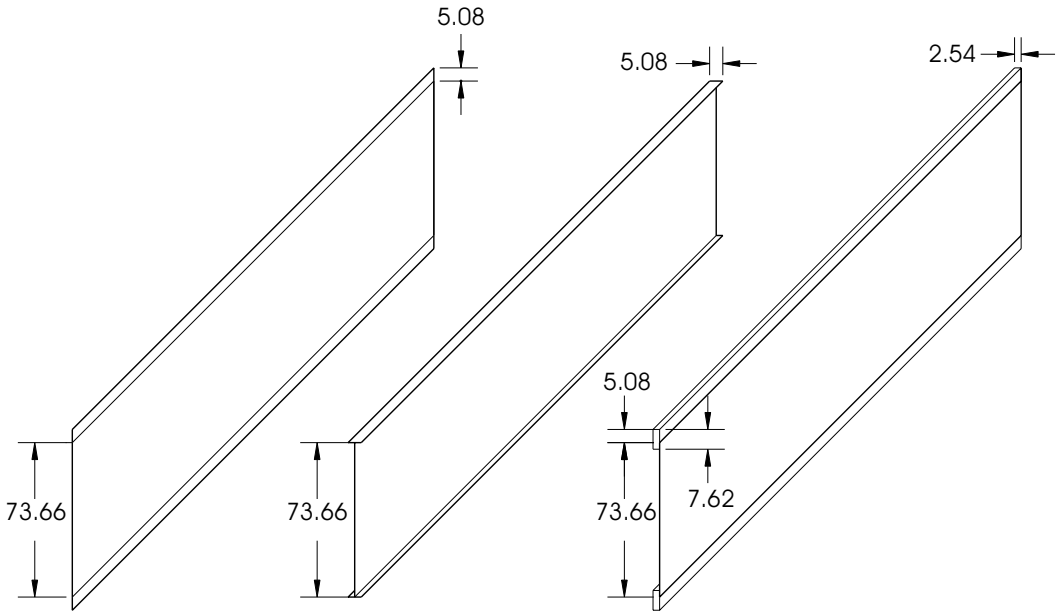

Figure 8.24. Configuration of various barrier designs.

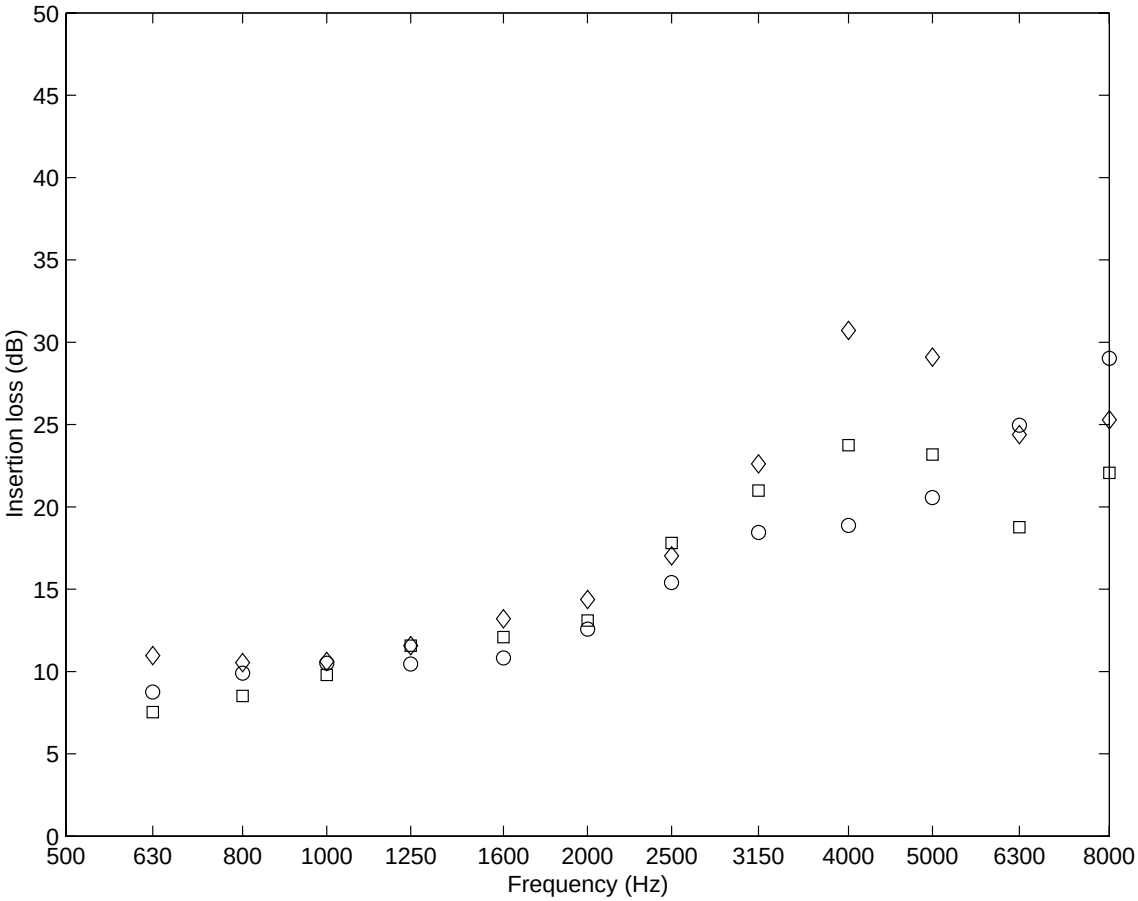

Figure 8.25. Comparison of insertion loss at the midpoint of the barrier height. ‘ ’: basic barrier with 5.08 *cm* extension; ‘□’: T-shape barrier with 5.08 *cm* wide cap, ‘◇’: straight barrier 7.62 *cm* wide sound absorptive treatment (2.54 *cm* overlap).

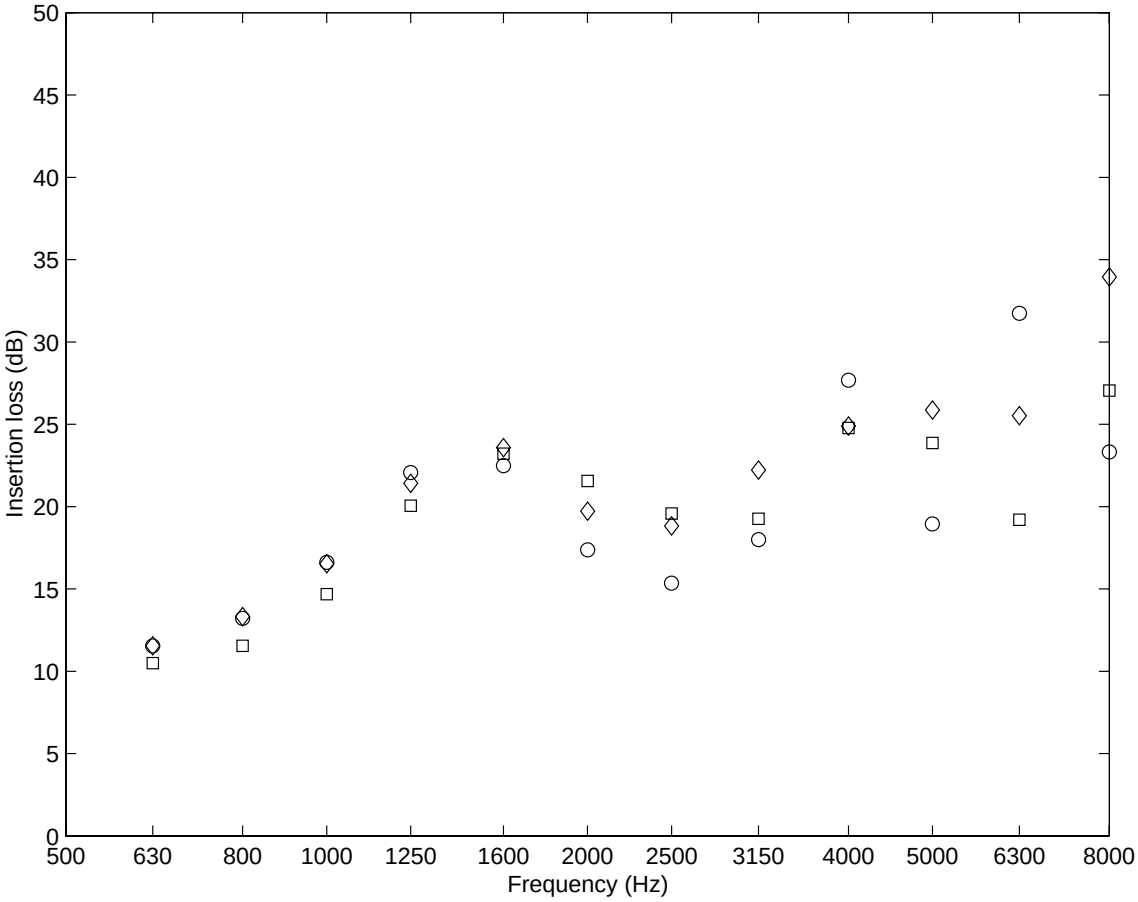

Figure 8.26. Comparison of insertion loss at the 5.08 *cm* off the midpoint of the barrier height. ‘ ’: basic barrier with 5.08 *cm* extension; ‘□’: T-shape barrier with 5.08 *cm* wide cap; ‘◇’: straight barrier 7.62 *cm* wide sound absorptive treatment (2.54 *cm* overlap).

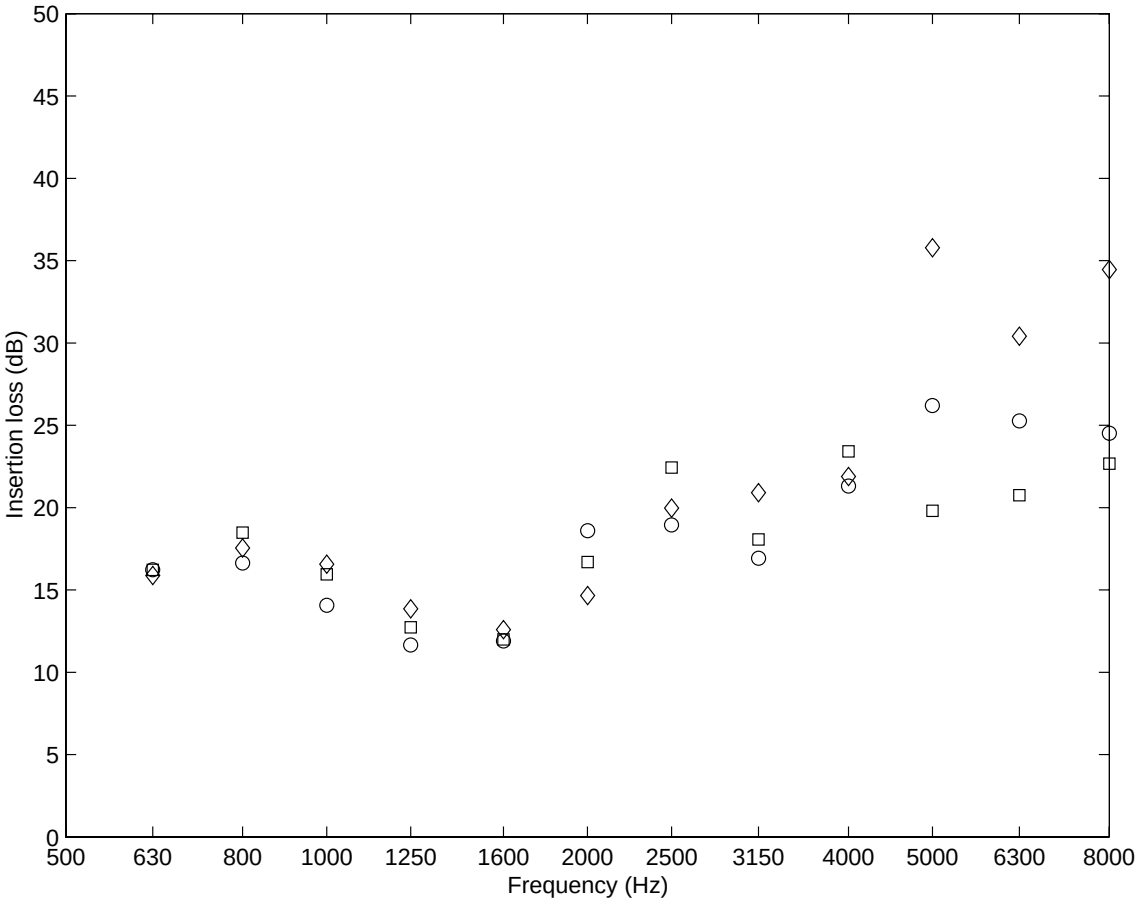

Figure 8.27. Comparison of insertion loss at the 10.16 *cm* off the midpoint of the barrier height. ‘ ’: basic barrier with 5.08 *cm* extension; ‘□’: T-shape barrier with 5.08 *cm* wide cap; ‘◇’: straight barrier 7.62 *cm* wide sound absorptive treatment (2.54 *cm* overlap).

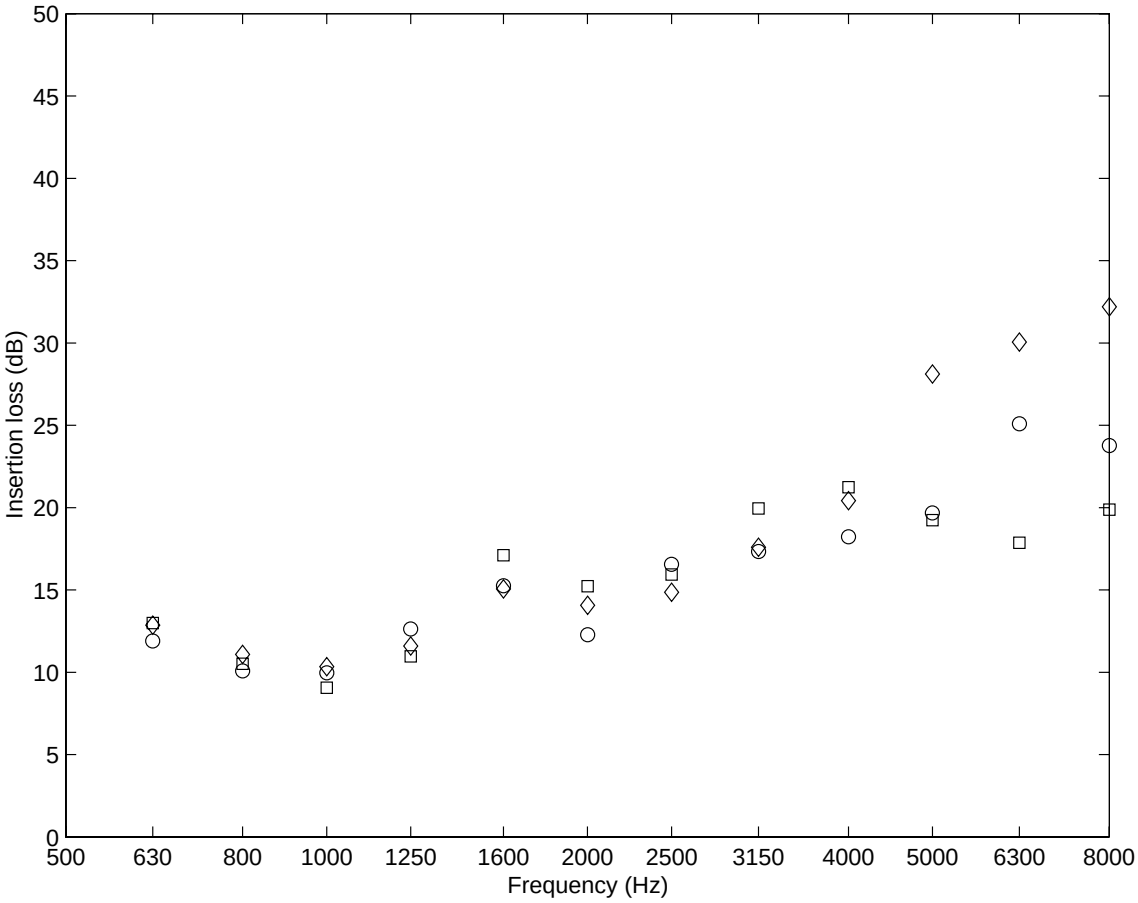

Figure 8.28. Comparison of insertion loss at the 15.24 *cm* off the midpoint of the barrier height. ‘ ’: basic barrier with 5.08 *cm* extension; ‘□’: T-shape barrier with 5.08 *cm* wide cap; ‘◇’: straight barrier 7.62 *cm* wide sound absorptive treatment (2.54 *cm* overlap).

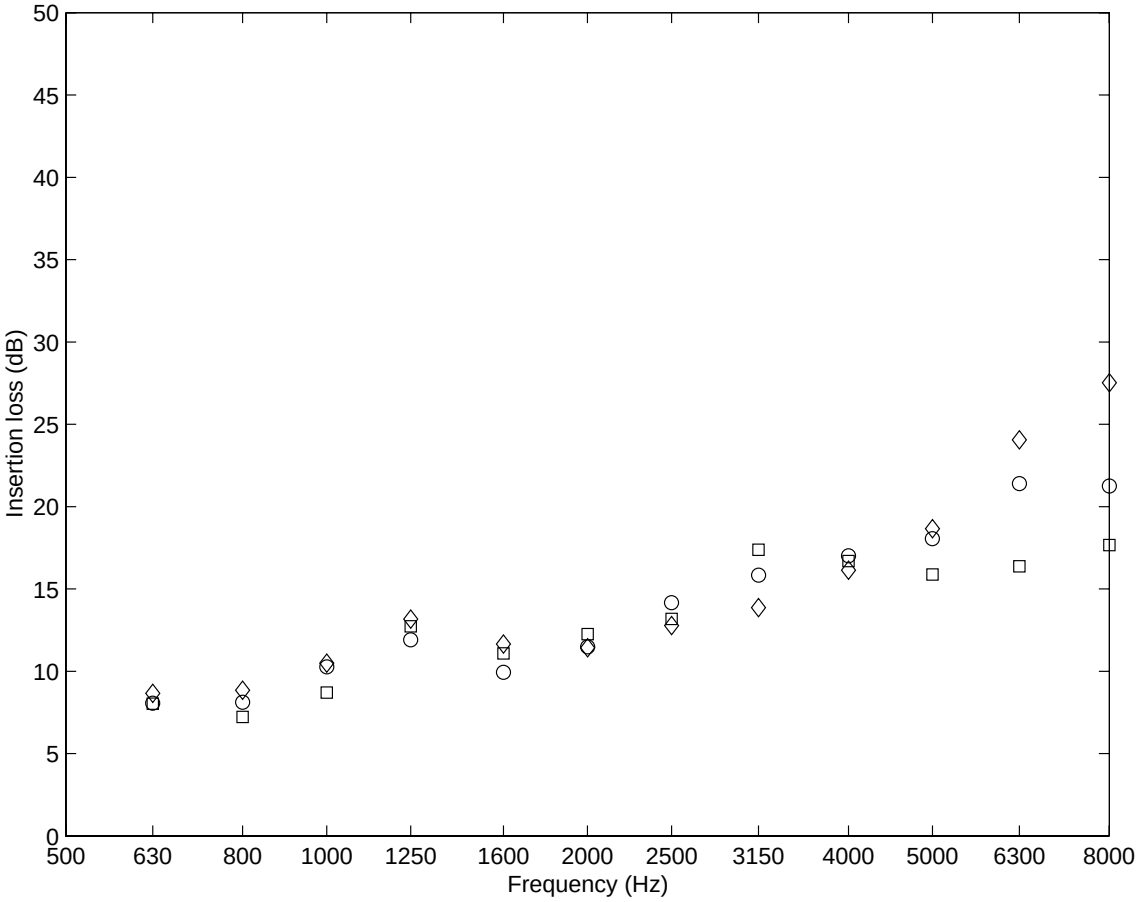

Figure 8.29. Comparison of insertion loss at the 20.32 *cm* off the midpoint of the barrier height. ‘ ’ basic barrier with 5.08 *cm* extension; ‘□’: T-shape barrier with 5.08 *cm* wide cap; ‘◇’: straight barrier 7.62 *cm* wide sound absorptive treatment (2.54 *cm* overlap).

9. CONCLUSION

The application of the boundary element method to the analysis of the noise barrier problem has been considered here, along with associated experimental work.

First, the boundary element model for the simple geometry of a circular disk was verified against experimental results. It was shown that varying the shape of the disk geometry alters the insertion loss at particular receiver locations, a finding that was verified using the numerical model. However, the shaped disks did not result in any significant advantage compared to the uniform disk when the sound power in the shadow region was used as a metric for barrier performance rather than the single point insertion loss. It was suggested as a result of these findings that the performance of a barrier having a relatively complicated geometry can be quantified most effectively by using a sound power based metric.

Scale models that were intended to represent highway noise barrier applications were considered next. A two-dimensional analysis was first performed to study the limitations of the widely used diffraction-based model. The performance of the finite length barrier was studied both with a boundary element model and with experiments. A post-processing technique that involves windowing in the time domain and filtering in the frequency domain was successfully implemented to eliminate experimental errors.

Following on from that work, the performance of various barrier configurations was compared. The performance of T-shaped barriers was compared with that of the equivalent straight barriers with extended height. It was found that the T-shaped barrier does not give a significant improvement over the simple extended barrier. The use of acoustical treatment on the top of the T-shape was also examined. It was found that the use of sound absorptive material results in improved insertion loss,

but mostly at high frequencies.

Finally, the use of sound absorptive material to extend the barrier height was considered as were the effect of positioning and overlap. It was found that sound absorptive treatments placed on the barrier edge are very effective at increasing the insertion loss at receiver locations deep in the shadow zone behind the barrier. It was illustrated that a glass fiber extension was more effective than a rigid extension, for example. In contrast, the use of complex geometries built of rigid materials, a T-shaped barrier, for example, did not result in a significant enhancement of the noise barrier performance.

The development of more sophisticated numerical modelling tools is required to predict the performance of noise barriers when the sound absorptive treatments without hard backing are applied to otherwise rigid barrier structures.

LIST OF REFERENCES

LIST OF REFERENCES

[1] Indiana toll road noise study for lake and porter counties. Technical report, Indiana Department of Transportation, Division of Preliminary Engineering & Environment, 1998.

[2] A. Sommerfeld. Mathematische theorie der diffraction. *Mathematische Annalen*, 47:317–374, 1896.

[3] H. M. MacDonald. A class of diffraction problems. *Proceedings of London Mathematical Society*, 14:410–427, 1915.

[4] J. B. Keller. Geometrical theory of diffraction. *Journal of the optical society of America*, 52(2):116–130, 1962.

[5] A. D. Pierce. Diffraction of sound around corners and over wide barriers. *Journal of Acoustical Society of America*, 55(5):941–955, 1974.

[6] R. Seznec. Diffraction of sound around barriers: Use of the boundary elements technique. *Journal of Sound and Vibration*, 73(2):195–209, 1980.

[7] D. C. Hothersall, S. N. Chandler-Wilde, and N. M. Hajimirzae. Efficiency of single noise barriers. *Journal of Sound and Vibration*, 146(2):303–321, 1991.

[8] D. Duhamel. Efficient calculation of the three-dimensional sound pressure field around a noise barrier. *Journal of Sound and Vibration*, 197(5):547–571, 1996.

[9] D. C. Hothersall, D.H. Crombie, and S. N. Chandler-Wilde. The performance of t-profile and associated noise barriers. *Applied Acoustics*, 32:269–287, 1991.

[10] G. F. Butler. A note on improving the attenuation given by a noise barrier. *Journal of Sound and Vibration*, 32(3):367–369, 1974.

[11] A. D. Rawlins. Diffraction of sound by a rigid screen with a soft or perfectly absorbing edge. *Journal of Sound and Vibration*, 45(1):53–67, 1976.

[12] A. D. Rawlins. Diffraction of sound by a rigid screen with a soft or perfectly absorbing edge. *Journal of Sound and Vibration*, 47(4):523–541, 1976.

[13] K. Fujiwara. Noise control by barriers. *Applied Acoustics*, 10(2):147–159, 1977.

[14] K. Fujiwara and N. Furata. Sound shielding efficiency of a barrier with a cylinder at the edge. *Noise control engineering journal*, 37(5):5–11, 1991.

[15] M. Moser and R. Volz. Improvement of sound barriers using headpieces with finite acoustic impdeance. *Journal of Acoustical Society of America*, 106(6):3049–3060, 1999.

[16] G. R. Watts and N. S. Godfrey. Effects on roadside noise levels of sound absoprtive materials on nosie barriers. *Applied Acoustics*, 58:385–402, 1999.

[17] Z. Maekawa. Noise reduction by screens. *Applied Acoustics*, 1:157–173, 1968.

[18] U. J. Kurze and G. S. Anderson. Sound attenuation by barriers. *Applied Acoustics*, 4:35–53, 1971.

[19] E. J. Rathe. Note on two common problems of sound attenuation. *Journal of Sound and Vibration*, 10(3):472–479, 1969.

[20] W. Bowlby, J. Higgins, and J. Reagan. Noise barrier cost reduction procedure: Stamina2.0 / optima: User's manual. Technical Report FHWA-DP-58-1, U.S. Department of Transportation Federal Highway Administration, Arlingoton, VA, 1982.

[21] G. S. Anderson, C. S. Y. Lee, G. G. Fleming, and C. W. Menge. FHWA traffic noise model, user's guide. Technical Report FHWA-PD-96-09, U.S. Department of Transportation Federal Highway Administration, Washington D.C., 1998.

[22] B. A. DeJong, A. Moerkerken, and J. D. van der Toorn. Propagation of sound over grassland and over an earth barrier. *Journal of Sound and Vibration*, 86(1):23–46, 1983.

[23] Y. W. Lam. Using maekawa's chart to calculate finite length barrier insertion loss. *Applied Acoustics*, 42, pages=, 1994.

[24] A. Muradali and K. R. Fyfe. A study of 2d and 3d barrier insertion loss using improved diffraction-based methods. *Applied Acoustics*, 53, pages=, 1998.

[25] T. Kawai, K. Fujimoto, and T. Itow. Noise propagation around a thin half plane. *Acoustica*, 38(?):313–323, 1978.

[26] D. N. May and M. M. Osman. The performance of sound absorptive, reflective, and t-profile noise barriers in toronto. *Journal of Sound and Vibration*, 71(1):65–71, 1980.

[27] K. B. Rasumssen. Model experiments related to outdoor propagation over an earth berm. *Journal of Acoustical Society of America*, 962(6):3617–3620, 1994.

[28] W. E. Scholes, A. C. Salvidge, and J. W. Sargent. Field performance of a noise barrier. *Journal of Sound and Vibration*, 16(4):627–642, 1971.

[29] G. R. Watts, D. H. Crombie, and D. C. Hothersall. Acoustic performance of new designs of traffic noise barriers: full scale tests. *Journal of Sound and Vibration*, 177(3):289–305, 1994.

[30] C. B. Burroughs and A. R. Bontomase. Noise propagation paths for highway noise barriers. In *INTER-NOISE 2001*, 2001.

[31] C. Steele. A critical review of some traffic noise prediction models. *Applied acoustics*, 62:271–287, 2001.

[32] J. L. Rochat. Observations of highway traffic noise measurements behind barriers and comparisons to FHWA's traffic noise. In *INTER-NOISE 2001*, 2001.

[33] R. L. Wayson, J. M. MacDonald, W. Arner, C. Corbisher, P. Tom, D. S. R. K Srinivas, and Brian Kim. Noise barrier measurement, modeling and evaluation at multiple sites in florida. In *INTER-NOISE 2001*, 2001.

[34] R. D. Ciskowski and C. A. Brebbia, editors. *Boundary element methods in acoustics*. Computational Mechanics Publications, Southampton, 1991.

[35] C. A. Brebbia and J. Dominguez. *Boundary elements an introductory course*. Computational Mechanics Publications, Southampton, third edition, 1992.

[36] T. W. Wu, editor. *Boundary element acoustics: Fundamentals and computer codes*. WIT press, Southampton, 2000.

[37] P. Menounou, M. R. Bailey, and D. T. Blackstock. Edge wave on axis behind an aperture or disk having a ragged edge. *Journal of Acoustical Society of America*, 107(1):103–111, 2000.

[38] LMS International, Leuven, Belgium. *SYSNOISE User's Guide*, 5.5 edition, 2001.

[39] MSC.Software Corporatoin, Santa Ana, U.S.A. *MSC.PATRAN User's Guide*, 9.0 edition, 2000.

[40] Spectral Dynamics, San Jose, U.S.A. *Siglab User's Guide*, 3.2.4 edition, 1998.

[41] S. T. Ho, I. J. Busch-Vishniac, and D. T. Blackstock. Noise reduction by a barrier having a random edge profile. *Journal of Acoustical Society of America*, 101(5):2669–2676, 1997.